

THÈSE

En vue de l'obtention du

DOCTORAT DE L'UNIVERSITÉ DE TOULOUSE

Délivré par :

Institut National Polytechnique de Toulouse (INP Toulouse)

Discipline ou spécialité :

Energétique et Transferts

Présentée et soutenue par :

M. LUCAS ESCLAPEZ

le vendredi 22 mai 2015

Titre :

NUMERICAL STUDY OF IGNITION AND INTER-SECTOR FLAME PROPAGATION IN GAS TURBINE

Ecole doctorale :

Mécanique, Energétique, Génie civil, Procédés (MEGeP)

Unité de recherche :

CERFACS (CERFACS)

Directeur(s) de Thèse :

MME BENEDICTE CUENOT

MME ELEONORE RIBER

Rapporteurs :

M. BENOIT FIORINA, ECOLE CENTRALE DE PARIS

M. FABIEN HALTER, UNIVERSITE D'ORLEANS

Membre(s) du jury :

M. MARC BELLENOUE, UNIVERSITE D'ORLEANS, Président

M. BRUNO RENOU, INSA ROUEN, Membre

Mme BENEDICTE CUENOT, CERFACS, Membre

Mme ELEONORE RIBER, CERFACS, Membre

Contents

1 Introduction **1**

1.1 Motivations 1

1.2 Aeronautical combustion systems 3

1.3 Ignition in aeronautical gas turbines 7

1.4 Objectives and outline 11

I Turbulent reactive flows **13**

2 Conservation equations for turbulent reactive flows **15**

2.1 Multispecies thermodynamics 15

2.2 Navier-Stokes equations 16

2.3 Transport properties 18

2.4 Chemical kinetics 18

3 Fundamentals of turbulent combustion **21**

3.1 Introduction 21

3.2 Laminar flames 22

3.3 Turbulent flames 31

4 Modeling of turbulent reactive flows **39**

4.1 Computationnal approaches 40

4.2 LES modeling 41

4.3 Combustion modeling 45

4.4 Chemical scheme for LES 49

4.5 Numerical methods in AVBP 53

II Single burner ignition **55**

5 Literature review on kernel initiation and expansion **57**

5.1 Phase 1: Initiation of a self-sustained expanding flame kernel 57

5.2 Phase 2: kernel expansion and transient flame propagation 65

5.3 Conclusion 76

6 Non-reacting flow in the KIAI single burner **77**

6.1 Experimental test rig 78

6.2 Numerical set-up 80

6.3 Non-reacting flow characteristics 82

6.4 Conclusion 93

7 Ignition of the KIAI single burner **95**

7.1 Experimental results 96

7.2 Numerical simulations 98

7.3 Numerical set-up 99

7.4 Results 102

7.5 Conclusions 128

8 Model for prediction of ignition probability **131**

8.1 Ignition probability models: literature review 132

8.2 Derivation of the model 137

8.3 Results 155

8.4 Conclusions 159

III Inter-sector flame propagation **161**

9 Inter-sector flame propagation: literature review **163**

10 Inter-sector flame propagation in KIAI multi-injector burner **167**

10.1 Experimental configuration 168

10.2 Numerical Set-up 169

10.3 Non-reacting flow 171

10.4 Flame propagation modes 175

10.5 Flame propagation mechanisms . . . 185
10.6 Conclusion . . . 192

11 Light-round in the MICCA annular combustion chamber 195
11.1 Experimental configuration . . . 196
11.2 Numerical set-up . . . 197
11.3 Non-reacting flow . . . 199
11.4 Ignition sequence . . . 203

12 Conclusions and Perspectives 213

Annexes 235

A Kernel Density Estimation 237

B Flame displacement speed in TFLES 239
B.1 Theoretical framework . . . 239
B.2 1D laminar test case . . . 241
B.3 2D cylindrical case . . . 243
B.4 3D turbulent ignition case . . . 246
B.5 Conclusion . . . 248

Acknowledgements

Je voudrais tout d'abord remercier les membres du Jury: B. Fiorina et F. Halter d'avoir relu et évalué le contenu de ce manuscrit, B. Renou, M. Bellenoue et S. Richard de les avoir rejoints au CERFACS pour assister à la soutenance et animer une séance de discussion intéressante et pleine de perspectives.

Je remercie ensuite mes encadrantes, Bénédicte Cuenot et Eleonore Riber, qui m'ont permis de mener à bien ces travaux dans un cadre de travail idéal, en y apportant leur expérience, leur enthousiasme et leur passion pour la recherche et la combustion. Je remercie aussi Thierry Poinsot de m'avoir en quelque sorte attiré au CERFACS à l'issue de mon cursus ingénieur, ainsi que de son accueil dans le groupe Combustion. Par ailleurs, cette thèse n'aurait pas existée sans le financement et le support de SNECMA, et en particulier de M. Cazalens, qui a suivi ces travaux tout au long de ces trois années.

Mes remerciements vont aussi à l'ensemble des séniors de l'équipe Combustion, qui ont toujours su m'apporter une oreille attentive ainsi que des conseils pertinents qui m'ont permis de résoudre les problèmes de thésard du quotidien: Laurent, Gabriel, Olivier, Antoine, Florent et dernièrement Jérôme. En parlant de problèmes de thésard du quotidien, il est difficile de ne pas remercier Marie et Nicole pour leur aide précieuse, l'ensemble de l'équipe CSG dont le travail nous facilite grandement la vie, ainsi que toute l'administration.

Je ne manquerai pas non plus de remercier l'ensemble des thésards CFD, et en particulier la bande qui a commencée fin 2011. L'équipe Coinche: Antho, Micka, Corentin, Raph pour l'ensemble de votre oeuvre dans les domaines du Panache, de la mauvaise foi et de la Chance Insolente qui sont venus agrémenter nos pauses du midi. A la mémoire de Dédé et Jojo, qui ont su remplir nos estomacs pendant les longues soirées d'hiver. A l'équipe Canyon: Raph, Corentin, Charlie pour ces weekends passé à faire de l'huile et des toboggans. A quand, le saut du Marc ? A Micka, Antho, Corentin, Raph, Dorian, Thomas, Charlie, Adrien également, pour les nombreuses boissons à base d'eau et de malt que nous avons partagées ainsi que les bons repas mijotés par Corentin. Et à tous les sportifs qui ont dû enchaîner les séances de grimpe et de Pelote pour compenser ! Un grand merci aussi à Greg, qui m'a guidé dans les méandres d'AVBP, de l'Euler-Euler et du CERFACS à mon arrivée; ainsi qu'à David avec qui j'ai travaillé sur KIAI et qui m'a lancé sur la bonne voie, dès mes débuts. A ceux qui viennent de finir ou qui finissent bientôt: Abdulla, Manqi, Dimitrios, Thomas J., Laure, Anne, ... A l'ensemble des plus jeunes, enfin, qui se préparent bientôt à finir et qui n'en voient pas (encore) le bout.

Cette thèse a aussi donné lieu à une merveilleuse rencontre. Anne avec qui je partage ma

vie depuis quelques mois maintenant, qui a su me faire sortir de mes soirée "monotâche" et qui a su m'accompagner pendant cette période pas toujours facile. J'espère que notre belle histoire se poursuivra pendant de longues années ponctuées de beaux moments et de ptits me voyages. Finalement, je tiens à remercier ma famille qui m'a soutenu dans ma démarche et qui a participé à la conclusion de ces trois années.

Ainsi la contemplation de la flamme pérennise une rêverie première. Elle nous détache du monde et elle agrandit le monde du rêveur. La flamme est à elle seule une grande présence, mais, près d'elle, on va rêver loin, trop loin: on se perd en rêveries. La flamme est là, menue et chétive, luttant pour maintenir son être, et le rêveur s'en va rêver ailleurs, perdant son propre être, en rêvant trop grand en rêvant au monde. La flamme est un monde pour l'homme seul.

La Flamme d'une Chandelle, Gaston Bachelard (1884-1962)

À mon père.

Nomenclature

Roman characters

Symbol	Definition
$\dot{\mathcal{Q}}_{sp}$	Spark energy source term
$\mathcal{A}$	Pre-exponential constant
$\mathcal{E}$	Efficiency function
$\mathcal{F}$	Thickening factor
$\mathcal{I}_{PFI}$	Flammability indicator
$\mathcal{K}$	Flame curvature
$\mathcal{Q}_j$	Progress rate of the reaction
$\mathcal{R}$	Perfect gases universal constant
c	Progress variable
C_p	Constant pressure heat capacity
C_v	Constant volume heat capacity
D_k	Molar diffusivity of the mixture
D_{th}	Thermal diffusivity
E	Total energy
E_a	Activation energy
F_f	Flammability factor
F'_f	Flammability dispersion
h_s	Sensible enthalpy
I_{tk}	Takeno index

J	Species diffusion flux
K_{eq}	Equilibrium constant
$K_{f,j}$	Forward reaction rate
$K_{r,j}$	Reverse reaction rate
L_{sp}	Inter-injector spacing (Chap. 10)
l_t	Integral length scale
P	Pressure
P_{ign}	Ignition probability
P_{ker}	Probability of kernel initiation
q	Heat flux
s	Stoichiomtrique mass ratio
S_c	Flame consumption speed
S_d	Flame displacement speed
S_T	Turbulent flamme speed
$S_{i,j}$	Velocity deformation tensor
S_L^0	Laminar flame speed
T	Temperature
u_i	Velocity component
V^c	Correction diffusion velocity
V^k	Diffusion velocity of species k
W	Molar mass
X	Molar fraction
Y	Mass fraction
z	Mixture fraction

Non-dimensional numbers

Symbol	**Definition**
Da	Damkhöler number

Ka	Karlovitz number
Le	Lewis number
Pr	Prandtl number
Pr^t	Turbulent Prandtl number
Re	Reynolds number
Re_t	Turbulent Reynolds number
S_w	Swirl number
Sc_k	Schmidt number of species k
Sc_k^t	Turbulent Schmidt number
St	Strouhal number

Superscript

Symbol	**Definition**
sgs	Subgrid-scale contribution
t	Turbulent contribution

Greek characters

Symbol	**Definition**
χ	Scalar dissipation rate
δ_r	Reactive layer thickness
Δ_s	Energy deposit diameter (ED model)
Δ_t	Energy deposit duration (ED model)
$\delta_{i,j}$	Kronecker symbol
δ_L^0	Flame thickness
$\dot{\omega}_k$	Reaction rate of species k
$\dot{\omega}_T$	Heat release rate
η_k	Kolmogorov length scale

γ_r	Flame kernel shape ratio
κ	Flame stretch
λ	Thermal conductivity
μ	Dynamic viscosity
ν	Kinematic viscosity
ν''_{kj}	Products stoichiometric coefficient
ν'_{kj}	Reactants stoichiometric coefficient
ν_{kj}	Global stoichiometric coefficient
ν_t	SGS viscosity
ϕ	Equivalence ratio
ρ	Density
Σ	Flame surface density
τ_c	Chemical time scale
τ_k	Turbulence Kolmogorov time scale
τ_t	Turbulence integral time scale
$\tau_{i,j}$	Viscous stress tensor
ε	Dissipation rate
ε_i	Energy deposit energy (ED model)

Subscripts

Symbol	**Definition**
0	Initial state
b	Burnt gas state
c	Critical
F	Fuel
f	Fresh gas state
fl	Flame
i	i-th component

j	j-th reaction
K	Kolmogorov
k	k-th species
ker	Kernel
O	Oxidizer
st	Stoichiometric
rms	*(root mean square)*

Acronyms

Symbol	**Definition**
AV	Artificial Viscosity
CFD	Computational Fluid Dynamics
CRZ	Corner Recirculation Zone
DNS	Direct Numerical Simulation
DTF	Dynamically Thickened Flame
ED	Energy Deposition model
FCG	Flame center of gravity
IRZ	Inner Recirculation Zone
LES	Large Eddy Simulation
LW	Lax-Wendroff
MIE	Minimum Ignition Energy
NGV	Nozzle Guide Vane
NSCBC	Navier-Stokes Characteristic Boundary Condition
OPR	Overall Pressure Ratio
PDF	Probability Density Function
PEA	Pre-exponential Adjustment
PLIF	Planar Laser-Induced Fluorescence
PVC	Precessing vortex core

RANS	Reynolds Averaged Navier-Stokes
RHS	Right Hand Side
SGS	Sub-Grid Scale
SPIV	Stereo Particle Image Velocimetry
SWJ	Swirled Jet
TFLES	TF model for LES
TTGC	Two-step Taylor-Galerkin version C

Chapter 1

Introduction

Contents

1.1 Motivations **1**
1.2 Aeronautical combustion systems **3**
1.2.1 Design of aeronautical combustors 3
1.2.2 Technologies of liquid injection systems 5
1.2.3 Technologies of ignition systems 6
1.3 Ignition in aeronautical gas turbines **7**
1.3.1 Current research on ignition process 8
1.3.2 Application to aeronautical gas turbines 10
1.4 Objectives and outline **11**

1.1 Motivations

Three major constraints drive the design of modern aeronautical engines: fuel consumption, noise and pollutant emissions. These constraints are driven by the growing market competition and increasing stringency of aeronautical pollution regulations. Fuel consumption and noise emissions are mostly controlled by overall design parameters such as overall pressure ratio (OPR) or bypass ratio, and details of turbine, compressor or exhaust design. Pollutant emissions, however, are largely governed by the combustor performances so that the combustion chamber design is directly affected by the regulatory constraints. Targeted pollutants are CO_2, NO_x, CO and unburned hydrocarbons, with particular attention to NO_x due to their higher health and environmental risks (Lee *et al.*, 2010). Indeed, a strong tightening of NO_x emissions regulation has been imposed over the last two decades. Figure 1.1 illustrates the evolution of NO_x emissions standards from CAEP2 (1991) to ACARE target (2020) (Advisory Council for Aeronautics Research in Europe, 2010) along with the emission levels of a large variety of current and future engines. The aim is to lower NO_x emissions by 80% by 2020.

Two main paths are currently investigated by engine manufacturers in order to reduce fuel consumption: increase of the propulsive efficiency with new technologies such as open-rotors (Hughes

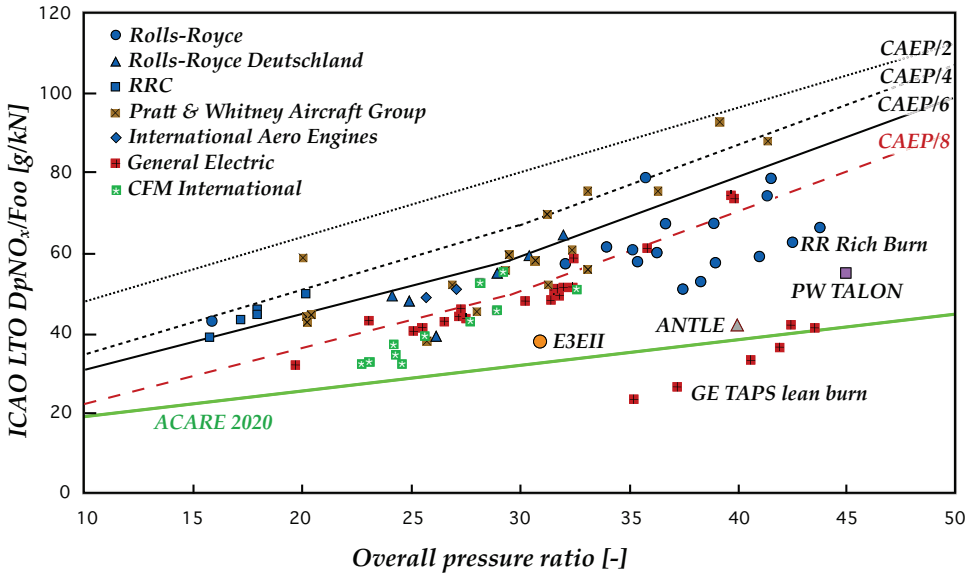

Figure 1.1: ICAO-CAEP NO_x stringency standards CAEP (2010)

& Gazzaniga, 1989) and increase of the core-engine cycle efficiency mainly through an increase of the OPR (up to 70 in the framework of the Low Emissions Core-Engine Technologies (LEMCOTEC) European project). One major drawback of increasing the OPR is the associated rise of combustor temperature, which in turns increases NO_x emissions (Lefebvre, 1998). To overcome this effect, engine manufacturers have developed several concepts: lean premixed prevaporised (LPP) (Allouis *et al.*, 2008), lean direct injection (LDI) (Read *et al.*, 2010) or multiple staged fuel injection (MSFI) (Barbosa *et al.*, 2009). As shown in Fig. 1.1, *low-NO_x* injection systems such as the GE TAPS can achieve the NO_x emissions targets set by the ACARE. *low-NO_x* designs rely on overall lean combustion to lower the maximum temperature in the combustor (Lefebvre, 1998). The design of *low-NO_x* combustors must also meet numerous constraints, the first being to guarantee a complete oxidation of fuel with a minimum pressure drop in order to maximize the overall efficiency. The design is further complicated by additional design elements required for the engine operability and maintenance: stable combustion regime without thermo-acoustic oscillation, efficient cooling of the structural elements or rapid and safe engine relight. All these requirements must be guaranteed over the wide range of operating conditions encountered in a flight envelope and often lead to contradicting technological solutions. One of the more stringent operability requirement is the relight capability: air safety regulations require engine in-flight relight capability at high altitude in the event of a flame-out. Similar constraints also drive the design of helicopter engines where the complex operational conditions require the engine to be back to full power in a handful of seconds. *low-NO_x* design increase the flow velocity in the combustor in order to reduce the equivalence ratio for a given amount of fuel. At the same time, engine designers tend to minimize the number of injection systems in order to cut down weight and maintenance costs. Both effects are detrimental to the relight capabilities and combined with the lack of feedback on these new designs, promote research for a better understanding of the ignition process in gas turbines.

1.2 Aeronautical combustion systems

1.2.1 Design of aeronautical combustors

When Frank Whittle in England and Hans Von Ohain in Germany invented the first jet engines in the 30ies, designing the combustion system appeared as an unsolvable issue. Indeed, the typical flow velocity at the compressor outlet of about 150 m/s, i.e. much higher than the turbulent flame velocity, was making the stabilization of the flame difficult. For the anecdote, H. Von Ohain, whose funding was about to be cut, tricked his sponsor using hydrogen during the demonstration of his first prototype since he could not manage to stabilize a kerosene/air flame.

Logically the first objective when designing a combustor was then to generate low velocity regions where the flame could survive. Early combustion chamber used obstacles called flame holders in the wake of which the flame was maintained. Nowadays, most combustors use swirled injection systems consisting of axial and/or radial swirlers which induce low velocity and/or backward velocity regions (Syred & Beér, 1974). Moreover, the additional rotation induces turbulence and increases mixing efficiency. Providing that the rotation is sufficiently strong, reverse flow regions are generated (Beer & Chigier, 1983) and act as a strong mechanism to stabilize the flame (Syred *et al.*, 1971). As shown in Fig. 1.2, the combustion system is generally preceded by a diffuser which smoothly reduces the incoming gas velocity with a limited pressure drop, and feeds a first cavity called the plenum which distributes the air between the injection system and the cooling of the structural parts of the combustion chamber.

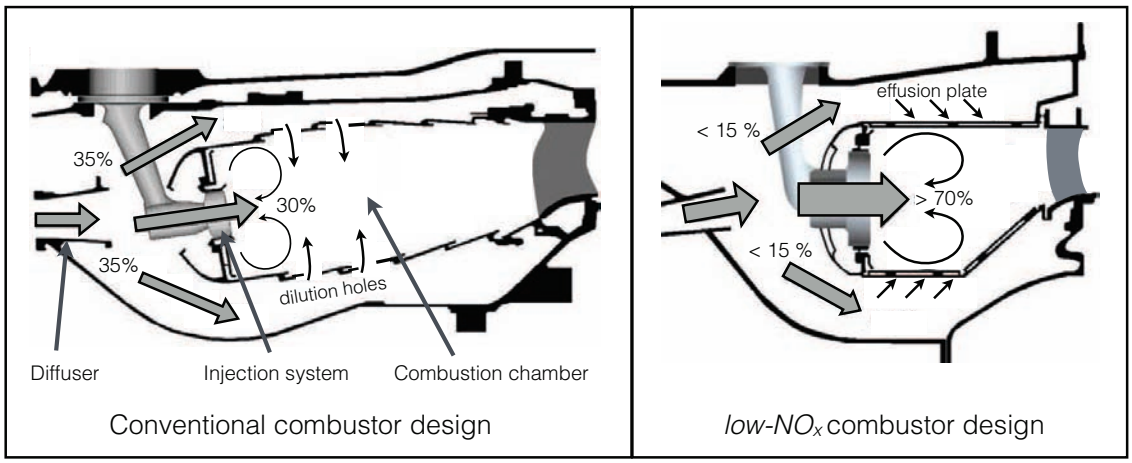

Figure 1.2: Typical design of conventional (left) versus low-NO_x (right) combustor (der Bank *et al.*, 2014).

Figure 1.2 shows both a conventional design and a *low-NO_x* concept to highlight the main differences. To achieve rapid mixing and reduction of the local equivalence ratio in the flame zone, a much larger portion of the flow goes through the injection system for *low-NO_x* design (70% vs. 30%). The combustor length is strongly reduced to minimize NO_x formation in the burnt gases since NO_x formation is directly linked to the residence time (Lefebvre, 1998). The primary zone of the conventional design located upstream of the dilution holes is suppressed. The

consequences of these technical changes are multiple:

- since most of the incoming air passes through the injection system the flame is leaner and more prone to thermo-acoustic instabilities in *low-NO_x* design.
- the reduced length of the combustor increases the temperature heterogeneities at the chamber exit, which can be destructive for the turbine.
- Since conventional design relies on low velocity and near stoichiometric conditions of the primary zone to achieve reliable ignition, *low-NO_x* design ignition capabilities are worse.

Ignition performance is usually expressed in terms of range of flight conditions over which combustion can be established. The size of the combustor is a critical design parameter that must be determined early in the design process and is generally dictated from the upper limit of the flight envelope where the relight constraint is critical (Nicholas, 2005). Indeed, the ignition capability is directly related to the residence time in the combustor, which must be higher than the ignition delay. In high altitude conditions, fuel evaporation, mixing and heat release processes are slowed down so that the ignition delays are maximum. Figure 1.3 shows the flight envelope in a Mach-altitude graph along with iso-levels of temperature. Dashed lines show how the changes of the combustor volume affects the ignition performance: from the baseline design (thick dashed line), a reduction of the combustor volume reduces the residence time and directly lowers the relight limit (Doerr, 2012). Finally, the combustor size is a trade-off between relight capability, weight and NO_x emissions.

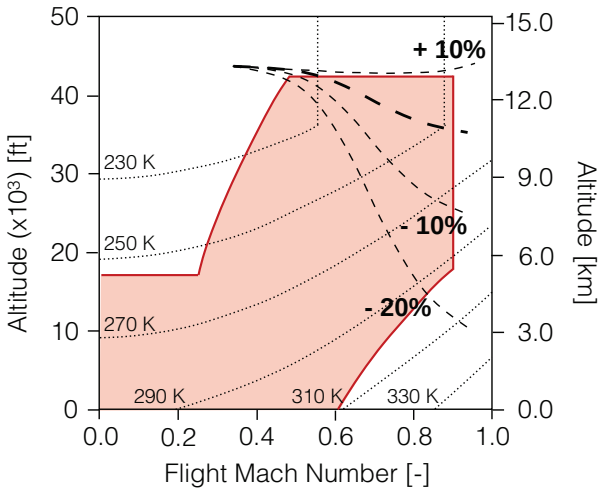

Figure 1.3: Effect of primary zone volume on the relight capability in an altitude-Mach number graph: thin dashed lines indicate ignition performances changing the combustor volume starting from an initial design (thick dashed line). Typical flight envelope (red) and isoline of temperature (dotted lines) are also reported. Adapted from (Doerr, 2012).

For conventional combustor design, engineers use a set of empirical correlations to scale the combustor dimensions adapted to new requirements, starting from an existing design (as shown is Fig. 1.3): dashed lines correspond to the empirical correlations, with the effect in a change in

the combustor volume (from -20% to +10%). These empirical design rules indicate the conditions that have been found to work in practice over a broad range of temperature, pressure and flow regime. But these rules do not rely on an appreciable understanding of the mechanisms involved nor indicate possible improvement paths. These design methods may be sufficient for conventional designs where the igniter is generally located in the primary zone of the combustor, in a region of relatively low fluid velocity and of mixture close to stoichiometry. However, *low-NO_x* designs drastically modify the flow, the spray and the spark igniter layout and these correlations do not hold anymore. The higher flow velocity at the spark position, the lower equivalence ratio, the shifted position of the spark igniter relative to the reverse flow regions have direct consequences on the flame kernel residence time at ignition, that are however not well understood. To address this issue, advanced experimental and numerical researches have been conducted over the last decade to support the design process with a sound understanding of the mechanisms in play. A specific issue of the relight constraint is that the volume of the combustion chamber must be decided early in the design process of the engine but it can only be validated late, when the combustor is installed in an experimental test bench reproducing sub-atmospheric conditions. Relight failure at this stage of the engine development would invalidate the whole design with huge financial consequences, since relight capabilities are mandatory for engine certification. The development of numerical tools able to validate the choice of the volume earlier in the design process would greatly be beneficial and help optimizing the igniter and combustor design.

1.2.2 Technologies of liquid injection systems

For their high energetic density and ease of handling, liquid fuels are employed in the vast majority of aeronautical gas turbines and must be vaporized prior to burn. In realistic high altitude conditions, the liquid phase can significantly affect the ignition performance because of the detrimental effect of the low temperature and low mass flow rate. The prime function of the injector is to increase the exchange surface between liquid and air by breaking up the liquid fuel in small droplets in order to enhance phase exchanges. Taking advantages of the strong air velocity generated by the injection system, liquid kerosene injection is generally intricately arranged with the injection system in order to efficiently atomize, disperse and evaporate the fuel. Several technologies have been developed and can be combined to ensure an efficient atomization of the liquid (Lefebvre, 1989):

- **Pressure atomizers**: the liquid fragmentation results from the pressure drop between the pressurized fuel lines and the combustion chamber pressure. The main advantage is that the droplet size is almost independent of the operating conditions but is rather controlled by the feeding line pressure and the injector nozzle design.
- **Vaporizer**: fuel is injected into a tube placed in the primary zone of the combustion chamber. The high temperature conditions around the tube allows a rapid vaporization of the fuel prior entering the combustion chamber but this can be highly detrimental to the tube lifetime due to high heat flux.
- **Air-blast atomizers**: rely on the air velocity to atomize the fuel. Fuel impacts the swirler passage walls and the resulting liquid film driven by the air flow towards an atomizing lip where the fuel is disintegrated into small droplets. This technology avoids using high

pressure supply lines, reducing the complexity and weight of the fuel system. However, at low power operation (as encountered during in-flight relight), the air velocity can be too low to ensure a sufficiently good atomization.

The fine droplets resulting from the primary and secondary atomization processes are then dispersed and mixed by the turbulent flow generated by the injection system, favoring premixed and pollutant free combustion. At in-flight relight conditions, the use of a pressure atomizer is favored since the air mass flow rate is too low to achieve fine droplets atomization with an air-blast atomizer.

1.2.3 Technologies of ignition systems

In aeronautical gas turbines, ignition is triggered by energy deposit since the conditions prior to ignition preclude the possibility of auto-ignition. Ignition systems are used to convert and transmit external energy (either electrical or chemical) to the gas and their design has a significant influence on the first phase of ignition. The igniter type, power and location are generally dictated by maintenance and accessibility constraints. For instance high power sparks may increase the ignition probability but lead to a faster erosion of the spark plug tip and more maintenance costs. Furthermore, due to the complexity of the engine auxiliary systems and the redundancy required in aviation, the space available for the igniter integration is generally very limited so that its size is an important parameter. Igniters are used in various applications with specific constraints which have led to the development of numerous researches. For instance, in spark ignited internal combustion engines, the number of ignition cycles is huge ($\simeq 10^7$) with a fairly high frequency (up to 40 Hz) and the spark must be reproducible with a high precision to avoid abnormal combustion. In gas turbines, the number of cycles and the frequency are lower but the flow conditions are less favorable for ignition success so that the power must be higher than for internal combustion engines. The major technical choices of igniter that have potential for gas turbines are a handful:

- **Spark plug** is the most commonly used igniter in gas turbines and ground transportation engines. Gas turbine sparks are usually constituted of a central electrode and a grounded outer electrode, the two being separated by a ceramic insulator. At the spark tip, the insulator terminates in a thin layer of semiconductor to ease ionization of the gap between electrodes (Lefebvre, 1998). An electrical circuit supplies a high voltage (greater than the breakdown voltage of the air gap between the electrodes) and enables to control the spark duration. Once the gas located within the gap is ionized, an intense electric arc is formed and only a small portion of its energy is transmitted to the surrounding gas (between 10% to 30% according to Teets & Sell (1988) and Maly & Vogel (1978)) due to losses in the electrical circuit, shock waves, radiation and conduction into the electrodes. Spark plugs suffer from one major drawback: their location is limited to the wall vicinity where significant heat losses to the cold wall can be encountered during the flame kernel growth.

- **Laser** is currently worked on by many research groups and is already used in lab-scale experiments (Bradley *et al.*, 2004). The purpose again in this case is to create a kernel

large and hot enough to generate a self-sustained flame. Here, the spark results from laser-induced breakdown where the photon radiation accelerates electrons at the focal point. High energy electrons are then able to ionize nearby molecules resulting in an increase of the medium opacity and the transmitted energy. Within 10 ns, a plasma approaching 100000 K and 1000 $atms$ is created in the ionized volume (Phuoc & White, 1999), which leads to the creation of a powerful shock wave (Phuoc & White, 2002). Contrary to spark plug, laser enables to control the deposit location. However, lasers are highly sensitive to high temperature so that the engine environment has prevented its use in realistic applications.

- **Torch igniter** is the combination of a spark plug and an auxiliary fuel jet (Lefebvre, 1998). It is generally employed in cryotechnic rocket engines but can also be found in gas turbines. The spark/fuel jet arrangement allows a safe ignition of the fuel jet and the hot gases produced ignite the neighbor burners. The main problem with torch igniter is its complexity and size that generally preclude its use in aeronautical gas turbines.

- **Plasma jet igniter** is close to the classical spark plug, but two successive sparks are used (Mittinti & Dabora, 1984). During the first spark, the gas contained in a small cavity at the igniter tip is ionized. The second spark induces a large overpressure in the small cavity, and a plasma jet issues from the igniter. The plasma is then located far from the combustor walls, which reduces heat losses to the walls. The main drawback of these igniters is the rapid erosion of the plasma cavity, preventing their use in spark ignition engines or gas turbines.

Current engines use classical spark plug igniters to initiate ignition sequences because of their relatively small size and ease of integration, reducing maintenance cost. However, the spark plug tip can suffer from excessive erosion due to wetting of its surface and a high energy deposit is required to overcome the effect of detrimental operating conditions and losses to the nearby walls. A better understanding of the ignition process could lead to significant improvement of the spark plug lifetime if the spark energy can be reduced and the spark position optimized.

1.3 Ignition in aeronautical gas turbines

Flame extinction inside a gas turbine can be caused by a quick modification of the air-flow through the engine during aircraft maneuvers or severe ingestion of ice or water. Even though such events are rare, the capability to perform an in-flight engine restart is mandatory and is the more stringent design criterion for the combustion chamber. The ignition of a gas turbine is a complex transient process, starting from the very small time and length scales at the spark deposit to the complete light-up of all injectors. To draw a clear picture of the numerous factors influencing the ignition process, it is generally decomposed in three successive phases identified by Lefebvre (1998) and sketched in Fig. 1.4:

- **Phase 1:** formation of flame kernel of sufficient size and temperature to be able to be propagated.

- **Phase 2:** propagation and first burner ignition to flame stabilization.

- **Phase 3:** spreading of the flame to all burners in the combustor, referred to as inter-sector flame propagation or light-round phase.

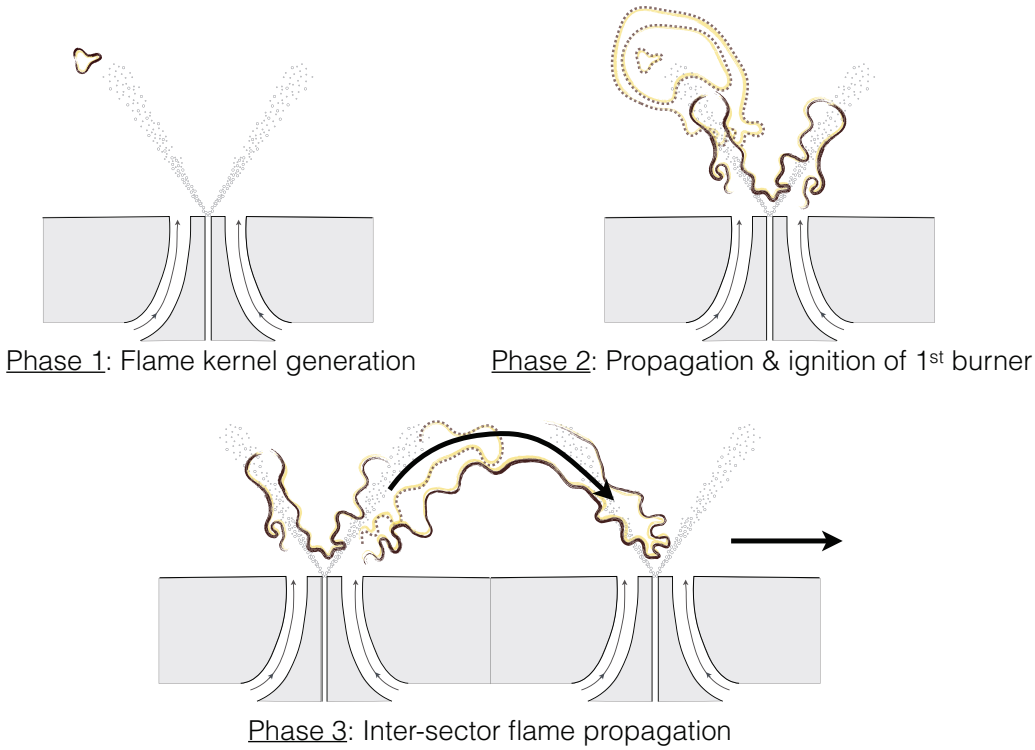

Figure 1.4: Schematic illustration of the ignition process. **Phase 1:** flame kernel creation, **Phase 2:** single burner ignition and **Phase 3:** light-around (Lefebvre, 1998).

A successful ignition is achieved if the combustor reaches a stable combustion state once the ignition system is turned off. For in-flight restart, a last phase might be added during which the progressive increase of heat release accelerates the gas turbine to its operational speed. This phase can be critical since an increase of the flow velocity could result in a blow-off if flames are not fully stabilized on the injectors. It is also interesting to note that Mastorakos (2009) split **Phase 2** into flame growth and burner ignition as distinct mechanisms. A failure of any of these steps will result in a failure of the engine ignition. This succession of phases helps to identify the critical parameters influencing each individual mechanism and point out which phase is the bottleneck to better performance.

1.3.1 Current research on ignition process

1.3.1.a Creation of a sustainable flame kernel

The igniter locally transfers energy from an auxiliary source to the flowing mixture. The ability of this energy source to initiate a sustainable flame kernel depends on multiple parameters and

it has been studied by numerous authors in the context of gas turbines (Ballal & Lefebvre, 1975; Rao & Lefebvre, 1976; Ballal & Lefebvre, 1977; Ouarti *et al.*, 2003), internal combustion engines (Pischinger & Heywood, 1990; Boudier *et al.*, 1992; Dale *et al.*, 1997; Dahms *et al.*, 2011) or fire safety (Lewis & von Elbe, 1987; Eckhoff *et al.*, 2010). The initiation of a flame kernel can be sufficiently simplified to perform theoretical studies (Zeldovich *et al.*, 1980; Deshaies & Joulin, 1984; Champion *et al.*, 1986; Vasquez-Espi & Linan, 2002): ignition can be triggered if the rate of heat released by the chemical reaction exceeds that of heat losses to the surrounding by molecular and turbulent transport. Theoretical and experimental researches introduce the concept of Minimum Ignition Energy (MIE) identified as the minimum energy required to initiate a flame kernel (Joulin, 1985; Lewis & von Elbe, 1987). The MIE is found to depend on the geometrical details of the igniter (Lewis & von Elbe, 1987; Kono *et al.*, 1984; Ko *et al.*, 1991), the mixture composition (Lewis & von Elbe, 1987; Ziegler *et al.*, 1985), the flow conditions and the turbulence level (Beduneau & Kim, 2003; Shy *et al.*, 2010; Cardin, 2013). Due to variability of both the deposited energy and initial flow field, **Phase 1** of ignition is a stochastic process. In turbulent flows, MIE is then defined statistically as the energy required to obtain typically 50% of ignition success (Kono *et al.*, 1984). The initiation of a sustainable flame kernel will be reviewed in further details in Chap. 5.

1.3.1.b Kernel growth and flame propagation

Once a flame kernel is created, it must expand and propagate to stabilize on the closest injector during **Phase 2**. Once again, the early flame growth and propagation are of interest for both gas turbines and internal combustion engines applications (Akindele *et al.*, 1982; Bradley *et al.*, 1996; Eichenberger & Roberts, 1999). As the kernel expands, it starts interacting with turbulence and transitions from a laminar to a turbulent propagating flame (Abdel-Gayed *et al.*, 1988; Bradley *et al.*, 2004). The kernel expansion has been studied in simple and well defined experimental configurations (Abdel-Gayed *et al.*, 1984; Renou, 2001; Mansour *et al.*, 2008; Galmiche *et al.*, 2012) where the effect of the turbulence on the kernel growth rate was highlighted: for low to mild turbulence, the kernel growth is enhanced by increasing turbulence intensity while for high turbulence the growth rate stabilizes then drops as velocity fluctuations are increased. These results are supported by numerous numerical studies, mainly using Direct Numerical Simulation (DNS) (Poinsot, 1991; Gashi *et al.*, 2005; Jenkins *et al.*, 2006; Fru *et al.*, 2011; Reddy & Abraham, 2013) where the turbulence is found to increase the flame surface due to wrinkling but to be also responsible for significant flame quenching. The effect on mixture composition is less studied experimentally since it requires complex experimental set-ups (Renou *et al.*, 2004; Ahmed *et al.*, 2007*b*). The shape and wrinkling of the kernel is found to be affected by the spatial distribution of fuel and in non-premixed conditions the propagation is found to be that of an edge flame. DNS allows to further investigate the effect of the mixture fraction and its gradient on the kernel growth (Chakraborty & Mastorakos, 2006; Neophytou *et al.*, 2010) and the combustion regime. The flame kernel development and subsequent flame propagation will be reviewed in further details in Chap. 5.

A detailed study of the flame propagation and subsequent stabilization on the injector nozzle necessitates the development of larger and more complex test rigs (Ahmed & Mastorakos, 2006; Ahmed *et al.*, 2007*a*; Read *et al.*, 2008; Marchione *et al.*, 2009; Garcia-Rosa *et al.*, 2011; Gebel

et al., 2012; Cordier, 2013) where sophisticated diagnostics are needed to investigate the flame front behavior. The dynamics of the flame front following the kernel phase is found to be driven by the underlying flow pattern and in non-premixed conditions the flame pathway follows the contours of stoichiometric mixture fraction and might adopt a tribranchial structure. To evaluate the ignition performance of these configurations, experimental ignition probability maps are constructed. These maps allows to distinguish favorable ignition locations with respect to the flow pattern for a given amount of energy. Ignition success is found to be correlated to the ability of the flame to reach the injector nozzle, i.e. to enter recirculation zones. These studies are supported by numerical simulations performed with Large Eddy Simulation (LES) due to the higher geometrical complexity and computational cost (Lacaze *et al.*, 2009*b*; Triantafyllidis *et al.*, 2009; Jones & Tyliszczack, 2010; Subramanian *et al.*, 2010; Jones *et al.*, 2011; Barré, 2014). As a first result, these studies prove that LES is well suited for the study of ignition sequences in single injector configuration where the non-reacting flow must be reproduced accurately to capture the subsequent flame dynamic. The detailed study of the flame structure and dynamics during the ignition transient process shows that the ability of the flame to stabilize on the injector nozzle is related to low/backward velocity regions. The direct evaluation of the ignition performance (probability maps) using brute force LES is limited by the current computational resources which do not allow to compute numerous realizations. Several methodologies have been therefore developed to estimate the ignition probability only from one non-reacting computation (Wilson *et al.*, 1999; Richardson, 2007; Neophytou *et al.*, 2012; Eyssartier *et al.*, 2013). Such methodologies allow to rapidly evaluate the ignition performance of **Phase 1** and possibly of **Phase 2** in realistic combustors at a limited computational cost. A more detailed review on the ignition probability models is proposed in Chap. 8.

1.3.1.c Light-around

In the last phase, the flame must propagate from one burner to its neighbor in order to finally light the full burner. This question is very little addressed in the open literature. The pioneering work of Boileau *et al.* (2008) focused on the ignition dynamics of a simplified annular helicopter combustor and demonstrated the capability of LES to tackle such complex flows. The authors also highlighted the effect of the burnt gases expansion on the flame propagation and the overall ignition delay but no experiments were available to validate the results. This topic has undergone recent progress with the development of in-line (Cordier, 2013) or annular (Bach *et al.*, 2013; Bourgouin *et al.*, 2013) multi-injector test rigs. Although limited to gaseous flows, these studies investigate the effect of the inter-injector spacing and the inlet mass flow rate on the light-around dynamics and shed some light on the mechanisms driving propagation and flame stabilization. Two of these test rigs are studied numerically in this thesis and will be described in Chaps. 10 & 11.

1.3.2 Application to aeronautical gas turbines

In gas turbines, the question regarding the igniter location is often raised as it directly affects the ignition performance and is strongly constrained by integration and maintenance issues. In a combustor, the local mixture and turbulence conditions can preclude ignition success regard-

less the amount of energy deposited and even if the spark is adequately located with respect to flammable mixture, the capability of the igniter to transfer energy to the gas can be strongly reduced by adverse conditions (such as wet surface of the igniter). In gas turbine, the igniter energy is then generally much higher than the MIE and the success of **Phase 1** mainly depends on the mixture flammability near the spark location (Lefebvre, 1998). The experimental and numerical studies in academic configurations clearly show that the flame kernel must be captured by the recirculation zone created by the injection system in order to increase the residence time. The increase of the flow in the combustor in *low-NO_x* design can be detrimental to the success of **Phase 2** because the increased turbulence level can quench the growing flame kernel and the higher mean flow velocity can blow the kernel out of the combustion chamber before it enters a recirculation zone. The ignition dynamics of flow at high turbulent conditions, closer to realistic conditions, is then required to investigate the full range of mechanisms controlling the ignition probability. From a design perspective, the number of injection systems sets both the distance between two consecutive injectors and the mass flow rate therethrough. These two parameters thus directly affect the light-around dynamics. In the context of cost and weight savings, the number of injection systems could be reduced, but this has a detrimental effect on the flame propagation. Due to the complexity of direct experimental investigation of the light-around mechanism in fully integrated core-engine, the development of numerical tools is a promising path to improve our understanding of the governing mechanisms. Several other phenomena not targeted in the experimental rigs listed above can affect the light-around: 1) the pressure rise during the light-around phase can induce sonic conditions at the combustor outlet which act as a bottleneck: the volume of the combustor and the design of the interface between the combustion chamber and the nozzle guide vane (NGV) can modify the hot gases expansion through the chamber; 2) the liquid fuel distribution in the combustion chamber is a crucial factor since it controls the ability of inter-sector regions to burn.

1.4 Objectives and outline

Over the last 20 years, CERFACS has developed an expertise in Computational Fluid Dynamics (CFD) and more specifically in LES with the solver AVBP co-developed by CERFACS and IFPEN. Started in the early nineties by Schönfeld & Rudgyard (1999), AVBP has been developed by numerous Ph.D. students and researchers and has been applied to study turbulent combustion in complex configurations (Selle *et al.*, 2004; Giauque *et al.*, 2005; Boileau *et al.*, 2008; Wolf *et al.*, 2012). Started with the work of Pascaud (2006) and Boileau (2007), numerical studies of ignition with AVBP have been continued by Lacaze (2009), Eyssartier (2012) and Barré (2014). The work of Boileau (2007) focused on two-phase flow ignition in both single sector and full annular simplified configurations. In the Ph.D. of Lacaze (2009), a model to mimic the spark deposit was developed and validated, and the first qualitative comparison of LES with experiments for a turbulent free methane jet showed promising results. Eyssartier (2012) built a methodology to predict ignition probability from non-reacting flow simulations. This methodology includes the local effect of the flow on the ignition success but is found to be inadequate if transport effects are dominant. Finally, Barré (2014) performed ignition sequences of the swirled burner studied in Chapter 7 but in premixed conditions. Both the early instants of ignition and overall ignition of the burner were investigated and the effect of the LES modeling parameters on the ignition

was evidenced by comparison with experiments.

The present work is sponsored by Snecma in the framework of the LEMCOTEC FP7 European project. The first objectives is to confirm the capacity of the AVBP code to predict ignition sequence and ignition statistics. Several configurations of increasing complexity are then investigated with LES, with the objective of increasing the understanding of the ignition process from the kernel phase at the early instants after energy deposit to the inter-sector flame propagation. A first part is devoted to a general description of the problem. Then, following the decomposition of the ignition sequence introduced by Lefebvre (1998), the next two parts are divided following to the successive phases of ignition:

- **Part 1** provides the baseline of combustion and computational fluid mechanics required to tackle the issue of ignition in gas turbines.

- **Part 2** focuses on the second phase of ignition. State of the art regarding **Phase 1** & **2** is first presented to underline recent advances of the scientific community and the potential for research. The LES of the partially premixed configuration of Cordier (2013) is presented and analyzed. The objectives of this LES study are two-fold: 1) confirm the capability of LES to reproduce the ignition scenarios observed in experiments as well as the ignition probability in flow conditions representative of gas turbines; 2) build an extensive LES database to identify the mechanisms leading to ignition success or failure in complex flow configurations. Finally, the LES database is used to construct and validate a new model for the prediction of ignition probability map based on non-reacting flow solutions. The model is built to encompass non-local flow effects that have been observed in both LES and experiments.

- **Part 3** is dedicated to the light-around phase. The study is built around two experimental setups: 1) the configuration of Cordier (2013) featuring a variable spacing capability is first studied and highlights some of the mechanisms responsible for flame propagation; 2) the azimuthal configuration of Bourgouin *et al.* (2013) is then computed to analyze the complete light-around and evidence the effect of the burnt gases expansion on the propagation.

Part I

Turbulent reactive flows

Chapter 2

Conservation equations for turbulent reactive flows

Contents

2.1 Multispecies thermodynamics 15
2.2 Navier-Stokes equations 16
2.3 Transport properties 18
2.4 Chemical kinetics 18

Fluid mechanics is the study of motion of liquid and/or gases. The mathematical description of fluid motion started in 1757 with the set of governing equations describing inviscid flows reported by Leonhard Euler (and called after him Euler equations). Then Claude-Louis Navier introduced the notion of viscosity in 1822 and George Stokes wrote the final set of equations describing the motion of viscous fluids in 1845. These equations are known as the 'Navier-Stokes equations' of fluid motion. From a mathematical point of view, these equations are nonlinear partial differential equations and, except in simple canonical cases, cannot be solved analytically. The equations for turbulent reactive flows include chemical source terms, and additional transport equations for species mass fractions involved in the chemical reactions are solved.

The aim here is to introduce the main variables describing reactive flows as well as the physical models used in the multispecies Navier-Stokes equations solved in AVBP. The derivation can be found in fluid mechanics textbooks such the one of Kuo (2005).

2.1 Multispecies thermodynamics

Dealing with combustion requires to describe multispecies mixtures, where each species k is characterized by its:

- mass fraction: $Y_k = m_k/m$, the ratio of the mass of species k, m_k over the total mixture mass m.

- density: $\rho_k = \rho Y_k$, where ρ is the density of the mixture
- molar mass of species k: W_k
- molar fraction of species k: $X_k = \frac{W}{W_k} Y_k$, where W is the molar mass of the mixture
- molar concentration of species k: $[X_k] = \rho \frac{X_k}{W}$
- constant pressure mass heat capacity: $C_{p,k}$
- mass enthalpy: $h_k = h_{s,k} + \Delta h^0_{f,k}$, where $h_{s,k} = \int_{T_0}^{T} C_{p,k} dT$ is the sensible enthalpy and $\Delta h^0_{f,k}$ is the formation enthalpy at reference temperature T_0

By construction, for a mixture composed of N species, $\sum_{k=1}^{N} Y_k = 1$, the mixture molar mass is given by:

$$\frac{1}{W} = \sum_{k=1}^{N} \frac{Y_k}{W_k} \tag{2.1}$$

Under the hypothesis of perfect gases, the mixture total pressure P is the sum of partial pressures p_k of each species:

$$P = \sum_{k=1}^{N} p_k \quad \text{where} \quad p_k = \rho_k \frac{\mathcal{R}}{W_k} T \tag{2.2}$$

where T is the mixture temperature and $\mathcal{R} = 8.314\ J.mol^{-1}.K^{-1}$ is the perfect gas universal constant. The equation of state yields:

$$p = \sum_{k=1}^{N} p_k = \sum_{k=1}^{N} \rho_k \frac{\mathcal{R}}{W_k} T = \rho \frac{\mathcal{R}}{W_k} T \tag{2.3}$$

The constant pressure mass heat capacity of the mixture C_p is given by:

$$C_p = \sum_{k=1}^{N} Y_k C_{p,k} \tag{2.4}$$

2.2 Navier-Stokes equations

The Navier-Stokes equations for multispecies mixtures using Einstein index notation write:

$$\frac{\partial \rho u_j}{\partial t} + \frac{\partial \rho u_i u_j}{\partial x_i} + \frac{\partial P \delta_{ij}}{\partial x_i} = -\frac{\partial \tau_{ij}}{\partial x_i} \quad \text{for} \quad j = 1, 3 \tag{2.5}$$

$$\frac{\partial \rho Y_k}{\partial t} + \frac{\partial \rho u_i Y_k}{\partial x_i} = -\frac{\partial J_{i,k}}{\partial x_i} + \dot{\omega}_k \quad \text{for} \quad k = 1, N \tag{2.6}$$

$$\frac{\partial \rho E}{\partial t} + \frac{\partial \rho u_i E}{\partial x_i} + \frac{\partial u_j P \delta_{ij}}{\partial x_i} = -\frac{\partial q_i}{\partial x_i} + \frac{\partial u_j \tau_{ij}}{\partial x_i} + \dot{\omega}_T + \dot{\mathcal{Q}}_{sp} \tag{2.7}$$

with u_j is the jth-component of the velocity, P is the static pressure, τ_{ij} is the viscous tensor, $J_{i,k}$ is the ith-component of the diffusive flux of species k, $\dot{\omega}_k$ and $\dot{\omega}_T$ are the species k and energy chemical source term, E is the total energy, q_i is the ith-component of the energy flux and $\mathcal{Q}_{sp}$ is the external energy source term, limited in this study to the spark. δ_{ij} is the Kronecker symbol equal to 1 if $i = j$ and 0 otherwise. Eqs. (2.5)-(2.7) are referred to as the momentum, k^{th}-species and energy conservation equations respectively.

The viscous tensor is proportional to the symmetric part of the deformation tensor (Newtonian fluid), and equality between mechanical and thermodynamic pressure (zero coefficient of bulk viscosity null, Stokes assumption) is assumed:

$$\tau_{ij} = 2\mu \left(S_{ij} - \frac{1}{3}\delta_{ij} S_{kk} \right) \tag{2.8}$$

with μ the dynamic viscosity and S_{ij} the deformation tensor:

$$S_{ij} = \frac{1}{2}\left(\frac{\partial u_j}{\partial x_i} + \frac{\partial u_i}{\partial x_j} \right) \tag{2.9}$$

The computation of the exact formulation of the diffusive flux of species k in the mixture is a very complex task. The Hirschfelder and Curtiss approximation (Hirschfelder *et al.*, 1969) is employed, yielding:

$$J_{i,k} = \rho Y_k V_{k,i} = -\rho \left(D_k \frac{W_k}{W} \frac{\partial X_k}{\partial x_i} - Y_k V_i^c \right) \tag{2.10}$$

with D_k the equivalent diffusion coefficient of species k in the rest of the mixture:

$$D_k = \frac{1 - Y_k}{\sum_{j \neq k} X_j / D_{jk}} \tag{2.11}$$

where D_{jk} is the binary diffusion coefficient of species j in species k. V_i^c in Eq. (2.10) is the correction velocity ensuring global mass conservation:

$$V_i^c = \sum_{k=1}^{N} D_k \frac{W_k}{W} \frac{\partial X_k}{\partial x_i} \tag{2.12}$$

The chemical source term $\dot{\omega}_k$ in the species conservation equation is described in Sec. 2.4. The energy flux is the combination of the Fourier flux and the enthalpy flux induced by species diffusion:

$$q_i = -\lambda \frac{\partial T}{\partial x_i} + \sum_{k=1}^{N} J_{i,k} h_{s,k} \tag{2.13}$$

where λ is the heat conduction coefficient of the mixture. Finally the reaction energy source term is linked to the species source terms by:

$$\dot{\omega}_T = -\sum_{k=1}^{N} \Delta h_{f,k}^0 \dot{\omega}_k \tag{2.14}$$

2.3 Transport properties

Simple transport models are used. The dynamic viscosity μ of the mixture is supposed independent of the species composition and only depends on the temperature through a standard power law:

$$\mu = \mu_0 \left(\frac{T}{T_0} \right)^b \tag{2.15}$$

where the exponent b depends on the mixture and typically lies between 0.6 and 1.0. The species diffusion coefficient is evaluated assuming a constant Schmidt number Sc_k for each species k that yields:

$$D_k = \frac{\mu}{\rho Sc_k} \tag{2.16}$$

The Schmidt number is a dimensionless number that compares the viscous and species diffusion rates. Similarly, the thermal conductivity λ is computed assuming constant a Prandtl number Pr of the mixture:

$$\lambda = \frac{\mu C_p}{Pr} = \rho C_p D_{th} \quad \text{with} \quad D_{th} = \frac{\nu}{Pr} \tag{2.17}$$

where the Prandtl number compares the viscous and thermal diffusion rates. Finally, the Lewis number Le_k that compares the thermal and species diffusion rates is introduced as:

$$Le_k = \frac{D_{th}}{D_k} = \frac{Sc_k}{Pr} \tag{2.18}$$

2.4 Chemical kinetics

N species reacting through M reactions are considered:

$$\sum_{k=1}^{N} \nu'_{kj} \mathcal{M}_k \Longleftrightarrow \sum_{k=1}^{N} \nu''_{kj} \mathcal{M}_k \quad \text{for } \; j = 1, M \tag{2.19}$$

where $\mathcal{M}_k$ is the symbol for species k, ν'_{kj} and ν''_{kj} are the molar stoichiometric coefficients of species k in reaction j. The reaction rate $\dot{\omega}_k$ of species k is the sum of all reaction rates $\dot{\omega}_{k,j}$ in reaction j:

$$\dot{\omega}_k = \sum_{j=1}^{M} \dot{\omega}_{k,j} = W_k \sum_{j=1}^{M} \nu_{kj} \mathcal{Q}_j \tag{2.20}$$

where $\nu_{kj} = \nu''_{kj} - \nu'_{kj}$ and $\mathcal{Q}_j$ is the progress rate of reaction j. Total mass conservation yields:

$$\sum_{k=1}^{N} \dot{\omega}_k = 0 \tag{2.21}$$

The progress rate of reaction j is given by:

$$\mathcal{Q}_j = K_{fj} \prod_{k=1}^{N} \left(\frac{\rho Y_k}{W_k} \right)^{\nu'_{kj}} - K_{rj} \prod_{k=1}^{N} \left(\frac{\rho Y_k}{W_k} \right)^{\nu''_{kj}} \tag{2.22}$$

K_{fj} and K_{rj} are the forward and reverse reaction rates of reaction j respectively. The forward reaction rate is described with an Arrhenius law:

$$K_{fj} = \mathcal{A}_j \exp\left(-\frac{E_{aj}}{\mathcal{R}T} \right) \tag{2.23}$$

where $\mathcal{A}_j$ and E_{aj} are the pre-exponential factor and the activation energy of reaction j respectively. At a molecular level, the Arrhenius law describes the probability that an atom exchange occurs due molecular collisions. The reverse reaction rate is given by:

$$K_{rj} = \frac{K_{fj}}{K_{eq,j}} \tag{2.24}$$

with $K_{eq,j}$ the equilibrium constant, defined following Kuo (2005):

$$K_{eq,j} = \left(\frac{P_0}{\mathcal{R}T} \right)^{\sum_{k=1}^{N} \nu_{kj}} \exp\left(\frac{\Delta S_j^0}{\mathcal{R}} - \frac{\Delta H_j^0}{\mathcal{R}T} \right) \tag{2.25}$$

where $P_0 = 1\ bar$, ΔH_j^0 and ΔS_j^0 are the enthalpy and entropy changes for reaction j respectively:

$$\Delta H_j^0 = h(T) - h(0) = \sum_{k=1}^{N} \nu_{kj} W_k (h_{s,k} + \Delta h_{f,k}^0) \tag{2.26}$$

$$\Delta S_j^0 = \sum_{k=1}^{N} \nu_{kj} W_k s_k(T) \tag{2.27}$$

where s_k is the entropy of species k.

Chapter 3

Fundamentals of turbulent combustion

Contents

3.1 Introduction **21**
3.2 Laminar flames **22**
3.2.1 Laminar premixed flame 22
3.2.2 Laminar diffusion flame 28
3.2.3 Triple flame propagation 30
3.3 Turbulent flames **31**
3.3.1 Basics of turbulence 31
3.3.2 Turbulent premixed combustion 33
3.3.3 Non-premixed combustion regimes 36

3.1 Introduction

The power required by aeronautic gas turbines implies to burn a large amount of fuel in a fairly small part of the engine. The high velocity flow coming from the compressor generates highly turbulent conditions that favor high heat release density and generate a partial premixing of the fuel with incoming air. As a consequence, a gas turbine is a turbulent partially premixed application. However, ignition is a transient process during which a wide variety of combustion regimes can be encountered. These regimes have been identified by the combustion community and are classically classified depending on the quality of the mixing between fuel and oxidizer prior to combustion (premixed or non-premixed) and the flow flow regime (laminar or turbulent).

The objective here is not to give an exhaustive description of all the combustion regimes, but to provide an overview of the mechanisms controlling the flame propagation, relevant for ignition problems. A complete description can be found in classical textbooks of Poinsot & Veynante (2011), Kuo (2005) or Peters (2000). The structure and propagation mechanism of laminar flames

is described in Sec. 3.2 while Sec. 3.3 focuses on turbulent flames with a brief reminder of some elements of turbulence.

3.2 Laminar flames

Focusing first on laminar flames is relevant for ignition applications since flame propagation may be initiated in this regime. The description of laminar flames is also a prerequisite to study turbulent combustion and many turbulent flame theories are derived from laminar flames.

3.2.1 Laminar premixed flame

3.2.1.a Laminar premixed flame characteristics

Mixture composition

Combustion generally involves numerous intermediate species and reactions to convert the reactant and oxidizer into combustion products. From a macroscopic point of view, combustion reduces to a redox reaction. The equivalence ratio ϕ is, together with the temperature and the pressure, characteristic of the fresh gas mixtures. Considering ν'_F and ν'_O, the stoichiometric coefficients of fuel and oxidizer respectively, the redox reaction writes:

$$\nu'_F F + \nu'_O O \rightarrow Products \tag{3.1}$$

The mixture is said stoichiometric when the fuel and oxidizer mass fractions of the fresh gases Y_F and Y_O follow:

$$\left(\frac{Y_O}{Y_F}\right)_{st} = \frac{\nu'_O W_O}{\nu'_F W_F} = s \tag{3.2}$$

where W_F and W_O are the molar mass of fuel and oxidizer respectively, s is the mass stoichiometric ratio and the subscript st denotes stoichiometric conditions. The equivalence ratio ϕ is given by:

$$\phi = s\frac{Y_F}{Y_O} = \left(\frac{Y_F}{Y_O}\right) \Big/ \left(\frac{Y_F}{Y_O}\right)_{st} \tag{3.3}$$

A mixture having $\phi > 1$ is called rich (excess of fuel) while lean mixture corresponds to $\phi < 1$ (excess of oxidizer).

Flame structure

In a one-dimensional stationary case, the reactive Navier-Stokes equations (2.5-2.7) can be simplified. The thermal theory proposed by Zeldovich, Frank-Kamenetski and Von Karman (ZFK) (Zeldovitch & Frank-Kamenetskii, 1938) is the first theoretical treatment of stationary one-dimensional flames. The ZFK analysis assumes a single-step global reaction with an Arrhenius type reaction rate and a high activation energy, unity Lewis number for all species and first

order dependance of the reaction rate to fuel and oxidizer. The flame front is then described by a single differential equation and can be viewed as a wave propagating from the burnt gases toward the fresh gases at a constant velocity S_L^0 (Zeldovitch & Frank-Kamenetskii, 1938):

$$\rho_u S_L^0 \frac{dT}{dx} = \frac{d}{dx}\left(\frac{\lambda}{C_p}\frac{dT}{dx}\right) - \frac{Q}{C_p}\omega \tag{3.4}$$

The authors also introduced the thermal structure of the laminar flame, as sketched in Fig. 3.1.

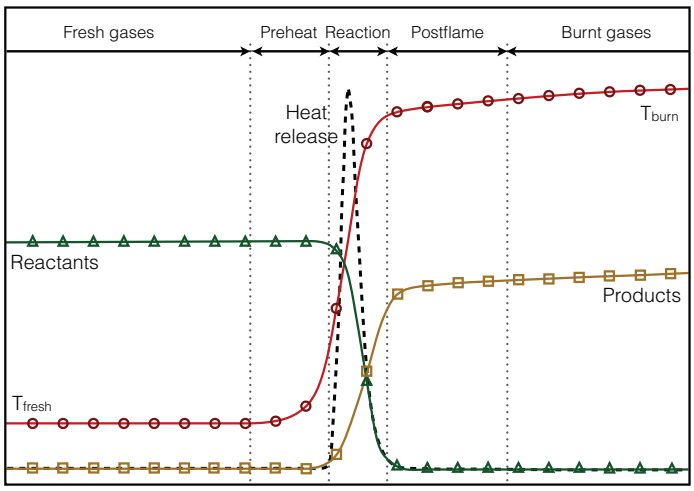

Figure 3.1: Schematic description of the laminar premixed flame structure.

Several characteristic zones can be identified from left (fresh gases) to right (burnt gases):

- the **preheat zone**, chemically inert, where heat diffuses progressively from the reaction zone and increases the gas temperature.
- the **reaction layer** where the fuel is decomposed in smaller hydrocarbons which react with radicals (O or H) to create secondary species such as CO, C_2 or H_2. The reaction layer has a thickness δ_r.
- the **post-flame region** where secondary species are transformed in final products of the reaction such as CO_2 or H_2O.

Most of the heat is released in the reaction layer, characterized by a strong temperature gradient. The chain branching reactions occurring in the reaction layer involve small hydrocarbons and free radicals at high reactions rates. On the contrary, the recombination reactions occurring in the post-flame region are much slower, and this region is much thicker than the reaction region.

Laminar flame speed

The ZFK thermal theory also derives an explicit expression of the laminar flame speed as a function of the thermal diffusivity D_{th} and the Arrhenius pre-exponential factor $\mathcal{A}$. The derivation assumes a null reaction rate in the preheat zone and a negligible convection term in the

reaction layer: from Eq. (3.4) the temperature balance can be written in both regions and an expression for S_L^0 is obtained by equating the temperature gradient at the frontier between these two regions:

$$S_L^0 \propto \sqrt{D_{th}\mathcal{A}} \tag{3.5}$$

Laminar flame thickness

The laminar flame thickness is a crucial flame characteristic, often required in combustion models for RANS or LES. Indeed, the size of the flame front is a critical parameter that controls the resolution required in numerical simulation. Several definitions of the laminar flame thickness are reported in the literature, among which:

- The diffusion thickness δ is based on the thermal diffusion of fresh gases (Poinsot & Veynante, 2011):

$$\delta = \frac{\lambda(T_f)}{\rho(T_f)C_p(T_f)S_L^0} = \frac{D_{th}}{S_L^0} \propto \sqrt{\frac{D_{th}}{\mathcal{A}}} \tag{3.6}$$

  where the subscript f denotes the fresh gases. This definition, which directly derives from the ZFK asymptotic theory, provides an estimation of the flame thickness. In practice the result is too approximate to determine the required mesh resolution.

- The thermal thickness δ_L^0 is based on the temperature gradient and is generally used to estimate the grid resolution required in LES or DNS computations:

$$\delta_L^0 = \frac{T_b - T_f}{max(|\nabla T|)} \tag{3.7}$$

  where the subscript b denotes the burnt gases. The computation of a 1D laminar flame allows to estimate the flame thermal thickness.

- The reaction layer thickness δ_r can also be used to estimate the flame thickness with $\delta_r = \delta_L^0/\beta$, where β is given by:

$$\beta = \alpha\frac{E_a}{\mathcal{R}T_b} \quad \text{and} \quad \alpha = \frac{T_b - T_f}{T_b} \tag{3.8}$$

  The parameters α and β measure the heat release by the flame and the activation energy respectively. Since typical values of β range between 10 and 20, $\delta_r < \delta_L^0$ and using this definition leads to stronger mesh resolution constraint.

3.2.1.b Laminar premixed flame propagation

Considering multi-dimensional laminar premixed flames in non-uniform flow, additional notions are required to investigate the flame propagation.

Definitions of flame speed

The front propagation speed is an intrinsic characteristic of laminar premixed flames. Theoretical descriptions of premixed flame propagation reduce the front to an interface between fresh and burnt gases. A progress variable c is therefore introduced. It could be any variable that ensures a monotonical behavior from 0 in the fresh gases to 1 in the burnt gases. Under the assumption of unity Lewis number, the definition of c can be based on the fuel mass fraction or on the mixture temperature such as:

$$c = \frac{Y_F - Y_{F,f}}{Y_{F,b} - Y_{F,f}} = \frac{T - T_f}{T_b - T_f} \tag{3.9}$$

leading to $c = 0$ in the fresh gases and $c = 1$ in the burnt gases. The flame front may be represented by an iso-surface of progress variable:

$$c(\boldsymbol{x}, t) = c^* \tag{3.10}$$

On this surface, the normalized local gradient of c defines the flame front normal direction:

$$\boldsymbol{n} = -\frac{\boldsymbol{\nabla} \boldsymbol{c}}{|\boldsymbol{\nabla} \boldsymbol{c}|}\bigg|_{c=c^*} \tag{3.11}$$

Using this convention, the normal is pointing towards the fresh gases. Several definitions of the flame speed based on the kinematic or chemical properties of the flame can be defined as illustrated in Fig. 3.2:

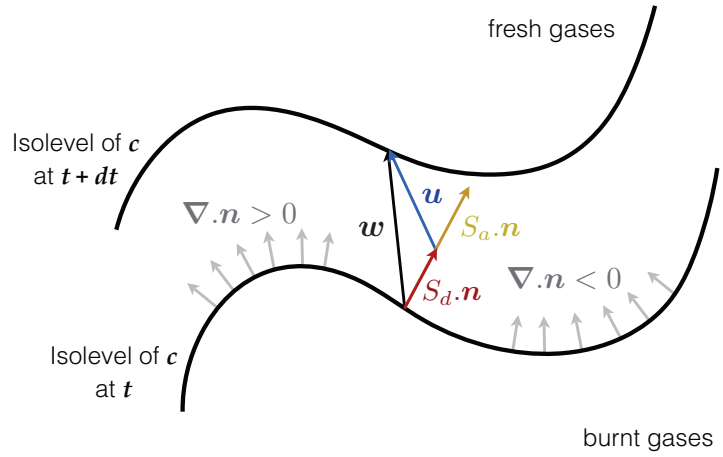

Figure 3.2: Notations for flame speed definitions following Poinsot & Veynante (2011).

- $\boldsymbol{w}$ is the local **flame front velocity** in a fixed reference frame and its definition derives from the differentiation of Eq. (3.10) with respect to time t (Peters, 2000)):

$$\frac{\partial c}{\partial t} + \boldsymbol{\nabla} \boldsymbol{c} \cdot \frac{\partial x}{\partial t}\bigg|_{c=c^*} = \frac{\partial c}{\partial t} + \boldsymbol{\nabla} \boldsymbol{c} \cdot \boldsymbol{w} = 0 \tag{3.12}$$

- S_a is the **absolute speed**, projection of $\boldsymbol{w}$ on the flame front normal $\boldsymbol{n}$. Using Eqs. 3.12 and 3.11, S_a is expressed as a function of c:

$$S_a = \boldsymbol{w} \cdot \boldsymbol{n} = \frac{1}{|\boldsymbol{\nabla} \boldsymbol{c}|} \frac{\partial c}{\partial t} \tag{3.13}$$

- S_d is the **displacement speed** of the flame relative to the underlying gaseous velocity $\boldsymbol{u}$, i.e. the difference between the absolute front flame velocity S_a and the flow velocity $\boldsymbol{u}$ projected on the flame normal. S_d is also expressed as a function of c:

$$S_d = S_a - \boldsymbol{u} \cdot \boldsymbol{n} = \frac{1}{|\boldsymbol{\nabla} \boldsymbol{c}|} \frac{\partial c}{\partial t} + \boldsymbol{u} \cdot \frac{\boldsymbol{\nabla} \boldsymbol{c}}{|\boldsymbol{\nabla} \boldsymbol{c}|} = \frac{1}{|\boldsymbol{\nabla} \boldsymbol{c}|} \frac{Dc}{Dt} \tag{3.14}$$

where D/Dt is the total derivative. Note that S_a and S_d are defined only on the flame front and derived only from the geometrical properties of the front. Gibson (1968) derived an expression for the displacement speed for non-reacting scalar, extended by Peters (2000) to take into account the chemical source term:

$$S_d = \left[\frac{\boldsymbol{\nabla} \cdot (\rho D_c \boldsymbol{\nabla} \boldsymbol{c}) + \dot{\omega}_c}{\rho |\boldsymbol{\nabla} \boldsymbol{c}|} \right]_{c=c^*} \tag{3.15}$$

where $\dot{\omega}_c$ is the chemical energy or species source term depending on the definition of c and D_c is the thermal or species diffusivity depending on the definition of c. Gran *et al.* (1996), Echekki & Chen (1999) and Peters *et al.* (1998) showed that the diffusive term appearing in Eq. (3.15) may be split into two contributions, one accounting for tangential diffusion and another one for diffusion normal to the iso-surface $c = c^*$:

$$\boldsymbol{\nabla} \cdot (\rho D_c \boldsymbol{\nabla} \boldsymbol{c}) = \underbrace{\boldsymbol{n} \cdot \boldsymbol{\nabla} (\rho D_c \boldsymbol{n} \cdot \boldsymbol{\nabla} \boldsymbol{c})}_{normal\ diffusion} \underbrace{-\rho D_c |\boldsymbol{\nabla} \boldsymbol{c}| \boldsymbol{\nabla} \cdot \boldsymbol{n}}_{tangential\ diffusion} \tag{3.16}$$

Finally, the displacement speed (on the iso-surface $c = c^*$) can be rewritten such as:

$$S_d = \underbrace{\frac{\boldsymbol{n} \cdot \boldsymbol{\nabla} (\rho D_c \boldsymbol{n} \cdot \boldsymbol{\nabla} \boldsymbol{c})}{\rho |\boldsymbol{\nabla} \boldsymbol{c}|}}_{normal\ diffusion} - \underbrace{D_c \boldsymbol{\nabla} \cdot \boldsymbol{n}}_{tangential\ diffusion} + \underbrace{\frac{\dot{\omega}_c}{\rho |\boldsymbol{\nabla} \boldsymbol{c}|}}_{reaction} \tag{3.17}$$

It is important to note that S_d is governed by the local balance between diffusion and reaction. The flame structure sketched in Fig. 3.1 is such that the diffusion/convection process dominates in the preheat zone while the reaction/diffusion process is important in the reaction layer. As a consequence, the magnitude of S_d components are changing through the flame front. To account for the gas expansion through the flame front, the density-weighted flame displacement speed noted S_d^* is generally preferred:

$$S_d^* = \frac{\rho}{\rho_f} S_d \tag{3.18}$$

- S_c is the **consumption speed** defined by the mass conservation across the flame front:

$$S_c = -\frac{1}{\rho(T_f) Y_{F,f}} \int_{-\infty}^{\infty} \dot{\omega}_F \, d\boldsymbol{n} \tag{3.19}$$

The consumption speed is the only global quantity. For this reason, the consumption speed is usually preferred when analyzing reactive flows, but its computation in complex tridimensional turbulent flames is not an easy task. Note that for an unstretched laminar premixed flame, the different flame speeds are related by:

$$S_L^0 = S_c = \frac{\rho}{\rho_f} S_d \tag{3.20}$$

Definition of stretch and effect on the flame front

The total flame stretch κ is defined as the time derivative of the fractional rate of a flame surface element A (Williams, 1985):

$$\kappa = \frac{1}{A}\frac{dA}{dt} \tag{3.21}$$

κ can be decomposed into a tangential strain rate contribution and a term accounting for the effect of flame front curvature (Candel & Poinsot, 1990):

$$\kappa = \underbrace{-\boldsymbol{nn} : \boldsymbol{\nabla u} + \boldsymbol{\nabla} \cdot \boldsymbol{u}}_{Tangential\ strain\ rate} + \underbrace{S_d \boldsymbol{\nabla} \cdot \boldsymbol{n}}_{Curvature} \tag{3.22}$$

where $\boldsymbol{nn} : \boldsymbol{\nabla}$ is the gradient operator normal to the flame surface. From Eq. (3.22), the rate of change of the flame surface area is obviously related to both the flow aerodynamics and the shape of the flame surface.

For stretched flames, it is not straightforward neither experimentally nor numerically to evaluate accurately the flame speed. Under the assumption of small strain rate and curvature contributions, using an asymptotic theory is the only way to obtain the flame response to stretch (Bush & Fendell, 1970; Clavin, 1985; Williams, 1985). The displacement and the consumption speeds are found to have a linear but different response to stretching:

$$\frac{S_d}{S_L^0} = 1 - M_a^d \frac{\kappa \delta_{th}}{S_L^0} \quad \text{and} \quad \frac{S_c}{S_L^0} = 1 - M_a^c \frac{\kappa \delta_{th}}{S_L^0} \tag{3.23}$$

where $\kappa\delta_{th}/S_L^0$ is a reduced Karlovitz number based on the diffusive thickness (Peters, 1986), that compares the chemical and small turbulence time scales. M_a^d and M_a^c are the Markstein numbers for the displacement and the consumption speeds respectively, proportional to the fuel Lewis number $(Le_F - 1)$. The Markstein numbers compare the stability wavelength of a curved flame (called Markstein length) to the thermal thickness of the flame front δ_L^0. The stability of the flame front depends on the sign of the Markstein number: for the displacement speed natural intrinsic thermo-diffusive instabilities of the flame front arise for negative Markstein numbers (Clavin, 1985). The typical asymptotic behavior of the consumption speed for stagnation flames is illustrated in Fig. 3.3 as a function of stretch for different values of the fuel Lewis number:

- For $Le_F = 1$, species and temperature gradients increase in the same proportions when increasing stretch. As a consequence, the flame is thinner but the consumption speed is not affected, at least for small stretch values.

- For $Le_F < 1$, the consumption Markstein number is negative and the consumption speed linearly increases with stretch, in the limit of small stretch values.
- For $Le_F > 1$, the consumption speed decreases with stretch.

In general for an adiabatic flame, quenching can be observed only for very large values of stretch but when heat losses are taken into account, extinction could occur for lower stretch values. For large values of stretch, the asymptotic theory is no longer valid, but numerical simulations showed that the linear response could still be applicable beyond the assumption of small stretch values with reasonable accuracy (Meneveau & Poinsot, 1991).

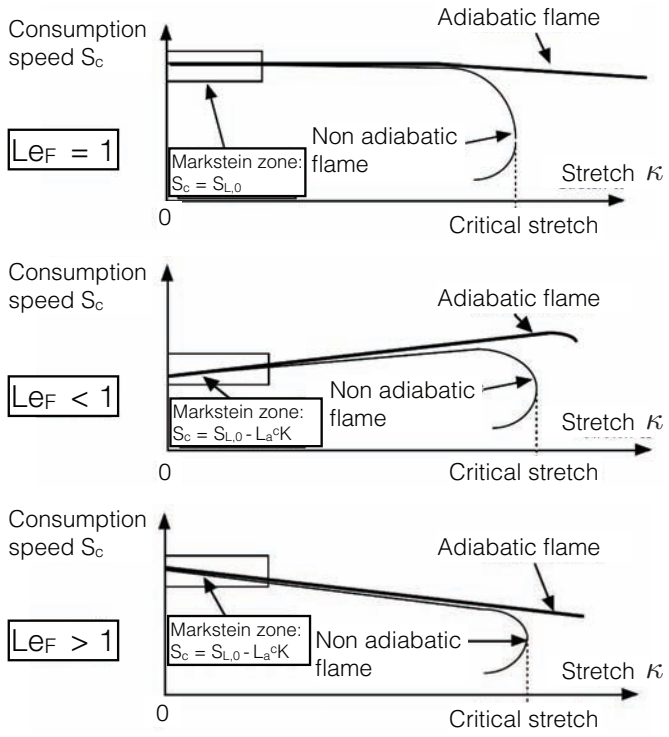

Figure 3.3: Asymptotic response of consumption speed to strain rate for different Lewis numbers (Poinsot & Veynante, 2011).

3.2.2 Laminar diffusion flame

In many applications, fuel and oxidizer are introduced separately in the combustion chamber, mainly to ensure a safe fuel storage. Depending on the design and the operating conditions, a partial premixing of fuel and oxidizer is achieved before burning and/or a reactive layer is found at the interface between fuel and oxidizer. In that sense, diffusion flames differ from premixed flames since they do not propagate and cannot be viewed as waves of finite speed and thickness.

Flame structure

The diffusion flame is sustained by diffusion of fuel and oxidizer towards the reaction zone, located around the stoichiometric mixture region. A schematic illustration of a diffusion flame structure is shown in Fig. 3.4.

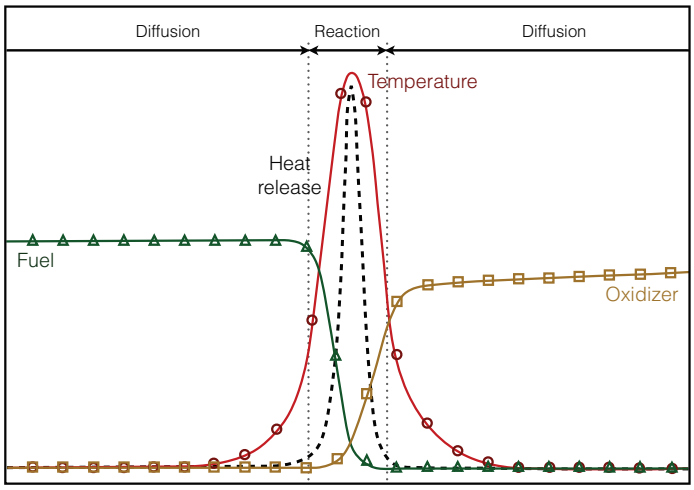

Figure 3.4: Schematic description of the laminar diffusion flame structure.

Flame characteristics

Two main length scales are related to diffusion flames (Bilger, 1989):

- **the diffusion layer thickness** l_d corresponds to the layer of the zone where the mixture fraction z goes from 0 to 1 and where fuel and oxidizer may coexist and diluted by combustion products.
- **the reaction zone thickness** l_r corresponds to the zone where reaction occurs and typically lies around the stoichiometric mixture fraction z_{st}.

These scales are not equivalent to the premixed flame thermal and reactive thicknesses defined in Sec. 3.2.1.a since they can evolve separately and depend on the flow conditions. A laminar diffusion flame can be characterized by the Damköhler number:

$$Da^{fl} = \frac{\tau_f}{\tau_c} \tag{3.24}$$

where the flow time scale can be estimated from the scalar dissipation rate at the stoichiometric point $\tau_f = \chi_{st}^{-1}$ (Libby & Williams, 1994) where $\chi = 2D(\boldsymbol{\nabla} \boldsymbol{z})^2$ and z is the mixture fraction. Since χ_{st} measures the mixture fraction gradient, it can also be used to estimate the diffusion layer thickness $l_d \simeq \sqrt{D/\chi_{st}}$. Asymptotic theories (Linan, 1974) prove that the reaction and diffusion layer thicknesses can be related through the flame Damköhler number Da^{fl}:

$$\frac{l_r}{l_d} \simeq (Da^{fl})^{-1/a} \tag{3.25}$$

where $a = \nu'_F + \nu'_O + 1$ is obtained from the stoichiometric coefficients of the global fuel redox reaction.

To describe non-premixed combustion, the mixture fraction z which is a chemistry-independent "conserved scalar" variable is essential. The conserved scalar satisfies the non-reactive transport equation:

$$\rho\frac{\partial z}{\partial t} + \rho\boldsymbol{u}\cdot\boldsymbol{\nabla z} = \boldsymbol{\nabla}\cdot(\rho D\boldsymbol{\nabla z}) \tag{3.26}$$

where D is the diffusivity (either thermal or species depending on the definition of z). All scalar quantities of the flow (temperature, concentration or density) are then uniquely related to the mixture fraction, which in turns decouple mixing from combustion. In this work, the mixture fraction is defined following Bilger (1989) and based on the coupling function β (Williams, 1985):

$$z = \frac{\beta - \beta_0}{\beta_1 - \beta_0} \tag{3.27}$$

with

$$\beta = \sum_{l=1}^{N_e}\gamma_l\sum_{k=1}^{N_s}\frac{a_{l,k}W_lY_k}{W_k} \tag{3.28}$$

where β_0 and β_1 are the of β evaluated in the fuel and oxidizer streams respectively, γ_l and W_l are the weighting factor and the atomic weight of the element l respectively, and $a_{l,k}$ is the number of atoms of element l in one molecule of species k. The choice of Bilger for γ_l is used in this work with $\gamma_C = 2/W_C$, $\gamma_H = 1/(2W_H)$, $\gamma_O = -1/W_O$ and $\gamma_N = 0$. Note that the definition of the mixture fraction is restricted to cases where the Schmidt numbers of all species are equal since preferential diffusion effects arising from non-equal Schmidt numbers do not lead to a passive scalar. z is linked to the equivalence ratio by:

$$\phi = \frac{z}{1-z}\frac{1-z_{st}}{z_{st}} \tag{3.29}$$

Assuming infinitely fast one step irreversible chemistry, Burke-Schumann proposed a solution to Eq. (3.27) in the mixture fraction space. There exists an infinitely thin non-equilibrium layer at $z = z_{st}$ and outside this layer, the mass fractions of fuel and oxidizer are either zero or piecewise linear function of z. Taking into account finite rate reversible chemistry, the Burke-Schumann structure is altered and fuel and oxidizer can coexist in the reaction zone, which thickness depends on the scalar dissipation rate χ. Once the solution of the mixing problem is known (Eq. (3.27)), χ can be evaluated and the flame structure can be determined in the mixture fraction space.

3.2.3 Triple flame propagation

After ignition in a partially premixed environment, the flame structure is that of a triple flame (Dold, 1989; Kioni *et al.*, 1993; Chakraborty & Mastorakos, 2008; Neophytou *et al.*, 2010). Triple flames are crucial for partially premixed configurations since they play a role in the flame stabilization mechanisms (Veynante *et al.*, 1994) or auto-ignition processes (Domingo & Vervisch,

1996). As sketched in Fig. 3.5, triple flames feature both premixed and non-premixed flame fronts: the premixed flame front spans from fuel-rich to fuel-lean mixtures. This premixed flame front has a leading edge (called triple point) in the stoichiometric mixture region that exhibits a maximum burning velocity. Downstream this triple point, a diffusion flame is stabilized and fed by the excess of fuel and oxidizer from the rich and lean premixed flames respectively.

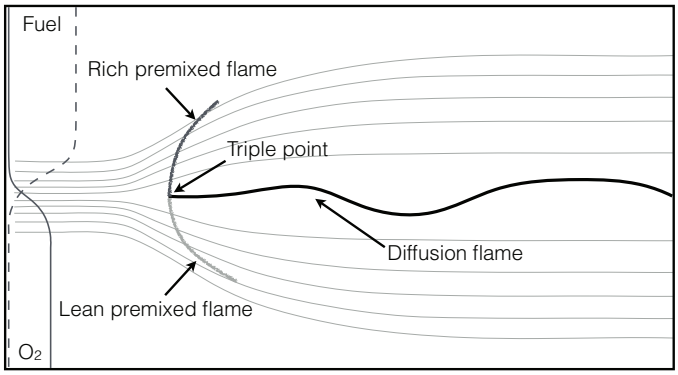

Figure 3.5: Schematic description of the triple flame structure

The propagation speed of a triple flame was found to be larger than a premixed laminar flame speed due to hydrodynamic effects associated with heat release in the premixed flame (Ruetsch *et al.*, 1995; Echekki & Chen, 1998) which redirects the flow in front of the flame (illustrated in Fig. 3.5). The propagation speed then depends on the gradient of mixture fraction: for small gradients, premixed flames are longer and the flow deflection in front of the triple point is larger than for strong gradients where the premixed flames are shorter.

3.3 Turbulent flames

3.3.1 Basics of turbulence

The transition from a laminar flow to a turbulent flow in our target application is characterized by the Reynolds number comparing inertia to viscous forces:

$$Re = \frac{|\boldsymbol{u}|l}{\nu} \tag{3.30}$$

where $\boldsymbol{u}$ and l are characteristic velocity and dimension of the flow respectively and ν is the kinematic viscosity. When inertia forces dominate (i.e. large Reynolds number), the flow is characterized by significant variations of the velocity field in space and time which presents a multitude of vortices of varying sizes, called eddies, convected by the mean flow. These eddies strongly interact with each other through a cascade process where large eddies split into smaller ones, transmitting energy from the large to the small scales. As compared to laminar flow, turbulence greatly enhances transfers of mass, momentum and heat. In a homogeneous isotropic turbulence, the spectral distribution of energy follows the typical sketch presented in Fig. 3.6

where the energy density $E(k)$ is plotted versus the eddy wave number k (inverse of the eddy length scale).

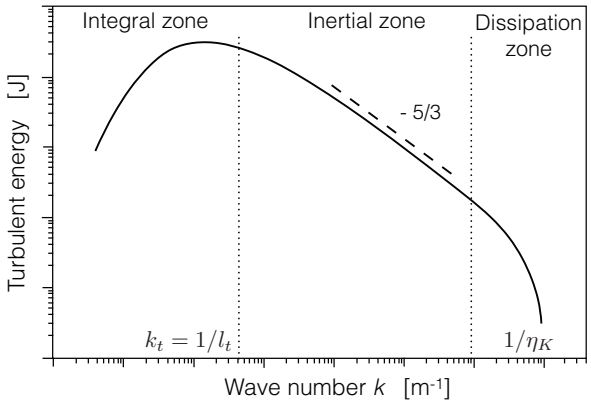

Figure 3.6: Sketch of energy density spectrum $E(k)$ in an homogeneous isotropic turbulence along with the distinction of the integral, inertial and dissipation zones (Richardson, 1922).

Following Pope (2000), three zones can be identified from the biggest to the lowest length scales:

- The **integral zone** is characterized by the lowest frequencies and is centered on the wave number k_t corresponding to the integral length scale l_t. It contains the biggest and most energetic eddies where the turbulent energy is produced and their size is of the order of the characteristic length of the geometry. The largest scales in a turbulent flow are mainly controlled by inertia and are not affected by viscous effects.

- In the **inertial zone** the large eddies become unstable and break down into smaller eddies via the 'cascade' process. No eddy dissipation is detected and the rate of energy transfer from the biggest to the smallest structures is constant following a $k^{-5/3}$ law for isotropic statistically steady turbulence (Kolmogorov, 1941).

- The **dissipation zone** is characterized by the highest wave numbers and is centered on the Kolmogorov wave number k_{η_K} corresponding to the Kolmogorov length scale η_K. At these scales, viscous forces dominate and the turbulent energy is dissipated into heat due to the kinematic viscosity ν. Kolmogorov length scale and speed can be estimated (in isotropic homogeneous turbulence) by:

$$\eta_K = \left(\frac{\nu^3}{\varepsilon}\right)^{1/4} \text{ and } u'_K = (\nu\varepsilon)^{1/4} \tag{3.31}$$

where the subscript K denotes the Kolmogorov scale and ε is the dissipation rate given by:

$$\varepsilon = 2\nu S_{ij} S_{ij} \tag{3.32}$$

3.3.2 Turbulent premixed combustion

3.3.2.a Turbulent premixed combustion regimes

In a first approach, turbulent premixed combustion is described as the result of interactions between the flame front and the flow eddies whose sizes range from the Kolmogorov to the integral scales and with characteristic speeds ranging from the Kolmogorov velocity u'_K to the integral Root Mean Square (RMS) velocity u'. Chemistry can be characterized by a chemical time scale:

$$\tau_c = \frac{\delta_L^0}{S_L^0} \tag{3.33}$$

where δ_L^0 and S_L^0 are respectively the thermal thickness and flame speed of an unstrained laminar premixed flame. This chemical time τ_c corresponds to the time required for the flame to propagate over a distance equal to its own thickness. This flame then interacts at the same time with the most energetic turbulent structures characterized by the turbulence time scale $\tau_t = l_t/u'_t$, and with the smallest turbulent scales characterized by the Kolmogorov time scale $\tau_K = \eta_K/u'_K$. Classical approaches therefore introduce two reduced numbers corresponding to the limiting values of the flow motion and sizes to describe the turbulence/flame interactions:

- The **Damköhler number** Da is defined as the ratio of the integral time scale τ_t to the chemical time scale τ_c:

$$Da = \frac{\tau_t}{\tau_c} = \frac{l_t}{\delta_L^0}\frac{S_L^0}{u'_t} \tag{3.34}$$

  Two cases must be distinguished:

  - for high Da number ($Da >> 1$), the turbulent time scale is much larger than the chemical time scale and the structure of the flame front is not modified by the turbulence. In this **flamelet regime** or **thin wrinkled flame regime**, the turbulent flame front can be assimilated to a collection of laminar flame elements called "flamelets".
  - for small Da number ($Da << 1$), the turbulent time scale is much smaller than chemistry and the reactants and products are mixed by turbulent motion before reacting via a slow chemical process. This corresponds to the **well stirred reactor** limit.

- The **Karlovitz number** Ka identifies the interactions between the turbulent small scales and the flame:

$$Ka = \frac{\tau_c}{\tau_K} = \frac{\delta_L^0}{\eta_K}\frac{u'_K}{S_L^0} \tag{3.35}$$

  Various expressions of the Karlovitz number can be found in the literature. Using the relation $S_L^0 \sim \nu/\delta_L^0$, a unity flame Reynolds number is obtained:

$$Re_{fl} = \frac{\delta_L^0 S_L^0}{\nu} = 1 \tag{3.36}$$

yielding:

$$Ka = \left(\frac{u'}{S_L^0}\right)^{3/2} \left(\frac{l_t}{\delta_L^0}\right)^{-1/2} = \left(\frac{\delta_L^0}{\eta_K}\right)^2 \tag{3.37}$$

using Eq. (3.31), showing that the Karlovitz number compares the laminar flame length scale to the smallest turbulent scale.

Since the Reynolds, Damköhler and Karlovitz numbers are related through $Re = Da^2 Ka^2$, the transition between the different combustion regimes can be completely defined using only two non-dimensional numbers. Following Peters (2000), a diagram of the various combustion regimes is presented in Fig. 3.7 as a function of length l_t/δ_L^0 and velocity u'/S_L^0 ratios, giving a qualitative distinction between the combustion regimes based on the Karlovitz, Damköhler and the flame Reynold numbers.

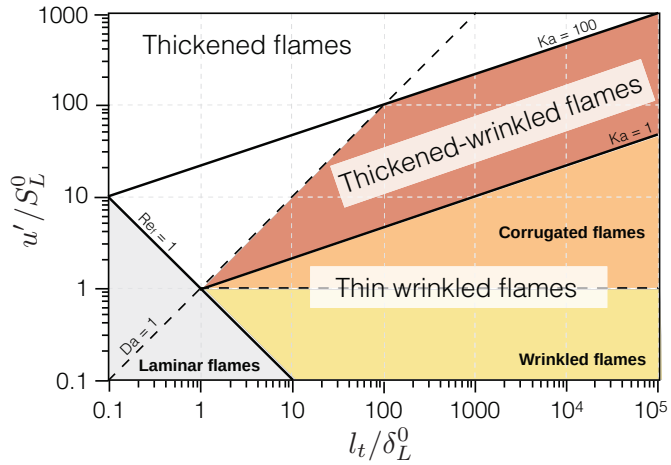

Figure 3.7: Combustion regime diagram for premixed turbulent combustion from Peters (2000).

3.3.2.b Turbulent flame propagation and quenching

In the flamelet regime, the turbulent flame can be viewed as a collection of laminar premixed flame elements distributed along a stretched and wrinkled front (see Fig. 3.8). As a consequence of the wrinkling, the turbulent flame area A_T is increased enhancing diffusion and reaction, hence increasing the propagation speed. The turbulent flame brush is propagating at a turbulent velocity S_T equal to the laminar flame speed weighted by the ratio of the wrinkled instantaneous flame front area A_T to the unwrinkled area A_L (Driscoll, 2008):

$$\frac{S_T}{S_L^0} = \frac{A_T}{A_L}\frac{\overline{S}_c}{S_L^0} \tag{3.38}$$

where the term $\overline{S}_c/S_L^0$ is the stretch factor that accounts for the effect of stretch on the flamelet velocity (Bray & Cant, 1991) using the turbulent flame brush mean consumption velocity $\overline{S}_c$.

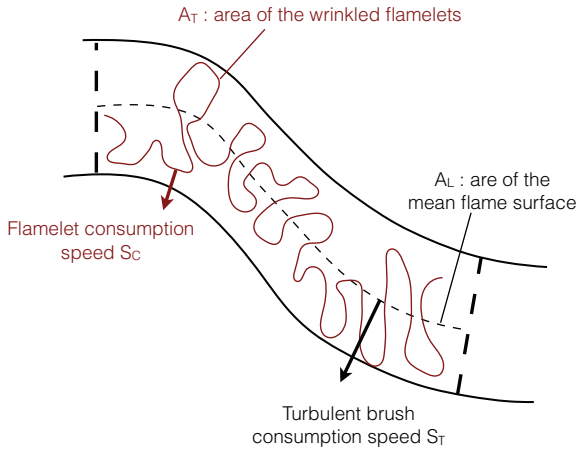

Figure 3.8: Sketch of the wrinkled area A_T and the mean flame surface A_L. Extracted from Driscoll (2008).

The turbulent velocity S_T increases with increasing turbulent intensity. Several relations linking the turbulent velocity fluctuations u' to the turbulent flame speed have been established, such as the simplest one proposed by Abdel-Gayed *et al.* (1984):

$$\frac{S_T}{S_L^0} \simeq 1 + \frac{u'}{S_L^0} \tag{3.39}$$

Relations such as Eq. (3.39) have been built from both experimental and theoretical studies, but with large disparities proving the difficulty of deriving a universal expression. Nonetheless, it is generally agreed that for high level of turbulence, S_T reaches a plateau followed by flame quenching if the turbulence intensity is further increased. Quenching in a turbulent flame front is the consequence of sufficiently strong aerodynamic stretch that can locally reduce or even completely suppress the combustion process. This point has been discussed in Sec. 3.2.1.b for laminar flame submitted to steady stretch. In turbulent flames, stretch is intrinsically time-dependent and results from the interaction with the full range of vortices. In the flamelet regime, the results of laminar studies using DNS (Poinsot *et al.*, 1991) and experiments (Roberts *et al.*, 1993) should be valid in turbulent flames. These studies investigate the canonical case of laminar flame/vortex interactions varying the vortex size and strength. The interaction is found to mainly depend on three parameters (Poinsot & Veynante, 2011): the vortex velocity to flame speed ratio, the Karlovitz number evaluated at the vortex size and the vortex power. The interaction of individual vortices with the flame can then be classified in a spectral diagram as reported in Fig. 3.9 following Poinsot *et al.* (1991).

Vortices in the "no effect zone" are either too slow to counteract the flame speed ($u'(r)/S_L^0 < 1$) or too weak ($(r/\delta_L^0)^2 < 1$) to penetrate the flame front and have no significant effect on the flame front. As the vortex size and strength increases, the flame is first wrinkled, then pockets of fresh gases are created and finally quenching of the flame front is observed past the quench limit. In Fig. 3.9, a Homogeneous Isotropic Turbulence (HIT) spectrum can be represented by a line following $u'(r)^3/r = \varepsilon$. Depending on whether this line crosses the quenching region or not,

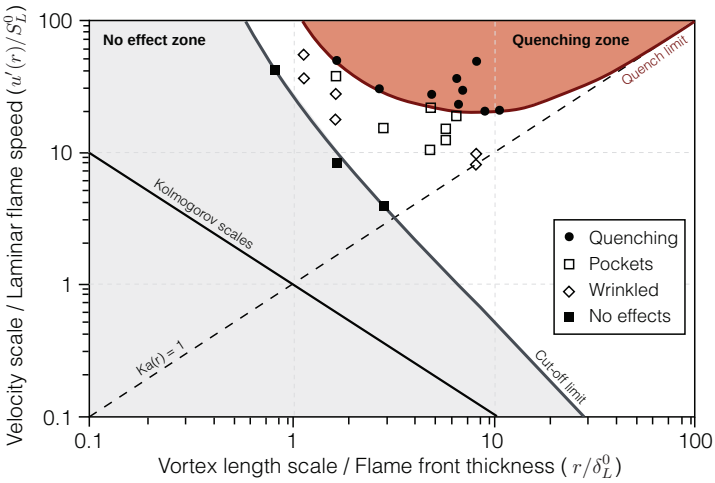

Figure 3.9: Spectral diagram obtained from DNS of laminar flame/vortex interaction. Extracted from Poinsot *et al.* (1991).

the flamelet regime or the thickened-wrinkled flame regime better characterize the combustion regime encountered in this flow (see Fig. 3.7).

3.3.3 Non-premixed combustion regimes

Similarly to the premixed combustion, non-premixed combustion regimes have to be identified in order to study the interaction of diffusion flames with turbulence and support the development of models. However, since diffusion flames do not exhibit well-defined characteristic scales this task is more difficult. Figure 3.10(left) illustrates a comparison between the laminar flame length scale introduced in Sec. 3.2.2 and the turbulence length scales.

As a first step towards the construction of a non-premixed turbulent combustion diagram, Cuenot & Poinsot (1994) investigated the ability of turbulent vortices to modify the laminar diffusion flame in a flame/vortex case where the flame characteristic scales can be defined unambiguously. Even though a combustion diagram cannot directly be derived from this study, it shows that the diffusion flame structure is controlled by Da^{fl} and that a simple classification can be proposed based on the transition flame Damköhler numbers Da^{LFA} and Da^{ext} where LFA stands for Laminar Flamelet Assumption and the superscript ext denote an extinction zone:

- For $Da^{fl} > Da^{LFA}$, the diffusion flame keeps its laminar flame structure.
- For $Da^{LFA} > Da^{fl} > Da^{ext}$, the flame structure is modified but the diffusion flame is not quenched because of unsteady effects: indeed the flame undergoes strain rates higher than predicted by asymptotic theories but is not quenched because of the short duration of the flame/vortex interaction.
- For $Da^{ext} > Da^{fl}$, the laminar diffusion flame is quenched because the strain rate is too strong.

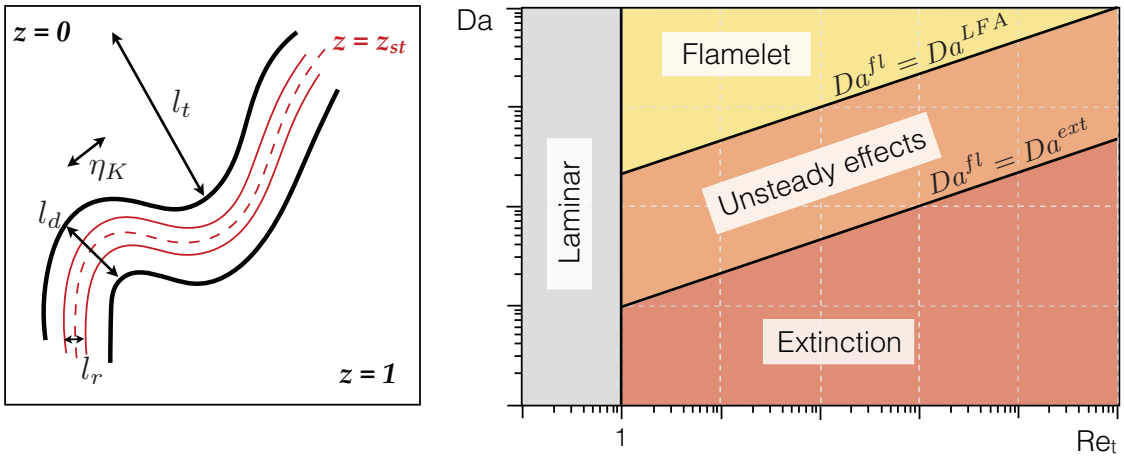

Figure 3.10: Definition of diffusion flame thickness and turbulence length scale (left). Non-premixed combustion diagram as function of the turbulent Reynolds number Re_t and Damköhler number Da (Cuenot & Poinsot, 1994) (right).

The non-premixed diagram derived from the identification of these transitions is presented in Fig. 3.10(right) as function of the turbulent Reynolds number Re_t and the Damköhler number $Da \simeq 2\sqrt{Re_t} Da^{fl}$ (Cuenot & Poinsot, 1994).

Chapter 4

Modeling of turbulent reactive flows

Contents

4.1 Computationnal approaches 40
4.2 LES modeling 41
4.2.1 Filtered governing equations 42
4.2.2 Filtered viscous fluxes 42
4.2.3 Subgrid fluxes closure 43
4.2.4 Modeling of the subgrid stress tensor 44
4.3 Combustion modeling 45
4.3.1 Overview 45
4.3.2 Thickened Flame LES (TFLES) model 46
4.4 Chemical scheme for LES 49
4.4.1 Methane chemistry 50
4.4.2 Propane chemistry 52
4.5 Numerical methods in AVBP 53
4.5.1 Numerical schemes 53
4.5.2 Boundary conditions 54

The numerical resolution of Eqs. 2.5-2.7 for turbulent flows in complex geometries is today still a challenge. Turbulent flows are characterized by a wide range of length scales. Indeed between the most energetic integral length scale l_t and the dissipative Kolmogorov length scale η_K, several orders of magnitude can be found, depending on the flow Reynolds number as (Kolmogorov, 1941):

$$\frac{l_t}{\eta_K} = Re^{3/4} \tag{4.1}$$

This ratio gives the discretization required in each direction to explicitly compute all the scales of the flow. Considering a three dimensional computation, the number of grid points N_{pt} scales as:

$$N_{pt} = \left(Re^{3/4}\right)^3 = Re^{9/4} \tag{4.2}$$

The Reynolds number in aeronautical combustor can go up to $Re = 1.10^6$, leading to numerical grid containing $N_{pt} = 3.10^{13}$, which is still out of reach with current computational ressources. Taking into account the chemical reactions further stiffen the problem since realistic combustion chemistry involves hundreds of species through thousands of reactions, and the characteristic chemical time scales spread over a very wide range.

4.1 Computationnal approaches

Three CFD methodologies have emerged to solve the compressible reactive Navier-Stokes set of equations and can be sorted based on the modeling effort required:

- Reynolds Averaged Navier-Stokes (RANS) computations do not solve for the instantaneous flow field but only the time-averaged values of all NS quantities. The governing RANS equations are obtained by (Reynolds or Favre) averaging the instantaneous equations (Eqs. 2.5-2.7), exhibiting unclosed terms for which models have been developed. These models represent the effect of the entire turbulence spectrum on the mean flow field. However, the largest scales of the turbulent motion strongly depending on the simulated configuration, the RANS closure models often lack universality. RANS computations have historically been the first possible approach thanks to their affordable computational cost.

- LES introduces a scale separation between the turbulent large scales and the smaller ones. The former are supposed to greatly depend on the geometry and are explicitly calculated while the latter are modeled. Modeling of the small scale is expected to be easier than RANS closure models since the small scale turbulence have a self-similar universal nature (at least far from boundary layers). The balance equations for LES are obtained by filtering the instantaneous balance equations as summarized in Sec. 4.2. Compared to RANS, LES main advantage is its intrinsic capability to capture unsteady features. LES has experienced a fast development over the last 20 years and appears to be an excellent candidate to investigate unsteady phenomena in complex configurations, in particular the ignition process studied in this work.

- DNS consists in explicitly resolving the full instantaneous Navier-Stokes equations from the largest to the smallest turbulent scales. In that sense, DNS is the opposite approach to RANS and is associated with very high computational costs. For a long time, DNS of realistic configurations has been prevented by the high numerical cost of the simulation. If DNS of full realistic configurations are not yet affordable, academic configurations (moderate Reynolds number) are now investigated by using High Performance Computing (HPC) (Chen *et al.*, 2009; Moureau *et al.*, 2011*b*). Nonetheless, DNS has changed the analysis of turbulent combustion and has been used to bring some fundamental understanding of the physical phenomena and build models for LES and RANS.

These three approaches are illustrated in Fig. 4.1 in the turbulent energy spectrum where the wave numbers of both the integral length scale l_t and the Kolmogorov length scale η_K are mentioned. By construction, LES tend towards DNS when the cut-off length scale goes to η_K.

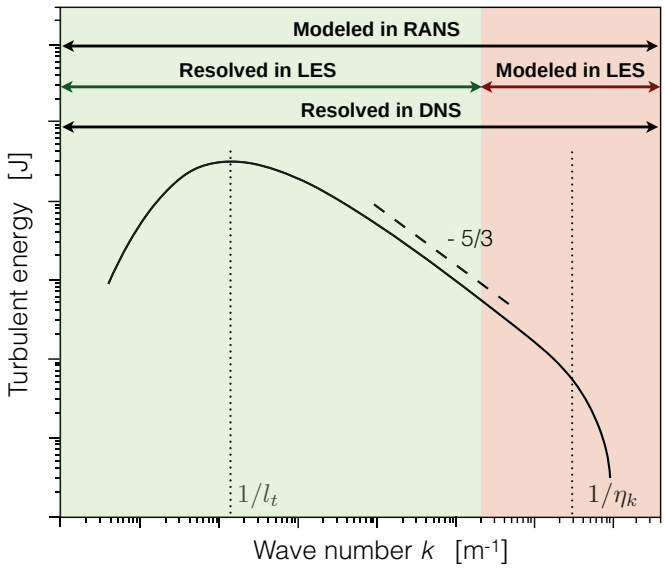

Figure 4.1: Turbulence energy spectrum plotted as function of the wave number k. RANS, LES and DNS are depicted in terms of spatial ranges explicitly resolved and modeled for each computational approach.

4.2 LES modeling

LES filtered quantities are obtained by the convolution product of any scalar quantity with a filter $\mathcal{G}_\Delta$:

$$\overline{f}(\mathbf{x},t) = \int f(\mathbf{x},t)\mathcal{G}_\Delta(\mathbf{x}-\mathbf{x}')\,dx \tag{4.3}$$

Two classes of LES can be distinguished depending on whether the filtering operation is applied explicitly to the conservation equations, which are subsequently resolved numerically (referred as "explicit LES") or results from the discretization on an under-resolved grid size (referred as "implicit LES"). In this work, only implicit LES will be used.

The unresolved or subgrid scale (SGS) contribution is defined by:

$$f'(\mathbf{x},t) = f(\mathbf{x},t) - \overline{f}(\mathbf{x},t) \tag{4.4}$$

Using the above definition, a source term appears in the filtered mass conservation equation corresponding to the correlation between density and velocity fluctuations (Poinsot & Veynante, 2011) and is uneasy to handle in CFD codes. Generally, a Favre averaged definition is preferred to avoid this issue:

$$\widetilde{f} = \frac{\overline{\rho f}}{\overline{\rho}} \tag{4.5}$$

4.2.1 Filtered governing equations

Applying the filtering operation to Eqs. 2.5-2.7 yields:

$$\frac{\partial \overline{\rho}}{\partial t} + \frac{\partial \overline{\rho}\widetilde{u}_i}{\partial x_i} = 0 \tag{4.6}$$

$$\frac{\partial \overline{\rho}\widetilde{u}_j}{\partial t} + \frac{\partial \overline{\rho}\widetilde{u}_i\widetilde{u}_j}{\partial x_i} + \frac{\partial \overline{P\delta_{ij}}}{\partial x_i} = \frac{\partial}{\partial x_i}\left[\overline{\tau}_{ij} - \overline{\rho}(\widetilde{u_i u_j} - \widetilde{u}_i\widetilde{u}_j)\right] \quad \text{for} \quad j = 1,3 \tag{4.7}$$

$$\frac{\partial \overline{\rho}\widetilde{Y}_k}{\partial t} + \frac{\partial \overline{\rho}\widetilde{u}_i\widetilde{Y}_k}{\partial x_i} = \frac{\partial}{\partial x_i}\left[\overline{J}_{i,k} - \overline{\rho}(\widetilde{u_i Y_k} - \widetilde{u}_i\widetilde{Y}_k)\right] + \overline{\dot{\omega}}_k \quad \text{for} \quad k = 1,N \tag{4.8}$$

$$\frac{\partial \overline{\rho}\widetilde{E}}{\partial t} + \frac{\partial \overline{\rho}\widetilde{u}_i\widetilde{E}}{\partial x_i} + \frac{\overline{\partial u_i P\delta_{ij}}}{\partial x_i} = \frac{\partial}{\partial x_i}\left[\overline{q_i} - \overline{\rho}(\widetilde{u_i E} - \widetilde{u}_i\widetilde{E})\right] + \overline{\tau_{ij}\frac{\partial u_i}{\partial x_j}} + \overline{\dot{\omega}}_T + \dot{\mathcal{Q}}_{sp} \tag{4.9}$$

In Eqs. 4.6-4.9, the Left Hand Side (LHS) contains the filtered inviscid fluxes while viscous and turbulent (or SGS) fluxes as well as source terms are in the RHS.

4.2.2 Filtered viscous fluxes

The filtered viscous fluxes appearing in the LES governing equations are given by:

- **Laminar filtered stress tensor** $\overline{\tau_{ij}}$:

$$\overline{\tau_{ij}} = \overline{2\mu\left(S_{ij} - \frac{1}{3}\delta_{ij}S_{kk}\right)} \tag{4.10}$$

$$\text{approximation: } \overline{\tau_{ij}} \simeq 2\overline{\mu}\left(\widetilde{S}_{ij} - \frac{1}{3}\delta_{ij}\widetilde{S}_{kk}\right) \tag{4.11}$$

$$\text{with: } \widetilde{S}_{ij} = \frac{1}{2}\left(\frac{\partial \widetilde{u}_j}{\partial x_i} + \frac{\partial \widetilde{u}_i}{\partial x_j}\right) \tag{4.12}$$

$$\text{and: } \overline{\mu} \simeq \mu(\widetilde{T}) \tag{4.13}$$

- **Diffusive species flux vector** $\overline{J}_{i,k}$:

$$\overline{J}_{i,k} = -\overline{\rho\left(D_k\frac{W_k}{\overline{W}}\frac{\partial X_k}{\partial x_i} - Y_k V_i^c\right)} \tag{4.14}$$

$$\text{approximation: } \overline{J}_{i,k} \simeq -\overline{\rho}\left(\overline{D}_k\frac{W_k}{\overline{W}}\frac{\partial \widetilde{X}_k}{\partial x_i} - \widetilde{Y}_k\widetilde{V}_i^c\right) \tag{4.15}$$

$$\text{with: } \widetilde{V}_i^c = \sum_{k=1}^{N}\overline{D}_k\frac{\partial \widetilde{X}_k}{\partial x_i} \tag{4.16}$$

$$\text{and: } \overline{D}_k \simeq \frac{\overline{\mu}}{\overline{\rho}Sc_k} \tag{4.17}$$

- **Filtered heat flux** $\overline{q}_i$:

$$\overline{q_i} = \overline{\lambda \frac{\partial T}{\partial x_i}} - \overline{\rho \sum_{k=1}^{N} V_{k,i} Y_k h_{s,k}} \tag{4.18}$$

$$\text{approximation: } \overline{q_i} \simeq \overline{\lambda} \frac{\partial \widetilde{T}}{\partial x_i} - \sum_{k=1}^{N} \overline{J}_{i,k} \widetilde{h}_{s,k} \tag{4.19}$$

$$\text{with: } \overline{\lambda} \simeq \frac{\overline{\mu}\,\overline{C_p}(\widetilde{T})}{Pr} \tag{4.20}$$

The species and thermal diffusion fluxes have been approximated using a simple gradient assumption.

4.2.3 Subgrid fluxes closure

The unresolved scales effect on the filtered quantities appearing in Eqs. 4.6-4.9 must be modeled. SGS closures are given by:

- **Unresolved Reynolds tensor** $\overline{\tau}_{ij}^{sgs} = -\overline{\rho}(\widetilde{u_i u_j} - \widetilde{u}_i \widetilde{u}_j)$:

$$\overline{\tau}_{ij}^{sgs} = 2\overline{\rho}\nu_t \left(\widetilde{S}_{ij} - \frac{1}{3}\delta_{ij} \widetilde{S}_{kk} \right) \tag{4.21}$$

  where ν_t is the SGS kinematic viscosity for which various expressions have been established (detailed in Sec. 4.2.4).

- **Unresolved species fluxes** $\overline{J}_{i,k}^{sgs} = -\overline{\rho}(\widetilde{u_i Y_k} - \widetilde{u}_i \widetilde{Y}_k)$:

$$\overline{J}_{i,k}^{sgs} = -\overline{\rho} \left(D_k^t \frac{W_k}{\overline{W}} \frac{\partial \widetilde{X}_k}{\partial x_i} - \widetilde{Y}_k \widetilde{V}_i^{c,t} \right) \tag{4.22}$$

$$\text{with: } \widetilde{V}_i^{c,t} = \sum_{k=1}^{N} \overline{D}_k^t \frac{\partial \widetilde{X}_k}{\partial x_i} \tag{4.23}$$

$$\text{and: } D_k^t = \frac{\mu_t}{\rho S c_k^t} \tag{4.24}$$

  where Sc_k^t is the turbulent Schmidt number of species k, equal for all species $Sc_k^t = Sc^t = 0.6$. Note that having one turbulent Schmidt number for all the species does not imply $\widetilde{V}_i^{c,t} = 0$ because of the ratio $W_k/\overline{W}$ in Eq. (4.22).

- **Unresolved energy flux** $\overline{q}_i^{sgs} = -\overline{\rho}(\widetilde{u_i E} - \widetilde{u}_i \widetilde{E})$:

$$\overline{q}_i^{sgs} = -\lambda_t \frac{\partial \widetilde{T}}{\partial x_i} + \sum_{k=1}^{N} \overline{J}_{i,k} \widetilde{h}_{s,k} \tag{4.25}$$

$$\text{with: } \lambda_t = \frac{\mu_t \overline{C}_p}{Pr^t} \tag{4.26}$$

4.2.4 Modeling of the subgrid stress tensor

LES models for the subgrid stress tensor (see Eq. (4.21)) are derived on the theoretical ground that the LES filter is spatially and temporally invariant. Generally, the influence of the SGS on the resolved motion is taken into account by a SGS model based on the introduction of a turbulent kinematic viscosity, ν_t (Boussinesq (1877) hypothesis). Such an approach assumes that the effect of the SGS field on the resolved field is purely dissipative. This assumption is essentially valid within the cascade theory introduced by Kolmogorov (1941). LES models for the subgrid stress tensor only differ through the estimation of ν_t. In this document, only the three models used during the thesis are presented: the Smagorinsky, the WALE (Wall Adapting Local Eddy-viscosity) and the SIGMA model. More information on the other models implemented in AVBP can be found for example in (AVBP, 2011).

- **The Smagorinsky model**

$$\nu_t = (C_s \Delta_x)^2 \sqrt{2 \widetilde{S}_{ij} \widetilde{S}_{ij}} \tag{4.27}$$

  where Δ_x is the filter characteristic length (cube-root of the cell volume), C_s is the model constant equal to 0.18 but can vary between 0.1 and 0.8 depending on the flow configuration. The Smagorinsky model (Smagorinsky, 1963) was developed in the sixties and heavily tested for multiple flow configurations. This closure has the particularity of supplying the right amount of dissipation of kinetic energy in homogeneous isotropic turbulent flows. Locality is however lost and only global quantities are maintained. It is known to be too dissipative and transitioning flows are not suited for its use (Sagaut, 2002). Moreover, this formulation is known for not vanishing in near-wall regions and therefore cannot be used when walls are treated as no-slip walls.

- **The WALE model**

$$\nu_t = (C_w \Delta_x)^2 \frac{(s^d_{ij} s^d_{ij})^{3/2}}{(\widetilde{S}_{ij} \widetilde{S}_{ij})^{5/2} + (s^d_{ij} s^d_{ij})^{5/4}} \tag{4.28}$$

  with

$$s^d_{ij} = \frac{1}{2}(\widetilde{g}^2_{ij} + \widetilde{g}^2_{ij}) - \frac{1}{3}\widetilde{g}^2_{kk}\delta_{ij} \tag{4.29}$$

  where $C_w = 0.4929$ is the model constant and $\widetilde{g}_{ij}$ is the resolved velocity gradient. The WALE mode was developed by Nicoud & Ducros (1999) for wall bounded flow in an attempt to recover the scaling of the laws-of-the-wall. Similarly to the Smagorinsky model locality is lost and only global quantities are to be trusted.

- **The SIGMA model**

$$\nu_t = (C_\sigma \Delta_x)^2 \frac{\sigma_3(\sigma_1 - \sigma_2)(\sigma_2 - \sigma_3)}{\sigma_1^2} \tag{4.30}$$

  where $C_\sigma = 1.35$ is the model constant. The SIGMA operator was proposed by Nicoud *et al.* (2011) based on singular values (σ_1, σ_2 and σ_3) of a tensor built using resolved velocity

gradients. Note that the singular values σ_i have the following near-wall behaviors:

$$\begin{cases} \sigma_1 = O(1) \\ \sigma_2 = O(y) \\ \sigma_3 = O(y^2) \end{cases} \tag{4.31}$$

where y is the normal coordinate to the wall surface and $O(y^p)$ denotes a term of the order of p, i.e. behaving like y^p when the distance to the solid boundary decreases: $y \mapsto 0$. Thus, the SIGMA model behaves correctly in the near-walls region: $\nu_t = O(y^3)$.

4.3 Combustion modeling

4.3.1 Overview

The region where chemical reactions take place, referred to as the flame front, is generally very small. Typical flame thickness at atmospheric pressure for kerosene/air flames is about 0.1 to 0.5 mm raising a problem for LES of reactive flows: the flame thickness δ_L^0 is generally smaller than the standard LES grid size Δ_x. Depending on the complexity of the chemical description and the operating conditions, 5 to 50 points are needed to correctly resolve the flame front. The resulting mesh size is out of reach with current computational resources considering the complexity of industrial configurations. In LES, combustion models have been developed to approximate the filtered species reaction rates $\overline{\dot{\omega}}_k$ (see Eq. (4.8)) from the resolved quantities. Reviews proposed by Veynante & Vervisch (2002), Pitsch (2006) or the textbook of Poinsot & Veynante (2011) give an overview of the combustion models. Combustion modeling is generally split between models for premixed and non-premixed regimes.

For turbulent premixed combustion, two main categories are distinguished:

- **Models assuming an infinitely thin reaction zone:** the turbulent premixed flame is modeled by fresh reactants and burnt products separated by an infinitely thin reaction zone. The local structure of the flame is assumed equal to a laminar flame for which the inner structure is not affected by turbulence (flamelet assumption). The Bray-Moss-Libby (BML) models (Bray & Moss, 1977), the flame surface density models (Hawkes & Cant, 2000), and the G-equation model (Moureau *et al.*, 2009) are some of the most popular models in this category.
- **Models describing the structure of the reaction zone thickness:** the turbulent premixed flame is characterized by a finite thin reaction zone that can interact with the turbulent flow and often behaves as a stretched laminar flame. Some examples are the Probability Density Function (PDF) models (Dopazo, 1994), the F-TACLES approach (Fiorina *et al.*, 2010) and the artificially Thickened Flame (TF) models (Colin *et al.*, 2000; Légier *et al.*, 2000).

In non-premixed systems, combustion is generally controlled by the rate of molecular mixing because chemistry is faster than turbulent motion. The mixing is then evaluated with a conserved

scalar, typically the mixture fraction z which is essentially a measure of the local equivalence ratio. Several methods have been proposed to measure the mixing rate in turbulent flows:

- **Probability Density Function (PDF) methods:** the Reynolds averaged values are obtained from the PDF of mixture fraction. Under the assumption of an infinitely fast chemistry, the local filtered reaction rate may be expressed as:

$$\overline{\dot{\omega}}_k(x,t) = \int_0^1 \dot{\omega}_k(z) P(z,x,t) dz \tag{4.32}$$

  where $P(z,x,t)$ is the subgrid scale mixture fraction PDF and $\dot{\omega}_k(z)$ is the non-filtered reaction rate obtained from a flamelet library. A popular method is to presume the shape of the PDF: Cook & Riley (1994) proposed to use β-function using the mean mixture fraction $\widetilde{z}$ and its variance $\widetilde{z''^2}$. A conservation equation for $\widetilde{z}$ is typically added to the NS set of equations while $\widetilde{z''^2}$ is obtained either from an algebraic closure or a balance equation. The PDF can also be explicitly computed from a balance equation (Pope, 1985). Similar approaches have been derived to encompass finite rate chemistry through the scalar dissipation rate χ (Cook & Riley, 1998), for which the PDF must be evaluated and the flamelet library extended to $\dot{\omega}_k(z,\chi)$.

- **Linear Eddy Model (LEM) methods:** they were proposed by Kerstein (1988) for which a turbulent stirring at the subgrid scale level is applied on a 1D scalar field and a 1D reaction-diffusion equation is integrated in each LES cell to represent unresolved mixing and chemical reactions.

Regardless of the combustion regimes, the artificially thickened flame model is considered in this work. Poinsot & Veynante (2011) recalled that the use of TFLES for non-premixed flame is not correct from a theoretical point of view, but the model has shown reasonably good results in several non-premixed configurations, mainly because the combustion regime in realistic gas turbine is generally partially premixed rather than purely non-premixed. Section 4.3.2 details the TFLES model.

4.3.2 Thickened Flame LES (TFLES) model

An attractive solution to explicitly resolve the flame front on the LES grid consists in artificially thickening the flame. This idea was first proposed by Butler & O'Rourke (1977). Since the reaction rate is still expressed using Arrhenius law, various phenomena can be accounted for without requiring ad-hoc sub models (ignition, flame/wall interactions, heat losess, ...). The whole TFLES method is based on a simple change of the spatial and temporal variables:

$$x \mapsto \mathcal{F}x \quad \text{and} \quad t \mapsto \mathcal{F}t \tag{4.33}$$

which corresponds to a thickening of the flame thickness by a factor $\mathcal{F}$. The thickened species reaction rates are then:

$$\overline{\dot{\omega}}_k^* = \frac{\dot{\omega}_k}{\mathcal{F}} \tag{4.34}$$

Following the theories of laminar premixed flame (Williams, 1985), the laminar flame speed S_L^0 then writes:

$$S_L^0 \propto \frac{D_{th}}{\delta_L^0} \mapsto \frac{D_{th}}{\mathcal{F}\delta_L^0} \tag{4.35}$$

In order to conserve the flame speed through the change of variables, the thermal and species diffusivities need to be multiplied by the same thickening factor $\mathcal{F}$ so that:

$$S_L^0 \propto \frac{\mathcal{F}D_{th}}{\mathcal{F}\delta_L^0} = \frac{D_{th}}{\delta_L^0} \tag{4.36}$$

When the flame is thickened by a factor $\mathcal{F}$, the interaction between the flame and the turbulence is modified: the flame becomes less sensitive to turbulent motions and vortices may affect the reaction zone. This interaction is characterized by the Damköhler number Da (see Eq. (3.34)):

$$Da = \frac{\tau_t}{\tau_c} = \frac{l_t}{u'}\frac{S_L^0}{\delta_L^0} \mapsto \frac{l_t}{u'}\frac{S_L^0}{\mathcal{F}\delta_L^0} = \frac{\tau_t}{\mathcal{F}\tau_c} \tag{4.37}$$

This point has been investigated using DNS by Angelberger *et al.* (1998) and Colin *et al.* (2000). The so-called efficiency function $\mathcal{E}$ has been proposed to properly account for the unresolved wrinkling effect (filtered at the thickened flame size $\Delta_e \sim \mathcal{F}\Delta_x$ where the subscript e stands for effective) on the filtered reaction rate:

$$D_{th} \mapsto \mathcal{E}\mathcal{F}D_{th} \quad \text{and} \quad D_k \mapsto \mathcal{E}\mathcal{F}D_k \tag{4.38}$$

$$\overline{\dot{\omega}}_k = \frac{\mathcal{E}\dot{\omega}_k}{\mathcal{F}} \tag{4.39}$$

so that:

$$S_L^0 \mapsto \frac{\mathcal{E}\mathcal{F}D_{th}}{\mathcal{F}\delta_L^0} = S_T \tag{4.40}$$

where S_T is the resolved turbulent flame speed.

In this work, two different efficiency functions $\mathcal{E}$ are employed. Both are based on the hypothesis that an equilibrium is reached between the turbulent motion and the flame surface at the subgrid scale level (i.e. the aerodynamic stretch and the stretch induced by the curvature of the flame front compensate each other so that there is no creation or destruction of flame surface at the subgrid scale level).

- In the **Colin model**, Colin *et al.* (2000) proposed an efficiency function $\mathcal{E}_{Colin}$ which compares the flame wrinkling with and without thickening, using the wrinkling factor Ξ:

$$\Xi(\delta_L^0) = 1 + \alpha\Gamma_{Co}\left(\frac{\Delta_e}{\delta_L^0}, \frac{u'_{\Delta_e}}{S_L^0}\right)\frac{u'_{\Delta_e}}{S_L^0} \tag{4.41}$$

  where α is a constant and Γ_{Co} is a function taking into account the subgrid strain rate depending on the effective filter size Δ_e and the fluctuating subgrid velocity u'_{Δ_e}. Note that

α requires an estimation of the integral length scale l_t, which is often unknown and varies in space and time. The efficiency function is then given by:

$$\mathcal{E}_{Colin} = \frac{\Xi(\delta_L^0)}{\Xi(\mathcal{F}\delta_L^0)} \tag{4.42}$$

Finally, this combustion model is closed by approximating the subgrid scale turbulent velocity u'_{Δ_e} with an operator based on the rotational of the velocity field to remove the dilatation part of the velocity and by estimating the constant α using HIT simulations (Angelberger *et al.*, 1998).

- In the **Charlette model**, Charlette *et al.* (2002) proposed a power-law model for the wrinkling factor which extends the Colin model:

$$\Xi(\delta_L^0) = \left(1 + \min\left[\frac{\delta_{\Delta_e}}{\delta_L^0}, \Gamma_{Ch}\left(\frac{\delta_{\Delta_e}}{\delta_L^0}, \frac{u'_{\Delta_e}}{S_L^0}, Re_{\Delta_e}\right)\frac{\delta_{\Delta_e}}{\delta_L^0}\right]\right)^{\beta} \tag{4.43}$$

where β is the model parameter to be specified and Re_{Δ_e} is the turbulent Reynolds at the effective filter size: $Re_{\Delta_e} = S_L^0\delta_L^0/\nu$.

In order to tackle non-premixed configuration where fuel and oxidizer can partially mix before burning, the TFLES model has been modified to avoid acceleration of the mixing process in the non-reacting zones. A dynamic thickening method (called DTFLES) depending on the flame position and the local resolution has been developed by Légier *et al.* (2000) and is therefore preferred. This method is called DTFLES, where the word dynamic refers to local application of the TFLES model and not a dynamic procedure to evaluate the model constant as recently done in Wang *et al.* (2011). The thickening factor $\mathcal{F}$ is not constant anymore but goes from unity in non-reacting zones to $\mathcal{F}_{max}$ in the flame. This is obtained by writing:

$$\mathcal{F} = 1 + (\mathcal{F}_{max} - 1)\mathcal{S} \tag{4.44}$$

where $\mathcal{S}$ is a sensor depending on the local reaction rate and $\mathcal{F}_{max}$ is given by:

$$\mathcal{F}_{max} = \frac{N_e}{\Delta_x}\delta_L^0 \tag{4.45}$$

with N_e the number of elements used to resolve the flame front. N_e depends on the chemical scheme used, but a typical value of 5 points guarantees to recover the correct flame speed of a 1D flame for global one step or two steps schemes. The sensor $\mathcal{S}$ is computed as:

$$\mathcal{S} = \tanh\left(\beta'\frac{\Omega}{\Omega_0}\right) \tag{4.46}$$

where β' is a constant equal to 50, Ω is a sensor function detecting the presence of a reaction front and Ω_0 corresponds to its maximum value and is extracted from a laminar 1D flame computation.

4.4 Chemical scheme for LES

Directly including detailed chemical mechanisms in LES is not a viable option because of the associated high computational cost. Indeed, each species requires an additional transport equation and the stiffness of the source term of some of them requires to reduce the time step. Two approaches have been developed to overcome this problem in LES:

- Reduced schemes result in a simplification of detailed mechanisms where the chemical behavior is correctly reproduced using as few species as possible. This approach is used in this work and will be detailed below.

- Tabulated chemistry rely on the fact that the kinetic scheme variables are linked: the flame structure is studied as function of a limited number of variables (temperature, mixture fraction, ...) (Maas & Pope, 1992; Gicquel *et al.*, 2000) and all the species of the detailed kinetics are available in the LES computation through a look-up table. Two problem arise using tabulated chemistry: 1) the size of the table can rapidly increase when the number of parameters increase and several methods have been proposed to ease its use (Veynante *et al.*, 2008; Fiorina *et al.*, 2009), 2) the choice of the prototype flame used to create the table is not obvious in complex configurations where the combustion regime is unknown.

Reduced schemes can be classified in two classes:

- Global schemes are built to reproduce macroscopic quantities such as the premixed flame speed or burnt gas state. These mechanisms are easy to build for a wide range of operating conditions and since the number of reaction is low (<= 4), their implementation in LES codes is easy. All information about intermediate species and the intricate flame structure disappears.

- Analytical mechanisms have been proposed to include more physical insight in the chemical description. The reduction of a detailed mechanism can be achieved through a two-step procedure, performing first a skeletal reduction to obtain a skeletal mechanism and then a second reduction to reduce the stiffness of the obtained mechanism. The construction of a skeletal mechanism aims at removing redundant species/reactions from the detailed mechanism using for instance Sensitivity Analysis (Tomlin *et al.*, 1992) or Directed Relation Graph Analysis (Lu & Law, 2006). The resulting skeletal scheme is generally still too large and too stiff for LES in complex geometries so that techniques such as the Computational Singular Perturbation (CSP) (Lam & Goussis, 1994) or Intrinsic Low-dimensional Manifold (ILDM) (Maas & Pope, 1992) are used to further reduce the number of species based on their lifetime.

In this work, the combustion of two hydrocarbons is studied: 1) the KIAI experimental benches studied in Chaps. 6-8 & 10 use methane, 2) the annular flame propagation in the MICCA burner studied in Chap. 11 uses propane. The chemistry description employed for both hydrocarbon is presented below.

4.4.1 Methane chemistry

Two methane mechanisms are used in this work to investigate the KIAI configurations: a global two-steps chemistry and an analytically 13 species reduced scheme. Unless specified otherwise, the simulations are performed with the global two-step mechanism due to its low computational cost but the effect of the chemical description is evaluated by comparison with the analytically reduced scheme. The performances of both schemes are compared to the GRI 3.0 detailed mechanisms.

4.4.1.a Global scheme: 2S_CH4_BFER

Most of the LES performed in this study use the 2S_CH4_BFER two-step mechanism of Franzelli *et al.* (2012) where the Pre-Exponential Adjustment (PEA) (Légier, 2001) method allows to reproduce the laminar flame speed over a wide range of equivalence ratio. This global scheme involves six species through two reactions given by:

$$CH_4 + 1.5\ O_2 \Longrightarrow CO + 2\ H_2O \tag{4.47}$$

$$CO + 0.5\ O_2 \Longleftrightarrow CO_2 \tag{4.48}$$

where the oxidation reaction (Eq. (4.47)) is irreversible and the recombination of CO into CO_2 is reversible (Eq. (4.48)). The Prandtl number is evaluated from the burnt gases transport properties $Pr = 0.7$ and the Schmidt numbers result from a constant unity Lewis number approximation for all species. The effect of this approximation is found to be low in Franzelli (2011) since the global scheme is fitted to reproduce the laminar flame speed. The mixture viscosity μ follows a power law (see Sec. 2.3) of parameter $\mu_0 = 1.84e^{-5}$ kg/m/s and $b = 0.6759$. When using a global scheme, the structure of the flame front is completely lost and only the global thermal balance between reaction and diffusion processes is reproduced to recover the flame speed.

4.4.1.b Analytical scheme: LU_13

The LU_13 mechanism (Sankaran *et al.*, 2007) is used to evaluate the effect of the chemistry description on the ignition kernel phase. It has been implemented in AVBP by Franzelli (2011), where several methane mechanisms were benchmarked in a partially premixed turbulent swirled flame and the LU was found to perform well compare to the GRI detailed mechanism. It takes into account 13 resolved species (CH_4, O_2, CO_2, CO, H_20, N_2, H_2, H, OH, O, HO_2, CH_3 and CH_2O) and 4 Quasi-Steady State (QSS) species (CH_2, CH_2S, HCO and CH_2OH) through 73 elementary reactions. The LU_13 mechanism does not use unity Lewis assumption and the species Lewis number are listed in Tab. 4.1 and the Prandtl number is equal to 0.7 (burnt gases state). The mixture viscosity μ follows a power law with the same parameter as the 2S_CH4_BFER scheme. The computational cost of LU_13 is about 1.68 times that of the 2S_CH4_BFER ones and it requires 63% more memory to store LES data.

CH_4	O_2	CO_2	CO	H_20	N_2	H_2	H	OH	O	HO_2	CH_3	CH_2O
0.967	1.0557	1.35	1.07	0.777	0.29	1.036	0.17	0.69	0.7	1.07	0.97	1.25

Table 4.1: Species Lewis numbers for the LU analytical mechanism

4.4.1.c Comparison of the two reduced schemes

Both the global and the analytically reduced schemes are able to reproduce the laminar flame speed over the whole range of flammable mixture with a fairly good agreement with experimental data (Franzelli, 2011) as shown in Fig. 4.2 where the adiabatic flame temperature and the laminar flame speed of both reduced schemes are plotted as functions of the equivalence ratio.

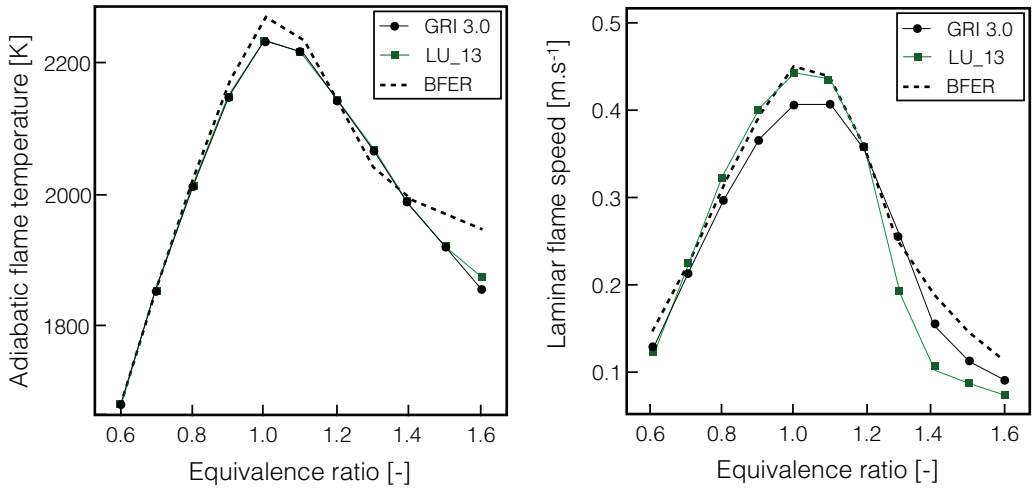

Figure 4.2: Comparison of the 2S_CH4_BFER and LU_13 schemes with GRI 3.0: adiabatic flame temperature (left) and laminar flame speed (right) (extracted from Franzelli (2011)).

When dealing with ignition, more complex flames properties should be evaluated, such as the flame response to strain and the ignition delay. To evaluate the performances of both mechanisms, the flame consumption speed is plotted against strain rate at ambient conditions in Fig. 4.3(left) and the ignition delay versus the fresh gas temperature reciprocal in Fig. 4.3(right). The results obtained with the GRI 3.0 detailed mechanism are also reported as a reference.

The LU_13 mechanism is found to recover quite well the flame response to strain for a wide range of strain rates compared to the GRI 3.0 while the 2S_CH4_BFER is less satisfactory but is able to reproduce the correct trend. Similarly, ignition delay predicted by LU_13 remains close to the GRI 3.0 mechanism (even though it can be one order of magnitude slower for low temperature) but the 2S_CH4_BFER scheme is about 100 times faster than the detailed mechanism. The effect of these differences will be evaluated in further analysis.

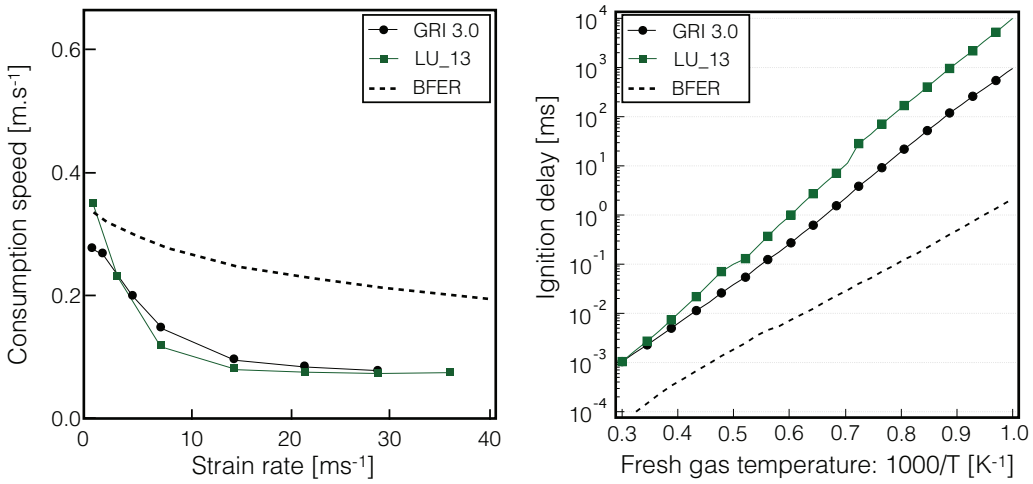

Figure 4.3: Comparison between the 2S_CH4_BFER and LU_13 schemes: consumption speed as function of strain (extracted from Franzelli (2011)) (left) and ignition delay as function of temperature reciprocal (computed with CANTERA) (right).

4.4.2 Propane chemistry

A two-step global mechanism is used to study the SIMAC configuration (Chap. 11). Since the experiment is perfectly premixed, the scheme is fitted to match the laminar flame speed at a single equivalence ratio $\phi = 0.76$. The laminar flame speed is $S_{L,0} = 0.239\ m.s^{-1}$ at this operating point. As the 2S_CH4_BFER scheme, this global scheme involves six species through two reactions given by:

$$C_3H_8 + 3.5\ O_2 \Longrightarrow 3CO + 4\ H_2O \tag{4.49}$$

$$CO + 0.5\ O_2 \Longleftrightarrow CO_2 \tag{4.50}$$

The rate of the oxidation reaction q_1 and the CO_2 recombination reaction q_2 are given by:

$$q_1 = \mathcal{A}_{f,1} \left(\frac{\rho Y_F}{W_F}\right)^{n_1^F} \left(\frac{\rho Y_{O_2}}{W_{O_2}}\right)^{n_1^{O_2}} \exp\left(\frac{E_{a,1}}{\mathcal{R}T}\right) \tag{4.51}$$

$$q_2 = \mathcal{A}_{f,2} \left[\left(\frac{\rho Y_{CO}}{W_{CO}}\right)^{n_2^{CO}} \left(\frac{\rho Y_{O_2}}{W_{O_2}}\right)^{n_2^{O_2}} - \frac{1}{K_e}\left(\frac{\rho Y_{CO_2}}{W_{CO_2}}\right)^{n_2^{CO_2}}\right] \exp\left(\frac{E_{a,2}}{\mathcal{R}T}\right) \tag{4.52}$$

where the constants are summarized in Tab. 4.2.

Once again, a constant and equal Lewis number assumption is used for all species with $Pr = 0.739$ and $Sc_k = Sc = 0.739$. The dynamic viscosity follows a power law with $\mu_0 = 2.5034e^{-5}$ kg/m/s and $b = 0.6695$.

	C_3H_8 oxidation	CO-CO_2 equilibrium
Acitivation energy	$4.15\ .10^4$	$2.0\ .10^4$
Pre-exponential factor	$2.2\ .10^{12}$	$2.5\ .10^{10}$
C_3H_8 exponent n_1^F	0.55	
O_2 exponent $n_1^{O_2}$ ($n_2^{O_2}$)	0.90	0.5
CO exponent n_2^{CO}		1.0
CO_2 exponent $n_2^{CO_2}$		1.0

Table 4.2: Activation energy $E_{a,i}$, pre-exponential factor $\mathcal{A}_{f,i}$, and reaction exponents for the C_3H_8 two-step global scheme. Units are: cal.mol^{-1} and csg.

4.5 Numerical methods in AVBP

The development of the AVBP solver started in the mid-nineties on the initiative of Schönfeld & Rudgyard (1999). The goal was to develop an efficient code handling unstructured grids of any element type in order to study complex geometries. AVBP is based on a *Cell-Vertex* finite volume formulation (Rudgyard, 1993) where the solution variables are stored at the nodes but the flux integration is computed on the cells. The cell residuals (or variations) are then distributed to the nodes in order to obtain the updated solution. From this perspective, *Cell-Vertex* schemes have a close affinity with weighted residual finite element methods (Morton & Paisley, 1989) and Colin & Rudgyard (2000) took advantage of this to implement finite element schemes in AVBP. Over the last decade, AVBP has been optimized to have a good scalability on thousands of processors on various machine architectures, allowing to have a reasonable return time even with large grid size ($\mathcal{O}^7$).

4.5.1 Numerical schemes

A complete review of the numerical schemes implemented in AVBP is presented in the Ph.D. of Lamarque (2007). The two numerical schemes used in this work are:

- The **Lax-Wendroff (LW) scheme** developed by Lax & Wendroff (1960) is a finite volume centered scheme using an explicit time integration with a single Runge-Kutta step. Its accuracy is of second order in both space and time. Its main advantage stems from the fact that its formulation includes a streamwise stabilization term making it quite robust and a mass lumping operation resulting in a low computational cost. Its use in this Ph.D. is limited to the initialization of non-reacting flows and the carburation of the combustion chambers.
- The **Two step Taylor-Galerkin 'C' (TTGC) scheme** developed by Colin & Rudgyard (2000) is a finite element scheme of the continuous Taylor-Galerkin family (Donea & Huerta, 2003). Its accuracy is of third order in both space and time (4th order on regular grid (Moureau *et al.*, 2005)). Specifically built for LES, TTGC has good properties regarding dissipation and dispersion. However, these advantages make it less robust than LW and the explicit mass matrix inversion increases the computational cost (about 2.5 time

more expensive than LW). TTGC is used in this work for both non-reacting flow preceding energy deposit and complete ignition sequences.

The numerical discretization methods in AVBP are spatially centered and prone to small-scale oscillations in the vicinity of steep solution variations. This is why it is common practice to add a so-called artificial viscosity (AV) term to the discrete equations, to control these spurious modes (also known as "wiggles"). These AV models are characterized by the "linear preserving" property which leaves unmodified a linear solution on any type of element. The models are based on a combination of a "shock capturing" term (called 2nd order AV) and a "background dissipation term" (called 4th order AV or hyper-viscosity). In AVBP, adding AV is done in two steps:

- first a sensor detects if AV is necessary, as a function of the flow characteristics,
- then a certain amount of 2nd and 4th AV is applied, depending on the sensor value and on user-defined parameters.

The 2nd order AV acts just like a "classical" viscosity activated only in certain regions of the flow. It smoothes local gradients, and introduces artificial dissipation. The 4th order AV is mainly used to control spurious high-frequency wiggles.

4.5.2 Boundary conditions

Boundary conditions are a crucial point of CFD codes, especially for compressible flows. In the case of AVBP, it is of particular importance since the goal is to study reactive flows in combustion chambers where the geometry has a direct effect on the flow and where the acoustic behavior is controlled by inlet and outlet impedances. For nodes at the boundary of the computational domain, it is necessary to correct the residual obtained from the convective and diffusive fluxes. To take into account acoustic at inlet and outlet boundary conditions, the residual is modified by translating the boundary condition in a problem of characteristic waves propagation (Struijs, 1994). This method called Navier-Stokes Characteristic Boundary Condition (NSCBC) developed by Poinsot *et al.* (1991) and extended to multi-species flows by Moureau *et al.* (2005) is implemented in AVBP and is used in all simulations presented in this work.

Part II

Single burner ignition

Chapter 5

Literature review on kernel initiation and expansion

Contents

5.1 Phase 1: Initiation of a self-sustained expanding flame kernel 57

5.1.1 Quiescent/laminar flows 58

5.1.2 Effect of turbulence 61

5.1.3 Models to mimic energy deposit 63

5.2 Phase 2: kernel expansion and transient flame propagation 65

5.2.1 Development of isolated flame kernel 65

5.2.2 Ignition of single burner configuration 71

5.3 Conclusion 76

5.1 Phase 1: Initiation of a self-sustained expanding flame kernel

Literally, ignition derives from the Latin *ignire* "set on fire" and designates the initiation of chemical reactions. It is also used in the literature in a broad sense to encompass the subsequent flame propagation and eventually the flame stabilization. In this section, the review is limited to its literal definition and emphasis is given to forced ignition, i.e. using an external source term, in contrast with autoignition. The main insights from the literature in both laminar and turbulent as well as premixed and non-premixed systems are first reported. Then the studies dedicated to the detailed transition from high temperature plasma to flame kernel are briefly reviewed and the models developed to mimic the igniter are listed.

5.1.1 Quiescent/laminar flows

The understanding of forced ignition in quiescent or laminar flow is not of practical importance for gas turbines or ground transportation engines, but it is crucial for fire and explosion safety issues in fuel transport or petrochemical activities. In any case, the case is sufficiently simplified to allow theoretical study that can shed some light on the fundamentals of the ignition process. Theoretical developments that have lead to the concept of Minimum Ignition Energy (MIE) in premixed flows are first reviewed and the effect of the operating conditions or fuel composition highlighted. Then, the effect of partial premixing and two-phase flow is presented.

Early theoretical work on ignition in quiescent mixture uses the fact that for a vast majority of fuel kinetics, heat release is strongly dependent on temperature and comparatively less sensitive to reactant concentrations (Gorbachev, 1981). Thus, during the first instants of ignition, variation of the reactant mass fractions are considered negligible whereas the variations of temperature are taken into account. Then, studying ignition reduces to a thermal balance: the chemical runaway can occur if the rate of chemical heat release in the system exceeds the rate of heat losses to the surroundings. This balance has been first formulated by Semenov (1928) and improved then by Frank-Kamenetskii (1942) in the study of thermal explosion in solids. Deshaies & Joulin (1984) briefly sumarize the results in terms of characteristic times for gaseous mixtures: the time t_{cond} for the initial temperature profile to relax to the surrounding temperature by conduction is estimated by $t_{cond} \propto r_i^2/D_{th}$, where r_i is the initial hot spot size. As for the chemical time t_{chem}, it is derived from a single step irreversible Arrhenius law:

$$t_{chem}(T_i) \propto \frac{1}{\rho \mathcal{A} e^{-E/\mathcal{R}T_i}} \tag{5.1}$$

where T_i is the initial temperature in the hot spot (after energy deposit) and $\mathcal{A}$ and E are the pre-exponential constant and the activation energy of the single step reaction respectively. A critical radius $r_{th,c}$ is obtained for $t_{cond} \simeq t_{chem}(T_i)$:

$$r_{th,c} \simeq \sqrt{\frac{D_T}{\rho \mathcal{A} e^{-E/\mathcal{R}T_i}}} \tag{5.2}$$

More recently Vasquez-Espi & Linan (2002) use the asymptotic analysis first introduced by Berman *et al.* (1981) to study the chemical initiation phase and a model is proposed in terms of Damkhöler number $Da_{ign} = t_{cond}/t_{chem}(T_i)$: ignition occurs for values of Da_{ign} higher than a critical value computed for planar, cylindrical and spherical cases as shown in Fig. 5.1. The study indicates that the critical diameter increases with the number of spatial dimensions considered since the rate of dissipation increases. This study gives one criterion for the size (or energy) of the initial deposit that must be fulfilled for the thermal runaway to occur but is not sufficient to ensure its subsequent propagation.

After the thermal runaway, the reaction starts consuming reactants and their depletion can no longer be neglected (Merzhanov & Averson, 1971). The rate of chemical heat release then depends on the diffusion rate of the limiting reactant towards the reaction zone to overcome the rate of losses to the surroundings. Taking into account the consumption and diffusion of the

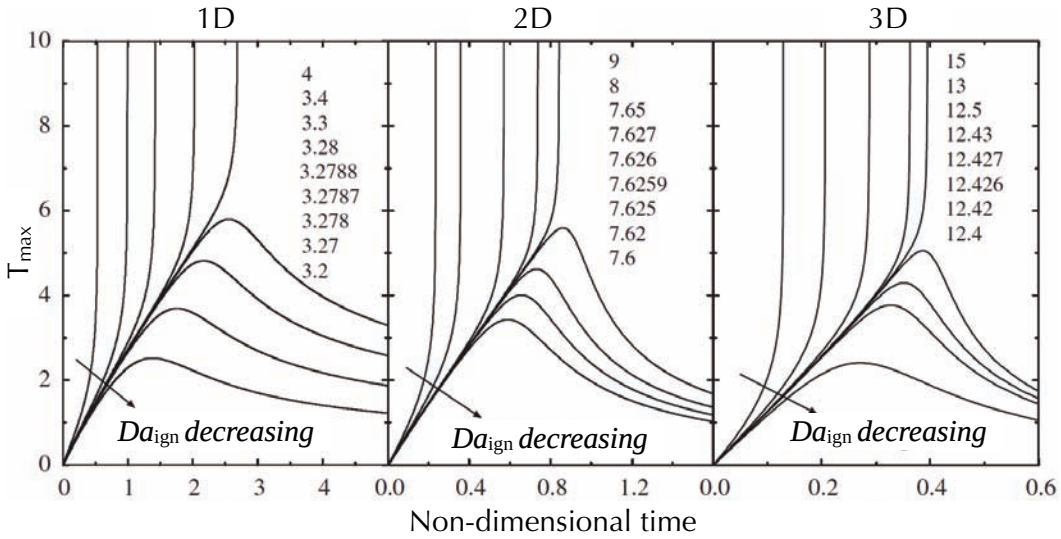

Figure 5.1: Temporal evolution of the temperature at the center of the energy deposit for various Damkhöler numbers Da_{ign}. Extracted from Vasquez-Espi & Linan (2002).

limiting reactant, Zeldovich *et al.* (1980) show the existence of a stationary unstable solution to the conservation equations. This solution consist in a spherical flame of radius r_c for which the reactant diffusion rate towards the flame is such that the chemical heat release balances the outward thermal conduction. This solution is unstable and a stability analysis (Zeldovich *et al.*, 1980) demonstrates that a negative radius perturbation results in a flame collapse while a positive perturbation initiates an outwardly propagating spherical flame. Thus, to generate a self-sustained flame, the energy deposit must drive the flame kernel beyond that critical radius r_c before the kernel temperature drops below the adiabatic temperature T_{ad}. As noted by Joulin (1985), in the case of high temperature hot spot such as encountered with spark deposit ($T_i >> T_{ad}$ (Maly & Vogel, 1978)), $r_{th,c} < r_c$ since $r_{th,c}$ strongly decreases with T_i: energy deposit can be sufficient to initiate the thermal runaway but too weak to drive the kernel beyond the critical size. Experiments show this behavior for propane-air mixture in Olsen *et al.* (1953).

The critical flame radius r_c is strongly dependent on the limiting reactant Lewis number of the limiting reactant (Deshaies & Joulin, 1984; He, 2000): r_c decreases with decreasing Lewis number. Flame initiation is then expected to be more difficult if the limiting reactant is heavier, which is in agreement with experimental observation of Lewis & von Elbe (1987). Starting from the unstable solution of the conservation equation and using high activation energy asymptotic development, Champion *et al.* (1986) explicitly derive a formula for the critical radius r_c:

$$r_c = \frac{\lambda(T_{ad})}{C_p(T_{ad})\rho(T_f)S_L^0}\frac{T_{ad}}{T_b Le_A}e^{\frac{E}{2\mathcal{R}T_{ad}}\frac{T_{ad}-T_b}{T_b}} \tag{5.3}$$

Note that for non-unity Lewis number, the adiabatic flame temperature and the burnt gas

temperature differ. For unity Lewis number mixture, the critical radius reduces to:

$$r_c = \frac{\lambda(T_{ad})}{C_p(T_{ad})\rho(T_f)S_L^0} \tag{5.4}$$

This definition is similar to the definition of the laminar flame thickness (Williams, 1985), but in this case λ and C_p are evaluated at the adiabatic temperature and not at the fresh gas temperature. Other studies report that the critical radius is of the order of the laminar flame thickness (Glassman & Yetter, 2008; Akindele *et al.*, 1982).

The critical energy is then theoretically defined as the energy required to increase to the adiabatic flame temperature of a sphere of radius r_c:

$$E_c = \frac{4}{3}\pi r_c^3 \rho(T_0) C_p(T_0)(T_{ad} - T_0) \tag{5.5}$$

This critical energy often referred as Minimum Ignition Energy (MIE) has been evaluated experimentally in a wide range of conditions representative of internal combustion engines. The extensive experimental study using reported in Lewis & von Elbe (1987) investigates the MIE of numerous hydrocarbons (methane, propane, heptane, ...) over a wide range of equivalence ratio using a spark plug igniter. Experiments shows fairly good agreement with theoretical values: the critical energy is found to be strongly dependent to the equivalence ratio (Lewis & von Elbe, 1987; Ballal & Lefebvre, 1977; Ziegler *et al.*, 1985; Beduneau & Kim, 2003) with a ϕ_{MIE} minimizing MIE in rich mixture. ϕ_{MIE} increases with the number of carbon atoms in the hydrocarbon. These results agree with the theory: MIE is controlled by the diffusion of the heavy hydrocarbon towards the flame front. In accordance with Eq. (5.4), MIE increases when pressure decrease. Ballal & Lefebvre (1975) and Kono *et al.* (1984) experimentally investigate ignition in laminar flow: MIE increases with the bulk flow velocity. DNS of spark ignition in flowing mixture performed by Baum & Poinsot (1995) demonstrates the same trends: the MIE increase is the consequence of convective heat losses and the fact that the energy in deposited on a larger volume.

The main findings from gaseous perfectly premixed flow are still valid for gaseous non-premixed flow, but the location of the spark compared to the stoichiometric mixture fraction iso-line and the lean and rich flammability limits z_{lean} and z_{rich} comes into play. If the ignition location is far from the flammable region, the temperature in the hot spot may decrease below the critical temperature before being able to reach a flammable mixture. The laminar counterflow configuration is often used in the literature to study ignition in non-premixed flames and the effect of strain. The first study of ignition in a laminar counterflow configuration is performed by Rashkovsky (1999), using a point source energy deposit and a one-step chemistry description. This configuration is also used by Richardson *et al.* (2007) using a complex chemistry. The study shows that there is a critical strain rate above which ignition is not possible regardless of the spark position relative to the stoichiometric mixture iso-line. The ignitability limits are found to differ from the mixture flammability limits due to the rapid transport of heat from inflammable regions towards more favorable mixtures.

Finally, ignition in non-premixed two-phase flow reviewed in Aggarwal (1998), is first studied in quiescent fuel mist by Ballal & Lefebvre (1978) by combining experiments with a phenomenological model. Experiments show that the MIE monotonically increases when the fuel droplet

Sauter Mean Diameter (SMD) increases and when the fuel volatility decreases. The MIE is also found to decrease with increasing prevaporized fuel mass fraction at a constant overall equivalence ratio. From these observations, the authors conclude that the ignition process is controlled by the evaporation rate rather than the chemical rate. Ballal & Lefebvre (1978) propose a phenomenaological model which is obtained by comparing t_{cond} with both the evaporation and the burning times of the droplets. Those are experimentally estimated using d^2-law (Sirignano, 1999) and an infinitely fast chemistry approximation. The model is further improved by Ballal & Lefebvre (1979) including convection effects and finite rate chemistry. The first numerical study performed by Aggarwal & Sirignano (1984) brings some new insights on the ignition process in two-phase flow that neither the limited range of equivalence ratios nor the polydispersion of the experiments of Ballal & Lefebvre are able to show. The study indicates the existence of an optimum equivalence ratio for a given droplet diameter and an optimum droplet diameter d_{opt} for a given overall equivalence ratio which minimizes MIE. This behavior is explained by the difference between the gaseous equivalence ratio ϕ_g and the total equivalence ratio ϕ_{tot} (sum of the liquid and gas equivalence ratios) and the dependence of MIE to the gaseous equivalence ratio shown for gaseous premixed flow. Considering a given ϕ_{tot}, droplets with a diameter $d_l > d_{opt}$ are less prompt to evaporate, leading to $\phi_g < \phi_{MIE}$. On the contrary, for $d_l < d_{opt}$ evaporation is faster resulting in $\phi_g > \phi_{MIE}$. d_{opt} is expected to change with fuel volatility or droplet temperature.

Even though quiescent or laminar flows exhibits very little variability, the initiation of the flame kernel is probabilistic due to the variability of the ignition system deposit size and strength (Kono *et al.*, 1984). In case of laminar two-phase flows, the randomness of droplets distribution also introduce stochasticity in the ignition process (Aggarwal & Sirignano, 1984).

5.1.2 Effect of turbulence

When sparking in a turbulent environment, it is difficult to distinguish between failures associated with the generation of a sustainable flame kernel or with the subsequent flame/turbulence interactions. Thus, experiments do not always explain the origin of the ignition failure observed.

A convenient and easy way to investigate the effect of turbulence is to introduce the concept of turbulent diffusivity. Akindele *et al.* (1982) perform a 1D numerical study of an expanding kernel in a turbulent environment. The effect of turbulence is encompassed in the thermal diffusivity $D_{th} = \lambda/(\rho C_p) + D_{turb}$ where D_{turb} is the turbulent eddy diffusivity given by (under the hypothesis of HIT):

$$D_{turb} = 0.44\, u' l_t \left(1 - \exp\left(-\frac{u' t}{0.44 l_t}\right)\right) \tag{5.6}$$

where u' and l_t are the turbulent intensity and turbulent integral length scale respectively. Note that D_{turb} is time dependent, and initially zero. Therefore, diffusion is controlled by the molecular transport at first and turbulent transport takes over later. Using Eq. (5.6) in Eq. (5.2) and Eq. (5.4), one can observe that turbulence increases both the thermal critical radius $r_{th,c}$ and the critical radius r_c. The critical radius is then defined as the radius of the laminar flame kernel when the turbulent transport becomes dominant. Similar approaches are developed in Ballal & Lefebvre (1977) and more recently by Klein *et al.* (2008) to estimate the critical radius. These simplified approaches allow to understand the effect of turbulence in a deterministic sense.

Considering the stochastic nature of turbulence, the MIE must be statistically defined. It is generally accepted to define the MIE as the energy required to obtain a 50% probability of success (Kono *et al.*, 1984; Ziegler *et al.*, 1985). Figure 5.2 displays the MIE experimentally measured in a methane-air mixture for varying equivalence ratio and increasing turbulence intensity (Huang *et al.*, 2007; Shy *et al.*, 2010). For low turbulence intensity, the MIE slowly increases when u'/S_l increases. There is critical turbulence intensity where the slope changes, the MIE increasing then quickly for increasing turbulence intensity. This transition in the ignition process is explained by the change of turbulent combustion regime: the flame switches from a wrinkled flamelet regime to a thin-reaction regime: vortices of significant energy are smaller than the thermal thickness of the flame and modifies the structure of the flame modifying the thermal balance and favoring the diffusion process which results in a rapid increase of the MIE with turbulent intensity. This transition is also observed by Cardin *et al.* (2013) for another experimental set-up and a wider range of equivalence ratios. The study shows that for very lean mixture, the delay for the chain branching reactions to start is increased, increasing the heat losses prior to chemical runaway.

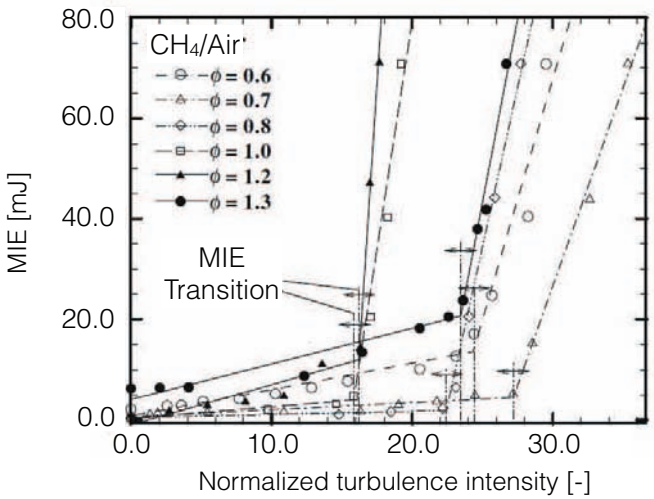

Figure 5.2: Evolution of the MIE in methane-air mixture as function of u'/S_l for various equivalence ratios from Shy *et al.* (2010).

The situation is more complex in non-premixed flows since both velocity and mixture variations control the generation of the flame kernel. As for laminar non-premixed flows, the location of the energy deposit compared to the flammable limits of the mixture determines the initiation of the combustion reactions. For turbulent non-premixed flows, the flammability factor F_f introduced by Birch *et al.* (1981) and Smith *et al.* (1986) enables to evaluate the probability of finding a flammable mixture at a given location by:

$$F_f = \int_{z_{lean}}^{z_{rich}} P(z)\, dz \tag{5.7}$$

where $P(z)$ is the PDF of mixture fraction.The probability of creating a flame kernel P_{ker} is defined as the number of ignition events that successfully initiate a flame kernel over the total number of ignition events. These studies show the strong correlation between F_f and P_{ker}. Cardin (2013) studies ignition in non-premixed homogeneous turbulent flow behind a grid, focusing on

the initiation of the flame kernel ($t < 1\ ms$). In an attempt to discriminate the effects of mixture fraction and the turbulence, the strength of the energy deposit is chosen so that ignition is alway successful when sparking in a premixed case in similar turbulence condition. The authors not only show that the ignition probability is strongly correlated with the mean mixture fraction in the energy deposit region at ignition time (Fig. 5.3 (left)), but also that the amount of fuel in the spark region is also crucial (Fig. 5.3 (right)). The amount of fuel is estimated with F_f where the PDF is constructed from the spatial distribution rather than the temporal distribution as in Birch *et al.* (1981). The study also demonstrates that even though F_f based on the initial field distribution is close to one, the kernel might be quenched due to detrimental conditions encountered later.

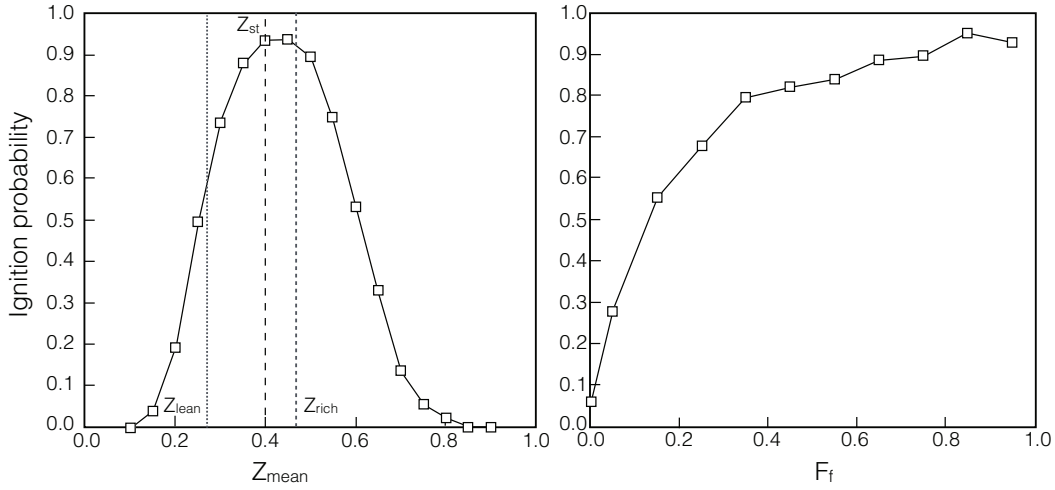

Figure 5.3: Evaluation of the ignition probability as function of the mean mixture fraction in the deposit region (left) or the amount of fuel in the same region (right). Extracted from Cardin (2013).

Ahmed & Mastorakos (2006) study the ignition probability in a turbulent methane jet where transport comes into play. The study demonstrates that $P_{ker} < F_f$ in region of high aerodynamic strain and demonstrates the joint effect of mixture and turbulence on the ignition probability. Results also reveals that P_{ker} can be non zero in regions where $F_f = 0$ which confirms the possibility to ignite by transport of heat from non flammable mixture zones as indicated in the laminar set-up of Richardson *et al.* (2007). The same distinction between F_f and P_{ker} is also observed by Ahmed *et al.* (2007*a*) in a bluff-body recirculating flow configuration: regions with F_f close to unity are showed to have P_{ker} of about 20% due to the high diffusion induced by turbulence. The maps of P_{ker} and F_f extracted from Ahmed *et al.* (2007*a*) are reported in Fig. 5.4: the results depict a large central region where $F_f \simeq 1$ but P_{ker} is low: this region corresponds to the recirculation bubble in the wake of the bluff body where turbulence is intense.

5.1.3 Models to mimic energy deposit

So far, the question of the igniter model has not been addressed. The fairly good agreement with the experiments of theoretical developments considering the igniter as an idealized energy source

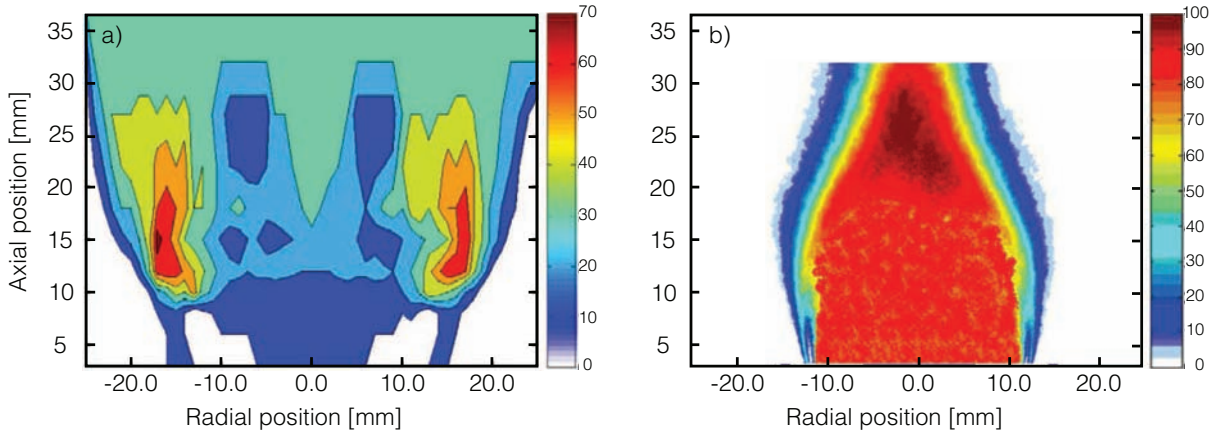

Figure 5.4: Spatial distribution of P_{ker} (a) and F_f (b) in a bluff-body methane/air burner. Extracted from Ahmed *et al.* (2007*a*).

term indicates that this strong approximation might be sufficient to study ignition. Nonetheless, questions remain open regarding the effect of the arc shape and deformation on the subsequent kernel formation, especially in turbulent flows. The exact composition of the gaseous mixture following the plasma phase is also unknown and could significantly affect the initiation of the chemical reactions.

As described by Maly & Vogel (1978), the generation of a flame kernel by a spark plug is subsequent to the creation of a plasma in the spark channels. But the complete simulation from the spark discharge to the creation of a flame front is not an easy task since the physics of plasma is not fully understood. Several attempts are conducted by Sher *et al.* (1992) or Kravchik *et al.* (1995) to couple the Navier-Stokes equations with a statistical thermodynamic model in order to capture the physics of the plasma phase. These studies show that the transition from the spark to the flame kernel could be split in two steps:

- during less than 5 μs, the pressure wave controls the plasma kernel expansion. The velocity is high compared to the flame speed and the chemical heat release is negligible
- a diffusive period follows, during which energy and mass are transferred from the plasma towards the unburnt mixture and a chemically active zone is created at the spark kernel surface.

More recent studies by Thiele *et al.* (2000) and Thiele *et al.* (2002) focus on the coupled resolution of the gaseous flow with the Navier-Stokes equations and complex transport, and the electric field using the Maxwell equations in order to model the spark. An experimental study is performed in parallel to validate the numerical results. The influence of the spark arc phase duration and electrode shape on the kernel expansion was found to be negligible in the studied temperature and pressure ranges.

Considering the grid resolution for LES, the creation of the plasma, the transition to a chem-

ically sustained kernel and its early expansion cannot today be explicitly included in LES simulations. Several models have been therefore proposed to externally solve the small-scale physics in 0D or 1D, mainly in the context of internal combustion engines, and then use the results as an input in LES or RANS:

- Boudier *et al.* (1992) solve for the first laminar expansion phase of the kernel in 0D and project the kernel on the LES grid once the turbulent stretch dominates the laminar one.
- The ATKIM model developed by Duclos & Colin (2001) for RANS simulations at IFPEN is composed of several elements: 1) a model for electrical circuit, 2) a description of the electrical arc using lagrangian particles, 3) tracking of multiple spark kernels that could result in a burnt gas kernel, and 4) fixed lagrangian particles to emulate the presence of the electrodes and estimate the heat losses. The model has been extended to LES in Richard *et al.* (2007), and the tracking of the spark kernel is replaced by a progress variable coupled to the flame surface density equation of the CFM-LES model.
- In the context of RANS simulations of two-phase flow gas turbines Ouarti *et al.* (2003), Garcia-Rosa *et al.* (2009) and Linassier *et al.* (2013) at ONERA developed a model to compute the early kernel laminar growth in a two-phase flow in a 1D configuration based on the flow properties at the spark deposit location.

A simpler model to mimic energy deposit is used in many DNS (Poinsot *et al.*, 1991; Baum & Poinsot, 1995; Chakraborty *et al.*, 2007) and LES (Lacaze *et al.*, 2009*a*; Jones & Prasad, 2011) studies where the spark is reduced to a source term in the transport equation for gaseous energy. The spatial and temporal distribution of the source term is found to vary between these studies (Gaussian distribution, hyperbolic tangent or Heaviside functions in both space and time). Finally, Sloane (1985) investigates ignition in quiescent methane-air mixture by addition either of a thermal energy source term or of both thermal and free radicals (H and O) source terms. The results indicate that, for the chemical scheme considered, the effect of free radicals addition is negligible, supporting the assumption that ignition is mainly driven by the thermal balance.

5.2 Phase 2: kernel expansion and transient flame propagation

If the energy deposit is sufficient to initiate chemical reactions and generates a sustainable flame kernel, the kernel must then be able to grow and the flame front must propagate to eventually stabilize on the injector nozzle (Lefebvre, 1998). Following Mastorakos (2009), the literature review proposed here for **Phase 2** of ignition is further split in two: first, the development of an isolated flame kernel interacting with turbulence (Sec. 5.2.1) and second, the ignition sequence in a complex turbulent flow where the convection of the flame front comes into play (Sec. 5.2.2).

5.2.1 Development of isolated flame kernel

Once a flame kernel is established, its survival depends on the turbulence level and the interactions between the turbulent flow and the flame front. Indeed, turbulence can induce deformation

and fragmentation of the kernel, wrinkling and stretching of the flame front as well as enhancement of the diffusion process. If it is well known that turbulence can have a beneficial effect on the burning rate of the flame, it can also induce local or global extinction of the flame kernel during the first few milliseconds after energy deposit. The study of a spherical flame kernel expansion without or with turbulence has been widely studied experimentally since it constitutes a canonical case to investigate laminar and turbulent burning velocity (Karpov *et al.*, 1959; Abdel-Gayed *et al.*, 1984; Weiss *et al.*, 2008; Galmiche *et al.*, 2012). However, only recent progress both in optical diagnostics and numerical simulations have allowed detailed investigation of the local flame front properties during the kernel development. Except for very intense turbulence, the early instants of kernel expansion are laminar due to the increase of viscosity with temperature, the small size of the kernel and the very short deposit duration. As time proceeds, the kernel transitiones to a turbulent expanding flame when vortices of increasing size start interacting with the flame.

5.2.1.a Transition from laminar to turbulent flame propagation

Initially, the burning velocity is controlled by the laminar stretch associated with the kernel expansion (Poinsot *et al.*, 1991). The stretch of a freely, outwardly propagating flame is expressed in terms of surface variation by (Poinsot & Veynante, 2011):

$$\kappa = \frac{2}{r_k}\frac{dr_k}{dt} \tag{5.8}$$

where r_k is the kernel radius. The laminar stretch is maximal for small radius and decreases as $1/r_k$ as the kernel expands (Renou, 2001). The overall growth rate of the kernel during the laminar phase strongly depends on the Lewis number of the fuel: for $Le_F < 1$, the stretch increases the flame consumption rate. It is the opposite for $Le_F > 1$ (Poinsot & Veynante, 2011). Since $Le_F < 1$ combustion flames are prone to thermo-diffusive instabilities, the Lewis number can also induce an increase of the flame surface enhancing the overall consumption rate (Poinsot *et al.*, 1991; Renou *et al.*, 2000) and trigger a faster transition to turbulent flame propagation. During this early phase, the flame kernel is only sensitive to turbulent scale having a turnaround time of the order of the time elapsed since the energy deposit (noted $t_{elapsed}$) (Abdel-Gayed *et al.*, 1988). Turbulent scales larger than the kernel size cause a bulk motion of the flame kernel with limited effect on its growth rate (at least in premixed flows). As time proceeds, the kernel grows and starts interacting with larger and more energetic turbulent scales, and the turbulent stretch becomes dominant. To represent this effect, Abdel-Gayed *et al.* (1988) introduce the concept of effective turbulent velocity u'_{eff}: it can be evaluated by the area under the curve of power spectral density versus frequency between the cut off frequency of the kernel given by $f_{ker} = 1/t_{elapsed}$ and the Kolmogorov frequency as illustrated in Fig. 5.5. At first u'_{eff} is zero and it progressively increases toward the overall turbulent velocity u'. u'_{eff} When $t_{elapsed}$ becomes larger than the turnaround time, $u'_{eff} \sim u'$. This concept is supported by both spark and laser ignited experiments (Abdel-Gayed *et al.*, 1987; Bradley *et al.*, 2011).

Bradley *et al.* (2004) Laser Induced Breakdown (LIS) experiments reported in Fig. 5.6 illustrate the effect of the effective turbulent velocity on the kernel growth rate: the kernel radius temporal evolution is similar in both laminar and turbulent environments during the early instants and diverge later. The time at which the temporal evolutions diverge is found to decrease

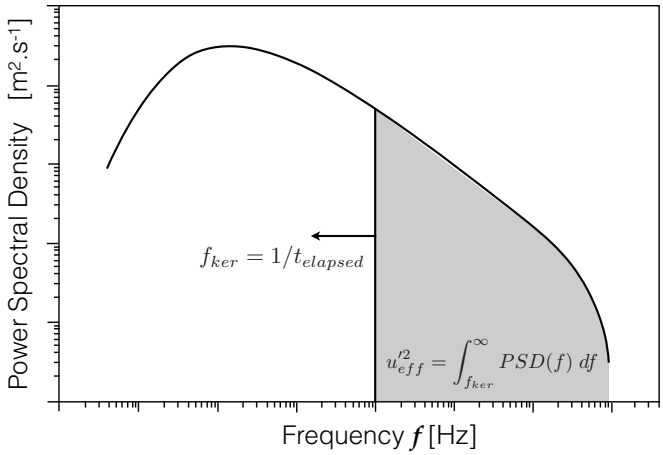

Figure 5.5: Frequency band of PSD used to evaluate the effective turbulent velocity u'_{eff}. Adapted from Abdel-Gayed *et al.* (1988)

with increasing turbulent intensity since the Kolmogorov length scale decreases. This trend is in accordance with the numerical results reported in Akindele *et al.* (1982).

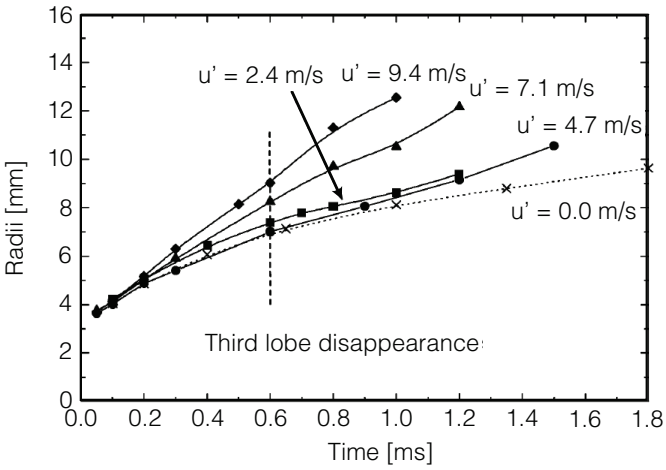

Figure 5.6: Temporal evolution of kernel equivalent radius for LIS ignition at various turbulence intensity levels. Extracted from Bradley *et al.* (2004)

In partially premixed or non-premixed flows, the early kernel growth rate is found to be well correlated with the amount of flammable mixture at the deposit location as shown by Cardin (2013). Two cases have to be considered separately depending on whether the distribution of mixture fraction stays on one side of the stoichiometric mixture fraction line (whether rich or lean) or spreads across z_{st} (Peters, 2000; Mastorakos, 2009). The former corresponds to stratified mixture ignition whereas the latter is referred to as non-premixed ignition. In the case of stratified mixture ignition, the kernel growth is quite similar to a premixed kernel expansion with spatial heat release variation due to inhomogeneity (Renou *et al.*, 2004). The local burning

rate variations induce wrinkling of the flame front which is found important for weakly turbulent cases but negligible for strongly turbulent flows as compared to aerodynamic wrinkling (Poinsot *et al.*, 1996). For non-premixed ignition, the flame front rapidly turns into a triple flame propagating along the stoichiometric iso-contours (Hartley & Dold, 1991; Chakraborty *et al.*, 2007). The growth rate of the flame kernel then depends on the ability of the triple flame to propagate: because the rich premixed branch of the triple flame exhibits higher reaction rates than its lean counterpart, the initial kernel growth is enhanced for overall richer mixture (Chakraborty & Mastorakos, 2008).

5.2.1.b Effect of turbulence on the flame kernel

As larger and more energetic scales start interacting with the kernel, wrinkling of the flame front is observed (Poinsot *et al.*, 1991; Kaminski *et al.*, 2000). As compared to a laminar case, the increase of flame surface associated with wrinkling enhances the kernel growth. The effect of u' on the flame surface is found to increase with increasing turbulent intensity, up to the point where local quenching of the flame front overcomes the beneficial effect of the higher flame surface. Indeed, development of the flame kernel after the transition is fairly similar to a turbulent flame propagation, so that the influence of turbulence on the kernel growth can be analyzed in a classical combustion diagram (Borghi, 1985; Peters, 1986). As the turbulent intensity increases, the flame/turbulence interaction regime goes from the wrinkled flamelet regime where the flame structure is that of an unstretched laminar flame, to the thin reaction zone regime where the vortices penetrate in the preheat zone, and eventually to the distributed reaction zone regime if the turbulence intensity further increases. The last two regimes are characterized by a modification of the flame structure and possible quenching by turbulence since the turbulent time scales are of the order (or smaller) of the chemical time scale.

To clarify the effect of the turbulence on the flame kernel, it is interesting to analyze the interaction of a flame kernel with a single vortex of varying size and strength. Initial experiments conducted by Eichenberger & Roberts (1999) and followed by Xiong *et al.* (2001) and Xiong & Roberts (2002) show enhancement of the overall burning rate for small vortex size but also local or overall flame quenching for vortex of size similar to the kernel. The DNS study of Kolera-Gokula & Echekki (2006) for premixed hydrogen-air mixture similarly reveals an increase of the overall growth rate due to distortion of the flame kernel and distinguishes two interaction regimes: the breakthrough regime where the vortex is strong enough to go through the kernel without global extinction, and the global extinction regime where larger vortices inducing global quenching of the kernel. Both regimes are characterized by a strong wrinkling of the kernel, flame-flame interaction and annihilation and strong effect of strain and curvature. This work is followed by the parametric study of Echekki & Kolera-Gokula (2007) in an attempt to build a kernel-vortex spectral diagram similar to classical spectral vortex/flame diagrams (Poinsot *et al.*, 1991). The diagram of Vasudeo *et al.* (2010) is reported in Fig. 5.7(a).

- In the **laminar regime**, characterized by small and/or weak vortex, the kernel is merely distorted and the vortex quickly dissipated by the increase of temperature through the flame front.
- As the size and strength of the vortex increase, the interaction enters the **wrinkled regime**

where large deformations of the kernel are observed and the vortex is able to penetrate in the kernel. However, the vortex is dissipated and does not break the leading edge of the kernel.

- If the size and/or strength further increases, the **breakthrough regime** is observed.
- Finally the **global extinction regime** is encountered for large and/or strong vortices.

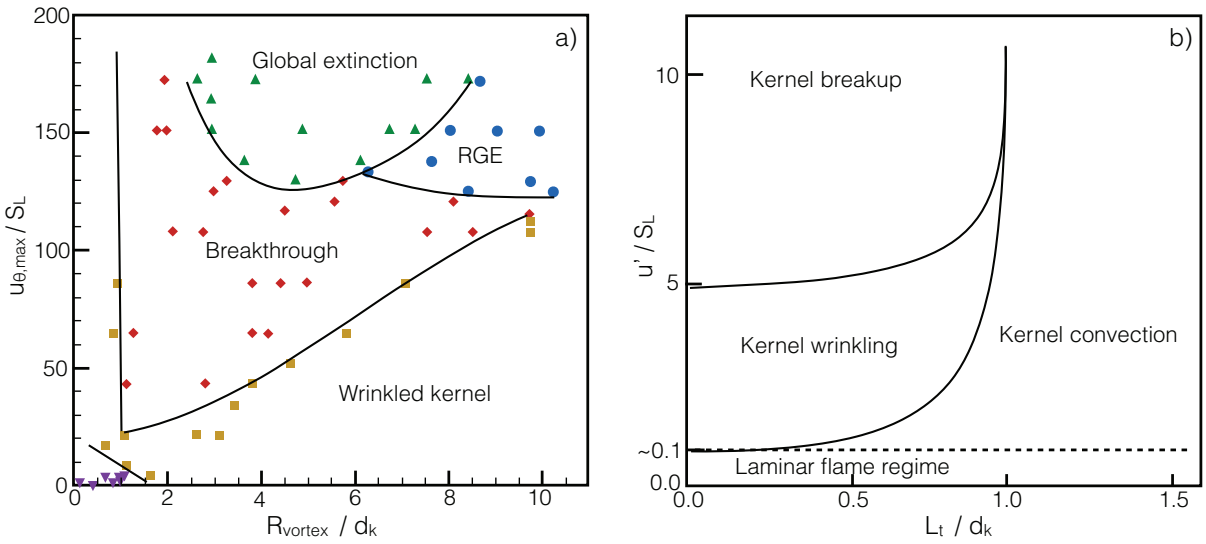

Figure 5.7: (a) Kernel-vortex interaction spectral diagram of Vasudeo *et al.* (2010). (b) Kernel-turbulence interaction map of Reddy & Abraham (2013)

Vasudeo *et al.* (2010) had a fifth regime (called Regeneration after Global Extinction (RGE) regime) in case where the vortex is strong enough to break the kernel into peaces but the flame front is reconstructed after the vortex has passed by. Both studies of Vasudeo *et al.* (2010) and Reddy & Abraham (2011) point out the effect of the chemical description on the kernel-vortex interactions: if a simple chemistry is able to capture the effect of strain and curvature as well as the main overall kernel growth, it might fail to reproduce local extinction and re-ignition associated with flame-flame interaction or kernel reconstruction. When considering kernel growth in a full turbulence spectrum, the resulting interaction cannot simply be viewed as a superposition of isolated vortices of various size and strength due to coupling and interaction between these scales. Reddy & Abraham (2013) perform 2D DNS of flame kernel interaction with fully developed turbulence in conditions representative of internal combustion engines with detailed chemistry. The study focuses on the kernel growth rate and highlights the influence of the parameter l_t/d_{ker} where d_{ker} is the kernel diameter. A kernel-turbulence interaction map is proposed (see Fig. 5.7(right)): regimes similar to kernel-vortex diagram are found, and the maximum growth rate is found in the kernel wrinkling regime.

The effect of turbulence on ignition in non-premixed cases is not easy to evaluate because of the coupling between velocity and mixture fraction fluctuations. Chakraborty *et al.* (2007) perform 3D DNS of forced ignition in a turbulent mixing layer with one-step chemistry. The study proves

that an increase of turbulent velocity is detrimental to the kernel growth since it results in an increase of the mixture fraction gradient, which in turn slows the triple flame propagation (Ko & Chung, 1999; Buckmaster, 2002).

Note that most of these DNS studies are limited to 2D configurations, but Thevenin *et al.* (2002) show that the maximum stretch undergone by the flame is higher in 3D and the curvature distribution is shifted towards positive values in 2D configurations. The differences between 2D and 3D curvature distributions are also highlighted in Gashi *et al.* (2005) by comparing 2D OH-PLIF measurement and 3D DNS results, so that it is necessary to be cautious when estimating three dimensional flame properties from 2D measurements or simulations.

All these studies show that the flame kernel growth is maximal in the wrinkled regime where the flame surface increase is beneficial to the overall burning rate with very little local extinction.

5.2.1.c Quenching mechanisms

The mechanisms leading to quenching of the kernel flame front is first studied using DNS, since the simultaneous measurement of the flame position and the velocity field is a complex task. The recent development of advanced optical diagnostics (Trunk *et al.*, 2013; Kerl *et al.*, 2013) allows to bring some new insight on the flame kernel development (Peterson *et al.*, 2015) and to validate numerical findings. Two mechanisms leading to local or global quenching of the flame kernel can be distinguished: 1) the modification of the kernel structure by large scale turbulence and 2) the modification of the flame structure by vortices which sizes are of the order of the flame front.

The first DNS of expanding flame kernel in premixed environment is performed by Poinsot *et al.* (1991) in a 2D decaying turbulence, for which no global quenching is reported. But the study points out the occurrence of 'catastrophic' events where pockets of burnt gases are separated from the kernel and can subsequently be quenched, resulting in a temporary reduction of the kernel growth rate. Such events are also captured in 3D DNS at various levels of turbulence and equivalence ratios performed by Fru *et al.* (2011). The frequency of pinch off events, where mutual flame annihilation creates pockets of hot gases in fresh gases, increases with the turbulent intensity. The temporal evolution of a flame kernel in intense turbulence extracted from Fru *et al.* (2011) show in Fig. 5.8 illustrates the strong wrinkling of the flame kernel and the creation of pockets.

This mechanism is also observed in the DNS of kernel-vortex interactions where significant flame surface destruction was captured in the breakthrough or quenching regime where large vortices interact with the flame kernel (Vasudeo *et al.*, 2010). The resulting pockets can either collapse if their size is too small (typically following the sustainable flame kernel criterion introduced in Sec. 5.1) or expand and contribute to the ignition process.

The second mechanism inducing local quenching is not specific to kernel propagation but results of the interaction of turbulence with the flame front. Unlike the first quenching mechanism which can occur at relatively low turbulence intensity, the second mechanism is observed in the thin-reaction zone regime (Peters, 1999), i.e. when vortices are sufficiently small to enter the preheat layer of the flame but too large to enter the reactive layer. Jenkins *et al.* (2006) perform 3D DNS of flame kernel propagation to evaluate the effect of strain rate and curvature on the

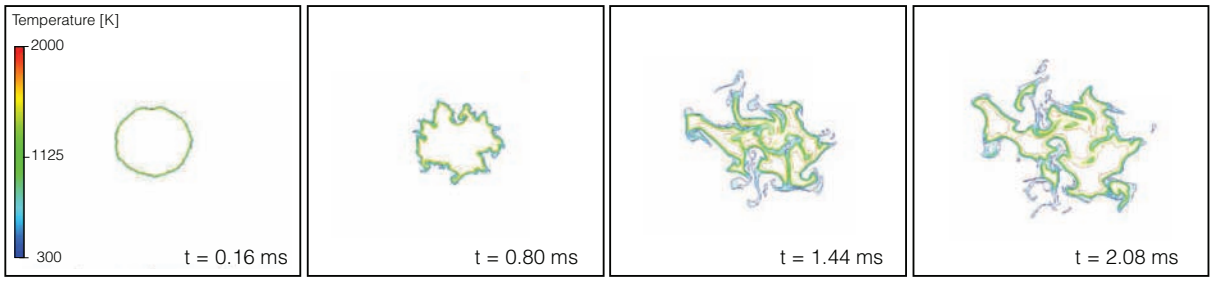

Figure 5.8: Temporal evolution of temperature iso-contours of flame kernel in decaying isotropic turbulence at $Re_T = 2462$. Extracted from Fru *et al.* (2011).

flame structure and propagation. To analyze the DNS data, the flame displacement speed S_d introduced by Echekki & Chen (1996) (Sec. 3.2.1.b) is used. The mean positive curvature experienced by the spherical flame front is found to be detrimental to the flame displacement speed due to an increase of the tangential diffusion component (as compared to a statistically planar turbulent flame). In a similar case, Klein *et al.* (2006) show that for high positive curvature, negative S_d could be found where the rate of thermal diffusion dominates that of heat release. Note that notion of negative S_d does not pertain to the flame consumption rate but to the propagation of a c iso-level relative to the flow. Negative displacement speeds have also been captured experimentally by Peterson *et al.* (2015) during the flame development following sparking in an internal combustion engine using 4D measurements. The study, however, shows no evidence of correlation between S_d and the curvature of the flame front as observed in DNS studies. Studies have indicated that $S_d < 0$ can be used an indicator of local extinction (Gran *et al.*, 1996; Chen & Im, 1998; Kolera-Gokula & Echekki, 2006). The occurrence of local extinction can then be related to the distribution of curvature: the studies of Jenkins & Cant (2002) and Reddy & Abraham (2013) indicate the broadening of the curvature PDF for increasing values of turbulent velocity u'.

5.2.2 Ignition of single burner configuration

The overall ignition success of a single burner is not solely guaranteed by the capacity of the flame kernel to overcome the detrimental effect of turbulence. In complex flow, the outcome of the ignition sequence depends on the ability of the flame to propagate and stabilize at the injector nozzle. Because the incoming flow velocity is generally much higher than the turbulent flame speed, practical injection systems generate recirculation zones which provide pathways for the flame to propagate from downstream location to the injector nozzle. The study of flame propagation following initiation of a flame kernel is rather recent and motivated by the new design trends. It requires well equipped complex experimental set-ups and computationally expensive numerical investigations.

5.2.2.a Jet configuration

The early works of Birch *et al.* (1981) and Smith *et al.* (1986) focus on the ignition of a turbulent free jet. The flame front propagation is not investigated in detail but the authors show that allthough the probability of creating a flame kernel P_{ker} along the jet axis correlates well with the flammability factor F_f, the overall ignition is not guaranteed. Two scenarios are identified: either flame propagates downstream and eventually blows-off or flame propagates upstream, against the flow, and results in a stable flame. A similar configuration is studied in Ahmed & Mastorakos (2006) with the objective of providing a detailed understanding of the flame propagation mechanisms at various stages of the ignition sequence. The results indicate that the region of non zero ignition probability is wider than the contours corresponding to the lean and rich flammability limits. This result is coherent with the observation of Richardson & Mastorakos (2007) in a laminar counterflow flame: the transport of energy from a spark location outside of the flammability contours to a flammable region can result in a successful ignition. Ahmed & Mastorakos (2006) demonstrate that the initially spherical flame kernel quickly turns into an edge flame due to the non-premixed configuration and the flame front propagates upstream along the stoichiometric iso-lines at a mean speed three to six times the laminar flame speed. The experimental configuration of Ahmed & Mastorakos (2006) is studied numerically using LES in Lacaze *et al.* (2009*b*) and Jones & Prasad (2011). Both numerical studies use a Gaussian source term in the energy equation to trigger ignition but Lacaze *et al.* (2009*b*) use the thickened flame model to handle the flame on the LES grid while Jones & Prasad (2011) use sub-grid *pdf* model. The two numerical studies are in good agreement with experimental data for the non-reacting flow as well as in terms of ignition phases. A comparison of the direct visualization of the flame extracted from experiments and the temperature field extracted from the LES of Lacaze *et al.* (2009*b*) is showed in Fig. 5.9. The triple flame propagation behavior and the lift-off distance are recovered by both LES studies, proving the capability of LES to capture the complex ignition transient.

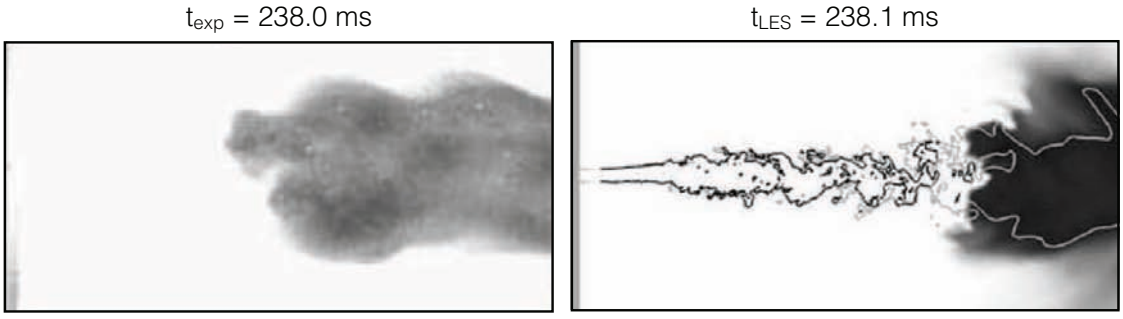

Figure 5.9: Ignition of a free jet burner: experiments from Ahmed & Mastorakos (2006) (left) versus temperature field (grayscale) in the LES of Lacaze *et al.* (2009*b*) (right)

5.2.2.b Recirculating flow configuration

Gaseous experiments

To study the *Phase 2* of ignition in a flow closer to real combustion chambers, Ahmed *et al.*

(2007*a*) experimentally investigates ignition in a non-premixed complex flow configuration exhibiting recirculation zones induced by a bluff-body. Both velocity and mixture fraction are measured to analyze the non-reacting flow and the flame position during ignition sequences tracked by high speed OH PLIF. Examples of flame snapshots during an ignition sequence is shown in Fig. 5.10. Failed and successful ignition events are visualized and ignition probability map is constructed. Three types of ignition failure are observed: failure of kernel initiation, blow-off of propagating flame kernel and global extinction after flame propagation and stabilization. The relation between flammability factor, kernel probability and ignition probability is investigated without and with swirl motion. The direction of flame propagation is proven to be related to the energy deposit location rather than to the instantaneous flow conditions at the energy deposit. An important finding is that the differences between ignition probability and flammability factor are mainly due to nonlocal effect (advection) and quenching by turbulence (Abdel-Gayed & Bradley, 1985).

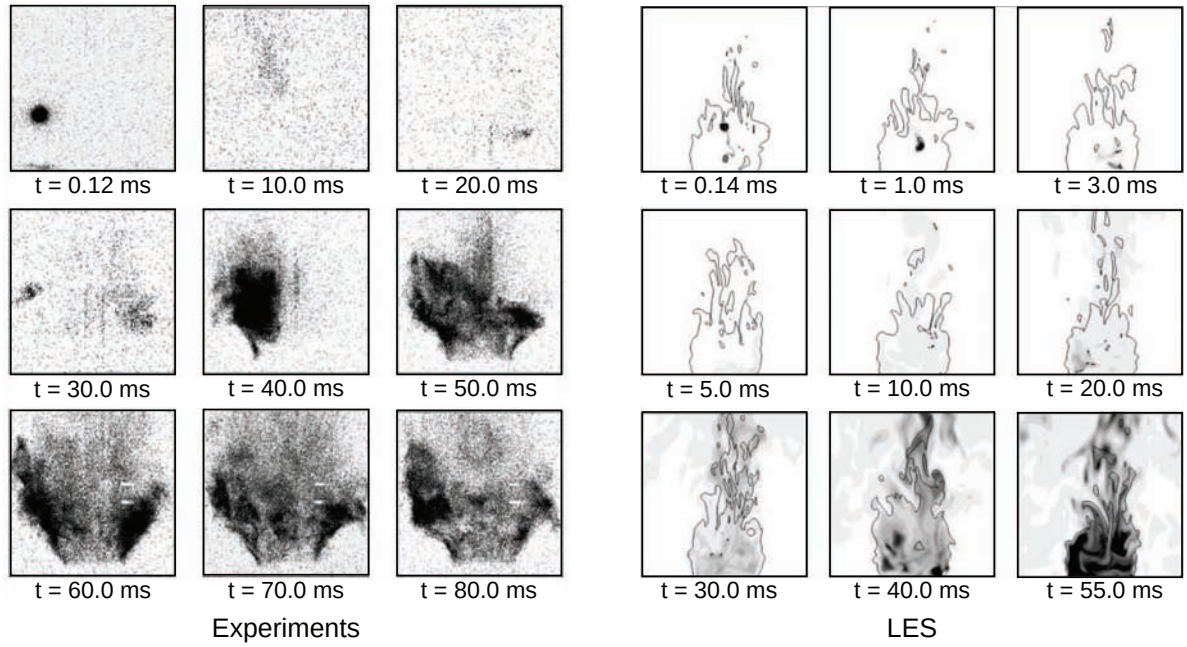

Figure 5.10: Ignition sequence in a non-premixed bluff-body burner: experiments from Ahmed *et al.* (2007*a*) and temperature field in the LES computation of Subramanian *et al.* (2010).

Cordier (2013) designs a lean swirled burner close to realistic lean burn aeronautical injection systems to study ignition in premixed and non-premixed configurations for two different swirl intensities. The ignition performances of the burner are evaluated by constructing ignition probability maps. Cordier *et al.* (2013*a*) show that the ignition efficiency is not only controlled by the local flow properties but also by the kernel trajectory. The mean effect of the swirl intensity is an increase of the turbulent intensity which can locally quench the flame kernel, but can also have a beneficial effect on the ignition probability due to changes of the flow aerodynamics. For the partially premixed case, the local increase of equivalence ratio enhances the ignition efficiency but has also detrimental effect in regions where air and methane are insufficiently mixed. Cordier *et al.* (2013*a*) and Cordier *et al.* (2013*b*) also construct ignition scenarios based on high

speed flame visualization pointing out the occurrence of kernel fragmentation and the subsequent quenching induced by turbulence.

Corresponding LES studies

The bluff-body configuration of Ahmed *et al.* (2007*a*) is numerically studied using two LES solvers with different combustion models: Triantafyllidis *et al.* (2009) use a detailed chemistry with Conditionnal Moment Closure (CMC) model while Subramanian *et al.* (2010) employ tabulated chemistry and a presumed-*pdf* model. Triantafyllidis *et al.* (2009) find a flame development very similar to the experimental results, and their results show that a detailed chemistry mechanism is necessary to reproduce the expansion rate. The flame kernel trajectory is found to depend on the spark location in accordance with experiments. Subramanian *et al.* (2010) show that sparking at the same location but varying deposit timing can lead to either ignition success or failure depending on the convection direction during the first instants after energy deposit. Two mechanisms are found to jeopardize the ignition success in region with favorable convection direction: quenching near the bluff-body wall and high strain rate encountered by the flame kernel. This last point shows that the effect of strain rate must be taken into account in the combustion closure modeling.

The premixed configuration of Cordier *et al.* (2013*a*) is studied in the work of Barré (2014). In this study, a two-step global chemistry along with the thickened flame model are used and the author indicates that during the early instants after sparking, the grid resolution should be chosen as to minimize the contribution of the combustion closure since it could alter the outcome of the ignition try. The key role of the combustion closure is further highlighted during the flame propagation through the combustion chamber: comparison of temporal pressure signals with experimental data shows that a closure adequate for highly turbulent regions results in overestimation of the sub-grid contribution in near laminar regions. The quenching mechanisms are investigated using both diagnostics of the flame displacement speed S_d and joint contributions of strain and curvature to flame stretch. The results are in accordance with the DNS study of Klein *et al.* (2008).

Two-phase flow experiments

The experiment of Marchione *et al.* (2009) is today the only detailed analysis of ignition in a two-phase flow environment. A swirling n-heptane academic burner is studied and high ignition probability is found to be correlated with regions of backward velocity and small droplet SMD and to coincide with location of total equivalence ratio (liquid and vapor) within the flammability limits. Multiple spark sequences are also investigated: the ignition efficiency is shown to increase with the ignition sequence duration. A similar configuration is studied in Letty *et al.* (2012) where the effect of swirl and fuel are briefly investigated. The three failure modes mentioned above are captured for both ethanol and n-heptane in the swirling configuration. Eyssartier *et al.* (2013) perform ignition sequences in the MERCATO configuration of Garcia-Rosa *et al.* (2011) at atmospheric conditions. The study focuses on the construction of a model to predict ignition probability, but the early instants of several ignition sequences are simulated with two-phase flow LES and large variability in the flame kernel development is captured.

5.2.2.c Realistic combustor

Experimental study of ignition in realistic temperature and pressure conditions have been conducted by Read *et al.* (2008), Read *et al.* (2010) and Garcia-Rosa *et al.* (2011). Detailed data on the velocity field and the spray pattern are not available is these studies due to the complexity of the test facilities. Read *et al.* (2010) study the ignition of a LDI injector by direct imaging of the kernel development in the combustor and failure modes similar to the one captured in Ahmed *et al.* (2007*a*) are observed. The study also shows a rapid disintegration of the flame kernel and convection of the fragments throughout the combustor. Figure 5.11 shows an ignition sequence in the test bench proposed by Garcia-Rosa *et al.* (2011). Right after energy deposit, the flame visible emissions are weak. The experiment shows that in realistic conditions, the kernel phase is quite long: the flame is convected downstream (in the right direction in Fig. 5.11) with little expansion. After 16 ms, the flame front rapidly expands in the whole chamber and eventually stabilizes on the nozzle.

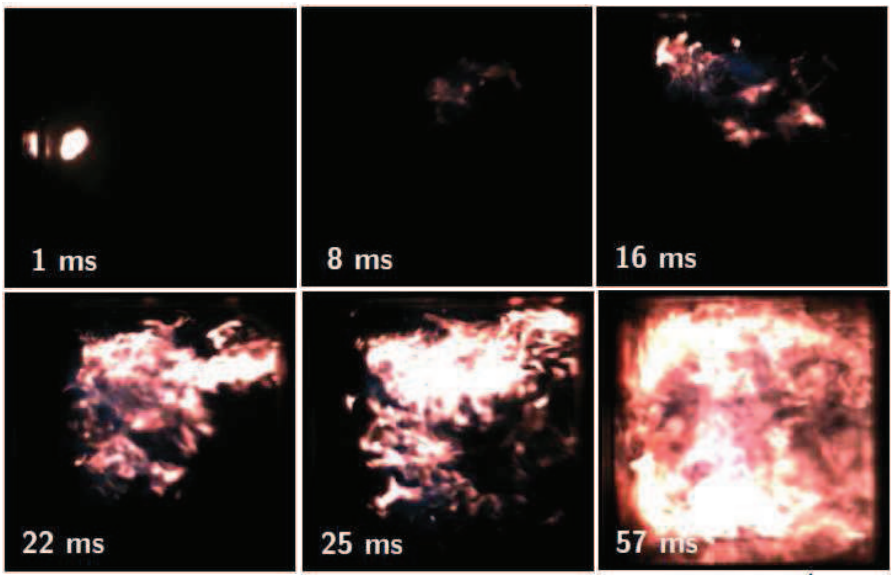

Figure 5.11: Ignition sequence in realistic two-phase flow combustor extracted from Garcia-Rosa *et al.* (2011).

Ignition sequence in realistic (but simplified) combustion chamber sector is performed in Boileau (2007) to demonstrate the feasibility of such computation with LES using an Eulerian dispersed phase formulation. Jones & Tyliszczack (2010) investigated the ignition sequence of a realistic gas turbine sector including the multiphase flow description, but in atmospheric conditions, using LES. A sub-grid *pdf* approach similar to the work of Jones & Prasad (2011) is employed for closure of filtered conservation equations, and a Lagrangian formulation is used for the liquid phase. Both ignition failure and success are obtained as function of the spark size and sparking timing but very little is reported regarding the precise effect of two-phase flow on the kernel development and flame propagation.

5.3 Conclusion

This review clarifies the key elements controlling the *Phase 1* of ignition in gas turbines but note that in gas turbine the spark igniter is generally sufficiently strong to initiate chemical reaction, regardless of the turbulence level at the spark location. Hence, the success of this phase is mainly conditioned upon the ability of the flow to provide a flammable mixture at the vicinity of the spark location.

The review on *Phase 2* of ignition demonstrates that the distinction introduced by Mastorakos (2009) between the development of isolated kernels and the subsequent flame propagation and stabilization is relevant since they are governed by different mechanisms:

- Kernels developing in turbulent flows are subjected to aerodynamic constraints that can either result in a faster growth rate, mainly due to an increase of the kernel surface, or in a quenching of the flame kernel. The later is found to be related to both the dislocation of the kernel structure and the imbalance between chemical heat release and heat losses associated with turbulent mixing. In non-premixed flow, the kernel rapidly turns into a propagating edge flame also highly sensitive to aerodynamic strain.
- The success of ignition in single burner configurations is mainly controlled by the residence time of the kernel in the burner. Indeed, long residence times allow to increase the temperature in recirculating regions, the key element of flame stabilization. The spark position should be such that flammable mixture is available nearby and the large scale flow motions bring the flame kernel towards low or backward velocity regions where it can propagate upstream. Otherwise, the kernel can be blown out even though the conditions necessary for its growth are met.

The literature review also highlights that numerical simulations have greatly contributed to the understanding of the ignition process through DNS of flame kernel development and more recently, LES of ignition sequences in complex configurations. Nonetheless, the validity of the LES approach for conditions approaching realistic gas turbines have not been fully demonstrated and the mechanisms leading to ignition failure in non-premixed, highly turbulent flows are not fully identified.

Chapter 6

Non-reacting flow in the KIAI single burner

Contents

6.1 Experimental test rig 78
6.2 Numerical set-up 80
6.2.1 Computational domain 80
6.2.2 Numerical parameters 80
6.3 Non-reacting flow characteristics 82
6.3.1 Flow characteristics 82
6.3.2 Flow pattern 82
6.3.3 Mean flow velocity 84
6.3.4 Mean mixture fraction 89
6.3.5 Pressure drop 89
6.3.6 Flow instability 91
6.4 Conclusion 93

Knowledge for ignition, acoustic and instabilities (KIAI) project is a FP7 european research project coordinated by SNECMA whose goal is to deliver CFD tools able to study unsteady phenomena in gas turbines. In the framework of the KIAI project, joint experimental and numerical studies of ignition in a single sector and a multi-burner configuration are performed. The single injector test rig is installed at CORIA (Rouen, FRANCE) and has been designed during the work of Frenillot (2011) and Cordier (2013).

Prior studying the ignition performance of the burner, the non-reacting flow is investigated in LES with two main objectives:

- Compare LES results with experiments and evaluate the sensitivity of the LES to numerical parameters. The influence of subgrid stresses model, numerical scheme, wall treatment and mesh refinement is especially targeted.

- Provide a complete description of the flow and precise data to identify the effect of the aerodynamics and mixture on the ignition sequence.

6.1 Experimental test rig

The KIAI test rig ams to study ignition, from the energy deposit (*Phase 1* of ignition as distinguished in Sec. 5.1) to the anchoring of the flame at the injector nozzle (**Phase 2**) in highly swirled confined environment. The design is inspired from test rigs reported in the literature: the partially-premixed burner from TU Darmstadt (Janus *et al.*, 2005), the PRECCINSTA burner installed at DLR (Weigand *et al.*, 2006) and the two-phase flow MERCATO burner experimented at ONERA (Garcia-Rosa *et al.*, 2011; Linassier, 2012). The major constraints of the design are the large optical access required to track the flame position during the whole ignition sequence, the capability to change the swirl intensity and the operability in both premixed and partially premixed modes. The last two features aim to quantify the effect of swirl and partial premixing on the ignition performance of the burner and have direct implications on the design of industrial injection systems.

Figure 6.1 is a picture of the burner illustrating its four major components, from bottom to top:

- A plenum is located upstream of the injection system to lower the turbulence of the flow generated in the feeding lines and a grid placed in the lower part helps to destroy the large structures.
- The swirl injection system is close to the one designed by Janus *et al.* (2005), the latter being inspired from the aeronautical industry. A radial swirler composed of 18 vanes inclined at 45° and followed by a convergent annular section acts as the main air (or premixed mixture) admission (see Fig. 6.2). The convergent annular section ends at the combustion chamber inlet with an outer diameter $D_{ext} = 20$ mm and an inner diameter $D_{int} = 9$ mm. The fuel injector tube of diameter $d = 4$ mm is nested in the air admission and enters the combustion chamber in the same plane as the first admissions.
- The combustion chamber is a square of 100 mm length by 260 mm height. Large optical accesses on three sides of the combustor enable to use non-intrusive optical diagnostics, direct visualization of the flame and ignition by laser induced breakdown.
- At the top, a convergent exhaust forces closure of the inner recirculation zone. The convergent also increases the pressure rise during the ignition sequence, which allows to use the pressure evolution as an indicator of the ignition progress.

The experimental facility is operated in ambient conditions and the fuel used is methane. Two operating modes are studied experimentally:

- The premixed case where the central tube and the plenum are fed with premixed flow is studied in the work of Barré (2014) but will also be used in this work to evaluate the performance of the ignition model (Chap. 8)



Figure 6.1: Picture of the KIAI single injector experimental test bench.

- The non-premixed case where the central tube is fed with pure methane and the plenum with air. This configuration is investigated here in LES.

The operating conditions of both mode are listed in Tab. 6.1.

	$\dot{m}_{tube}$ [g/s]	$\dot{m}_{plenum}$ [g/s]	Global ϕ_g	T [K]	P [Atm]
Premixed	0.236	5.612	0.75	298	1.0
Non-premixed	0.234	5.43	0.75	298	1.0

Table 6.1: Operating conditions studied experimentally in the KIAI single burner.

Stereo-Particle Image Velocimetry (SPIV) and Planar Laser-Induced Fluorescence (PLIF) measurements are used to characterize the initial cold flow field and fuel mixing. The experimental data are based on 1000 instantaneous measurements. High speed OH* emission recording is used to track the flame during ignition as well as a pressure sensor in the combustion chamber. More details on the experimental facility and diagnostic technics can be found in the work of Cordier (2013).

6.2 Numerical set-up

6.2.1 Computational domain

The computational domain includes the four components of the experimental test rig, as reported in Fig. 6.2. The grid placed in the plenum of the test rig is not included in the numerical domain but replaced by a laminar air injection at the inlet of the plenum. The axial direction is referred to as the z-axis, corresponding to the main flow direction, while the x-axis and y-axis denote the transverse directions. Space dimensions are non-dimensionalized by D_{ext}, where $D_{ext} = 20$ is the outer diameter of the swirler passages.

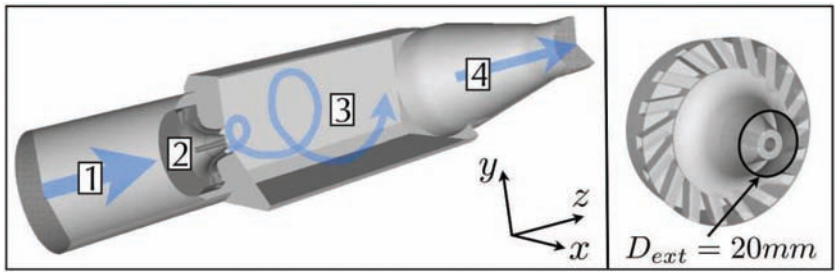

Figure 6.2: Computational domain and injection system details. Main components are: 1. Plenum, 2. Injection system, 3. Combustion chamber, 4. Convergent exit.

In order to evaluate the dependence to the numerical set-up, three meshes have been generated and their main characteristics are listed in Tab. 6.2. The first two meshes are composed of tetrahedral elements only, with a significant reduction of the characteristic size in the convergent section and at the vicinity of the methane jet for *MeshT31M* compared to *MeshT09M* (see Fig. 6.3). A hybrid mesh *MeshP12M* with a layer of prisms on the injection system walls enables to strongly reduce the y^+ in the swirler and in the convergent while keeping the overall mesh size reasonable since the grid size in the rest of the domain is similar to *MeshT09M*. This hybrid mesh is used to evaluate the effect of the mesh resolution of the pressure drop.

	Nb. elements [M]	Nb. vertices [M]	V_{min} [m^3]	Swirler $\overline{y^+}$
MeshT09M	9.1	1.63	$6.835\,e^{-13}$	~ 60
MeshT31M	31.1	5.64	$1.85\,e^{-14}$	~ 25
MeshP12M	11.7	2.19	$1.62\,e^{-13}$	~ 8

Table 6.2: Characteristics of meshes used to study non-reacting flow.

6.2.2 Numerical parameters

LES are performed with AVBP and unless specified otherwise, the numerical parameters of the solver are listed in Table 6.3. In addition, to assess the accuracy of the numerical results, results obtained with YALES2, a low Mach number LES solver developed at CORIA (Moureau *et al.*,

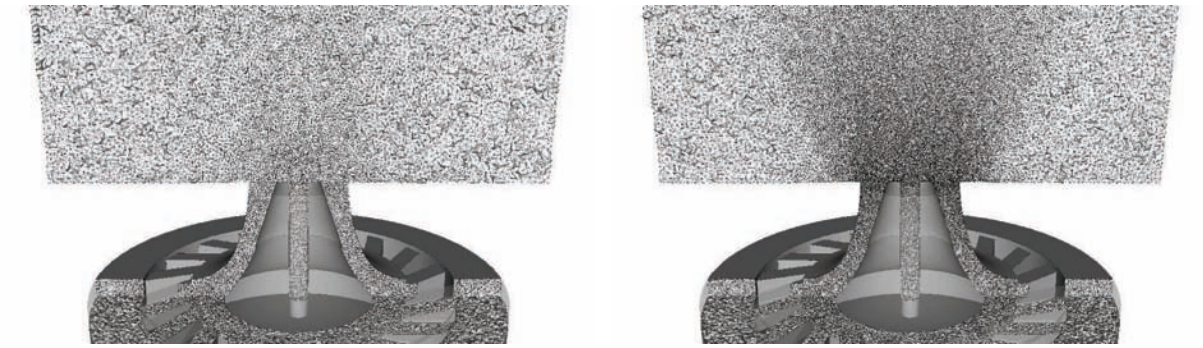

Mesh09M *Mesh31M*

Figure 6.3: Slices in the computational domain for *Mesh09M* and *Mesh31M* illustrating the mesh difference in refinement.

2011*a*) are also reported. Unless specified otherwise, YALES2 simulations are performed using the same LES modeling as for AVBP in Table 6.3. WALE subgrid model with adiabatic non-slipping walls. Numerics in YALES2, however, strongly differs from AVBP: a 4th-order finite-volume scheme for the spatial resolution and the TVF4A 4th-order explicit time integration (Kraushaar, 2011) are used with a Deflated PCG method for the Poisson solver (Nicolaides, 1987).

	Numerical Parameters
Convection scheme	TTGC: $\mathcal{O}(3)$ in space & time (Colin & Rudgyard, 2000)
Diffusion scheme	2Δ operator
SGS model	WALE (Nicoud & Ducros, 1999)
Artif. viscosity	Colin model: $\epsilon^{(2)} = 0.01$, $\epsilon^{(4)} = 0.005$
	Boundary conditions
CH_4 inlet	NSCBC (Poinsot & Lele, 1992) (velocity, 10% turbulence)
Air inlet	NSCBC (Poinsot & Lele, 1992) (velocity)
Walls	Adiabatic non-slipping walls

Table 6.3: Numerical parameters for AVBP.

	Numerical Parameters
Convection scheme	$\mathcal{O}(4)$ finite volume in space & $\mathcal{O}(4)$ TVF4A time integration
Diffusion	implicit
Poisson solver	DPCG (Nicolaides, 1987)
SGS model	WALE (Nicoud & Ducros, 1999)
	Boundary conditions
CH_4 inlet	Dirichlet (velocity, 10% turbulence)
Air inlet	Dirichlet (velocity)
Outlet	Dirichlet (pressure)
Walls	Adiabatic non-slipping walls

Table 6.4: Numerical parameters for YALES2.

Note that, in both code, turbulence is injected through the CH_4 inlet corresponding to 10% of the bulk velocity in order to mimic turbulence induced by the feeding line shape.

6.3 Non-reacting flow characteristics

6.3.1 Flow characteristics

Prior to present the results of the numerical simulations, the main flow characteristics are introduced:

- the convective time scale is evaluated from the volume in the combustion chamber V_c and the inlet flow rate $\dot{m}$:

$$\tau_{conv} = \frac{\rho V_c}{\dot{m}} = 0.73\ s \tag{6.1}$$

- the rotation time scale is evaluated at the combustion chamber inlet:

$$\tau_{rot} = \frac{\pi R_i}{u_{\theta,i}} = 0.81\ ms \tag{6.2}$$

  where R_i is the mean radius of the convergent inlet and u_θ is the mean azimuthal velocity component in the inlet plane.

- the Reynolds number is evaluated at the combustion chamber inlet:

$$Re = \frac{|\vec{u}|_i D_i}{\nu} = 21000 \tag{6.3}$$

  where $|\vec{u}|_i$ is the norm of the velocity vector in the inlet plane, D_i is the mean diameter of the convergent inlet and ν is the kinematic viscosity.

6.3.2 Flow pattern

Figure 6.4 shows time-averaged streamlines in a central x-normal plane (left) and a z-normal plane (right). The flow pattern is typical of highly swirled configurations: the swirled jet (SWJ) issued from the swirler generates a reverse flow region along the axis of the burner referred to as Inner Recirculation Zone (IRZ). The presence of the IRZ is due to an axial adverse pressure gradient. Indeed, the strong rotation of the incoming flow results in centrifugal forces that are compensated by a radial pressure gradient. As the SWJ expands in the combustion chamber, the conservation of circulation implies a decay of the azimuthal velocity, hence a decay of the radial pressure gradient (Billant *et al.*, 1998). If the axial pressure gradient is strong enough, a bifurcation called vortex breakdown occurs (Lucca-Negro & O'Doherty, 2001), characterized by a reverse flow region nested in the SWJ.

The onset of vortex breakdown is generally related to the Swirl number S_w (Beer & Chigier, 1983; Billant *et al.*, 1998). There are several definitions of the swirl number in the literature,

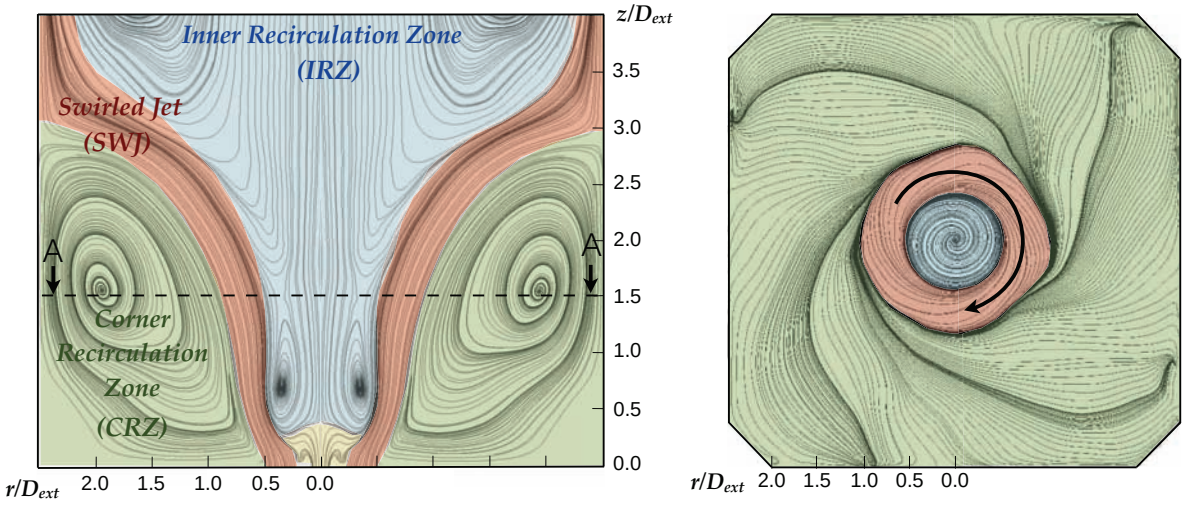

Figure 6.4: Time-averaged streamlines in a central x-normal plane (left) and the A-A z-normal plane (right). The main flow regions are identified: Swirled Jet (SWJ), Inner Recirculation Zone (IRZ) and Corner Recirculation Zone (CRZ).

including or not the axial momentum due to the pressure gradient or the velocity fluctuations. A complete derivation of the Swirl number can be found in Palies (2010) along with a brief overview of the various relations found in the literature. To define S_w, it is convenient to introduce a cylindrical referential (r,θ,z) whose z-axis is aligned with the z-axis of the cartesian referential presented in Fig. 6.2. Following the definition of Ivanic *et al.* (2003), S_w writes:

$$S_w = \frac{G_\theta}{R_{ext} G_z} = \frac{\int_0^{R_{ext}} \rho u_z u_\theta 2\pi r^2 dr}{R_{ext} \int_0^{R_{ext}} \rho u_z^2 2\pi r dr} \tag{6.4}$$

where G_θ is the flux of azimuthal momentum, G_z is the flux of axial momentum, $R_{ext} = D_{ext}/2$ is the outer radius of injection and u_θ and u_z are the azimuthal and axial velocity components respectively. Note that S_w is the result of an integral in a given z-normal plane and theoretically independent of the z position but its value decreases as progressing downstream of the injection plane due to dissipation. The swirl number in the LES simulation is evaluated in the injection plane ($z = 0.0$) of the combustion chamber at 0.81, close to the experimental value reported in Cordier *et al.* (2013*a*) ($S_{exp} = 0.76$). Billant *et al.* (1998) derives a critical theoretical value S_c above which vortex breakdown occurs, based on assumption that the incoming flow velocity profile is that of a Rankine vortex: $S_c = 0.707$. This value is evaluated against experimental measurements and is found to agree in several configurations (Billant *et al.*, 1998; Liang & Maxworthy, 2005). The value find in both experiments and LES is above $S_{w,c}$, in agreement with the flow pattern observed in the LES. The IRZ is closed downstream due to the presence of the convergent exhaust. In confined environment, the SWJ also induces recirculation on its outer part, referred to as Corner Recirculation Zones (CRZ), closed at $z/D_{ext} = 3$. At the bottom of Fig. 6.4(left), the flow coming from the methane injection meets with the air back flow of the IRZ. At the meeting point, the zero axial velocity location is called the stagnation point. Its axial location results from the equilibrium between the momentums of the methane jet and the IRZ flow. Finally, strong shear layers are located at the interfaces between the SWJ and both IRZ

and CRZ.

6.3.3 Mean flow velocity

Figure 6.5 shows time-averaged mean and RMS fields of the velocity components in the central x-normal plane. Data are recorded during 150 ms in order to obtain converged statistics and the mean and RMS of a quantity ψ are evaluated respectively by:

$$\langle\psi(\vec{x})\rangle = \frac{1}{T_m}\sum_{n=1}^{N_T}\psi(\vec{x},t^n)\Delta t_m \tag{6.5}$$

$$\psi(\vec{x})_{RMS} = \sqrt{\langle\psi(\vec{x})^2\rangle - \langle\psi(\vec{x})\rangle^2} \tag{6.6}$$

where T_m is the recording duration, N_T is the total number of instantaneous snapshots and Δt_m is the time delay between two consecutive snapshots. Note that this definition corresponds to a Reynolds average so that the density difference between methane and air is not taken into account. Moreover, the RMS value does not account for the subgrid scale contribution.

The high velocity of the SWJ is clearly visible on the axial velocity component. The jet opening is first limited resulting in a arrow IRZ while further downstream the SWJ is fully opened. Such IRZ shape called *bottle-neck* is also observed in the MERCATO test rig. The highest axial velocity is located in the methane jet and very rapidly decreases near the stagnation point. It is interesting to note that the time-averaged position of the IRZ goes up to the wall between the methane jet and the SWJ. The high swirl number of the injection system is demonstrated by the tangential velocity component with $u_{x,max} \sim u_{\theta,max}$ at the injection plane. The RMS field of the axial component shows the strong turbulence intensity at the vicinity of the stagnation point and the inner shear layer. The other two components illustrate the flapping motion of the methane jet with high turbulence along the wall between the methane jet and the SWJ: as the axial velocity quickly decreases near the stagnation point, the conservation of the mass flow rate implies a rapid increase of the radial component.

LES results are compared with experiments using time-averaged statistics profiles. Figures 6.6 & 6.7 show the first two statistical moments of the three components of velocity at five axial positions downstream of the injection system: $z/D_{ext} = 0.25, 0.5, 1, 1.5, 2$ (see bottom left cut inFig. 6.5). For the sake of clarity, only the results for *MeshT09M* and *MeshT31M* using AVBP are reported. The results obtained with *MeshP12M* are very similar to those of *MeshT09M*. The velocity profiles show that the velocity field is in good agreement with experiments past the first profile at $z/D_{ext} = 0.25$. The LES is able to accurately capture the jet opening angle and the velocity components. The fluctuations are lightly over-predicted but fully recovered downstream. The large differences observed at $z/D_{ext} = 0.25$ denote the slightly too strong penetration of the methane jet: an offset in the jet penetration is found compared with experiments, which greatly modifies the velocity profile since the mean field has a strong gradient in the stagnation point region. Note that the increase in mesh resolution from *MeshT09M* to *MeshT31M* is able to significantly improve the jet penetration prediction but the position of the stagnation point is not fully recovered in LES.

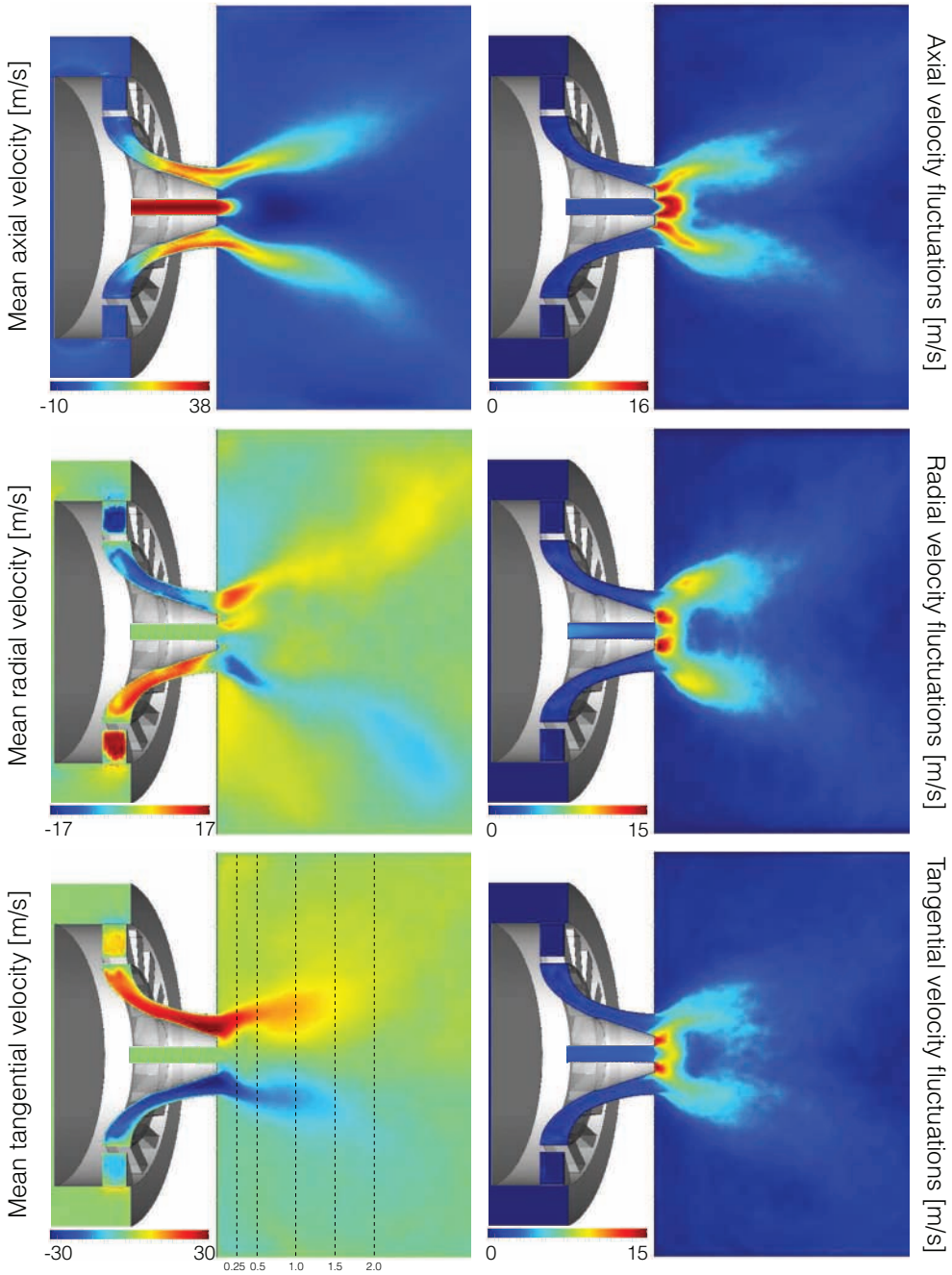

Figure 6.5: Mean and RMS velocity components in a central x-cut plane through the combustion chamber on *Mesh31M* with AVBP.

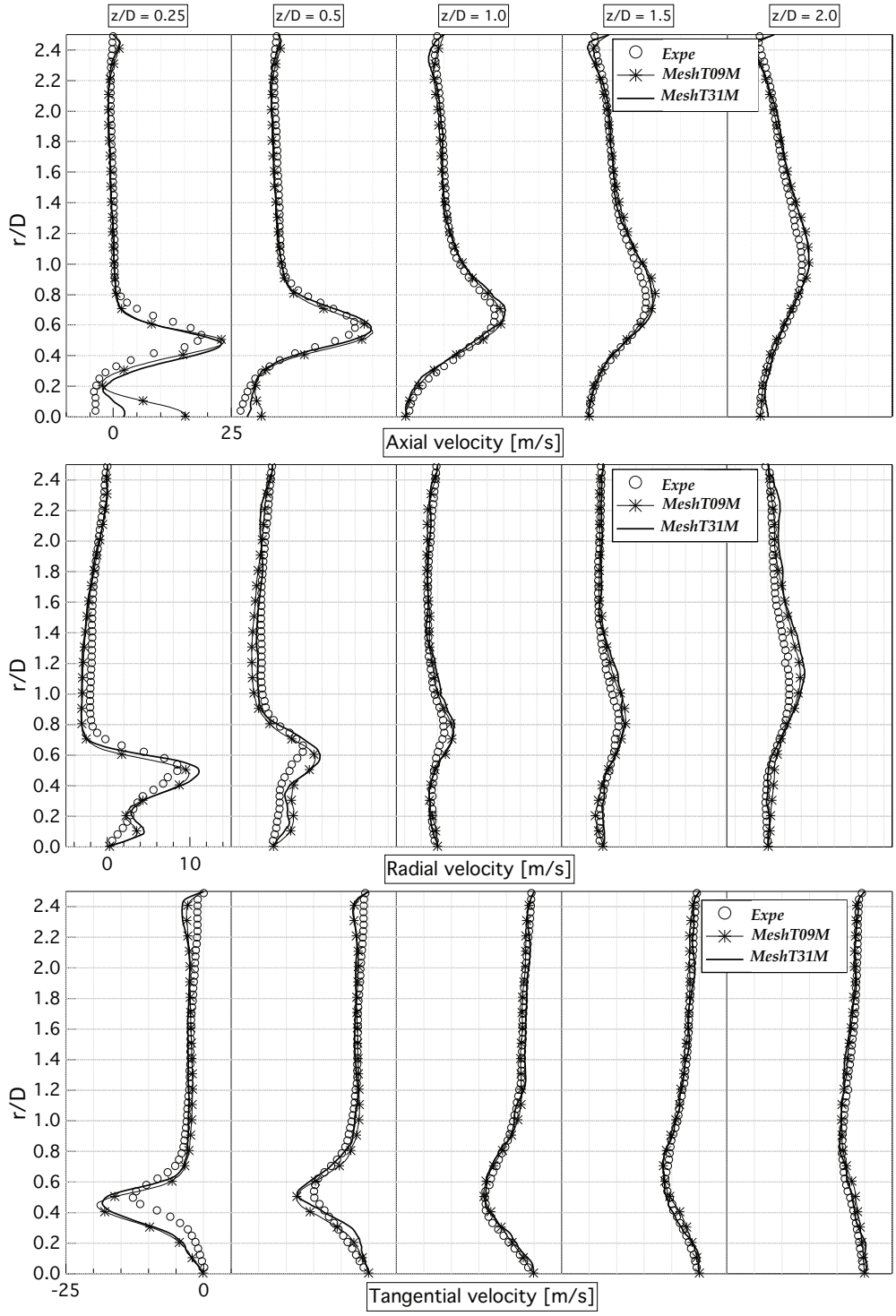

Figure 6.6: LES versus experiments: mean velocity components profiles obtained with AVBP at 5 axial positions $z/D_{ext} = 0.25, 0.5, 1, 1.5, 2$.

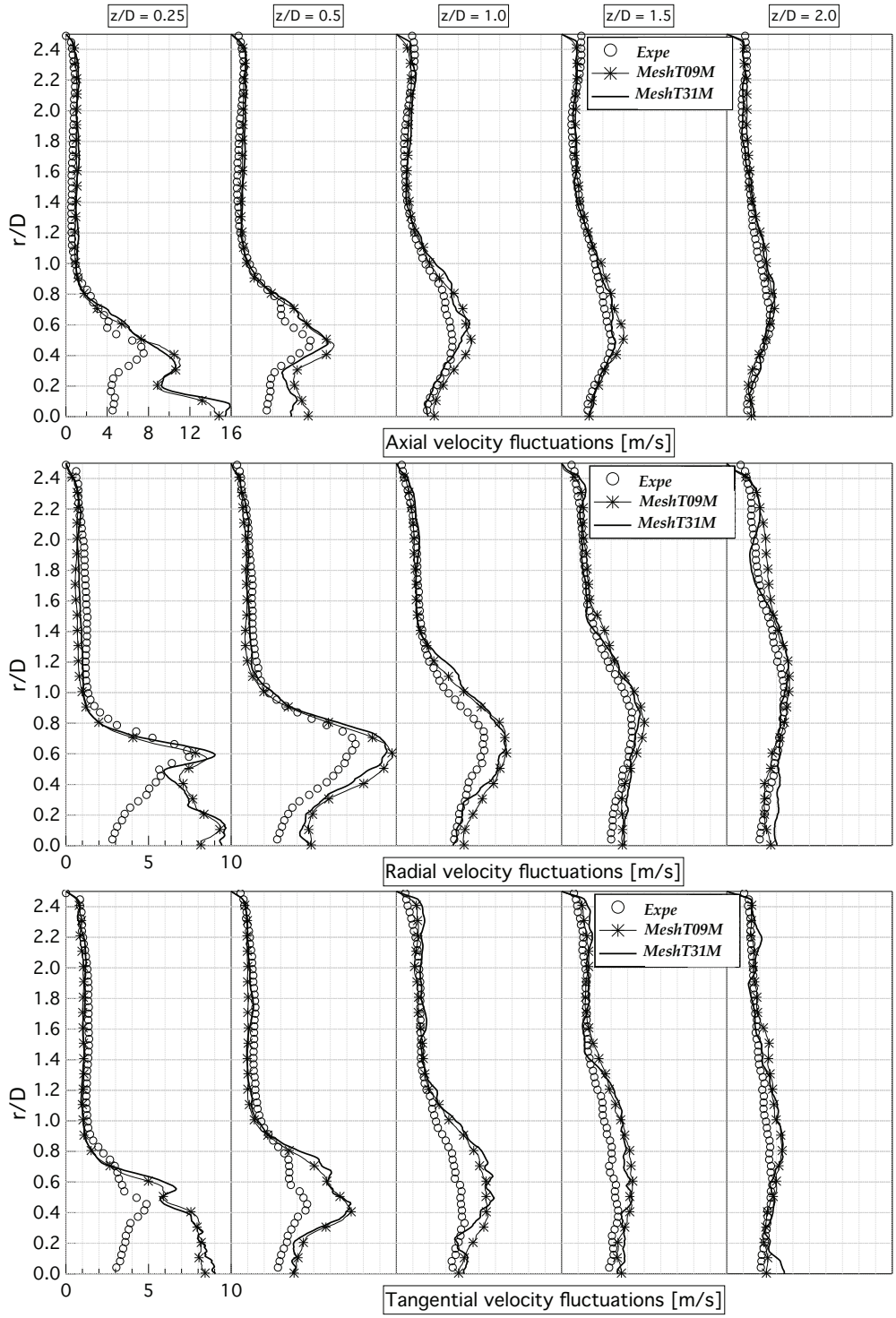

Figure 6.7: LES versus experiments: RMS velocity profiles obtained with AVBP at 5 axial positions $z/D_{ext} = 0.25, 0.5, 1, 1.5, 2$.

In Tab. 6.5, the methane jet penetration is taken as an indicator to compare the LES performed varying the physical and numerical parameters. Changing the subgrid stresses model from WALE to SIGMA keeping non-slipping walls or Smagorinsky in combination with a law-of-the-wall on *MeshT09M* results in a greater offset with the experimental position of the stagnation point ($z_{jet}/D_{ext} = 0.18$) . The results are also worse when using LW rather than TTGC. The results obtained with *MeshP12M* are fairly similar to those of *MeshT09M* and shows that the change in jet penetration is not controlled by the resolution of the boundary layer in the swirler or the convergent section. The most accurate results are obtained with *MeshT31M* when using the baseline numerical set-up. The same conclusion can be drawn with YALES2. Note that a very fine mesh containing 70 millions of cells has been tested with no significant improvement of the jet penetration.

Solver	Models	Num. scheme	Mesh	z_{jet}/D_{ext}
AVBP	*SMAGO/Wall-law*	TTGC	*MeshT09M*	0.501
	SIGMA/No-slip	TTGC	*MeshT09M*	0.421
	WALE/No-slip	LW	*MeshT09M*	0.428
		TTGC	*MeshT09M*	0.418
			MeshT31M	**0.285**
			MeshP12M	0.402
YALES2	*WALE/No-slip*	4th-order FV	*MeshT09M*	0.388
			MeshT31M	0.292
			MeshP12M	0.378

Table 6.5: Numerical predictions of the methane jet penetration z_{jet}/D_{ext} measured as the position of the zero z-axis component of velocity along the injector axis. (Expe: $z_{jet}/D_{ext} = 0.18$).

The axial velocity profile along the central axis of the burner is shown in Fig. 6.8 for AVBP and YALES2 simulations on *MeshT31M*: both codes are in good agreement, but the stagnation point exhibits an offset of about 2 mm with experiments.

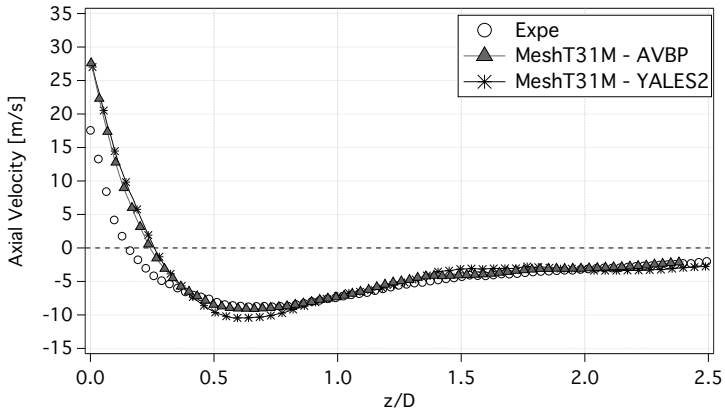

Figure 6.8: LES on *MeshT31M* versus experiments: velocity components fluctuations profiles at 5 axial positions $z/D_{ext} = 0.25, 0.5, 1, 1.5, 2$.

6.3.4 Mean mixture fraction

For a similar mass flow rate, the Reynolds number of swirling flows is increased compared to non-swirling flows due to the additional azimuthal velocity component. Hence, strongly swirled flows generally show very good mixing capabilities since the turbulent mixing is increased. The mean and RMS mixture fraction fields shown in Fig. 6.9 illustrate the good mixing properties of the current design: most of the combustion chamber is filled with a mixture close to the global equivalence ratio ($\phi_g = 0.75$, corresponds to $z_g = 0.042$), the pure methane injected through the central jet does not penetrate far downstream in the chamber.

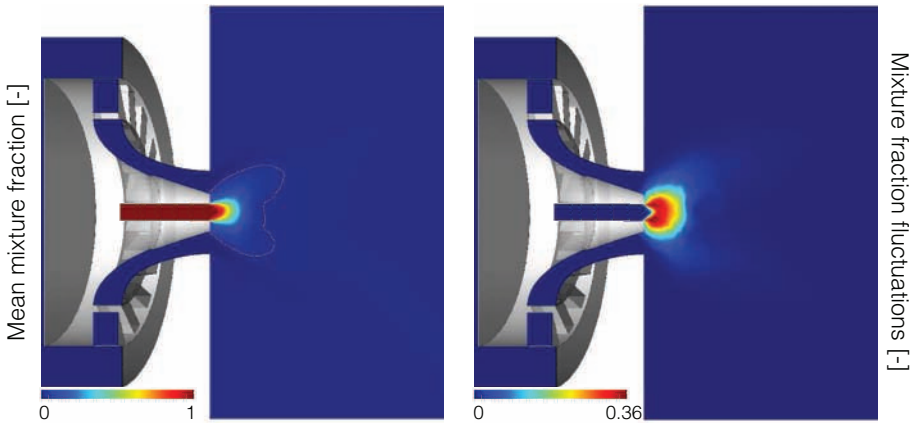

Figure 6.9: Mean and RMS mixture fraction in a central x-cut plane through the combustion chamber. The iso-line $z_{st} = 0.055$ is shown in white.

Once again, the mixture fraction mean and RMS profiles displayed in Fig. 6.10 & Fig. 6.11 are compared with experimental results at 4 axial positions $z/D_{ext} = 0.3, 0.5, 0.9, 1.1$ (different from the position used for the velocity profiles). Only results obtained with AVBP on *Mesh31M* are presented. The dotted-dashed lines indicate the positions of the lower and upper flammability limits. The inaccurate penetration of the methane jet greatly modifies the two statistical moments of the mixture fraction distribution on the first profile.

6.3.5 Pressure drop

The pressure drop through complex geometries, such as swirled injection systems, is a key design parameter since it has a direct influence on the engine efficiency (Nicholas, 2005). However, the prediction of the pressure drop is not an easy task to achieve using LES and numerous parameters of the computation affect the results (Kraushaar, 2011; Barré *et al.*, 2013). The pressure drop is the results both of singular losses due to geometrical changes and linear losses due to friction at the walls. The pressure drop can be evaluated from the conservation of total energy between two planes located upstream and downstream of the injection system. In the following, the pressure drop is simply defined as the total pressure difference between point A located upstream and point B located downstream of the injection system as shown in Fig. 6.12.

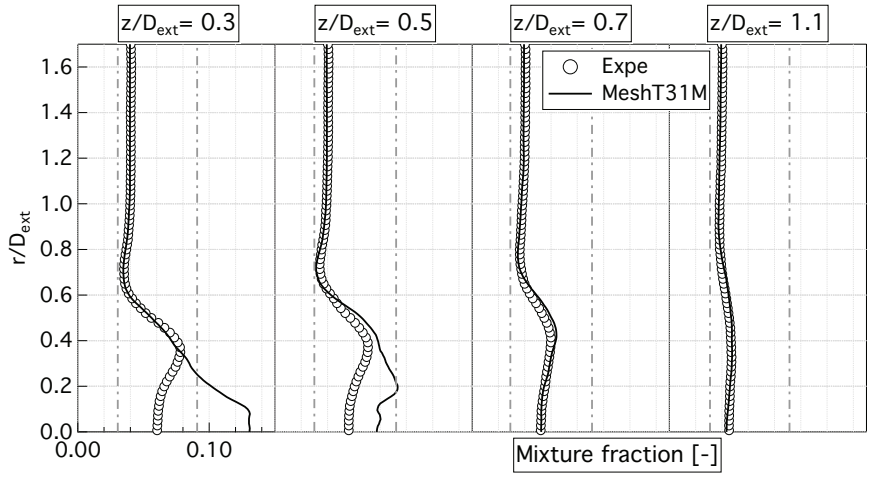

Figure 6.10: LES versus experiments: mixture fraction profiles at 4 axial positions $z/D_{ext} = 0.3, 0.5, 0.7, 1.1$.

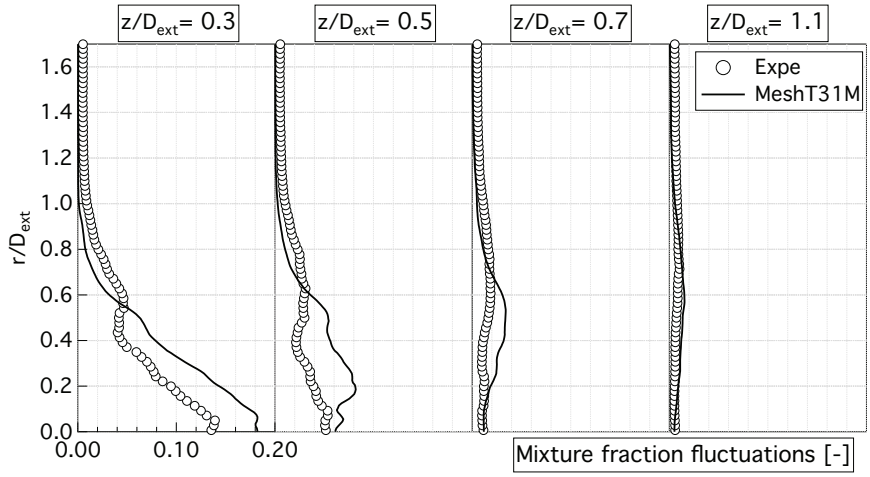

Figure 6.11: LES versus experiments: mixture fraction fluctuations profiles at 4 axial positions $z/D_{ext} = 0.3, 0.5, 0.7, 1.1$.

Using time-averaged LES results:

$$\Delta P = \overline{P}_{tot,up} - \overline{P}_{tot,down} \tag{6.7}$$

with

$$\overline{P}_{tot} = \overline{P} + \frac{1}{2}\overline{\rho}(\widetilde{u}^2 + \widetilde{v}^2 + \widetilde{w}^2) \tag{6.8}$$

where $\overline{P}$ is the filtered static pressure. The pressure drops measured experimentally is $\Delta P_{exp} = 593Pa$. The pressure drops measured in LES for all numerical set-ups investigated in this study

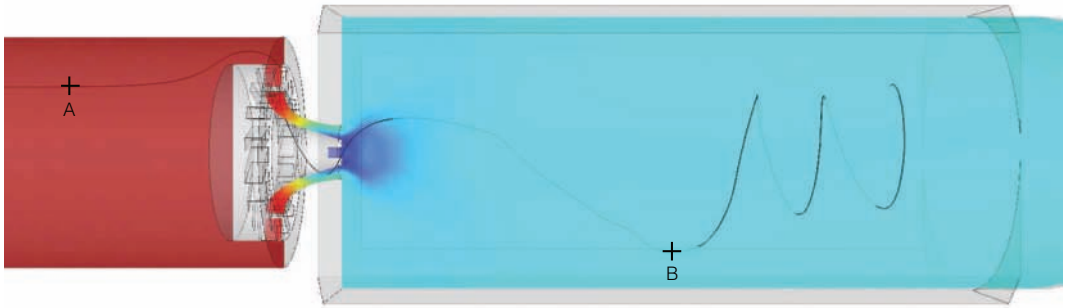

Figure 6.12: Position of point A and point B along a streamline for the evaluation of the pressure drop. The central cut plane is colored by the mean static pressure P.

are summarized in Table 6.6. From the AVBP simulations, the pressure drop is found to be strongly reduced when increasing the mesh resolution. The best prediction is obtained using TTGC and *MeshT31M*, with less than a 3.2% offset as compared to experiments. On the coarse mesh, the best predictions are obtained using *SMAGO/Wall-law* combination rather than *WALE/No-slip*, which is coherent with the observations of Barré *et al.* (2013). The prediction obtained with *MeshP12M* are very similar to the results obtained with *MeshT31M*, showing that the smaller $\overline{y^+}$ does not improve pressure drop predictions. The effect of the mesh resolution on the prediction is also reproduced in YALES2, but the prediction are higher than those obtained with AVBP.

Solver	Models	Num. scheme	Mesh	Pressure drop $[Pa]$
AVBP	*SMAGO/Wall-law*	TTGC	*MeshT09M*	700
	SIGMA/No-slip	TTGC	*MeshT09M*	764
	WALE/No-slip	LW	*MeshT09M*	790
		TTGC	*MeshT09M*	775
			MeshT31M	**612**
			MeshP12M	614
YALES2	*WALE/No-slip*	4th-order FV	*MeshT09M*	821
			MeshT31M	785
			MeshP12M	692

Table 6.6: Numerical prediction of pressure drop $[Pa]$ ($\Delta_{P,exp} = 593[Pa]$).

6.3.6 Flow instability

Swirled flows at super-critical swirl number ($S_w > S_{w,c} = 0.707$) are prone to hydrodynamic instabilities due to the ability of the perturbation to propagates upstream through recirculation zones (Liang & Maxworthy, 2005). Axial and azimuthal instabilities arise in the shear layers in the form of a precessing vortex core (PVC) (Ruith *et al.*, 2003; Roux *et al.*, 2005). In the present LES, the PVC is a large scale coherent structure evolving in the inner shear layer between the SWJ and the IRZ. A less intense counter-part is found in the outer shear layer between SWJ and the CRZ. The PVC as shown in Fig. 6.13 is tracked by an iso-surface of low static pressure and

colored by the radial gradient of axial velocity to differentiate the inner (grey) and outer (white) shear layer structures. In the present case, the PVC has a two branches structure in the inner shear layer with a helical shape. Figure 6.13(a) indicates the sign convention: the flow has a clockwise rotation, considered as positive. Following this convention, the PVC helical structure is winded in a negative direction around the axis of the swirler, but is rotating in the positive direction. The PVCs captured in Roux *et al.* (2005) or García-Villalba *et al.* (2006) have similar winding and rotation orientation, although theory is not yet able to predict which unstable mode will dominate the flow. The outer shear layer vortices do not show a clear helical shape, but they are placed in symmetrical arrangement with the inner one around the SWJ region.

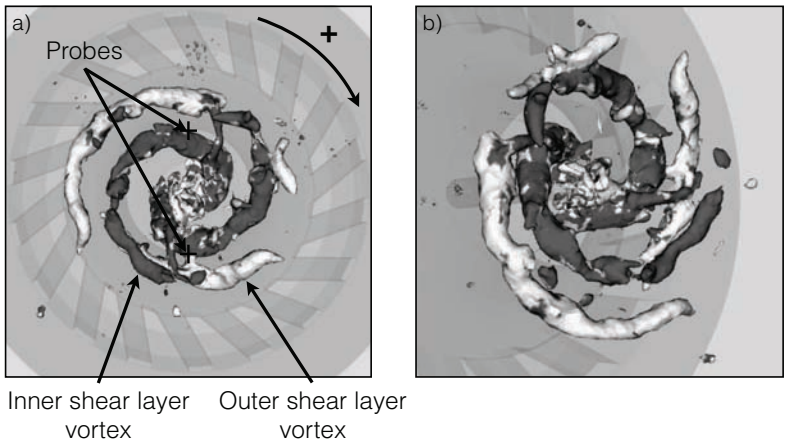

Figure 6.13: Precessing Vortex Core in a z-axis top view (a) and perspective (b). Vortices are colored by the radial gradient of axial velocity: positive regions in grey (inner shear layer) and negative regions in white (outer shear layer).

Figure 6.14 plots the cross spectra of two diametrically opposed probes ($x/D_{ext} = \pm 0.5$, $z/D_{ext} = 0.5$ see Fig. 6.13(left)) time series and shows a clear indication of a periodic oscillation having a similar influence on pressure (a), z-velocity component (b) and mixture fraction (c). The peak activity at 1150 Hz is accompanied by two smaller intensity frequencies at about 575 Hz and 1725 Hz. The experiments reported in Cordier (2013) use a temporally resolved diagnostic (Doppler Laser Anemometry (DLA)) to capture the PVC frequency on the velocity fields. The present case is not investigated, but a perfectly premixed case with the same geometry shows activity at 507 Hz and 999 Hz. The Strouhal number of the perturbation can be evaluated:

$$St = \frac{D_{ext} f}{|\boldsymbol{u}|_{inlet}} \tag{6.9}$$

where f is the frequency of the instability and $|\boldsymbol{u}|_{inlet}$ the norm of the velocity at the combustion chamber inlet. $St = 0.72$ is found using the frequency of the most energetic perturbation which is coherent with the experimental observations reviewed in Syred (2006) and the characteristics of PVC.

The coherence between pressure, velocity and mixture fraction signals indicates that the PVC of the inner shear layer (starting between the methane jet and the SWJ) traps rich mixture

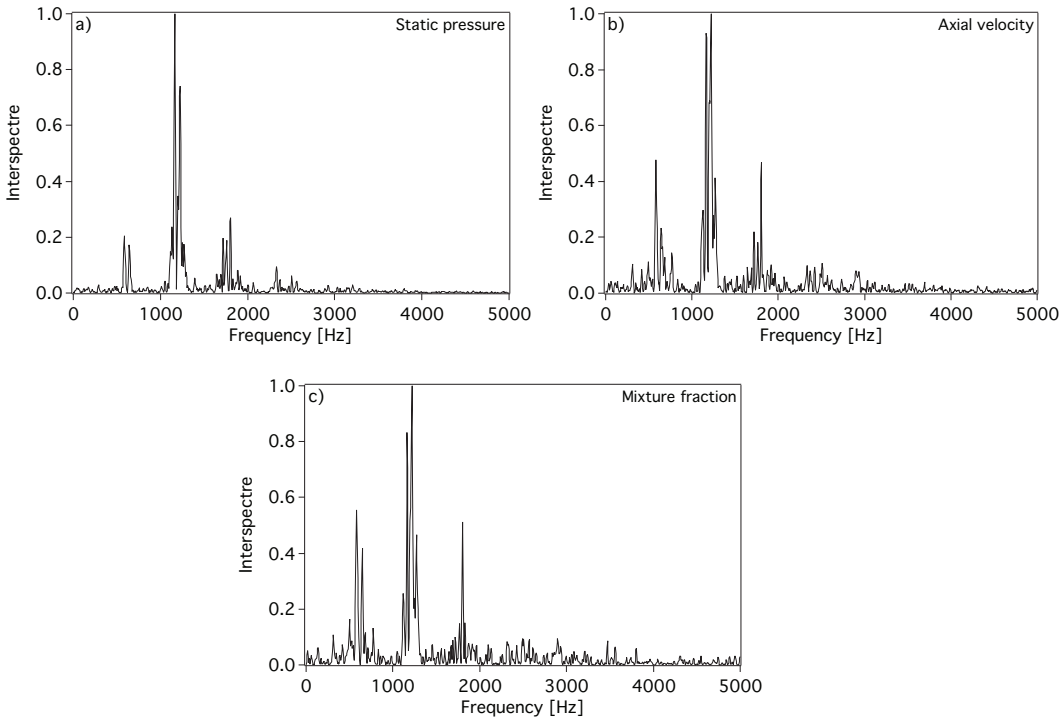

Figure 6.14: 2-points cross spectra of static pressure (a), streamwise velocity (b) and mixture fraction (c) of probes located in the inner shear layer.

in its core. Figure 6.15 shows instantaneous pressure distribution in a central x-normal plane. The white iso-contour indicates the position of the rich flammability limit mixture fraction ($z_{rich} = 0.089$). The contour is wrapped by the PVC, tracked here by low-pressure regions. This mechanism has also been observed experimentally by Cordier (2013) and by Cheng *et al.* (2012) in a close configuration. On the contrary, pockets of lean mixture are also found in the outer shear layer (between the SWJ and the CRZ) due to the presence of the PVC.

6.4 Conclusion

Simulations of the non-reacting flow in the KIAI single burner have been performed and the two main objectives set out in introduction can be summarized as follows:

- LES is found to be mainly sensitive to the mesh resolution and to a lesser extend to the LES subgrid and wall modeling. Comparison with experiments shows that the best numerical set-up gives satisfactory results, allowing to now investigate ignition sequences. The close vicinity of the methane injection is not well reproduced and several leads have been investigated without significant improvement of the LES predictions. In the following, numerical simulations of ignition will be performed on a grid having the same properties as *MeshT31M*.

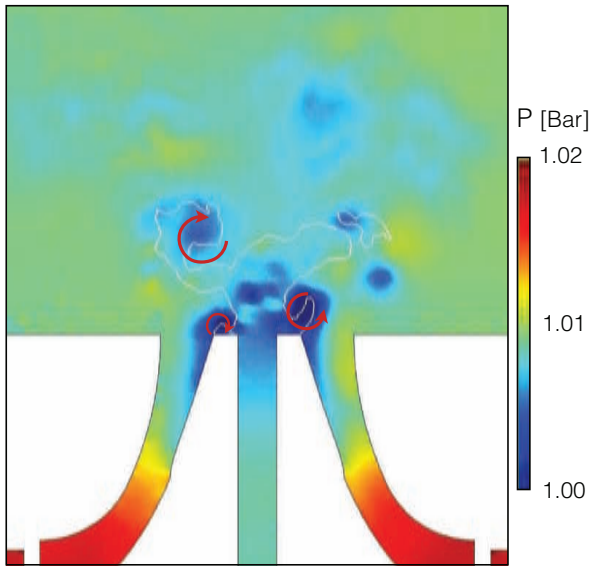

Figure 6.15: Pressure field in a central x-cut plane. $z_{rich} = 0.089$ iso-contour is reported in white.

- LES reveals a flow pattern typical of highly swirled configurations similar to experimental observations. The recirculation zones are expected to play an important role during the ignition process. The partial premixing generates a rich zone at the bottom of the IRZ and a lean zone at the beginning of the SWJ region while the downstream of the combustion chamber is fully premixed. A coherent structure is observed in both the inner and outer shear layers resulting in periodic perturbation of the local mixture fraction and velocity fields. No evidence of correlation between the PVC and the ignition success or failure has been reported in the literature but it is at least expected to affect the kernel trajectory.

Chapter 7

Ignition of the KIAI single burner

Contents

7.1 Experimental results 96
7.2 Numerical simulations 98
7.3 Numerical set-up 99
7.3.1 Numerical parameters 99
7.3.2 Energy deposit model 100
7.3.3 Combustion modeling 101
7.3.4 Meshes 101
7.4 Results 102
7.4.1 Ignition scenario at the 3 sparking locations 103
7.4.2 Flame structure and propagation 111
7.4.3 Mechanisms leading to ignition failure 116
7.4.4 Indicators affecting ignition outcome 124
7.5 Conclusions 128

Over the last 5 years, several LES studies of ignition sequences in simple burner configurations (Lacaze *et al.*, 2009*b*; Triantafyllidis *et al.*, 2009; Subramanian *et al.*, 2010; Jones & Prasad, 2011) have demonstrated the capacity of the LES approach to investigate ignition in complex configurations and shed some light on flame propagation mechanisms following energy deposit. However, these studies suffer from two main limitations:

- they are limited to free jet or bluff-body configurations with low velocity fluctuations, far from highly swirled conditions as encountered in realistic gas turbines.
- the small number of LES of ignition sequences performed does not allow to study the stochastic character of ignition.

Barré (2014) was the first to numerically investigate the configuration of Cordier (2013), in premixed mode. Several ignition sequences were computed and the effect of the numerical parameters on the ignition outcome was highlighted. In particular, Barré (2014) recommended to use

well resolved LES to minimize the effect of the model for flame/turbulence interactions on the flame/kernel interactions.

The objectives of the present study are multiple:

- Perform multiple LES of ignition sequences and evaluate the capability of LES to reproduce the ignition scenarios and statistics observed in the experiment.
- Investigate the growth of flame kernels in a highly turbulent partially premixed environment.
- Identify the mechanisms leading to quenching of the flame kernel by a systematic analysis of multiple LES.
- Use LES of full ignition sequences to directly predict ignition probability.

Part of the results presented in this Chapter has been published in Esclapez *et al.* (2015):

Esclapez L., Riber E. & Cuenot B. 2015. Ignition probability of a partially premixed burner using LES. *Proceedings of the Combustion Institute* **35** (3), 3133-3141.

7.1 Experimental results

Focusing on the ignition of a single burner, the experimental study conducted by Cordier (2013) had two main objectives:

- investigate the ignition performance of the burner by constructing ignition probability maps for two swirl number values both in premixed and non-premixed modes. In combination with measurements on the non-reacting flow field, ignition maps provide a better understanding of the relation between local or global properties and ignition capabilities.
- build ignition scenarios depending on the ignition location and analyze ignition sequences using the non-reacting flow pattern.

To achieve the first objective, a small zone of the combustion chamber near the methane jet is selected. A cartesian 2D grid is drawn in the combustion chamber central cut plane and 50 ignition tries are performed at each grid point. The 2D grid is composed of 88 points so that the total number of ignition sequences captured experimentally is 4400. The experimental ignition probability $P_{ign,XP}$ is computed as the number of successful ignition sequences over the total number of trials. The uncertainty on the ignition probability is evaluated by the standard deviation:

$$\sigma = \left(\frac{P_{ign,XP}(1 - P_{ign,XP})}{N} \right)^{1/2} \tag{7.1}$$

where N is the number of trials. Using 50 trials, the uncertainty is maximum for $P_{ign,XP} = 0.50$ and equal to 7 %. The ignition probability map of the operating point studied in this work

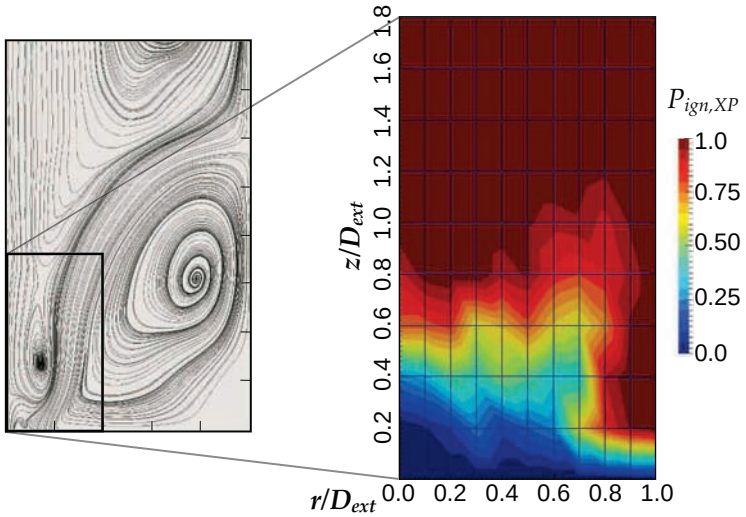

Figure 7.1: Experimental ignition probability map extracted from Cordier (2013).

is presented in Fig. 7.1: the region of interest extends from ($r/D_{ext} = 0.0$; $z/D_{ext} = 0.0$) to ($r/D_{ext} = 1.0$; $z/D_{ext} = 1.8$).

Note that the value $P_{ign,XP} = 0$ on the line $z/D_{ext} = 0$ denotes the lack of experimental data due to the vicinity of the chamber wall. Along the burner z-axis, $P_{ign,XP}$ is found to go from zero near the methane jet to one in the downstream region with a steep gradient around $z/D_{ext} = 0.5$. A large region in the top half of the domain exhibits a maximum probability $P_{ign,XP} = 1$, but the region of $P_{ign,XP} < 1$ extends downstream along the position of the SWJ (at $r/D_{ext} = 0.7$). Cordier (2013) also reported comparisons of the ignition probability with the local turbulence intensity and flammability factor and showed no direct correlation between the pointwise non-reacting flow characteristics and the ignition probability. Ignition scenarios were constructed from high speed OH* recordings. The knowledge of both the flame kernel motion and flame expansion allows to evaluate the path and mechanisms leading to either ignition success or failure. Figure 7.2 shows an example of ignition sequence with sparking at a downstream location in the IRZ at $z/D_{ext} = 1.4$ and $r/D_{ext} = 0.0$. The flame kernel is found to propagate upstream at first, then to expand downstream in the IRZ. The flame front subsequently propagates through the whole combustion chamber and overall ignition is reached after 14.5 ms.

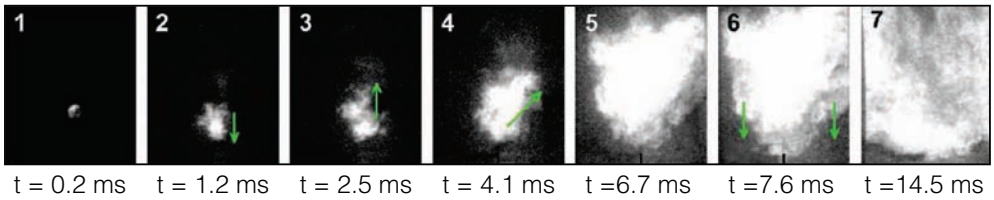

Figure 7.2: Direct visualization of OH* emission during ignition when sparking at $z/D_{ext} = 1.4$ and $r/D_{ext} = 0.0$. Extracted from Cordier (2013).

7.2 Numerical simulations

Due to the high computational cost of LES, reproducing the complete experimental ignition map is today not feasible. Therefore, to achieve the objectives defined for the numerical study, three spark locations have been selected. These points have been selected from the experimental ignition map: they should show different kernel trajectories and exhibit intermediate values $P_{ign,XP}$, indicating important stochastic behavior. The position of these 3 points is illustrated in Fig. 7.1(right) and Tab. 7.1 gives the coordinates, the main flow features and the experimental ignition probability for each location.

	z/D_{ext}	x/D_{ext}	Location	$P_{ign,XP}$
PT1	0.5	0.0	IRZ	[28%-70%]
PT2	0.4	0.4	Shear Layer	50%
PT3	0.8	0.7	SWJ	80%
	F_f	F'_f	k $[m^2.s^{-2}]$	l_t $[mm]$
PT1	0.80	$9.67\ .10^{-3}$	63.7	9.8
PT2	0.46	$13.41\ .10^{-3}$	93.5	32.1
PT3	0.81	$17.62\ .10^{-3}$	67.5	20.5

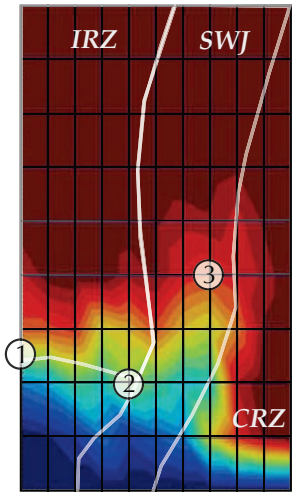

Table 7.1: Position of the ignition locations studied in LES, corresponding flow structure, experimental ignition probability and local non-reacting flow characteristics.

To provide a first idea of the flow characteristics at each location, the flammability factor F_f (see Eq. (5.7)), the flammability dispersion F'_f, the turbulent kinetic energy and an estimation of the integral length are also reported in Tab. 7.1. The flammability dispersion measures the dispersion around stoichiometry of a flammable mixture by:

$$F'_f = \frac{\int_{z_{lean}}^{z_{rich}} |z - z_{st}| P(z)\, dz}{F_f} \tag{7.2}$$

where the stoichiometric, lean and rich mixture fractions of pure methane in air are $z_{st} = 0.055$, $z_{lean} = 0.029$ and $z_{rich} = 0.089$ respectively. F'_f is high when the most probable value for the z disturbution is within the flammable mixture but far from the stoichiometric conditions, and small for a PDF peaked near z_{st}. The turbulent kinetic energy k is directly evaluated from the variance of the resolved velocity field. As for the integral length scale l_t, it is estimated under the assumption of homogeneous isotropic turbulence $l_t = u'^3/\langle\varepsilon\rangle$ with the ensemble averaged scalar dissipation rate (Pope, 2000) given by:

$$\langle\varepsilon\rangle = \frac{1}{N}\sum_{n=1}^{N} 2\nu S_{ij,n} S_{ij,n} \tag{7.3}$$

where $S_{ij,n}$ is the strain rate tensor of the n-th LES snapshot. The turbulent kinetic energy is fairly high at each ignition position but especially at point PT2 located in the shear layer between the SWJ and the IRZ regions. At point PT2, due to the PVC, a large scale coherent structure significantly increases the size of the most energetic eddies as compared to points PT1 or PT3. The flame/turbulence interaction can be characterized in terms of combustion regimes, as introduced in Sec. 3.3.2.a. To estimate the Karlovitz number, the flame properties S_L^0 and δ_L^0 are estimated from the mean mixture fraction conditioned on the flammable range. Placed in the premixed regime diagram, the result indicates that ignition lies in the thin reaction-zone regime where the flamelet hypothesis does not hold because significant quenching of the flame front can occur and the flame preheat layer is modified by small vortices. Note that these results only denote the general trend, and are susceptible to significantly change from one ignition try to the next due to the change in instantaneous equivalence ratio and turbulence fields.

At each location, 20 ignition sequences are computed in LES. Using Eq. (7.1), the uncertainty on the resulting LES probability is about 11.7 %. As shown in Sec. 6.3.6, the vicinity of the injector nozzle undergoes periodic perturbations due to the PVC. The time period of these oscillations is about 1.6 ms, so that ignition is triggered every 0.2 ms in order to span over the whole cycle. Note that, due to the offset observed on the non-reacting flow at the vicinity of the methane jet, PT1 is shifted downstream and is not located on a grid point of the experimental ignition probability map.

7.3 Numerical set-up

7.3.1 Numerical parameters

LES of ignition sequences are performed with AVBP using the numerical parameters listed in Table 7.2, similar to those used for the non-reacting study in Chapter 6.

	Numerical Parameters
Convection scheme	TTGC: $\mathcal{O}(3)$ in space & time (Colin & Rudgyard, 2000)
Diffusion scheme	2Δ operator
SGS model	WALE (Nicoud & Ducros, 1999)
Artif. viscosity	Colin model: $\epsilon^{(2)} = 0.01$, $\epsilon^{(4)} = 0.005$
	Boundary conditions
CH_4 inlet	NSCBC (Poinsot & Lele, 1992) (velocity, 10% turbulence)
Air inlet	NSCBC (Poinsot & Lele, 1992) (velocity)
Atmosphere Outlet	NSCBC (3D) (Granet *et al.*, 2010) (pressure)
Walls	Adiabatic non-slipping walls

Table 7.2: Numerical parameters of AVBP.

7.3.2 Energy deposit model

In the present study, energy deposit is performed using the energy deposit (ED) model developed by Lacaze *et al.* (2009*b*). The ED model follows the methodology proposed by Poinsot *et al.* (1991) where the spark is modeled as a source term in the energy conservation equation. In a TFLES context and in order to avoid undesirable dissipation of the deposited energy, the thickening is not applied before the mass fraction of burnt species exceed 90% of the chemical equilibrium value. The source term follows a Gaussian shape both in time and space given by:

$$\mathcal{Q}_{sp}(r,t) = \frac{\epsilon_i}{4\pi^2\sigma_t\sigma_s^3} e^{-\frac{1}{2}\left(\frac{r}{\sigma_s}\right)^2} e^{-\frac{1}{2}\left(\frac{t-t_0}{\sigma_t}\right)^2} \tag{7.4}$$

where ϵ_i is the amount of energy deposited, r is the Euclidian distance to the center of the deposit x_0, t_0 is the deposit timing and σ_s and σ_t are the characteristic size and duration of the deposit respectively. The parameters of the ED model Δ_s and Δ_t are derived from the Gaussian standard deviation so that 98% of the energy is deposited in $\Delta_s^3\Delta_t$: $\Delta_s = 2\sqrt{ln10^4}\sigma_s$ and $\Delta_t = 2\sqrt{ln10^4}\sigma_t$. Because AVBP is limited to a maximum temperature of 5000 K, the deposit size cannot exactly match a real spark and is increased in the ED model as shown in Fig. 7.3 so that the integral of the power remains the same for the ED model and the real spark, and temperature profile does not exceed 5000 K.

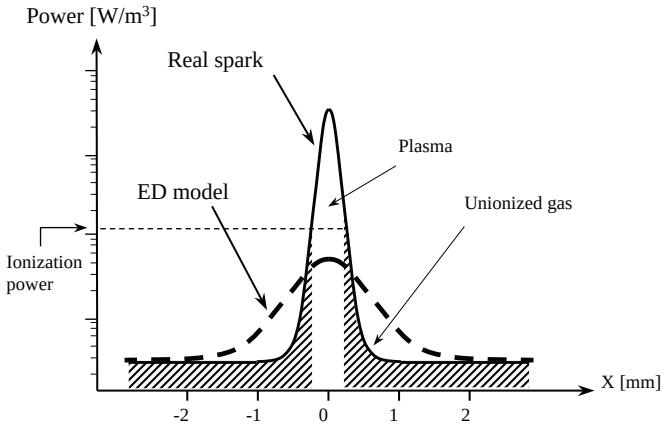

Figure 7.3: Sketch of power distributions for real spark and for the ED model. Extracted from Lacaze *et al.* (2009*b*).

The exact amount of losses induced by the formation of the shock wave and conduction in the electrodes after the spark is not well quantified experimentally. The choice here is to estimate the parameters of the ED model considering that 30% of the deposited energy is transferred to the gas, leading to $\epsilon_i \simeq 29\ mJ$ (Teets & Sell, 1988) measured experimentally. Δ_s is derived from Eq. (7.4):

$$\Delta_s = \frac{4\sqrt{ln10}}{\sqrt{2\pi}} \left(\frac{\epsilon_i}{\rho_f C_p (T_{max} - T_f)} \right)^{1/3} \tag{7.5}$$

where T_{max} is the maximum temperature desired in the kernel and T_f, ρ_f and C_p are the fresh gas properties. The energy deposit time duration is kept constant $\Delta_t = 100\mu s$. Note that Eq. (7.4)

is derived neglecting conduction losses and possibly heat release during the deposit so that the maximum temperature reached in the LES simulation can significantly differ from this prescribed value and vary from one ignition to the next depending on the mixture fraction.

7.3.3 Combustion modeling

The DTFLES model (Colin & Rudgyard, 2000) is employed using the efficiency function from Charlette *et al.* (2002) to handle the flame front on the LES grid. In the context of partially premixed flame, the DTFLES is modified in order to adapt locally the model parameters to the equivalence ratio (Franzelli, 2011). Thus in thickening and efficiency function, S_L^0, δ_L^0 and Ω_0 based on the 2nd reaction of the 2S_CH4_BFER scheme are tabulated versus equivalence ratio from a collection of unstrained laminar premixed flame calculated with CANTERA (Goodwin *et al.*, 2014). The evolution of the DTFLES model parameters as function of the equivalence ratio is reported in Fig. 7.4. The laminar flame speed obtained with the GRI-MECH3.0 detailed scheme is also reported showing a good agreement between the 2S_CH4_BFER scheme used in this study (Sec. 4.4) and a detailed mechanism.

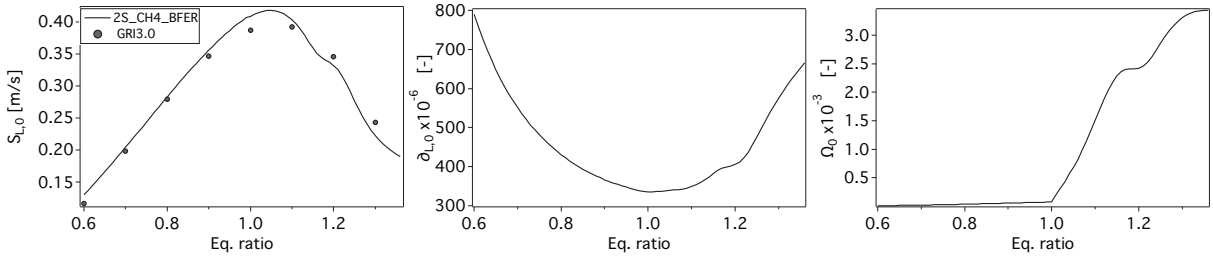

Figure 7.4: Dynamic TFLES model parameters computed versus equivalence ratio from a collection of 1D laminar flames using the 2S_CH4_BFER scheme: S_L^0 (left), δ_L^0 (center) and Ω_0 (right).

The main objective when tabulating the DTFLES parameters versus equivalence ratio is to reduce the thickening factor in regions where the flame burns at lean or rich equivalence ratio since the laminar flame thickness can be more than twice that of the stoichiometric flame depending on the equivalence ratio.

7.3.4 Meshes

All the LES of ignition sequences are performed on fully tetrahedral meshes of about 22 million elements. The global mesh is shown in Fig. 7.5(right) and Fig. 7.5(left) details the mesh in the vicinity of the injector. Note that a large volume is added at the end of the combustion chamber as compared to the non-reacting simulations. The aim of this modification is to avoid the strong dependance of the LES to the outlet boundary conditions during the propagation phase previously observed by Barré (2014). The characteristic mesh size is about 150 μm in the swirler and the mixing regions, 800 μm in the upstream part of the combustion chamber and rapidly increases to about 2 mm downstream.

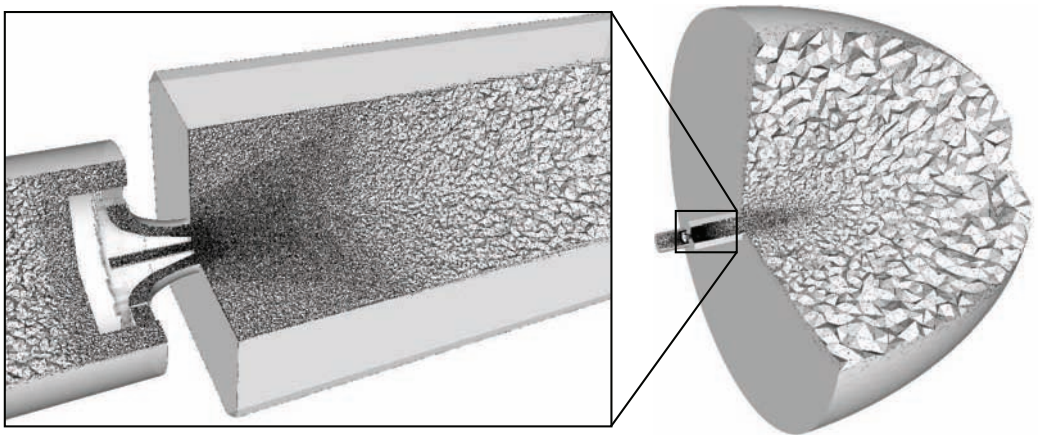

Figure 7.5: LES grid for ignition sequences: full computational domain (right) and details of the injection system region (left).

To comply with the requirements of the ED model (Lacaze *et al.*, 2009*b*) and the recommendations of Barré (2014), three other meshes are generated for each ignition location numerically studied, PT1 PT2 and PT3. Indeed, to fully resolve the initial laminar and small scale kernel without artificially thickening the flame front, a locally refined mesh around the ignition location (in a region of size $20\delta_L^0$ where $\delta_L^0 = 0.51$ mm is the laminar flame thickness at the overall equivalence ratio $\phi_g = 0.75$) is used for the first instants of the simulation, where the cell size is reduced to $\Delta_x = \delta_L^0/6$. Meshes with a refined zone used in this study are presented in Fig. 7.6. Once the flame kernel has sufficiently grown, the refined zone is suppressed and the mesh resolution goes back to LES ($\Delta_x = 1.6\delta_L^0 \sim 0.8$ mm).

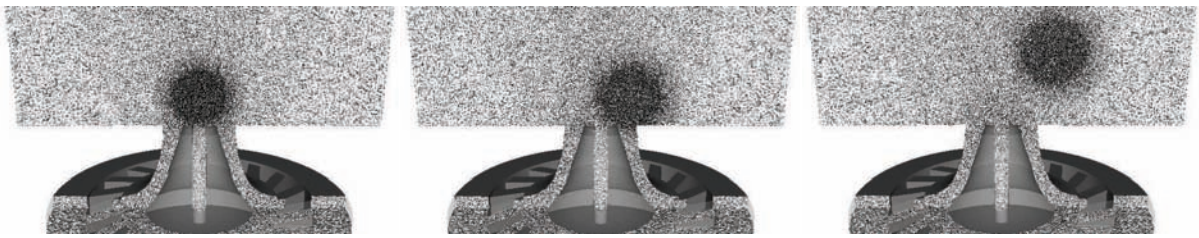

Figure 7.6: LES grids with a refined region at the three energy deposit locations used for the simulation of the first instants after energy deposit.

7.4 Results

60 full LES of ignition sequences have been performed in order to show the capability of LES to reproduce ignition probability at the 3 points of interest and to build a sufficient database to provide a comprehensive understanding of the various mechanisms occurring simultaneously

during the ignition transient. At each location, the 20 ignition trials correspond to 20 realizations of the ignition sequence, only changing the initial flow conditions. Over the 60 ignition sequences computed at the 3 ignition locations, 32 result in a successful ignition of the burner. The ignition probability obtained with LES, noted $P_{ign,LES}$ and reported in Table 7.3, compares well with the experimental $P_{ign,XP}$ listed in Table 7.1 demonstrating the capability of LES to reproduce quantitatively the variability of ignition. The probability of creating a sustainable flame kernel $P_{ker,LES}$ is also estimated based on the temporal evolution of the heat release: cases where the overall heat release drops to zero within the first ms after energy deposit are considered to be failures of kernel generation.

	$P_{ign,XP}$	$P_{ign,LES}$	$P_{ker,LES}$
PT1	80 %	40%	90 %
PT2	46 %	50%	70 %
PT3	81 %	75%	85 %

Table 7.3: $P_{ign,XP}$ along with LES prediction of ignition probability $P_{ign,LES}$ and kernel generation probability $P_{ker,LES}$ at the three ignition locations PT1, PT2 and PT3.

On the basis of the good agreement between $P_{ign,LES}$ and $P_{ign,XP}$, combined with the good LES predictions of the non-reacting flow statistics shown in Chap. 6, the results can be analyzed to identify the mechanisms controlling ignition. As a first step, Sec. 7.4.1 gives an overview of the ignition scenarios captured for each sparking location and highlights the variability resulting of the change in spark timing. Then details of the combustion regime and flame front propagation are proposed, followed by an analysis of the mechanisms leading to ignition failure in Secs. 7.4.2 and 7.4.3. Finally, the ignition sequences are treated as a whole in an effort to relate the ignition outcome to the non-reacting flow properties.

7.4.1 Ignition scenario at the 3 sparking locations

To give an overview of the LES results, ignition sequences are first analyzed using global indicators and qualitatively compared to the experimental observations of Cordier (2013).

7.4.1.a PT1: $z/D_{ext} = 0.5$, $x/D_{ext} = 0.0$

PT1 is located at the bottom of the IRZ, close to the stagnation point. As shown in Sec. 6.3 and in Tab. 7.1 , this position is located in a region of high turbulence intensity and small turbulent structures. The flammability factor indicates locally a strong probability of flammable mixture but $\overline{z}$ is well towards rich mixture and the mean gradient of z is large. As illustrated in Fig. 7.7(left) where the flame is materialized by an iso-surface of temperature $T = 600\ K$, the ignition scenario following sparking at PT1 can be decomposed as follows:

- convection of the kernel towards the methane jet
- development of a highly turbulent partially premixed flame kernel
- expansion of the flame kernel in the IRZ

- flame propagation towards the top of the chamber and expansion in the CRZ

In the successful case, the flame kernel growth is limited during about ~ 5 ms by the high turbulence levels and the vicinity of inflammable mixture at the bottom of the IRZ. In this case, the progressive temperature increase of the IRZ eventually allows the flame kernel to expand and ignite the full burner. In the failed event illustrated in Fig. 7.7(right), a flame kernel is generated but is quickly quenched (< 2 ms) before a sufficient amount of heat is generated. Mechanisms leading to overall flame quenching will be studied in detail in Sec. 7.4.3

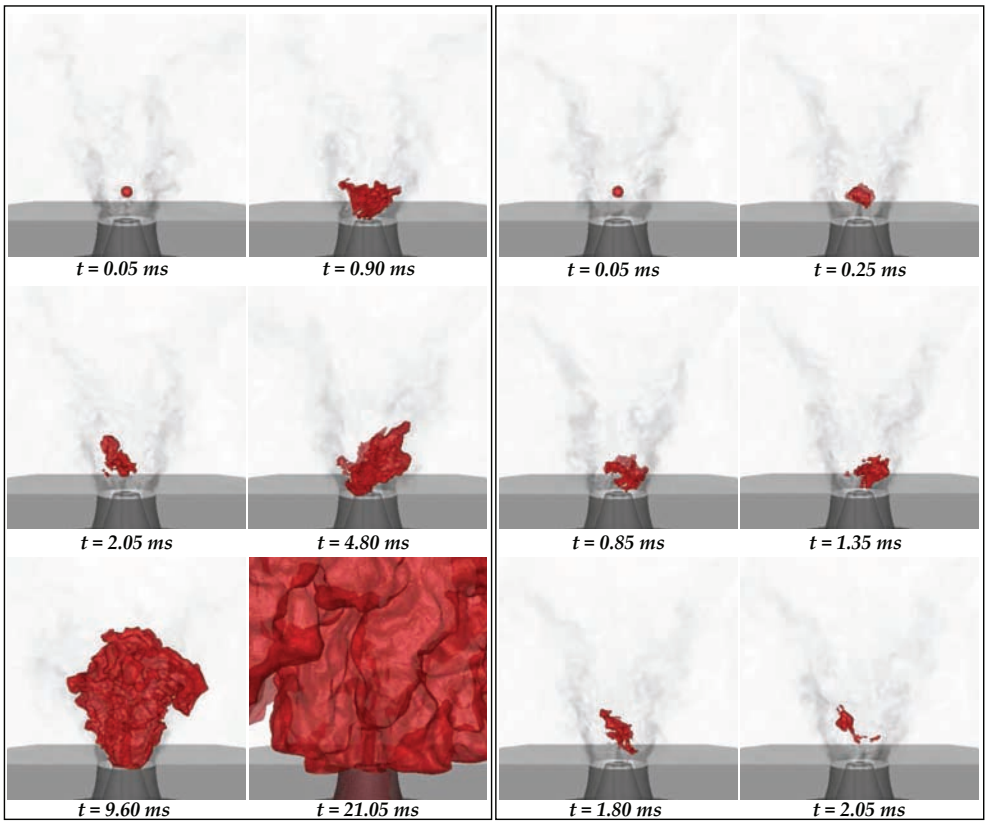

Figure 7.7: Instantaneous flame position tracked by an iso-surface $T = 600$ K in case of ignition success (left) or failure (right) at sparking location PT1.

A qualitative comparison with experiments shows that the LES scenarios for ignition success or failure at PT1 described above match experimental visualization. In accordance with experiments, no case of late failure is observed since once hot gases have filled a sufficient portion of the IRZ, the ignition success is guaranteed. This behavior may be explained by the operating conditions, chosen far from the blow-off conditions by Cordier (2013). The focus is given here on the first instants of ignition and a detailed study of the late flame propagation and stabilization is not performed.

The early flame kernel behavior is investigated in Fig. 7.8 showing flame kernel trajectories projected in a x-z view. Successful ignition events are colored according to the time after ignition ($t - t_{ign}$) while failed events are in white. The flame kernel trajectories are obtained by tracking

the Flame Center of Gravity (FCG). The coordinates of the FCG are defined as the barycentric coordinates of the vertices having a temperature above 1300 K:

$$x_{i,FCG} = \sum_{n=1}^{N} \frac{\rho_n V_n x_{i,n}}{\rho_n V_n} \tag{7.6}$$

where $x_{i,FCG}$ is the i-th coordinate of the FCG, ρ_n and V_n are the density and volume at the n-th node and N is the number of nodes having a temperature $T_n > 1300\ K$. Note that these trajectories only indicate the general trends of the kernel displacement and can significantly differ from the actual kernel motion if large chunks of flame are separated from the bulk. The variability of the velocity field at ignition time scatters the FCG trajectories, but in all cases the FCG first goes downstream the combustion chamber before being deflected out of the burner axis due to the rich methane jet. In cases of successful events, trajectories show that the flame kernel is able to move downstream in an helical motion following the inner shear layer. These trajectories also indicate that, at PT1, there is no evident flame pathway that guarantees ignition success.

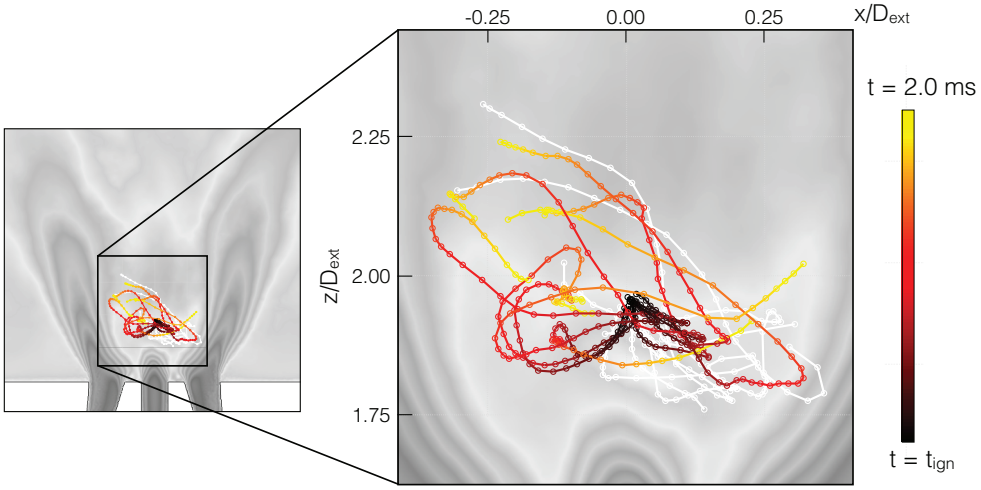

Figure 7.8: Trajectories of the FCG at sparking location PT1 superimposed on the time-averaged velocity field. Successes are colored by the time while failures are in white.

As the flame kernel moves along its trajectory, it grows and interacts with the surroundings. The temporal evolution of the mean heat release rate in the computational domain is plotted in Fig. 7.9 for the first two milliseconds after energy deposit at PT1 and is used as an indicator of the kernel growth. Successful cases are reported in black while plain grey symbols correspond to failed events. The first observation is the wide spreading of the curves and the fact that the distinction between failed and successful events is not obvious even after 1 ms. For all cases, the evolution of heat release is non monotonic, revealing that the flame experiences significant quenching. This shows the high turbulence conditions around the energy deposit, far above the DNS of kernel growth or LES of burners reported in the literature (Poinsot *et al.*, 1991; Subramanian *et al.*, 2010; Reddy & Abraham, 2013). The early peak in heat release denotes the effect of the over-adiabaticity resulting from the energy deposit. This peak is observed for all cases except two, and the peak amplitude is found to vary from one simulation to the other.

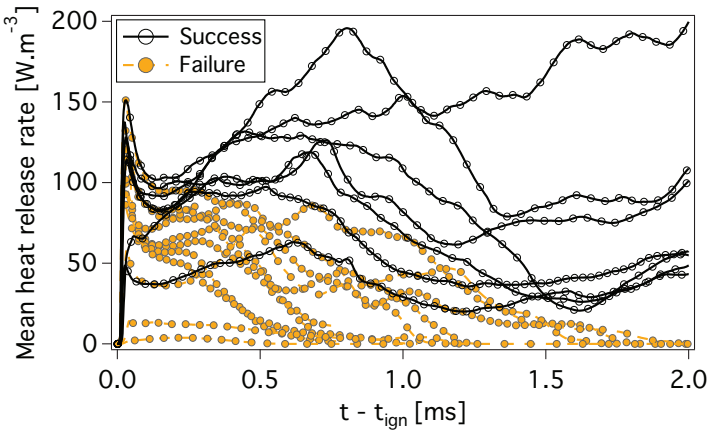

Figure 7.9: Temporal evolution of the mean heat release in the computational domain following energy deposit at sparking location PT1.

7.4.1.b PT2: $z/D_{ext} = 0.4$, $x/D_{ext} = 0.4$

PT2 lies in the shear layer between the IRZ and the SWJ. Due to the presence of the PVC, this region undergoes large fluctuations of mixture fraction between the pure air of the SWJ and the rich mixture at the bottom of the IRZ. The size of the most energetic structures is also significantly larger than at the other two ignition locations (see Tab. 7.1). Apart from the early changes due to the shifted energy deposit location, the ignition scenario is quite similar to the one described for PT1:

- in most cases, the kernel is convected radially inward towards the IRZ and downstream
- a highly turbulent partially premixed flame kernel develops
- the flame kernel in the IRZ expands
- flame propagates towards the top of the chamber and expands in the CRZ

Figure 7.10 shows a successful (left) and failed (right) ignition event at sparking location PT2. The flame kernel is found to expand faster than for PT1 due to the near stoichiometric mixture and the lower level of turbulence experienced in the intermediate part of the IRZ. When convected towards the methane jet, the kernel size is sufficient to overcome the local extinction effects and fills the whole IRZ. The failed ignition event shown in Fig. 7.10 is very short. It corresponds to a failure mode where the amount of flammable mixture at the sparking time and location is insufficient to generate a sustainable flame kernel.

Trajectories of the FCG are reported in Fig. 7.11. The large vortices passing at PT1 induce a large spreading of the trajectories. Since the deposit is performed in the inner shear layer, most kernels go inward. Some misfires are emitted towards the lean SWJ region or maintained in the shear layer. All successful cases penetrate in the IRZ, slightly larger than PT1, at a location of near stoichiometric mixture fraction. However, this path does not guarantee ignition success.

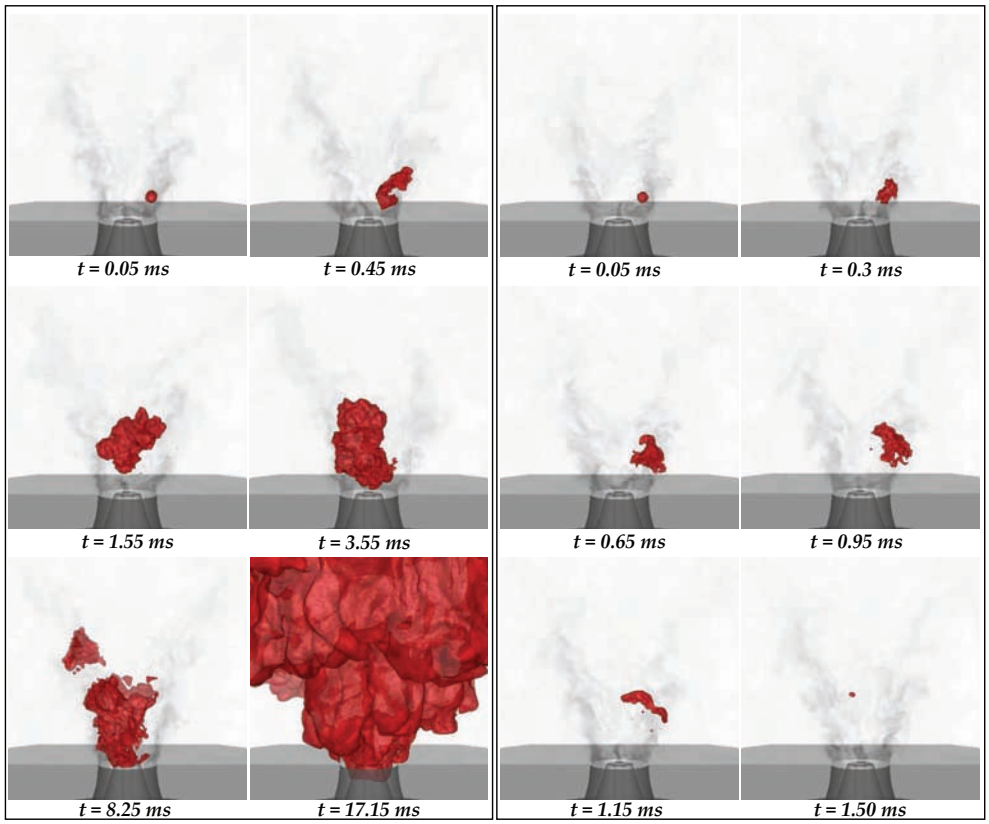

Figure 7.10: Instantaneous flame position tracked by an iso-surface $T = 600\ K$ in case of ignition success (left) or failure (right) at sparking location PT2.

The mean heat release is displayed as function of time in Fig. 7.12. Once again, the change in ignition timing results in a high variability of the kernel growth and the non monotonic evolutions also indicate the occurrence of local extinction. The initial heat release peak is also observed for most cases, but it is interesting to notice that some successful ignition sequences are exempted: energy is delivered to a mixture that is not flammable and the subsequent transport of heat towards flammable regions is responsible for the progressive increase of heat release. As for PT1, it is not possible to unambiguously distinguish success from failure from the early flame development, and global extinctions are observed up to 4 ms after energy deposit.

7.4.1.c PT3: $z/D_{ext} = 0.8$, $x/D_{ext} = 0.7$

PT3 is located in the SWJ region, slightly downstream of the two other ignition points. The flammability factor reported in Tab. 7.1 indicates that at this location, flammable mixture is available most of the time. The turbulence intensity is close to that of PT1, but the size of the turbulent eddies are about twice as large. Two main ignition scenarios are observed:

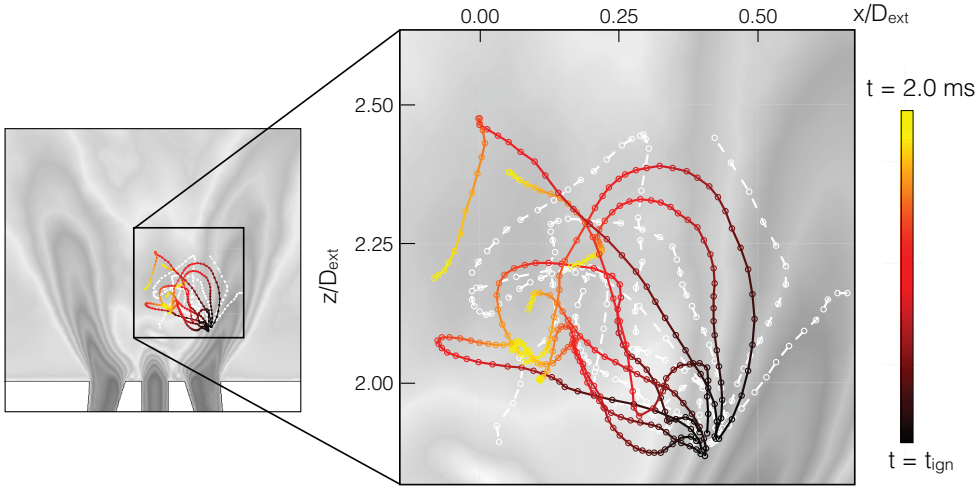

Figure 7.11: Trajectories of the FCG at sparking location PT2 superimposed on the time-averaged velocity field. Successes are colored by the time while failures are in white.

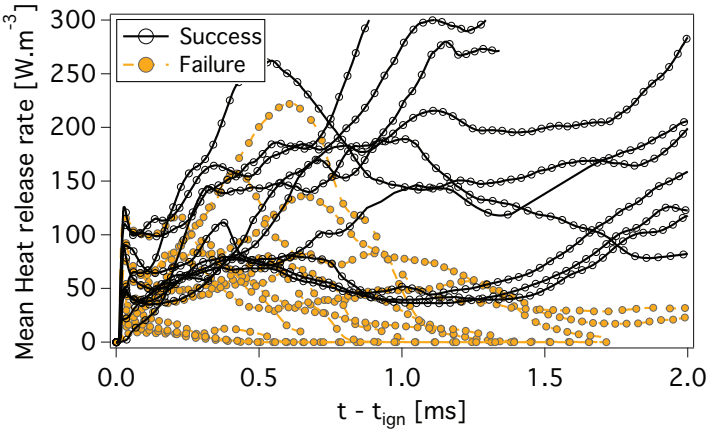

Figure 7.12: Temporal evolution of the mean heat release in the computational domain following energy deposit at sparking location PT2.

Scenario 1:

- the kernel is convected downstream and radially inward
- the flame rapidly develops in the upper part of the IRZ
- the flame propagates towards the injector nozzle
- the flame quickly expands in the whole chamber

Scenario 2:

- The kernel is strongly convected downstream
- the flame develops in the top of the combustion chamber
- the flame front propagates upstream, promoted by both IRZ and CRZ

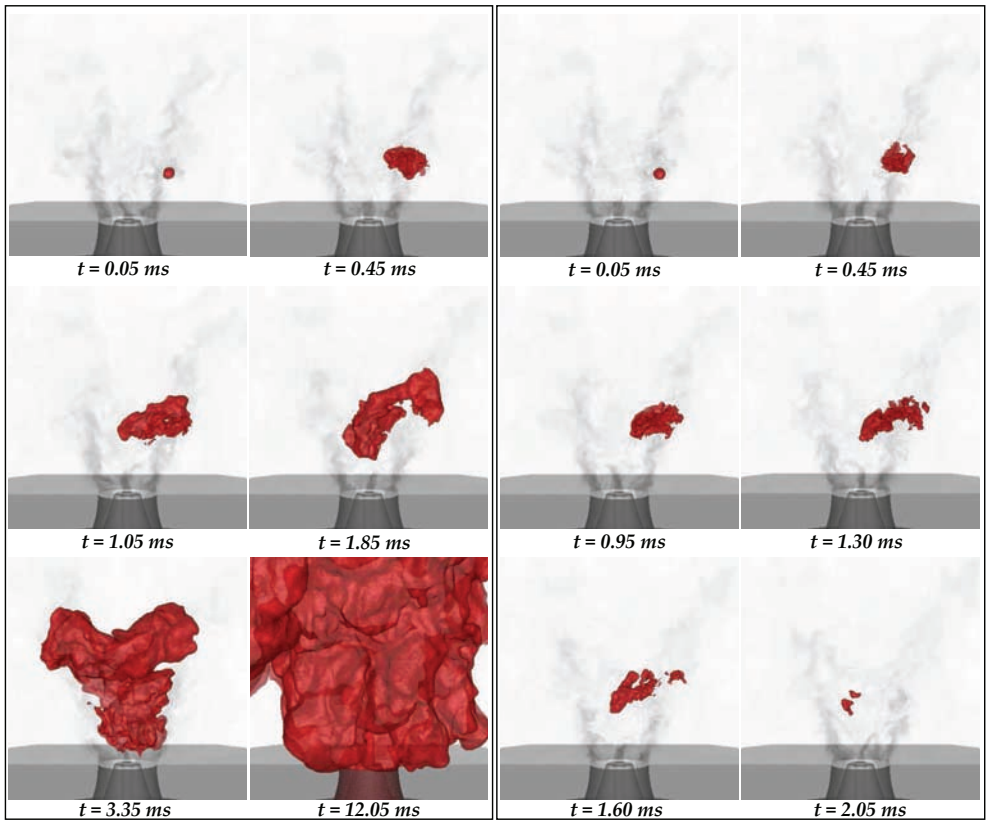

Figure 7.13: Instantaneous flame position tracked by an iso-surface $T = 600\ K$ in case of ignition success (left) or failure (right) at sparking location PT3.

Flame position snapshots in Fig. 7.13 illustrate ignition success (left) and failure (right) at sparking location PT3. The successful case follows Scenario 1 described above. The flame enters the IRZ downstream and is able to expand both towards the injector nozzle and against the slow backward flow in the top of the IRZ. The weak turbulence level and favorable mixture fraction then allows a fast flame expansion with limited local extinction and the overall ignition is reached in less than 15 ms. In the other case, failure is the result of a lean mixture pocket passing at the ignition location at the sparking time. The limited heat release is unable to counter the heat dissipation induced by the turbulence of the SWJ and even though a fragment of the flame is convected in the IRZ, its size is insufficient for its survival.

The FCG trajectories shown in Fig. 7.14 clearly support the existence of 2 scenarios: part of the flame kernel goes towards the IRZ while the other mainly follows a downstream motion. Ignition scenarios reported in Cordier (2013) do not focus on the exact same location, but the second scenario is similar to experiments when sparking in the SWJ. The first scenario seems to guarantee the overall ignition success, at least for all cases performed in LES. On the contrary, the second scenario can lead to ignition failure, in particular if the downstream motion is accompanied of a radially outward displacement. Finally, the overall ignition is reached faster for the first scenario.

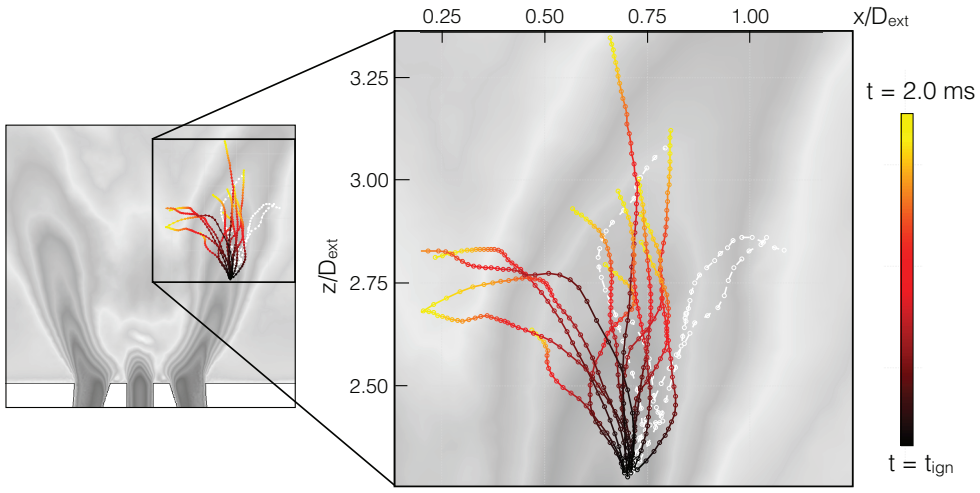

Figure 7.14: Trajectories of the FCG at sparking location PT3 superimposed on the time-averaged velocity field. Success are colored by the time while failures are in white.

The kernel growth is tracked by the mean heat release in Fig. 7.15. Due to the more homogeneous mixture fraction and the lower turbulence intensity at sparking point PT3, the growth rates are much stronger than at the two other locations. For all successful cases, the heat release is found to increase continuously, without any strong reduction of the heat release related to the quenching of large flame portions.

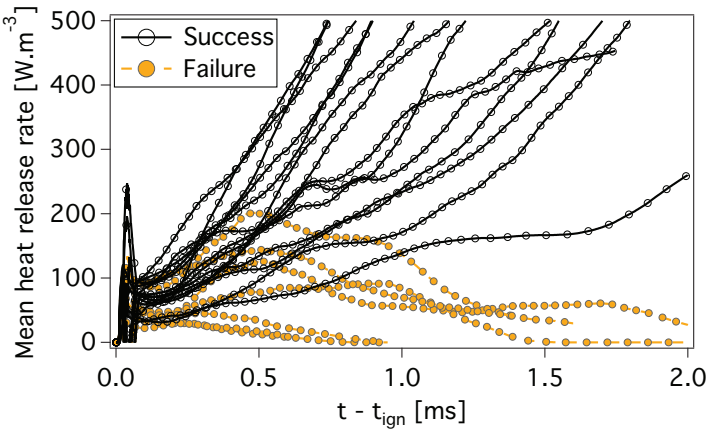

Figure 7.15: Temporal evolution of the mean heat release in the computational domain following energy deposit at sparking location PT3.

7.4.2 Flame structure and propagation

7.4.2.a Combustion regime

A first step towards a better understanding of the parameters driving ignition is to investigate in detail the flame front in terms of combustion regime. The PDF of mixture fraction given in Fig. 7.16 for each ignition location indicates three distinct mixing behaviors:

- at PT1 the most probable mixture fraction is slightly lean but $\overline{z}$ is significantly higher than z_{st} due to the long tail of the PDF towards rich mixture. The long tail denotes the proximity of the methane jet that results in non-zero probability of pure methane pockets at this location.

- at PT2 the PDF is bimodal with nearly equal probability of slightly lean mixture ($z = 0.5$) and pure air. The distribution is characteristic of the intermittent behavior of the mixture in the shear layer between the pure methane jet and the pure air SWJ.

- PT3 shows the most probable mixture at a lean but flammable mixture and is much narrower than the other ignition locations. This is mainly due to the fact that PT3 is located downstream, allowing longer time for mixing.

Two situations must be distinguished depending on the PDF position relative to the stoichiometric mixture fraction: for PT1 and PT2 the PDF of z reported in Fig. 7.16 indicates that the probability of finding lean and rich flammable mixture is fairly equivalent while at PT3 the occurrence of rich mixture is much lower than that of lean one. Thus, it is expected that both non-premixed and premixed combustion regimes might coexist during ignition at PT1 or PT2 but lean stratified premixed combustion should be dominant at PT3.

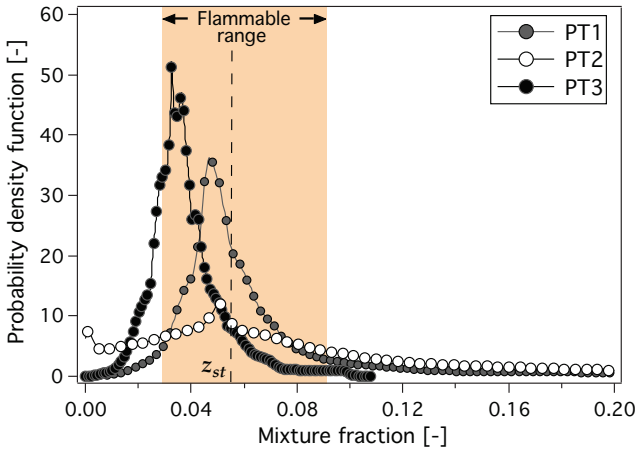

Figure 7.16: PDF of mixture fraction z at the three ignition locations.

To evaluate the respective contribution of both combustion regimes, the Takeno index I_{tk} (Yamashita *et al.*, 1996) is introduced:

$$I_{tk} = \frac{\nabla\vec{Y}_F.\nabla\vec{Y}_O}{|\nabla\vec{Y}_F.\nabla\vec{Y}_O|} \tag{7.7}$$

which evaluates the alignment of the fuel and oxidizer gradients based on a one dimensional geometrical argument. Even though its extension to 3D turbulent flames is not trivial, 3D DNS studies demonstrate the validity of such flame index (Mizobuchi *et al.*, 2002). It is generally argued that diffusion flame are characterized by opposed gradients ($I_{tk} = -1$) and premixed flame by aligned gradient ($I_{tk} = 1$). Note that Fiorina *et al.* (2005) showed that this description breaks down in certain regimes of partially premixed combustion where the gradients of fuel and oxidizer are aligned but combustion remains diffusion-controlled. The integrated heat release conditioned by the Takeno index is evaluated and plotted against time in Fig. 7.17 where a representative example is shown for each ignition location. For ignition at PT1 and PT2, both premixed and non-premixed combustion is encountered but most of the heat release is produced in premixed regions (about 90%). For ignition at PT3, most of the time the combustion is fully premixed even though non-premixed flame front can be found at later time when the flame front reaches the bottom of the IRZ.

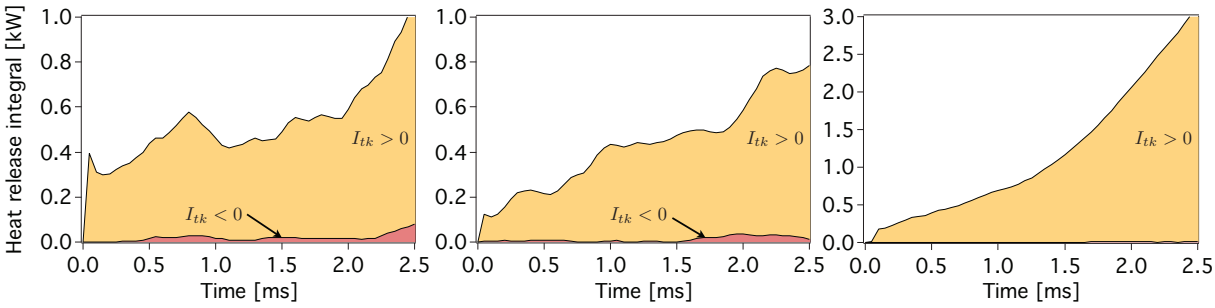

Figure 7.17: Temporal evolution of the conditioned heat release integral for PT1, PT2 and PT3 respectively: orange (or light grey in black and white) denotes premixed combustion ($I_{tk} > 0$) and red non-premixed regime ($I_{tk} < 0$).

An example of the intricate mixing of diffusion and premixed fronts is shown in Fig. 7.18 (for ignition at PT1). The color scale corresponds to the heat release rate while the black line shows the stoichiometric mixture fraction and the grey lines notice the lower and upper static flammability limits. Several flame elements are captured: 1) on the upper LHS, a premixed flame front spanning from lean to rich mixtures is visible with a triple point at the bottom location, 2) on the lower part a diffusion flame front is present along the stoichiometric iso-line. Due to the intense turbulence, diffusion flame fronts are rapidly quenched and re-ignited as vortices propagate downstream in the shear layer between methane and air.

7.4.2.b Flame propagation

The early flame propagation is sustained by the over-adiabaticity resulting from the energy deposit. Due to the very short ignition delay of the 2S_CH4_BFER (Fig. 4.3 in Chap.4) global

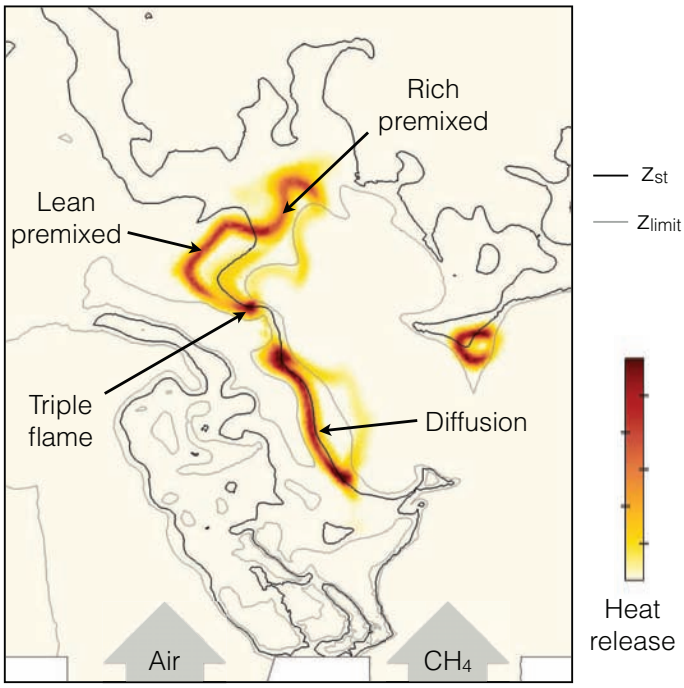

Figure 7.18: Instantaneous field of heat release (color scale) at $t = 0.75\ ms$ at PT1. Black iso-line indicates the stoichiometric mixture fraction iso-line position while grey lines notice the static flammability limits.

kinetic scheme, the maximum temperature and the amplitude of the initial heat release peak is closely related to the amount of fuel readily available at the vicinity of the sparking location. Within the first 700 μs, the temperature of the flame kernel drops to the adiabatic flame temperature and the flame propagation then depends on both the fresh mixture composition and the level of turbulence. Since most of the heat is released in premixed flame mode, the analysis of the flame front is performed on the premixed flame only and unless specified otherwise, the diagnostics are conditioned on positive I_{tk} regions. The overall flame propagation is first studied using the consumption speed:

$$S_c = -\frac{1}{\langle\rho_0\rangle(\langle Y_F^f\rangle - \langle Y_F^b\rangle)A_f}\int_V \dot{\omega}_F\ dv = \frac{1}{\langle\rho_0\rangle(\langle Y_F^f\rangle - \langle Y_F^b\rangle)A_f\mathcal{Q}_{r,CH4}}\int_V \dot{\omega}_T\ dv \tag{7.8}$$

where $\langle\rangle$ indicates averaged over the flame front to take into account the mixture heterogeneity, A_f is the flame surface and $\mathcal{Q}_{r,CH4}$ is the heat of combustion of methane. Defining the flame surface of a turbulent flame front is not an easy task, especially in the thin reaction zone regime since small vortices can significantly increase the thickness of the preheat zone. In this study, A_f is computed from the flame surface density (FSD) Σ and several tests indicate that this evaluation gives results close to those obtained with those of an iso-surface $c = 0.2$.

$$A_f = \int_V \Sigma_{tot}\ dv = \int_V \mathcal{E}\Sigma_{res}\ dv \tag{7.9}$$

where Σ_{tot} and Σ_{res} are the total and resolved FSD respectively. The FSD is based on the gradient of the progress variable c, $\Sigma_{res} = |\boldsymbol{\nabla c}|$ and in this analysis, the progress variable is the reduced

temperature:

$$c = \frac{\widetilde{T} - T_f}{T_{ad} - T_f} \tag{7.10}$$

Note that in partially premixed environment, the definition of the progress variable should be adapted to the local composition by changing the adiabatic temperature T_{ad}. The effect of the definition of c on the description of the flame structure is detailed in Appendix B. The evolutions of S_c for successful and failed ignition events are plotted in Fig. 7.19 for each ignition location.

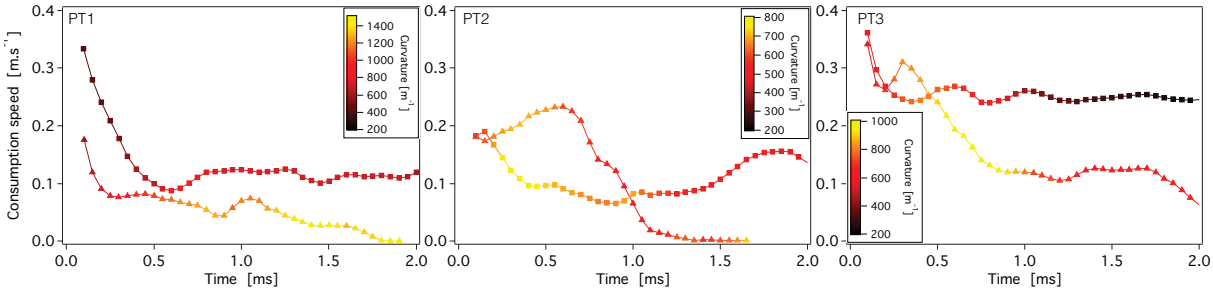

Figure 7.19: Temporal evolution of the consumption speed S_c for successful (square) and failed (triangle) ignition events at each ignition location. Markers are colored by the mean curvature along the flame front.

The consumption speed is found to be initially high due to the high temperature in the kernel. For all successful cases, S_c stabilizes to a value which corresponds to 60% of the unstrained laminar flame speed at the mean equivalence ratio about the flame front so that S_c is higher at PT3 than at PT1 or PT2 due to the near stoichiometric mixture. The mean curvature along the flame front is found to have a significant effect on the consumption speed since high mean curvature is associated with a reduction of the consumption speed.

To further study the flame front motion, the flame velocity is split into a convective contribution induced by the underlying flow and the displacement speed contribution resulting from the thermo-diffusive processes within the flame front. This distinction is related to the definitions of flame speeds introduced in Sec. 3.2.1.b. A formula for the flame density-weighted displacement speed S_d^* is derived in Appendix B:

$$S_d^* = \frac{\overline{\rho}}{\rho_0} S_d = \frac{\overline{\rho}}{\rho_0} \frac{1}{\overline{\rho C_p} |\boldsymbol{\nabla} \widetilde{\boldsymbol{T}}|} \left[\frac{\mathcal{E}}{\mathcal{F}} \dot{\omega}'_T + \boldsymbol{\nabla} \cdot (\mathcal{E} \mathcal{F} \lambda \boldsymbol{\nabla} \widetilde{\boldsymbol{T}}) - \boldsymbol{\nabla} \widetilde{\boldsymbol{T}} \left(\sum_{k=1}^{N} C_{p,k} \overline{J}_{i,k} \right) \right] \tag{7.11}$$

Two tests are performed in Appendix B to ensure that this definition holds within the TFLES context and a detailed study of the components of S_d^* on a 3D ignition case is also reported to clarify its evolution across the turbulent flame front.

In order to evaluate the main contributor to the flame motion, PDFs of displacement speed S_d^* and absolute speed S_a are given for a successful ignition case at PT2 in Fig. 7.20(left). PDFs are computed for $c = 0.25 \pm 0.1$. S_d^* has a near Gaussian distribution bounded between -1 and 2 $m.s^{-1}$ and a mean value around 0.5 $m.s^{-1}$. This value corresponds to the resolved turbulent flame speed: $\mathcal{E}.S_L^0$. The mean absolute flame speed on the other hand ranges from -20 to 20 $m.s^{-1}$,

with a mean value several times higher than the displacement speed. This indicates that the flame motion is mainly driven by the convection induced by the underlying flow and clearly supports the fact that the kernel trajectories reported in Figs. 7.8, 7.11 & 7.14 is linked to variation of the initial flow field rather than the flame displacement speed magnitude and direction.

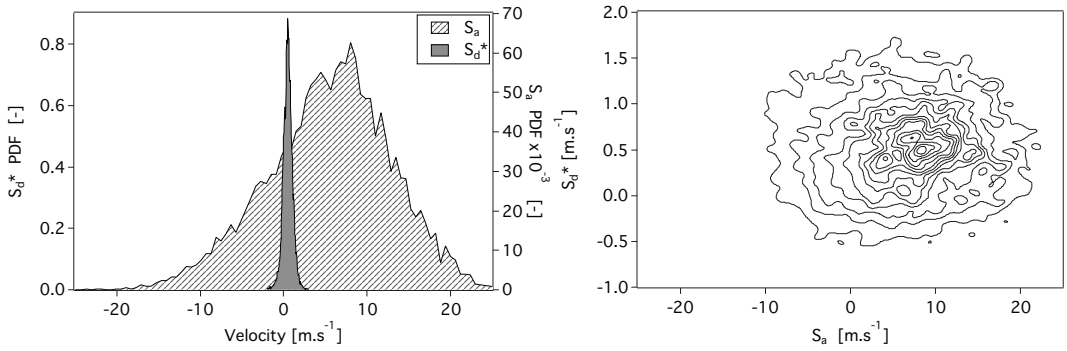

Figure 7.20: PDF of flame density-weighted displacement speed S_d^* and absolute flame speed S_a (left) and joint-PDF of S_d^* and S_a (right) computed for $c = 0.25 \pm 0.1$ at sparking location PT2.

The joint PDF of S_d^* and S_a displayed in Fig. 7.21(right) and shows that there is no correlation between these two quantities: the flame is not able to impose its own expansion dynamics to the surrounding flow due to the high turbulence conditions. The frequent occurrence of negative S_a also indicates that the convection can locally be strong enough to induce a reverse motion to the flame front and participate to the formation of burnt gas pockets.

Thermo-diffusive process however however strongly influence the kernel growth. Unlike S_c (see Eq. (7.8)), S_d^* is a local quantity and its magnitude varies depending on the local mixture fraction and stretch. The decomposition of the flame stretch into two terms, one related to the aerodynamic strain tangential to the flame front and one due to curvature is used hereafter. The effect of curvature is highlighted by the joint PDF of S_d^* and $\mathcal{K}$ reported in Fig. 7.21(left): the displacement speed is inversely proportional to curvature through the tangential diffusion term (see Appendix B). On the contrary, S_d^* is not correlated to the tangential strain rate as shown in Fig. 7.21(right). The fact that the curvature effect dominates the flame response to stretch is coherent with the modeling approach developed by Peters (1999) for flame/turbulence interaction in the thin reaction zone regime. Such results are also obtained in the DNS of Chakraborty & Cant (2004) and Jenkins *et al.* (2006). The kernel growth is then reduced in cases where turbulent structures are able to induce large flame curvature, i.e. for strong turbulence intensity and small length scales.

The dependance of S_d^* to the equivalence ratio follows that of the laminar flame speed: maximum near the stoichiometry and rapidly decreasing for rich and lean mixture. As a consequence, the kernel growth rate is closely correlated to both the amount of flammable mixture around the sparking location but also to its equivalence ratio.

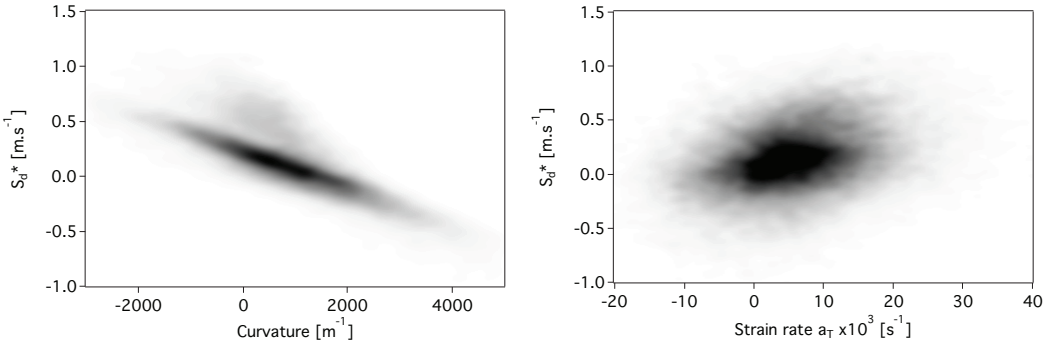

Figure 7.21: Joint-PDF of S_d^* versus $\mathcal{K}$ (left) and a_T (right) computed for $c = 0.25 \pm 0.1$ at sparking location PT2.

7.4.3 Mechanisms leading to ignition failure

In about half of the 60 LES, the deposited energy fails to initiate a stabilized combustion regime. The two failure modes identified can be related to two ignition probabilities as proposed by Birch *et al.* (1981) and used by Ahmed & Mastorakos (2006) and Mastorakos (2009):

- **mode 1**: the deposited energy induces an insufficient amount of heat release due to the lack of flammable mixture around the ignition location or too strong turbulence conditions. Ignition fails to create a flame kernel. The occurrence of this type of failure is quantified by the probability of generating a flame kernel P_{ker}.
- **mode 2**: a flame kernel is created, but the subsequent flame/turbulence interactions in partially premixed turbulent flow leads to its quenching. The overall ignition probability P_{ign} is affected.

An example of **mode 1** is presented in Fig. 7.13 when trying to ignite at PT3 while **mode 2** is illustrated in Fig. 7.10 at PT2. In the case of **mode 1**, the overall dissipation of the flame kernel is reached very rapidly after energy deposit since the turbulent environment strongly enhances heat diffusion. On the contrary, **mode 2** generally occurs at longer times and has been observed during the entire kernel phase duration (up to 3 ms after sparking). The distinction between P_{ker} and P_{ign} is not made in the experiments of Cordier (2013) since this distinction it is not easy to observe from measurements.

7.4.3.a Failure of flame kernel generation

In the present study, failed initiation of the kernel is always due to the lack of flammable mixture at ignition time. Such cases occur at all ignition locations as shown in Figs. 7.9, 7.12 and 7.15 by the rapid disappearance of the chemical source term for some cases. An example of both lean and rich failures at PT3 and PT2 is presented in Fig. 7.22 showing the temporal evolution of the PDF of mixture fraction computed on the vertices where the heat release rate is higher than

10^5 $W.m^{-3}$. The PDF is estimated using a Kernel Density Estimator (KDE) (Silverman, 1986) to avoid the issue related to the number of sample points and change in the PDF range. More details on the KDE method can be found in Appendix A. For the sake of clarity, the distribution at each snapshot used to build such graph is normalized in order to follow the position of the most probable value so that it is not strictly speaking a PDF. The dashed horizontal lines correspond to the lower and upper flammability limits.

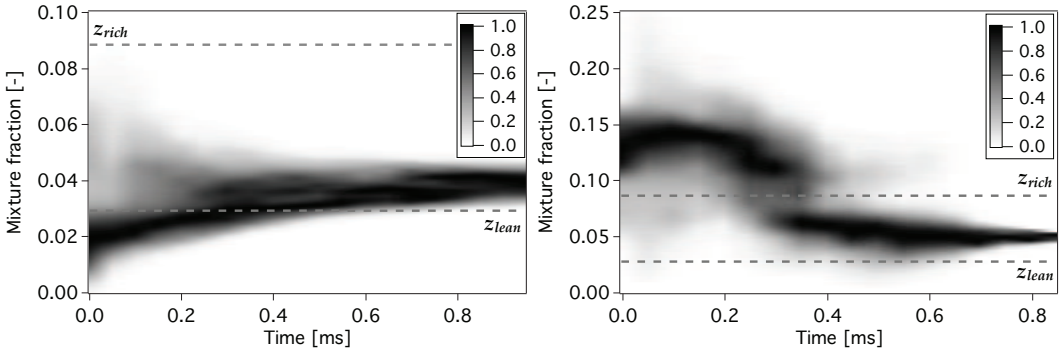

Figure 7.22: Temporal evolution of the z PDF on the reactive flame kernel for a failed ignition event at PT3 (left) and PT2 (right).

Figure 7.22(left) corresponds to an ignition sequence at PT3, where the mixture at the initial deposit location is almost entirely too lean to burn. In Fig. 7.22(right) an ignition at PT2 is reported for which the initial distribution of z is above the rich flammability limit. In both cases, the z distribution stays outside of the flammability limits during the first 200 to 400 μs. Later, since only reactive mixture locations produce heat, the PDF tends towards flammable mixture but the remaining burning gases are unable to compensate for the heat losses that are enhanced by the local turbulent conditions.

7.4.3.b Quenching

Quenching of the flame kernel at longer time can result from the combination of several mechanisms sketched in Fig. 7.23:

- effect of the partial premixing on the flammability of the fresh mixture: quenching due to lack of flammable mixture
- large scale deformation, fragmentation of the flame kernel: thermal quenching of burnt gases pockets
- effect of the strain and curvature on the flame consumption rate: modification of the flame structure

These mechanisms are closely related but not limited to the stretch direct and indirect quenching mechanisms identified in Poinsot *et al.* (1991). If the flame kernel size is of the order of the

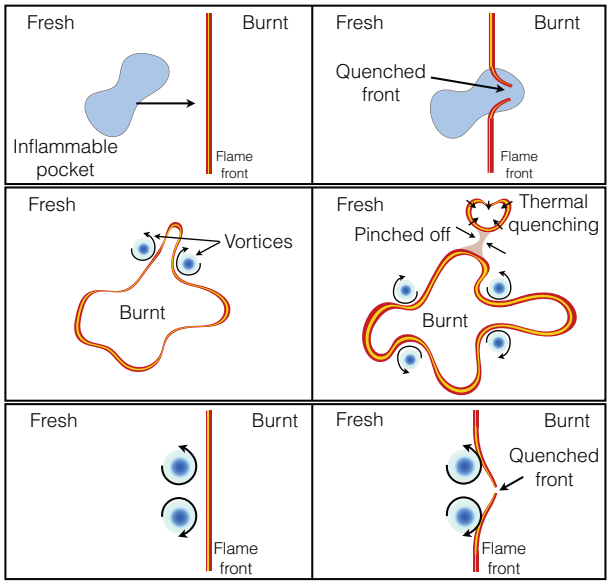

Figure 7.23: Schematic description of flame kernel quenching mechanisms in partially premixed flows: mixture heterogeneity (top row), kernel large scale deformation and fragmentation (middle row) and direct stretch quenching of the flame front (bottom row).

aerodynamic or mixture perturbations, the first two mechanisms can result in overall quenching of the flame kernel. On the contrary, the last mechanism can only induce a significant decrease of the kernel growth rate or local quenching in extreme cases.

- Partial premixing effect

Flame front quenched by inflammable mixture is considered to represent a net loss of energy since fresh gases are heated but do not subsequently produce any significant heat release. From the PDF of mixture fraction reported in Fig. 7.16 and the flammability factor given in Tab. 7.1, the occurrence of partial quenching due to lack of flammable mixture is more frequent at PT2 than PT1 or PT3. However, considering that PT1 is located in a region of strong gradient of z, this quenching mechanism is also critical for PT1. An example of such behavior is illustrated in Fig. 7.24 where the heat release field (color scale) is plotted along with the position of the stoichiometric (black) and lean and rich (gray) flammability mixture fraction iso-contours in a central cut plane through the burner.

Following sparking at PT1, a flame kernel is created in a rich but flammable mixture region. The reverse flow from the IRZ and a burst of pure methane emitted from the jet quench large portions of the flame kernel as the flame front meets the rich flammability limits. The flame kernel completely looses its spherical shape and flame fragments are distributed in the flow. A similar behavior is observed at PT3 during the interaction of the flame kernel with pockets of lean gases in the wake of the SWJ. But at PT3, the kernel is rapidly convected downstream where the mixture distribution is more favorable.

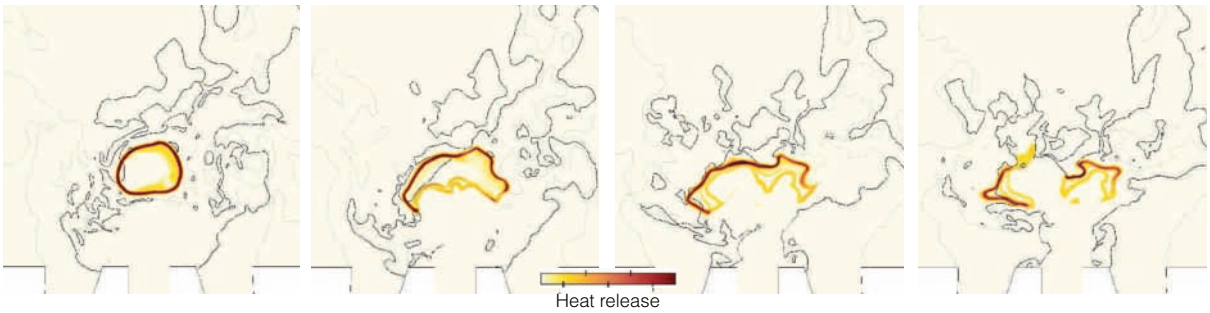

Figure 7.24: Heat release field in a central cut plane through the combustion chamber along with mixture fraction stoichiometric (black) and flammability limits (gray) iso-contours. Interaction of the flame kernel with the methane jet at PT1.

In an attempt to quantify the losses of reactive flame front due to inflammable mixture, the portion of flammable mixture in the preheat zone of the flame is tracked in time. The preheat zone is limited here as the region where $0.4 < c < 0.5$ and the preheated gases flammability indicator $\mathcal{I}_{PFI}$ is simply given by:

$$\mathcal{I}_{PFI} = \int_{z_{lean}}^{z_{rich}} P(z)\, dz \tag{7.12}$$

where $P(z)$ is computed on the grid nodes having $0.4 < c(n) < 0.5$. The temporal evolution of $\mathcal{I}_{PFI}$ is reported for both ignition failure and success at each ignition location in the top row of Fig. 7.25. In order to correlate the evolution of $\mathcal{I}_{PFI}$ with the growth of the kernel, the temporal evolution of the mean heat release is given on the bottom row of Fig. 7.25. At PT1, the kernel is triggered in a flammable mixture but $\mathcal{I}_{PFI}$ rapidly drops due to the convection toward the pure methane jet and this fall occurs sooner in the case of the failed ignition sequence so that the overall heat release is lower from the start. Both ignition sequences at PT2 are initiated in inflammable mixture and the hot gases kernel meet flammable mixture sooner for the failed ignition event resulting in higher overall heat release. After 0.3 ms, more than 80% of the temperature front meets flammable mixture for the successful case against less than 60% for the failed one so that the overall heat release evolution crosses. At PT3, more flammable fuel is initially available in the failed case but the opposite is found soon later and the heat release of the successful case swiftly grows. The flame growth in all these cases is also modulated by the other mechanism described below and $\mathcal{I}_{PFI}$ is only a first step to help distinguishing failed from successful ignition events.

- Flame kernel fragmentation

Under the effect of the large scale turbulence, the flame kernel is wrinkled and deformed. The particular effect of the PVC on the kernel structure will be studied in further detail in Sec. 7.4.3.c. As seen Fig. 7.20, the convection of the flame front is able to counteract the outward expansion of the flame kernel. Locally, flame fronts can be convected toward each others so as to be quenched by mutual annihilation and a burnt gases pocket is created in the process. This mechanism differs from the pocket formation captured in Poinsot *et al.* (1991) and studied in Chen & Im (1998) since it creates pockets of burnt gases in the fresh gases with back-to-back flame annihilation rather than pockets of fresh gases in the burnt gases with face-to-face flame annihilation.

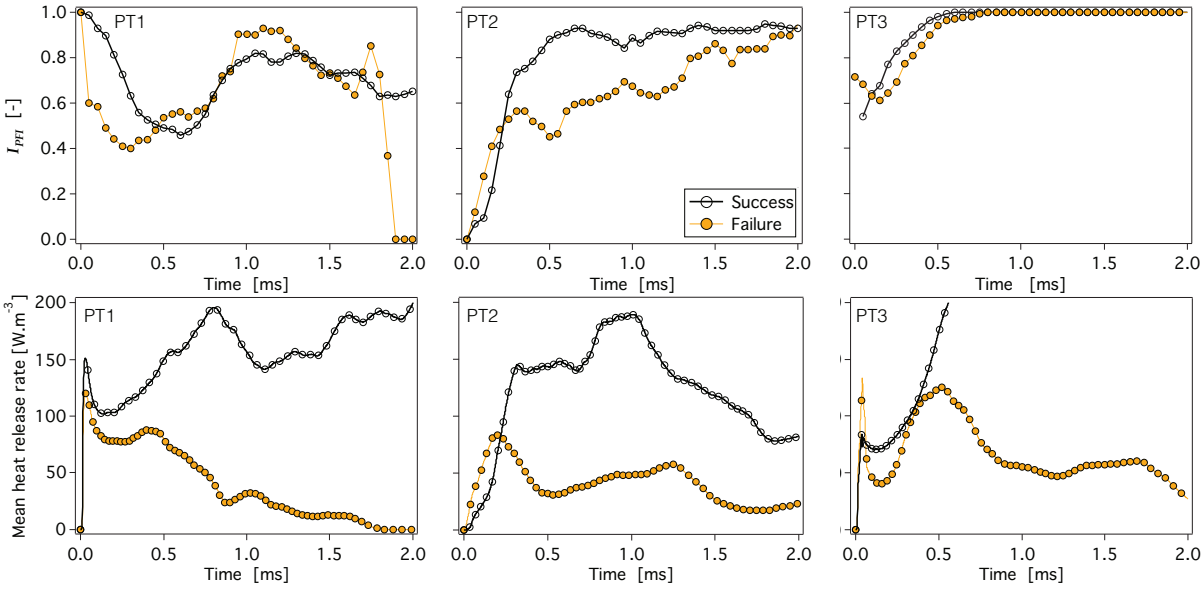

Figure 7.25: Temporal evolution of $\mathcal{I}_{PFI}$ (top row) and overall heat release (bottom row) for a failed and successful ignition event at each ignition location.

Examples of this behavior are illustrated for an ignition at PT3 in Fig. 7.26. The flame kernel is tracked by an iso-surface of temperature at 1700 K colored by the mixture fraction and vortices materialized using an iso-surface of the Q-criterion. Long vortical structures interact with the flame front and generate thin flame branches that are subsequently separated from the kernel bulk. These burnt gases pockets are then quenched since their rate of heat release is unable to counteract the diffusion rate to the surroundings.

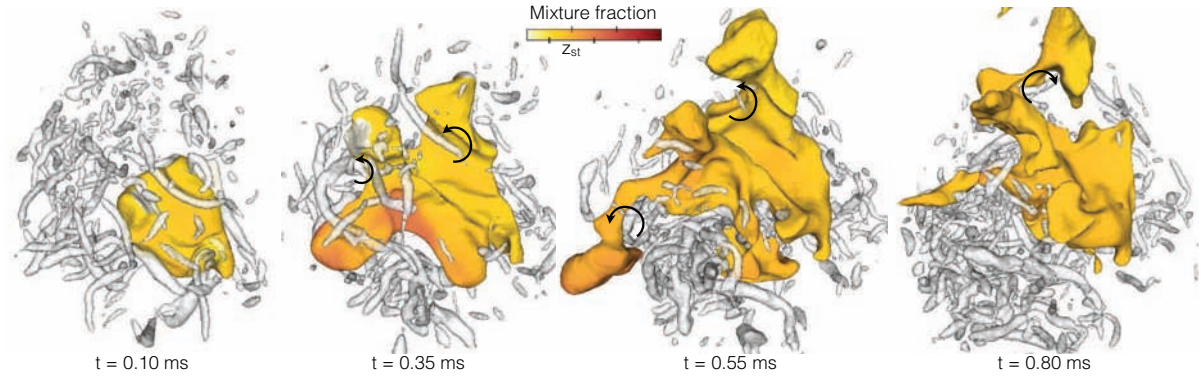

Figure 7.26: Instantaneous snapshots of the flame kernel tracked by an iso-surface of temperature at 1700 K and colored by the mixture fraction. Vortices are captured by an iso-surface of Q-criterion.

To globally quantify this mechanism, the temporal evolution of the shape ratio γ_r defined as the surface of the kernel over its volume is shown for a successful and a failed ignition event at each ignition locations in Fig. 7.27. To focus on the effect of the flame kernel shape only, the

selected cases are nearly free of quenching due to inflammable mixture. At each ignition location, γ_r is found to be higher in the failed ignition than in the successful cases indicating that the flame kernel surface is highly deformed and possibly fragmented.

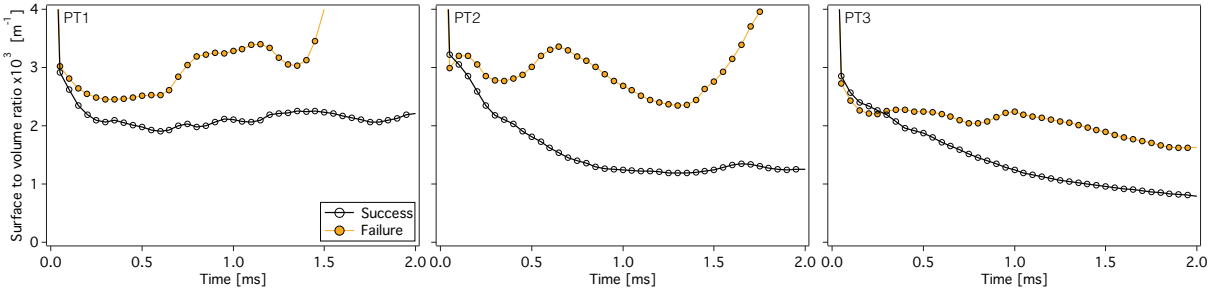

Figure 7.27: Temporal evolution of the shape ratio γ_r for a failed and successful ignition event at each ignition location.

- Flame quenching by stretch effect

As indicated from the turbulent velocity magnitude and length scale reported in Tab. 7.1, the flame/interaction of the present study lies in a region of the premixed turbulent combustion diagram where the flame front structure can be significantly modified by the small vortices of the flow. An illustration of the premixed flame front structure is given in Fig. 7.28 showing the heat release field and several iso-contours of progress variable. The preheat zone thickness (tracked here with $c = 0.2$ and $c = 0.4$ iso-contours) is found to vary from one point of the flame to the other, while the reactive layer thickness (tracked here with $c = 0.6$ and $c = 0.8$ and above) is found to be nearly constant. This confirms that the small vortices are locally able to penetrate the preheat layer inducing its thickening due to an enhanced diffusion process. Poinsot *et al.* (1991) point out that direct quenching of the flame front by stretch only occurs for very large stretch values unless the flame undergoes heat losses.

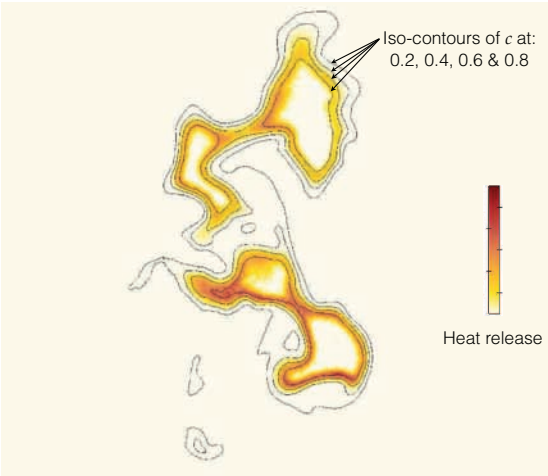

Figure 7.28: Cut through the flame kernel colored by heat release along with several iso-levels of c.

The PDF of S_d^* reported in Fig. 7.20 indicates a non-negligible proportion of negative displacement speed. DNS studies have shown that negative S_d does not pertain to the flame consumption rate but the propagation of a given c iso-level relative to the flow (Gran *et al.*, 1996; Chen & Im, 1998). This differential displacement of c iso-levels indicates a local modification of the flame thickness. To better illustrate that negative S_d corresponds to a thickening of the flame front, the conditional mean value of the flame surface density, which can be interpreted as the inverse of the flame thickness, is computed for both negative and positive regions of S_d and reported in Fig. 7.29(left).

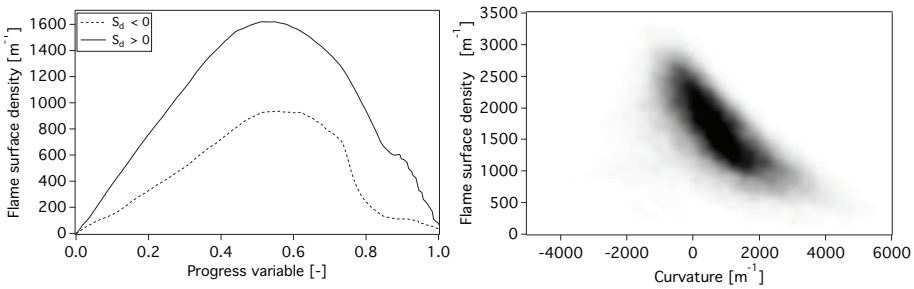

Figure 7.29: Conditional mean of the flame surface density conditioned on S_d positive and negative values regions.

The value of the flame surface density is found to be notably lower for negative S_d, indicating a thicker flame front as compared to the value conditioned on positive S_d. As demonstrated in Fig. 7.21, S_d^* is negatively correlated with curvature so that regions of high positive curvature are thicker and exhibits negative S_d^*. This correlation between curvature and flame thickness is also illustrated in Fig. 7.28 where the c iso-levels are more spaced in positive curvature regions and clearly visible from the joint-PDF of Σ versus $\mathcal{K}$ in Fig. 7.29(right). The thickening of the flame front denotes an imbalance of the reaction-diffusion processes within the flame front and can lead to local quenching of the flame front where heat is diffused away from the reaction zone faster than it is produced. S_d^* can then be used as an indicator of the flame thermal equilibrium with negative values of S_d^* denoting an imbalance and possible extinction of the flame front. The temporal evolution of the mean S_d^* in the $c = 0.25 \pm 0.1$ range for a failed and successful ignition event is plotted in Fig. 7.30 for each ignition location.

For failed ignition events, the flame displacement speed is found to drop below zero at least for a short period of time. Similarly to the consumption speed showed in Fig. 7.19, the local equivalence ratio induces lower S_d^* at PT1 and PT2 and more occurrence of negative values. The dependence of S_d^* is illustrated by the colorscale and confirm its negative correlation with curvature.

7.4.3.c Interactions of the flame kernel with the PVC

The present experimental set-up is the first dedicated to ignition where the swirl is sufficiently strong to observe a PVC. Due to the complexity of the configuration and the required diagnostics, the interaction of the PVC with the flame kernel during ignition was not investigated in the

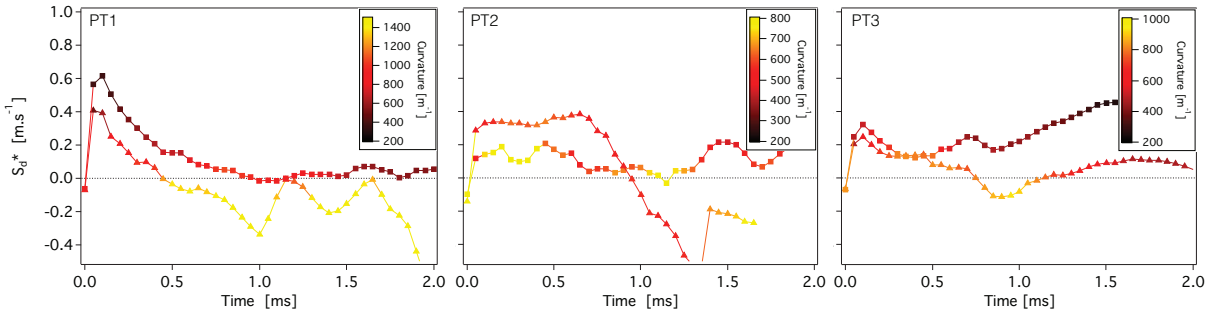

Figure 7.30: Temporal evolution of the mean S_d^* in the $c = 0.25 \pm 0.1$ range for a failed (triangle) and successful (square) ignition event at each ignition location. Markers are colored by the mean flame curvature in the same c range.

experiments. The LES observation reported in Sec. 6.3.6, indicates that the PVC is responsible for periodic fluctuations of the velocity, pressure and mixture field. This structure is particularly strong at the vicinity of the injector nozzle but rapidly degenerates downstream. To evaluate more precisely its interaction with the growing flame kernel, its dynamics is now further investigated.

PT2 is precisely located in the wake of the PVC and PT1 is nested between its two helical branches as depicted in Fig. 7.31.

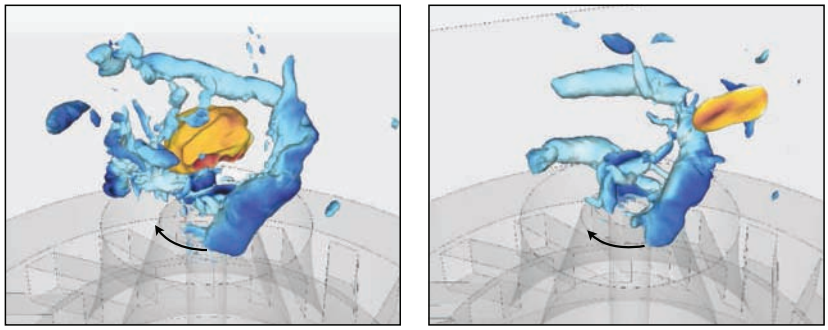

Figure 7.31: Instantaneous snapshot of the relative PVC/kernel positions at ignition time for PT1 (left) and PT2 (right). PVC is tracked by an iso-surface of pressure at $P = 101050\ Pa$ and the kernel by a $T = 1700\ K$ iso-surface.

As shown in Fig. 7.8 for PT1, the IRZ flow pushes the kernel toward the injector nozzle, where large portions of the flame front are quenched by the too rich mixture. The kernel is deflected from the injector axis but is also maintained outside of the PVC core due to its strong rotation so that it is convected between its helical branches. The kernel follows the winding pattern of the PVC as indicated in the top row of Fig. 7.32 and rotates along with the PVC, following the swirl direction. Later, the PVC is sufficiently strong to induce large scale deformation of the kernel and separate flame chunk from the bulk that are then quenched by the turbulence (see Fig. 7.32 bottom row). As the flame kernel gradually heats up the bottom of the IRZ, the PVC becomes

weaker and completely disappears during the second phase of ignition.

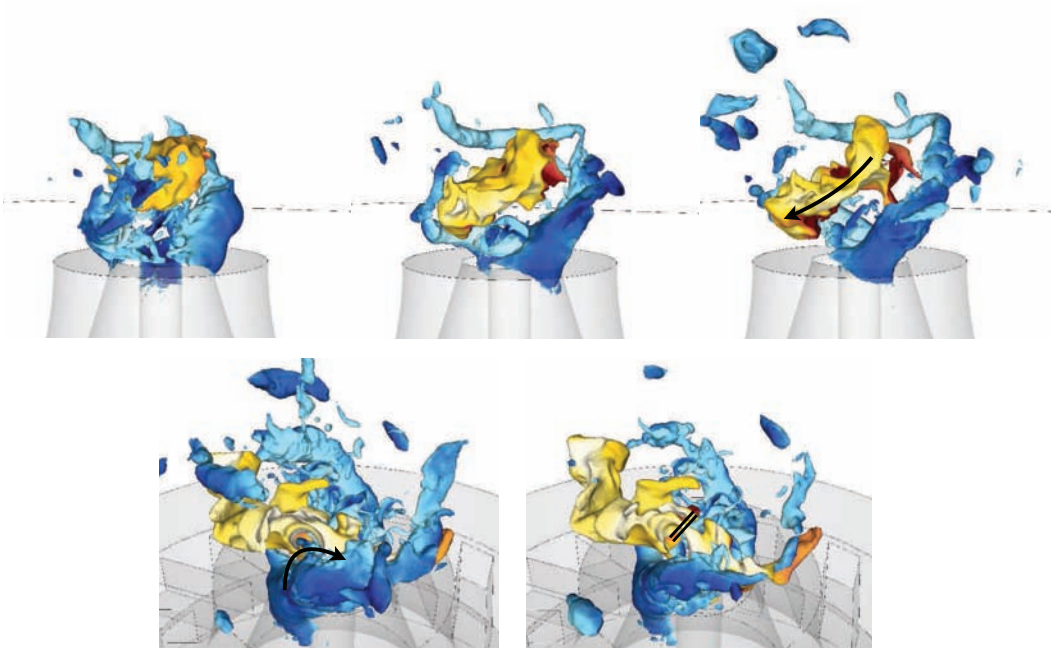

Figure 7.32: Instantaneous snapshots of the PVC/kernel interaction. Top row: winding of the kernel between the PVC branches. Bottom row: large scale deformation of the kernel. The PVC is tracked by an iso-surface of pressure at $P = 101050\ Pa$ and the kernel by a $T = 1700\ K$ iso-surface.

At PT2, the interaction between the flame kernel and the PVC depends on the delay between the energy deposit and the passage of the PVC at the spark location. From the 20 ignition sequences computed, general trends are identified but the number of samples conditioned on the PVC phase is too small to draw a clearer correlation between the PVC passages and the ignition probability. If the PVC passes at the spark position later than 0.6 ms after energy deposit, the kernel as sufficiently grown and undergoes large scale deformation without overall quenching (see top row of Fig. 7.33). When the PVC passes at the spark position within the 0.3 ms following energy deposit, the kernel is rapidly destroyed by the coherent structure and the remaining flame fragments are too small to result in a successful ignition (see bottom row of Fig. 7.33).

7.4.4 Indicators affecting ignition outcome

Having identified the main mechanisms leading to either success or failure of ignition, the aim now is to construct indicators that can be used to distinguish success from failure. Failure of initiating a sustainable flame kernel is expected to be related to the flow properties at the spark location and timing but the quenching at later time has been shown to result from the combination of several mechanisms simultaneously or subsequently during the kernel development. Then, the pointwise or space averaged flow characteristics at the spark timing are first used to recover P_{ker}. Then temporal average indicators are computed to identify the subsequently quenching events.

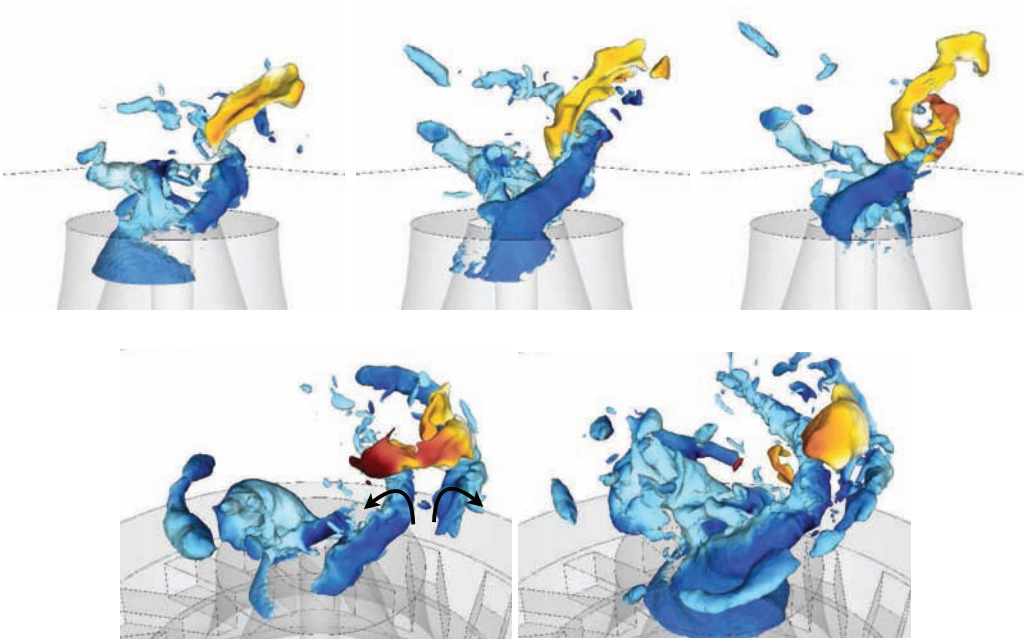

Figure 7.33: Instantaneous snapshots of the PVC/kernel interaction. Top row: winding of the kernel between the PVC branches. Bottom row: large scale deformation of the kernel. The PVC is tracked by an iso-surface of pressure at $P = 101050\ Pa$ and the kernel by a $T = 1700\ K$ iso-surface.

7.4.4.a Initial flow properties at t_0

In a first attempt to discriminate deposits that failed to create a flame kernel, the time history of mixture fraction and velocities have been recorded at the energy deposit locations and are reported in Fig. 7.34. The vertical lines show the timing of a series of ignition LES and differentiate between late failure (red, dashed lines), kernel initiation failure (brown, dotted-dashed) and success (yellow, dotted lines). Subramanian *et al.* (2010) provided similar data for a bluff-body configuration but the magnitude of the velocity fluctuations was much lower than reported here, therefore less detrimental to the kernel survival. At PT1, the axial velocity is found to be globally negative (toward the nozzle) and the mixture fraction above the rich flammability at first, then still rich but flammable later. For PT2, the mixture fraction varies from pure air to rich mixture as also supported by the PDF shown in Fig. 7.16. The axial velocity is alternatively positive and negative with strong fluctuations. At PT3, the mixture fraction stays low with smaller fluctuations as compared to the other locations and the axial velocity is mostly positive with strong fluctuations. For all ignition locations, mixed successful and failed ignition events are found and there is no evident correlation between the pointwise non-reacting flow characteristics and the capability of creating a sustainable flame kernel or ensure its survival, as was also observed by Cordier (2013).

A better indicator can be constructed using spatial distribution around the ignition location rather than pointwise data. The flammability factor F_f is estimated from the cold flow LES at the ignition timing following Cardin (2013). Note that in this case, F_f represents the portion of the

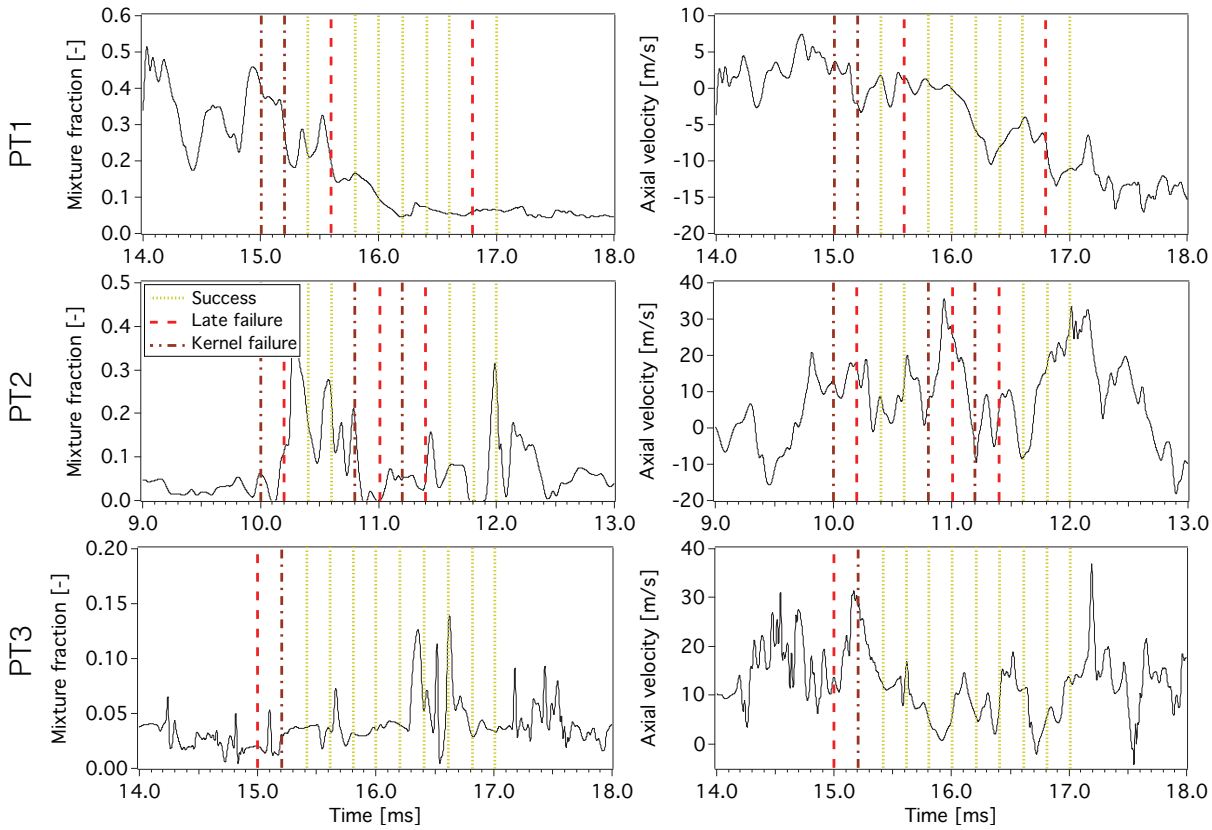

Figure 7.34: Temporal evolution of mixture fraction (left) and axial velocity (right) during non-reacting simulation. Vertical lines correspond to several ignition timing: green dotted line indicates ignition success while red dot-dashed line indicates failure.

spark surroundings that contains flammable mixture. To compute F_f, the PDF of z is constructed in two spherical volumes with different radius around the sparking location at the deposit time. The results are presented in Fig. 7.35for locations PT1, PT2 and PT3 for a spherical volume of radius 1.5 mm (top row) and 2.5 mm (bottom row) respectively. the first volume is about the size of the initial kernel, while the 2.5 mm sphere is larger. The x-axis is the flammability factor while y-axis is the mean mixture fraction in the same spherical domain. Markers are colored depending on the outcome of the ignition event.

At each ignition location, the results show some separation between ignition success and failure. However, the separating line changes from one ignition location to the other and depends on the size of the averaging volume. For PT1, F_f is negatively correlated with the mean mixture fraction and failure of the kernel generation is captured for very low F_f (high $\overline{z}$). As the averaging volume increases, the same trend is observed, but the separation moves toward higher F_f due to the proximity of the rich but flammable IRZ. At PT2, both too lean and too rich mixtures induce low values of F_f but failure is only observed for overall rich mixtures. A clear limit in terms of F_f is not found using the 1.5 mm averaging volume, but it becomes evident for the larger volume. Since PT2 is located in the shear layer, the kernel can rapidly switch from a lean to a rich mixture (or the opposite) and the larger averaging volume allows to better encompass this aspect.

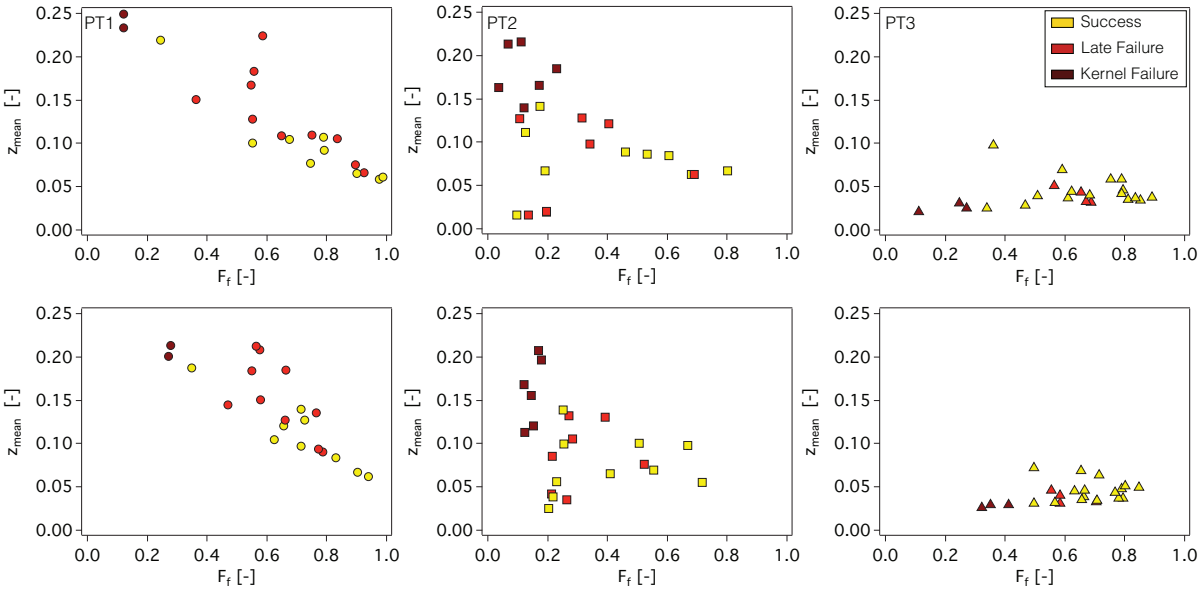

Figure 7.35: Flammability factor $F_f/\overline{z}$ maps colored by the ignition outcome. F_f and $\overline{z}$ are computed in spatial volumes of two sizes (top: 1.5 mm radius, bottom: 2.5 mm radius) around the ignition location at the sparking time.

Finally, values at PT3 do not exhibit a strong separation in terms of $\overline{z}$ but F_f clearly points out a boundary between the failed and successful kernel initiation regions. Although F_f seems to be a good candidate to identify ignition success or failure no threshold value can be determined since it is dependent on the averaging volume size, i.e. the local flow time scale. Finally, Fig. 7.35 also clearly shows that local mixture properties are not able to anticipate the kernel failure at longer time since success and late failure are mixed for all sparking locations.

7.4.4.b Flame/turbulence indicators

To identify indicators that could anticipate kernel quenching, the time history of the flame characteristics are recorded during the flame kernel growth for all simulations where a flame kernel has successfully been initiated. To be consistent with the analysis performed in Sec. 7.4.3, data are restricted and averaged on the $c = 0.25 \pm 0.1$ range located in the preheat zone of the flame. Finally, to provide general trends in a compact way the data are time-averaged over the kernel life time. The time and space averaged values of curvature, S_d^* and tangential strain rate are plotted against mixture fraction for all events that have successfully initiated a flame kernel. Markers are colored by the ignition outcome: yellow denotes success while black indicates failure. The trend described in Sec. 7.4.3.b also appears here with a clear distinction in terms of curvature or S_d^*: the probability of ignition success is strong for low values of curvature and rapidly decreases as the mean curvature exceeds $\simeq 600\ m^{-1}$. Ignition at PT1 (triangles) have $\overline{z}$ above the rich flammability limit and higher values of critical curvature. Consistently with the negative correlation between curvature S_d^*: low values of S_d^* preclude ignition success while the probability of

success increases with higher values of S_d^*. No correlation is found between the tangential strain rate and the ignition success.

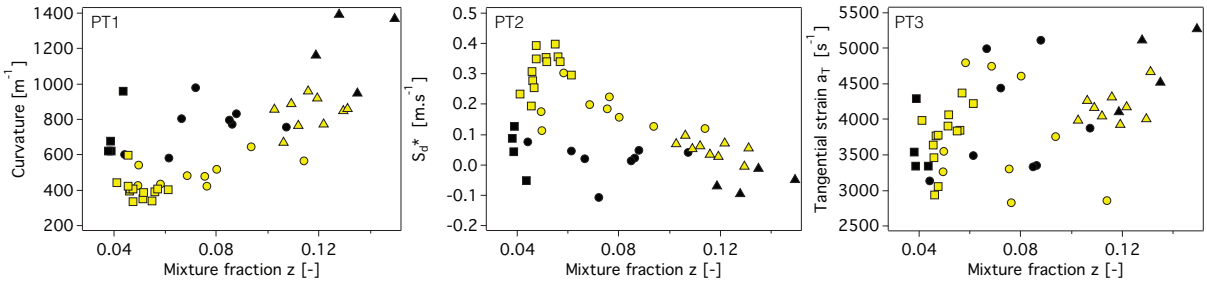

Figure 7.36: κ-$\overline{z}$, S_d^*-$\overline{z}$ and a_T-$\overline{z}$ maps of spatio-temporal mean values for all ignition events colored by the ignition outcome (yellow: success, black: failure). PT1: triangles, PT2: circle and PT3: square.

7.5 Conclusions

Series of LES of ignition sequences in the highly swirled partially premixed KIAI burner have been performed to reveal physical and statistical aspects of the ignition process in complex flow configurations. With respect to previous LES burner studies or DNS kernel expansion simulations, the present configuration makes a step towards gas turbine conditions. Several conclusions can be drawn:

- LES ignition sequences are in good agreement with experiments in terms of flame kernel bulk motion and ignition scenario demonstrating that LES is able to reproduce the driving mechanisms of ignition. At the three ignition locations studied, LES is able to reproduce quantitatively the ignition probability, proving its capability to capture the stochastic nature of the ignition process.
- Flame kernel trajectories are constructed and demonstrate the high variability resulting from the variability of the initial velocity field. There is however no evident correlation between ignition success or failure and the kernel trajectory or its ability to enter recirculation zones (at least at the three locations studied).
- The kernel expansion is found to be highly non-monotonic due to significant flame quenching. Several quenching mechanisms are highlighted: 1) the partial premixing can directly preclude the formation of a flame kernel or quench large chunks of the flame front due to pockets of inflammable mixture; 2) the large scale turbulence induces global deformation of the flame kernel leading to flame-flame interactions and thermal quenching of small burning gases pockets; 3) the flame structure is altered by the turbulence which can significantly lower or even prevent the flame propagation.
- In highly swirled configurations, the presence of a PVC in the region where the flame stabilizes (namely the IRZ) affects the kernel growth if its size is of the order of the PVC structure.

- The probability of creating of sustainable flame kernel is found to be related to the fuel distribution around the spark location at the ignition time rather than to pointwise flow quantities. This is consistent with the previous observation of Cardin (2013) and Cordier (2013).

Chapter 8

Model for prediction of ignition probability

Contents

8.1 Ignition probability models: literature review 132
8.1.1 Pointwise flow characteristics models 132
8.1.2 Trajectory based models 134
8.1.3 Conclusions 137
8.2 Derivation of the model 137
8.2.1 Overview of the model 137
8.2.2 Prediction of the kernel probability of presence 138
8.2.3 Statistical indicators for kernel quenching 147
8.2.4 Combination of both statistics 153
8.3 Results 155
8.3.1 Premixed case 156
8.3.2 Non-premixed case 158
8.4 Conclusions 159

As demonstrated in the previous chapter, LES is able to predict quantitatively the ignition probability. However, the computational cost remains expensive and faster practical tools have been developed for the optimization of combustion chamber. Such methods have been developed in order to predict the ignition probability from the non-reacting flow properties and the empirical knowledge of the ignition process observed from both experiments and numerical simulations. The objective here is to develop a new model capable of easily estimating the ignition probability based on non-reacting LES flow taking into account the kernel displacement during the early stages of its development. The late flame propagation and stabilization to the injector nozzle are not targeted by the model.

At first, a review of the various methods found in the literature is presented and their limitations are highlighted. Secondly, the derivation of the new model is detailed and validated when

possible against numerical data extracted from LES. Finally, the results obtained on the KIAI single injector burner in both premixed and non-premixed modes are presented.

8.1 Ignition probability models: literature review

The various ignition probability models presented in the literature can be split in two classes: models based on local properties of the non-reacting flow and models tracking the spatio-temporal evolution of the kernel. From the literature review presented in Chap. 5, one can relate the first class of models to the prediction of kernel generation P_{ker} while the second focuses on the whole ignition probability P_{ign}.

8.1.1 Pointwise flow characteristics models

The first attempt to correlate the ignition probability to non-reacting flow properties has been performed by Birch *et al.* (1977), Birch *et al.* (1981) and Smith *et al.* (1986) in the case of a free methane jet. As mentioned previously (see Sec. 5.1.2), these studies demonstrated the correlation between the flammability factor F_f and the probability of successfully creating a flame kernel P_{ker}. F_f is defined as the local probability of finding a flammable mixture at a given location:

$$F_f = \int_{z_{lean}}^{z_{rich}} P(z)dz \tag{8.1}$$

where $P(z)$ is the PDF of mixture fraction z and z_{lean} and z_{rich} are the lower and upper flammability limits, respectively. The simplicity of the free jet case allowed to go further and Smith *et al.* (1986) constructed a composite formula in order to evaluate $P(z)$ from the first two statistical moments of the measurements. The formula of $P(z)$ is based on the work of Bilger *et al.* (1976) and Kent & Bilger (1977) where experiments showed that $P(z)$ can be constructed from a Dirac delta function and a Gaussian distribution such as:

$$P(z)_c = (1-\gamma)\delta(z-\overline{z}) + \gamma\frac{1}{\sqrt{2\pi}\,z'}\exp^{-\frac{(z-\overline{z})^2}{2z'^2}} \tag{8.2}$$

where $\overline{z}$ and z' are the mean and RMS values of mixture fraction respectively, $\delta(x)$ the Dirac delta function and γ the intermittency factor. Using Eq. (8.1) and Eq. (8.2), the flammability factor is evaluated by:

$$F_{f,c} = \gamma\frac{1}{2}\left[\mathrm{erf}\left(\frac{z_{rich}-\overline{z}}{\sqrt{2}\,z'}\right) - \mathrm{erf}\left(\frac{z_{lean}-\overline{z}}{\sqrt{2}\,z'}\right)\right] + (1-\gamma)\delta_z \tag{8.3}$$

with

$$\delta_z = \begin{cases} 1 & \text{if } z_{lean} < \overline{z} < z_{rich} \\ 0 & \text{otherwise} \end{cases} \tag{8.4}$$

This work was recently continued by Schefer *et al.* (2011) for both methane and hydrogen free jets and the results also showed a good agreement of the reconstructed $F_{f,c}$ with P_{ker}. The range

of position along the jet centerline where overall ignition is possible was found to narrow as the jet velocity is increased.

Although these experiments have brought fundamental understanding of the relation between non-reacting flow quantities and ignition probability, they are restricted to simple configurations with limited practical interest for realistic gas turbine ignition. Recently, Eyssartier *et al.* (2013) developed a methodology called I-CRIT-LES to predict ignition probability in complex configurations. Compared to the study mentioned above, this method encompasses the effect of the spark deposit properties, the possible presence of fuel droplets, quenching near walls and the mean velocity at the sparking location. The ignition is successful if the energy deposit validates a series of criteria defined as:

- **C1**: local mixture equivalence ratio in the flammability range
- **C2**: power input is sufficient to initiate the chemical reactions
- **C3**: in two-phase flow, the balance between fuel chemical consumption and evaporation must be in favor of evaporation
- **C4**: the kernel is not quenched at the walls
- **C5**: upstream flame propagation is possible

These criteria are evaluated from the combination of several independent snapshots (typically 50 to 100), enabling to construct an ignition probability at each LES grid point and identify the limiting parameter. The model was applied to the two-phase flow MERCATO academic test bench and showed a fairly good agreement with experimental results. The limitation induced by the local formulation of the ignition probability were also highlighted and the model failed in regions where convective effects were dominant.

A similar approach has been developed at ONERA by Linassier (2012) specifically for two-phase flows, with three criteria:

- **Criterion 1**: ignition of the droplet mist
- **Criterion 2**: laminar growth of the kernel
- **Criterion 3**: upstream flame propagation

Once again, the objective is to use local quantities extracted from RANS or LES simulations. The laminar growth of the kernel was computed with the 1D spherical model developed by Garcia-Rosa *et al.* (2011). The model was also applied to the MERCATO bench and the results are coherent with experiments. As compared to the results of Eyssartier *et al.* (2013), this model was able to predict the ignition failure in the central recirculation zone due to a more stringent criterion on the droplet mist ignition and kernel growth.

These models based on local quantities extracted from experiments or RANS/LES simulations have been proven relevant to predict P_{ker} even though events such as described in the previous

section, where the kernel is convected from non flammable toward flammable mixture, are not captured. However, these models proved deficient by themselves to predict the subsequent flame propagation and overall ignition probability. This motivated the development of models able to take into account the history of the kernel.

8.1.2 Trajectory based models

The first attempt to evaluate the ignitability of a combustor from the non-reacting flow by tracking of the flame kernel was reported in Wilson *et al.* (1999) where the authors proposed a post-processing technique of RANS solutions. The local value of the Karlovitz stretch factor (Abdel-Gayed & Bradley, 1989) was evaluated on the CFD solution and the kernel trajectory was followed by a conserved scalar method. The temporal evolution of the kernel's fraction experiencing Karlovitz below the quenching limits of Abdel-Gayed *et al.* (1987) was computed and used to estimate the ignition performance. This simple approach was found to reproduce qualitatively the effect of the igniter position and air mass flow rate on ignition performance, but no further validation was available.

The next attempt was reported in the work of Richardson *et al.* (2007) based on RANS simulations in a simpler configuration. Inspired by the ATKIM model (Duclos & Colin, 2001), a Lagrangian particle based flame tracking approach was adopted. The model was developed and validated on the experimental configuration of Ahmed & Mastorakos (2006) and applied to several academic configurations as well as a more realistic combustor designs.

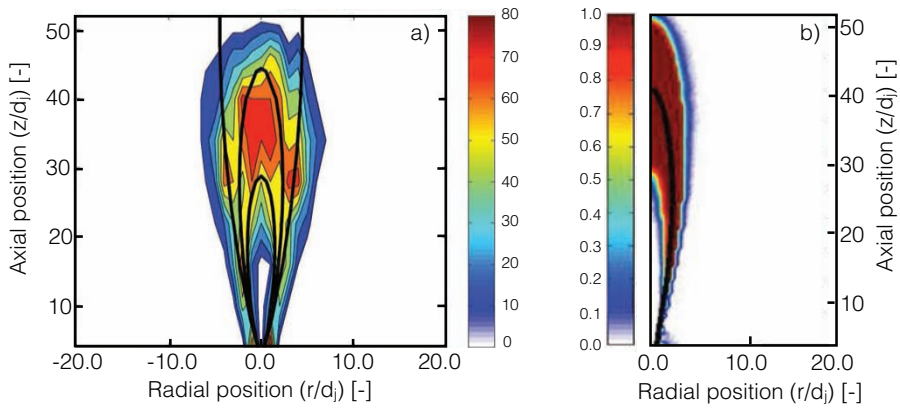

Figure 8.1: Experimental ignition map of Ahmed & Mastorakos (2006) (a) versus spark effectiveness (b). Extracted from Richardson *et al.* (2007).

The flame propagation was modeled with either a turbulent premixed combustion or an edge flame correlation depending on the local value of the Edge Flame Index (EFI). The EFI is defined as the product of the probability of finding a rich and a lean mixture fraction at a given location. Its value is maximum where the probability of finding a lean mixture equates that of finding a rich one for which edge flame propagation is used. As one probability becomes dominant, the EFI goes to zero and a premixed combustion regime is considered. A thermal memory effect is included so

that flame particles are not instantaneously quenched when going through an inflammable region. The particle turbulent convection is treated with a simplified Langevin model with a stochastic Wiener increment to represent the stochasticity of each velocity realization. The particles velocity is the combination of the stochastic convection velocity and the flame velocity. A flame particle is deemed successful if it enters an upstream propagation region before its temperature falls below a critical value. At the beginning of the computation, numerous flame particles are placed at the ignition location and the proportion of successful particles is called spark effectiveness. This model was able to recover the contours of ignition probability in the methane free jet of Ahmed & Mastorakos (2006) even though some discrepancies were found, as shown in Fig. 8.1.

A similar concept was used by Weckering *et al.* (2011) in order to evaluate the probability of upstream flame propagation in a free methane jet in a LES framework. Once again, the model was validated on the methane free jet configuration of Ahmed & Mastorakos (2006). The model uses Lagrangian tracking of individual sparking events, and based on experimental evidence, the pointwise Lagrangian particles are replaced by a 35 mm flame kernel after 10 ms. Based on the intersection between the kernel surface and the region where upstream flame propagation is possible, ignition statistics are constructed with the use of the flammability factor at the sparking location. Although the trends given by this model were found in agreement with experiments, the model results were strongly conditioned by user-defined parameters (such as the upstream flame propagation region definition). Similarly to Richardson *et al.* (2007), no quenching mechanisms were included in the model.

The SPINTHIR model proposed by Neophytou *et al.* (2012) aimed at the prediction of the process of flame expansion and overall flame propagation in the combustion chamber. The model was composed of several steps, some of them being derived from the work of Richardson *et al.* (2007). Starting from a time-averaged CFD solution:

- the computational domain is filled with regular grid cells whose state is either cold or burnt
- ignition is modeled by defining an initial spark volume and the cells within this volume are switched to burnt state and release a flame particle
- flame particles are tracked by a stochastic Langevin model based on the CFD solution statistics and can extinguish on the basis of a Karlovitz number criteria. As a flame particle enters a cold state cell, its state is switched and another particle is emitted.
- the ratio of the burnt volume to the total volume of the regular grid π_{ign} is tracked in time and at the end of the simulation compared to a critical value $\pi_{ign,crit}$ that determines whether the ignition try is a success or a failure.
- the probability is evaluated from multiple computations and repeated at several ignition locations to obtain a probability map.

The model was found to reproduce fairly well the ignition maps of several configurations (bluff-body methane burner of Ahmed *et al.* (2007*a*), spray burner of Marchione *et al.* (2009) or counterflow configuration of Ahmed *et al.* (2007*b*)) even though the estimation of P_{ign} was found to strongly depend on $\pi_{ign,crit}$ and to be sensitive to the regular grid resolution and the number of ignition tries. One issue of the model comes from the construction of the ignition probability: a

Monte-Carlo like method is used and a very large number of individual ignition event must be computed to ensure convergency of the result. This could significantly increase the computational cost of the methodology. Another issue is linked to the prediction of the late flame propagation when the flow field can significantly differ from the non-reacting CFD solution due to flame effects. Nonetheless, the model can be used for a quick and cheap estimation of ignition performances. The SPINTHIR model was improved in Soworka *et al.* (2014) by including stochasticity to the local value of the Karlovitz number and introducing history effects on flame particles: a particle entering an inflammable cell is not instantaneously extinguished but changed to *hot gas* state from which it can either return to *burning* state if flammable mixture is encountered again within the next few instants, or extinguish otherwise. The modified model was applied to a lean burn configuration at high altitude conditions and predicted with moderate accuracy the lean ignition limit obtained experimentally for two different designs.

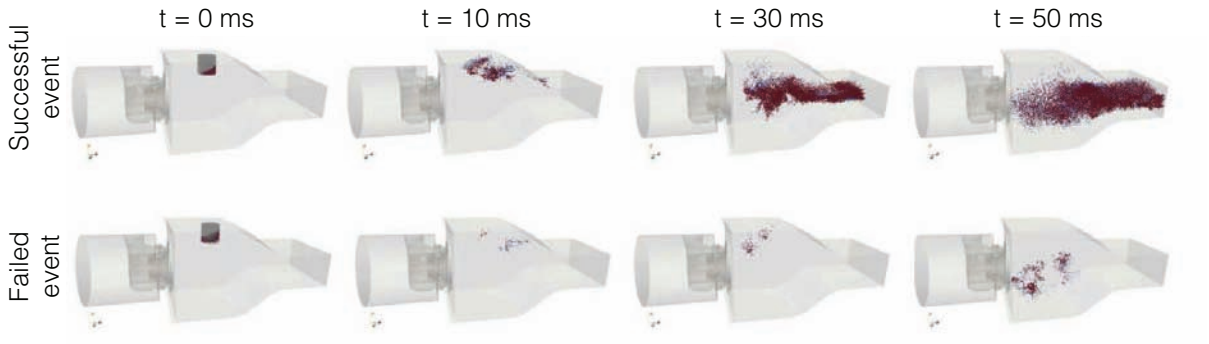

Figure 8.2: Successful and failed ignition events captured with SPINTHIR on a lean burn combustor. Extracted from Soworka *et al.* (2014).

Finally, Cordier *et al.* (2013*b*) developed a model based on the same philosophy as SPINTHIR to evaluate the ignition performance of the single injector KIAI burner using experimental data. The model tracks flame particles emitted from the ignition location using a simplified Langevin equation, and the stochasticity of the non-reacting velocity field is included through a random draw of the field in the experimental database. Each particle represents a flame kernel whose growth is computed based on literature correlations and can be divided in two separate particles if its size exceeds the local value of the integral length scale. Quenching of flame particles is incorporated using a critical Karlovitz number criterion. Ignition success is conditioned on both the number of particles and their location at the end of the simulation. The model was able to reproduce some of the main features of the experimental probability map and ignition scenario but locally deviated from experiments in regions of intense turbulence. Since the ignition probability is constructed with the same methodology as the SPINTHIR model, it also suffers from the issue regarding the number of individual ignition events required to ensure the convergence of the Monte-Carlo method.

8.1.3 Conclusions

As demonstrated in this short review, models based solely on local flow characteristics are computationally very cheap and provide insight on the spark performances but appear to be inadequate to capture ignition failure occurring later during the kernel phase. On the other hand, tracking based models encompass the kernel transport effects but do not focus specifically on kernel quenching and suffer from convergence issue.

In the following, a new model is derived with the objective of taking advantage of both aforementioned approaches: the low CPU cost of pointwise model is kept in a new approach combining it to transport effects through an evaluation of a statistics of the kernel trajectories.

8.2 Derivation of the model

The objective is here to develop a model capable of predicting the ignition probability from non-reacting flow statistics. As compared to the previous model I_CRIT_LES developed at CERFACS (Eyssartier *et al.*, 2013), the aim is to incorporate some of the time history effects. This point cad indeed the main weakness of the I_CRIT_LES methodology, and its importance was highlighted in the fully resolved LES ignition sequences performed in Chap. 7. Driven by the increasing computational power, the number of elements of the LES meshes used for industrial studies increases leading to a growth of the memory requirements. Thus, to simplify the application of the present model, one constraint is to only use time-averaged CFD fields to estimate the ignition probability.

8.2.1 Overview of the model

The model focuses on the prediction of the ignition probability at the end of the kernel expansion phase, thus evaluating the probability of success of **Phase 1** and of the beginning of **Phase 2**. This choices is motivated the LES results presented in Chap. 7 where most of the failures occured within the first 5 ms after energy deposit. The kernel quenching was the consequence of two mechanisms: 1) inflammable mixture pockets could locally quench the flame front or even prevent the kernel formation, 2) kernel/turbulence interactions could lead to large scale deformations of the kernel and induce flame/flame interactions and flame front stretching. Thus, to construct the ignition probability, two elements are combined as schemed in Fig. 8.3:

- a statistic of the kernel motion is evaluated by constructing the temporal evolution of the kernel presence probability density function $P_{pres}(\boldsymbol{x}, t)$.
- statistics of the non-reacting flow characteristics are evaluated at each grid point to encompass possible quenching of the flame kernel.

Both statistical information are then combined to provide an estimation of the ignition probability.

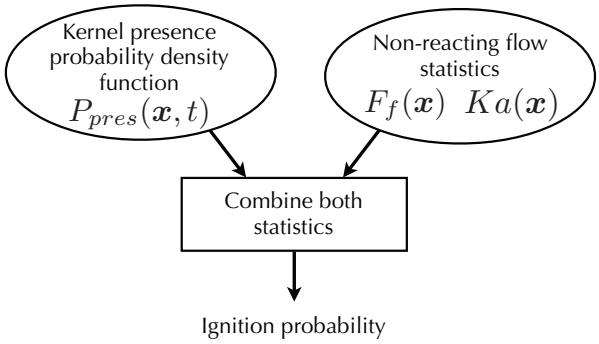

Figure 8.3: Overview of the model elements.

More precisely, the algorithm of the model is described by the following steps:

- Perform a non-reacting CFD simulation to obtain time-averaged fields (velocity, mixture fraction).
- Compute statistical indicators required to evaluate the local occurrence of quenching, from non-reacting flow statistics
- Use the spark characteristics to evaluate the kernel size and the time required to drop from the high temperature of the kernel to the adiabatic flame temperature. This step is performed in 0D assuming that the kernel temperature is only dictated by the balance between reaction rate and turbulent dissipation.
- Compute the temporal evolution of the kernel, by constructing its probability of presence combined to the indicators of step 2. The kernel growth is also computed, and if the kernel size is beyond a critical value, the kernel is considered to successfully ignite the burner since local quenching can no longer result in global quenching.

8.2.2 Prediction of the kernel probability of presence

In contrast with previous models using Lagrangian tracking of individual kernels (Neophytou *et al.*, 2012; Cordier, 2013), the present model intends to track the kernel displacement through its presence PDF $P_{pres}(\boldsymbol{x}, t)$. The main idea is to use the cold flow statistics to reconstruct kernel trajectories statistics, rather than recalculating numerous individual trajectories. At first, the validity of the hypothesis required to construct $P_{pres}(\boldsymbol{x}, t)$ are evaluated in Sec. 8.2.2.a. Then, details of the construction of $P_{pres}(\boldsymbol{x}, t)$ are presented in Sec. 8.2.2.b and the results are partially validated in Sec. 8.2.2.c.

8.2.2.a Evaluation of the hypothesis validity

To construct the kernel probability of presence, three hypotheses have been made:

- **H1**: the velocity components follow a Gaussian distribution.
- **H2**: the statistics of the non-reacting flow (mean and fluctuations) are not modified during the first milliseconds after energy deposit.
- **H3**: the self-propagating velocity of the flame is low compared to the total flame velocity (using notation introduced in Sec. 3.2.1.b: $S_a > S_d$)

The validity and limitations of these hypotheses are evaluated using the LES results. **H3** has already been evaluated in Sec. 7.4.2.b where the PDF of flame displacement speed S_d has been shown to be much smaller than the absolute flame velocity S_a.

H1: Velocity components Gaussian distribution

The first assumption necessary to derive a model predicting the kernel presence PDF is that the velocity components follow a Gaussian distribution. Although this assumption is perfectly true from a turbulence point of view (Pope, 2000), it is often made when deriving models. To evaluate the validity of this assumption in the present case, PDF of velocity components are constructed from temporal recording at numerous locations in the computational domain of the LES. The data are recorded during 100 ms corresponding to more than 25 rotations of the PVC. An example of obtained distributions is shown in Fig. 8.4 along with the corresponding Gaussian distribution.

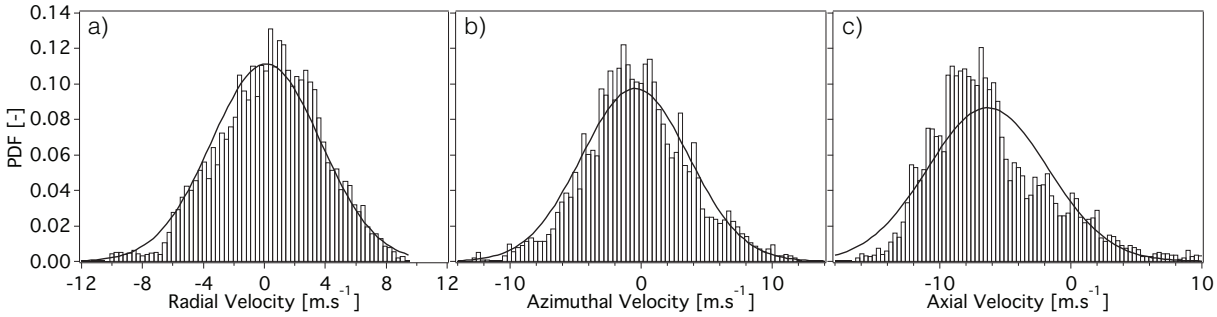

Figure 8.4: PDF of the three velocity components at $z/D_{ext} = 0.5$ and $x/D_{ext} = 0.0$ along with the Gaussian distribution (lines).

For this particular position, the Gaussian assumption seems to be valid for radial and azimuthal velocity components but the axial component exhibits a significant positive skewness, of factor $\gamma_1 = 0.89$. This skewness factor, which can be viewed as a measure of the deviation to Gaussian distribution, is mapped from 1326 probes on Fig. 8.5.

The results show that, departure from a Gaussian distribution can be locally significant. The radial velocity component exhibits strong positive skewness factor in the CRZ while the axial velocity skewness is significant in the IRZ. However, for the largest part of the map, the skewness factor stays in the [-1,1] range for which a Gaussian approximation is reasonable for the level accuracy desired for the approach.

H2: Kernel effect on the velocity field

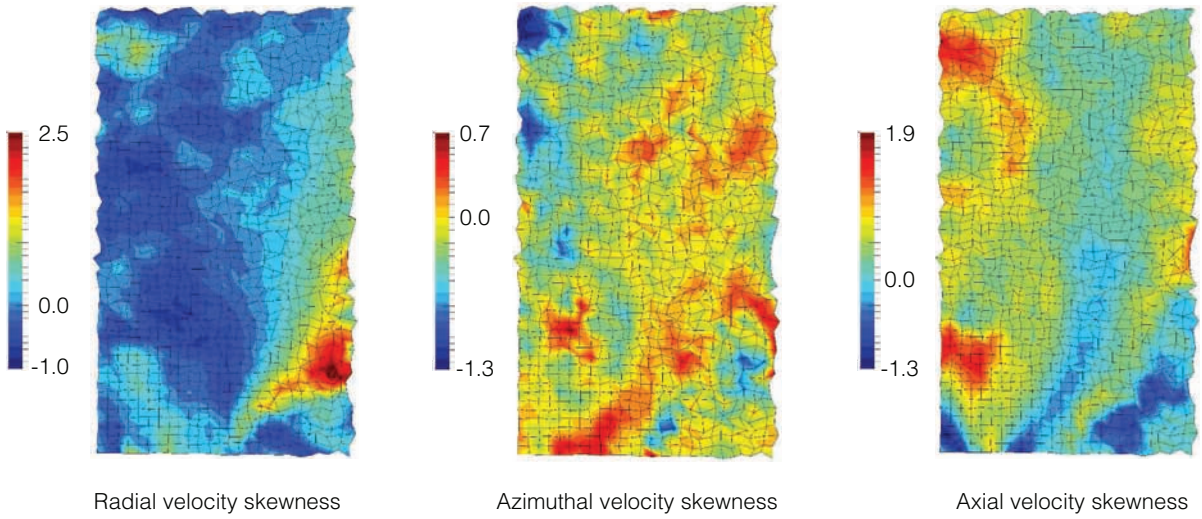

Figure 8.5: Map of skewness factor γ_1 for the three components of velocity in a y-normal cut plane through the center of the combustion chamber.

It is assumed that during the early instants after energy deposit, the statistics of velocity are not greatly modified in the region where the kernel develop and stay those of the cold flow. This assumption is expected to be inadequate at longer times due to the modification of the fresh gases aerodynamics induced by the kernel expansion.

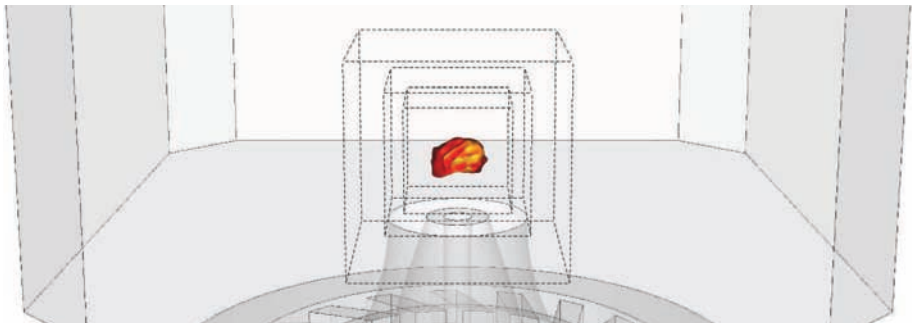

Figure 8.6: Sampling boxes for the construction of spatial distribution of velocity for ignition at PT1.

To estimate the limits of this assumption, three cubic boxes of increasing size centered at the energy deposit location are defined ($c = 1.5$, 2 and 3 cm). An example of these boxes for ignition at PT1 is shown in Fig. 8.6. The grid vertices located in these boxes are then used to build the spatial PDF of the velocity components. The small box is sufficient to evaluate the effect of the kernel during the early instants after energy deposit, but kernel growth and displacement might bring the kernel out of the box. On the contrary, the kernel stays within the limits of the larger box during its entire growth, but the large number of sample points masks the changes in the PDF shape. All three boxes are tested here to highlight the effect of the sample size on the PDF evolution in time.

In order to take into account the flow unsteadiness, several instantaneous solution of the non-reacting flow are employed. The PDF is then computed at several instants after energy deposit during the kernel growth. An example of the results is presented in Fig. 8.7 for an ignition sequence at PT1 for the z-axis and the x-axis velocity components (note that in this case, the PDF of the x-axis and the y-axis components are the same). The grey zone corresponds to the inert flow envelope (mean $\pm$ RMS) and the PDF at four instants are plotted. Prior to $t = 2.2\ ms$ the PDF lies within the grey region but the PDF gradually shifts as time proceeds.

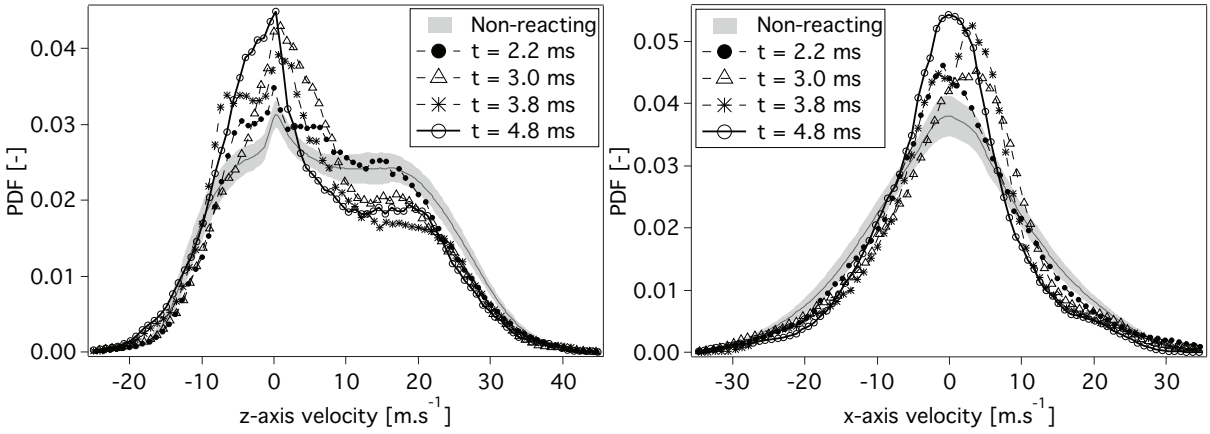

Figure 8.7: Comparison of axial (left) and radial (right) velocity components PDF between non-reacting (grey area) and ignited cases at several instants after ignition at PT1 using the intermediate 2 cm square box. The full line is the mean non-reacting flow PDF.

The effect of the box size is illustrated in Fig. 8.8 where the PDF of z-axis velocity component at PT1 is plotted for the three boxes. For the larger box, the number of nodes is so high that the PDF is barely affected by the kernel growth even after long times. On the other hand, the small box is more erratic, with significant changes of the PDF already at $t = 2.2\ ms$ and opposite trend at $t = 4.8\ ms$. This results from the fact that the kernel has extended beyond the limits of the sampling box at $t = 4.8\ ms$.

The time limit at which the modification of the PDF is too important to consider that the non-reacting velocity statistics are still relevant is subjective and changes from one ignition location to the other. A general trend is that past 2 ms, the PDF not anymore representative of the non-reacting flow. Going back to the temporal evolution of the global heat release plotted in Figs. 7.9, 7.12 & 7.15, this critical time of 2 ms appears greater than most of the failed events captured in LES. It can be then assumed that the cold flow statistics can be used.

8.2.2.b Construction of $P_{pres}(\boldsymbol{x}, t)$

The time-averaged statistics of the non-reacting flow are obtained from the LES simulation. The mean $\overline{u}_i$ and RMS u'_i of the i-th component of velocity are then used to construct the PDF of the

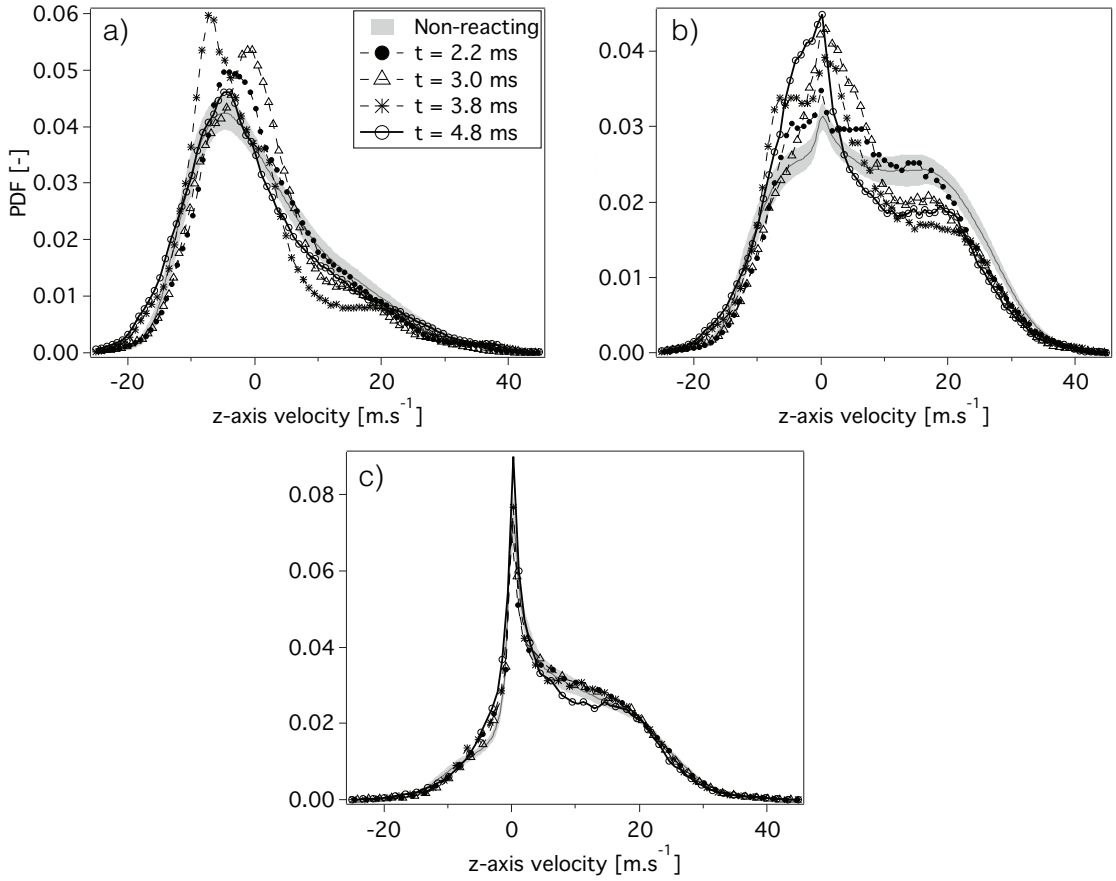

Figure 8.8: Effect of the box size on the PDF of velocity. From left to right, $c = 1.5$ (a), 2 (b) and 3 (c) *cm*. Non-reacting case is represented wit the grey area.

velocity component u_i, assuming a Gaussian shape:

$$P(u_i) = \frac{1}{\sqrt{2\pi}\ u_i'} \exp^{-\frac{(u_i - \overline{u_i})^2}{2u_i'^2}} \tag{8.5}$$

The aim is now to construct the envelope of the possible trajectories, with the mean trajectory given by $\overline{u}_i$ and its dispersion resulting of u_i'. The velocity Gaussian PDF must be transformed in a position PDF. Starting from the definition of the velocity in 1D $dx/dt = u$, the PDFs of velocity and position are related by:

$$\frac{dP(x)}{dt} = P(u) \tag{8.6}$$

and $P(x)$ can be evaluated by integration of $P(u)$:

$$P(x) = \int P(u)dt = P(u).dt = P(u.dt) \tag{8.7}$$

where $P(u)$ is supposed to be independent of time and the time step dt is constant. $P(x)$ can then be rewritten from $P(u)$:

$$P(x_0, x) = \frac{1}{\sqrt{2\pi}\ u_i'.dt} \exp^{-\frac{(x-\mu)^2}{2(u_i'.dt)^2}} \tag{8.8}$$

where the argument x_0 is added to indicate the emission point and μ is the mean position of the kernel corresponding to the convection by the mean flow:

$$\mu = x_0 + \overline{u}.dt \tag{8.9}$$

In a multidimensional case, a multivariate Gaussian distribution is used and an example of the kernel presence PDF field is schematically illustrated in Fig. 8.9 where the probability of finding at time $t_0 + dt$ a particle emitted from a single point x_0 at time t_0 is represented in 2D.

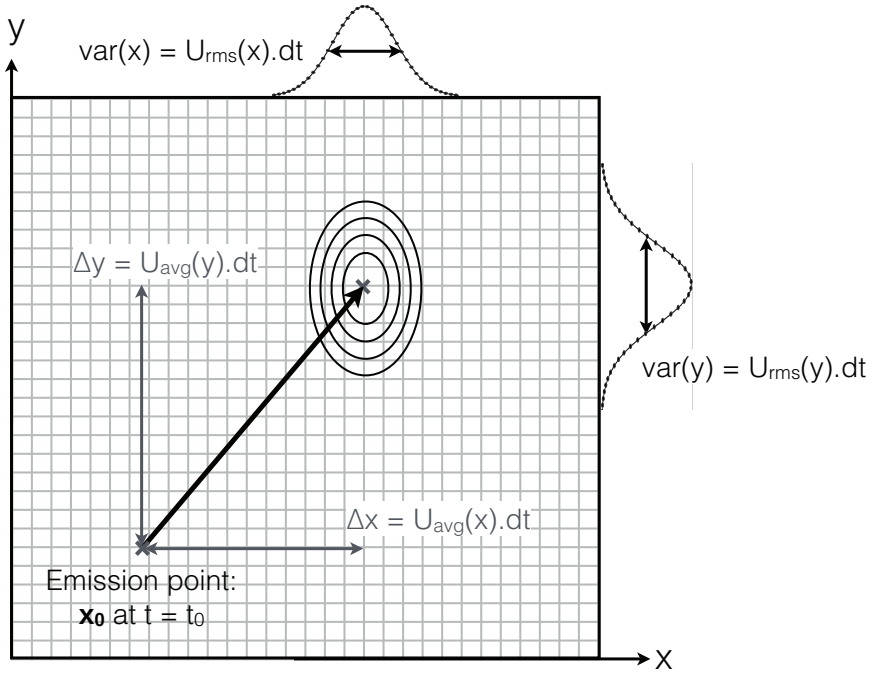

Figure 8.9: 2D schematic illustration of the probability of presence field at $t = t_0 + dt$ resulting of the emission of a point at $\boldsymbol{x_0}$ at $t = t_0$.

When considering the general case of an ensemble of emission points in a three-dimensional case, the kernel presence PDF at point $\boldsymbol{x}$ $P_{pres}(\boldsymbol{x}, t)$ is the sum of all possible trajectories contributing to the kernel presence PDF, given by:

$$P_{pres}(\boldsymbol{x}, t) = \sum_{n=1}^{N} \underbrace{P_{pres}(\boldsymbol{x_n}, t - dt).V((\boldsymbol{x_n})}_{\substack{\text{Probability of being at point} \\ \boldsymbol{x_n} \text{ at } t-dt}} \underbrace{P(\boldsymbol{x_n}, \boldsymbol{x})}_{\substack{\text{Gaussian PDF of } \boldsymbol{x} \\ \text{for an emission at } \boldsymbol{x_n}}} \tag{8.10}$$

where N is the number of nodes having a non-zero probability of presence at time $t - dt$, $\boldsymbol{x_n}$ and $V(\boldsymbol{x_n})$ are the coordinates and the nodal volume of the n-th node respectively, and $P(\boldsymbol{x_n}, \boldsymbol{x})$ is the multivariate Gaussian distribution giving the PDF value of $\boldsymbol{x}$ from an emission point $\boldsymbol{x_n}$. $P(\boldsymbol{x_n}, \boldsymbol{x})$ is the three-dimensional extension of Eq. (8.8):

$$P(\boldsymbol{x_n}, \boldsymbol{x}) = \frac{1}{\sqrt{(2\pi)^3 |\boldsymbol{\Sigma_n}|}} e^{-\frac{1}{2}(\boldsymbol{x}-\boldsymbol{\mu_n})^T \boldsymbol{\Sigma_n}^{-1}(\boldsymbol{x}-\boldsymbol{\mu_n})} \tag{8.11}$$

where $\boldsymbol{\mu_n}$ and $\boldsymbol{\Sigma_n}$ are the mean position and covariance matrix of the multivariate Gaussian distribution of the n-th emission point. The Gaussian distribution is normalized to ensure that $\int_V P_{pres}(\boldsymbol{x}, t) d\boldsymbol{x} = 1$. The mean position vector components are given by:

$$\mu_{i,n} = x_{i,n} + \overline{u}_{i,n}.dt \tag{8.12}$$

where $\overline{u}_{i,n}$ is the time-averaged velocity i-th component at node n. The covariance matrix is obtained from the RMS of the non-reacting flow:

$$\boldsymbol{\Sigma_n} = \begin{bmatrix} (u'_{x,n}.dt)^2 & 0 & 0 \\ 0 & (u'_{y,n}.dt)^2 & 0 \\ 0 & 0 & (u'_{z,n}.dt)^2 \end{bmatrix} \tag{8.13}$$

where $u'_{i,n}$ is the i-th velocity component RMS. Note that as a first step only the diagonal terms are kept, but off diagonal terms could be taken into account to encompass correlations between velocity components. The model then entirely relies on the velocity statistics of the non-reacting flow to evaluate the temporal evolution of the probability of presence through the computational domain. The computation is initiated by setting $P_{pres}(\boldsymbol{x}, t) = 1/V(n_{spark})$ at the closest grid point from the exact spark position n_{spark}.

8.2.2.c Application to the KIAI burner and *a-priori* validation

An example of the result is given in Fig. 8.10 as iso-contours of the probability of presence for a spark located at $x/D_{ext} = 0.0$ and $z/D_{ext} = 0.6$ and the results are projected in the 2D x-z plane to ease the visualization. At first, the probability of presence is found to follow the motion of the IRZ toward the methane jet with little spreading since the turbulent intensity is low. As it reaches the stagnation point, the PDF spreads radially toward the SWJ due to the high turbulence intensity and is then rapidly convected downstream by the high axial velocity of the SWJ.

In order to validate at least qualitatively the prediction of the model, the full LES of ignition sequences presented in the previous Chapter are post-treated individually to evaluate the probability of finding a flame element in space at a given instant after energy deposit. The probability of finding a flame element is given by:

$$P_{fl}(\boldsymbol{x}, t) = \sum_{s=1}^{N_{LES}} \frac{V(n)}{\sum_{n=1}^{N} V(n)} \tag{8.14}$$

where N_{LES} is the number LES full ignition sequences used, N is the number of vertices having a heat release rate above 1.0 e^6 $W.m^{-3}$ and $V(n)$ is the volume associated with the $n-$th node.

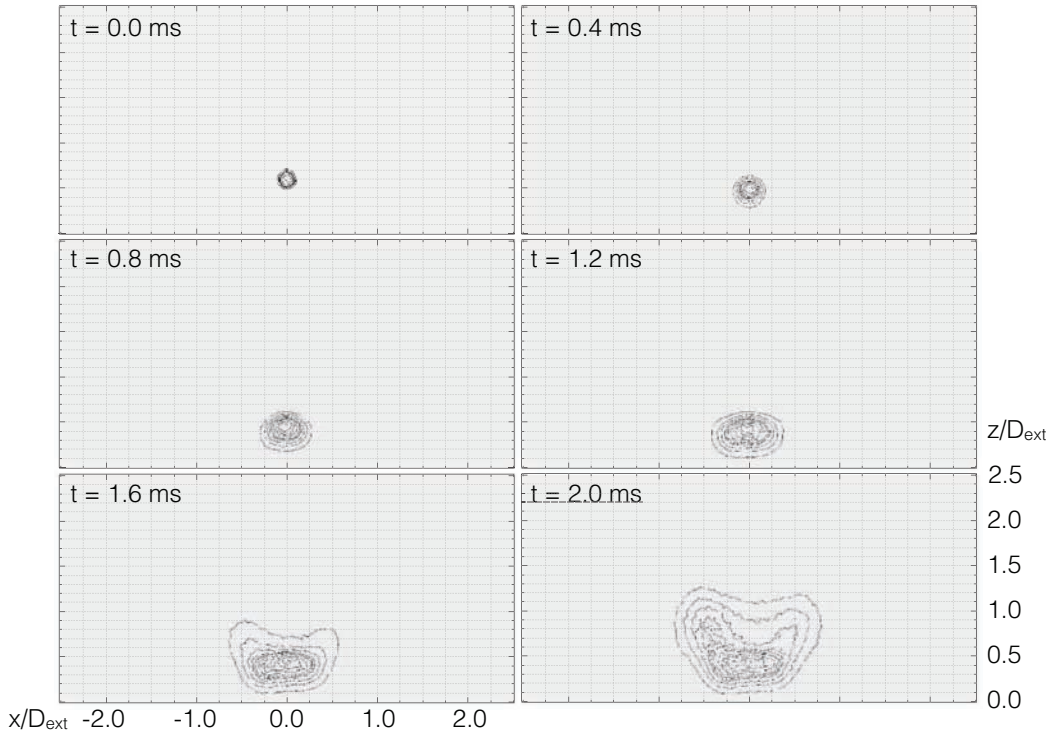

Figure 8.10: Temporal evolution of projected probability of presence iso-contours for an ignition at $x/D_{ext} = 0.0$ and $z/D_{ext} = 0.6$ predicted by the model.

Note that this LES result intrinsically includes the extinction of flame elements due to the local flow characteristics. The number of LES sequences used to evaluate $P_{fl}(\boldsymbol{x}, t)$ is small (maximum 15, depending on the number ignition event failing to initiate a flame kernel), so that $P_{fl}(\boldsymbol{x}, t)$ is poorly converged, which becomes less representative as time advances. For each ignition location studied with LES, several snapshots of the flame position are presented in Fig. 8.11 and compared to the model predictions.

The model is found to reproduce fairly well the trend observed from the ensemble averaged LES results. At PT1, the model probability of presence is first convected downstream before being deflected from the injector axis near the stagnation point. In the LES, the kernel is also convected towards the methane jet at first, but the convection of $P_{fl}(\boldsymbol{x}, t)$ at longer time is not observed. This difference can be related to the strong occurrence of quenching in the methane jet region observed in LES (see Fig. 7.24), not included in the evaluation of $P_{pres}(\boldsymbol{x}, t)$. At PT2, the model predicts both the convection of the kernel downstream due to the SWJ and the upstream motion induced by the IRZ. In the LES, large chunk of flame in the SWJ are quenched due to the lean mixture composition and since this effect is not taken into account in the model, the probability of presence in the SWJ is significant while rapidly dissipated in the LES. For PT3, the bulk convection of the kernel downstream is well captured by the model even though the small number of LES sequences results in a inward displacement of the probability, stronger than the model prediction. Although this validation of the kernel presence PDF is only qualitative, the model seems to reproduce the main motion of the kernel and the objective is now to use the

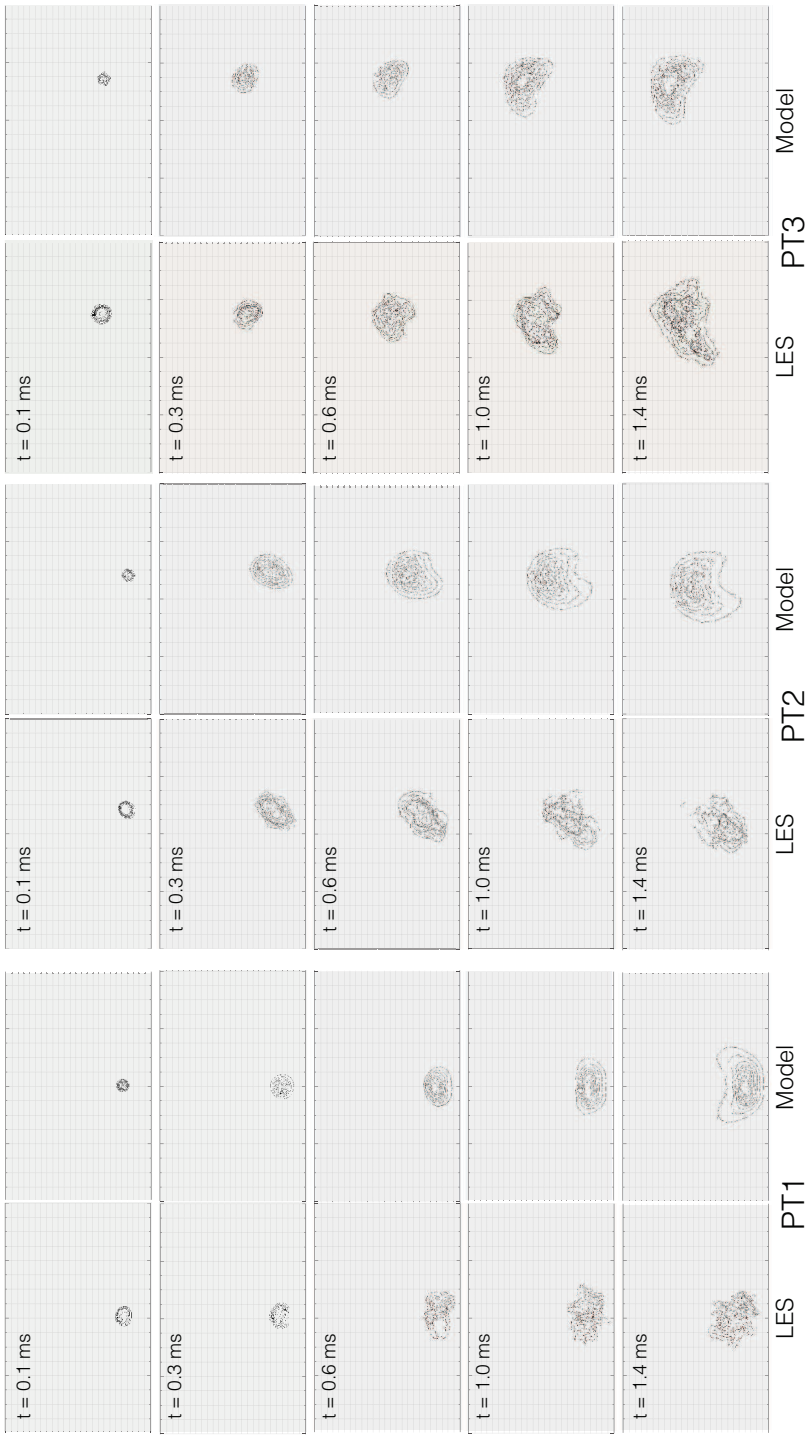

Figure 8.11: Comparison of $P_{pres}(\boldsymbol{x}, t)$ evaluated by the model and $P_{fl}(\boldsymbol{x}, t)$ computed from the LES database at the three ignition locations studied in Chap.7 at 5 instants.

knowledge of the flame position to evaluate the underlying flow properties and the probability of ignition success.

8.2.3 Statistical indicators for kernel quenching

From the analysis of the LES results presented in Chap. 7, the two main flow characteristics affecting the ignition success are the mixture composition and the turbulence intensity. In this section, statistical indicators based on these mechanisms are built.

8.2.3.a Mixture composition

Flammability factor

The various ignition studies in non-premixed flow available in the literature clearly point out the fact that the flammability factor F_f is a critical parameter (Birch *et al.*, 1977; Ahmed *et al.*, 2007*a*; Neophytou *et al.*, 2012; Eyssartier *et al.*, 2013). This is also confirmed by the present LES of fully resolved ignition: F_f is closely related to the probability of creating a sustainable flame kernel or leading to quenching. The time-averaged statistics obtained from the non-reacting LES can then be used to construct the flammability factor statistics, similarly to the early work of Birch *et al.* (1977) and Birch *et al.* (1981). As mentioned in Sec. 8.1.1, these studies proposed to use a composite PDF to evaluate the flammability factor from the measured mixture field average and RMS values. In the free methane jet case, the combination of a Gaussian and a delta Dirac functions provided a fairly good estimate of F_f. In the more complex flow pattern of the KIAI burner, a wide variety of PDF are encountered and simple PDF are less accurate.

A map based on 1326 probes, where the temporal evolution of mixture fraction was recorded, is constructed from the non-reacting LES simulation presented in Chap. 6. The map covers the same area as the experimental ignition probability map presented in Fig. 7.1 and focuses on the vicinity of the methane jet. At each probe, the mixture fraction is recorded during 100 ms at a frequency of 50 kHz in order to obtained converged first and second statistical moments of the mixture fraction distribution and build a PDF of z sufficiently resolved. To investigate further the PDF moments, a map of skewness factor γ_1 is also constructed and plotted in Fig. 8.12. γ_1 is given by:

$$\gamma_1 = \frac{\overline{z^3} - 3\overline{z}z'^2 - \overline{z}^3}{z'^3} \tag{8.15}$$

In Fig. 8.12, the first two statistical moments are similar to the results showed in Fig. 6.9. The magnitude of the skewness factor clearly indicates that the Gaussian hypothesis does not hold in a large part of the combustion chamber. Note that the map exhibits on the top a high skewness but small RMS, indicating that the PDF is narrow. The skewness factor is mainly positive, which means that the most probable value of z is lower than its mean.

From the recorded PDF of z, the flammability factor can be directly evaluated and will be used as reference. The map of F_f is shown in Fig. 8.13 along with the PDF of z at several locations. The flammability factor is found to go from zero near the methane jet and the swirler

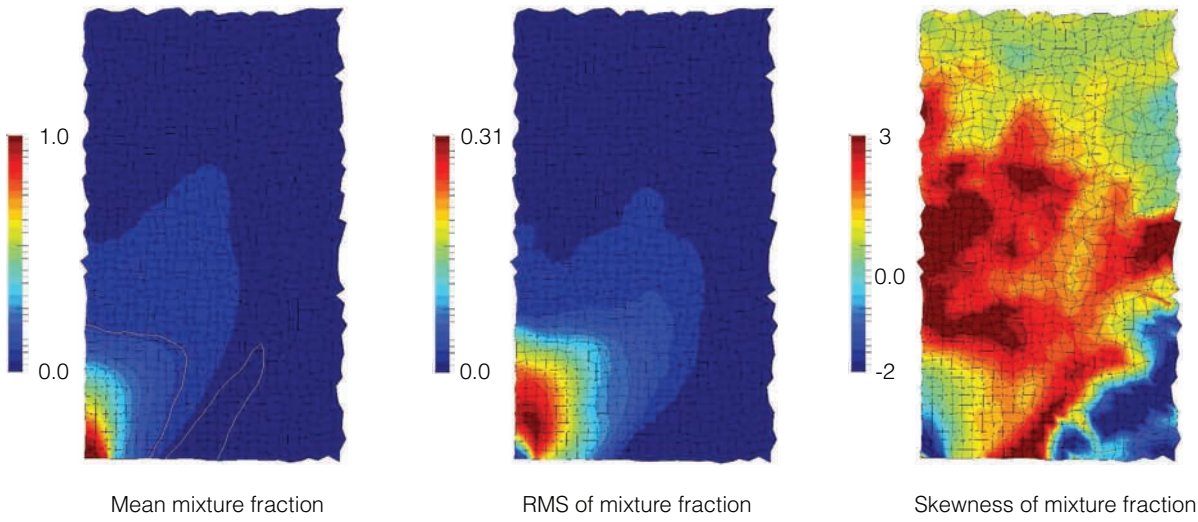

Figure 8.12: From left to right: maps of mean, RMS and skewness factor of the mixture fraction PDF in a y-normal cut plane through the center of the combustion chamber.

inlet, to one in the downstream region where the time allowed for mixing is longer, leading to a mixture fraction near the overall equivalence ratio and with small RMS value. The PDFs of z at a few selected locations give an overview of the wide variety of mixing behavior resulting from the complex flow pattern. PDF labeled a) was picked in the wake of the wall separating the SWJ and the methane jet, where mixing is controlled by the turbulence and the large helical structure of the PVC: the PDF peaks in pure air but has a strong probability of mixture near stoichiometry and a long tail toward rich mixture. PDF b) is spread from pure air to pure methane, with a peak in pure methane. The nearly equi-probability over a wide range of z indicates that this location is in the mixing layer between the pure methane of the jet and the lean flow from the IRZ. Located further downstream on the injector axis, PDF c) peaks in rich but flammable mixture indicating that the lean flow from the IRZ has been enriched by diffusion from the pure methane jet. PDF given in d) is located in the shear layer between the SWJ and the IRZ and its most probable value is near stoichiometry, but there is a significant probability of finding pure air due to the PVC structure. PDF e) is in the SWJ, but the pure air is mixed to a certain extent with the fuel so that the probability of finding mixture between 0 and 0.05 is strong but rapidly decreases for higher z. Finally, PDF f) is located in the SWJ but close to the entry plane so that very little mixing has occurred yet and pure air is mostly found.

From the PDF provided in Fig. 8.13, it appears that estimating F_f based presumed PDF parametrized by the mean and RMS values of the z field only, will not be accurate. Following Birch *et al.* (1977), tests for three PDF shapes are made:

- Gaussian distribution:

$$F_{f,gauss} = \frac{1}{2}\left[\mathrm{erf}\left(\frac{z_{rich} - \overline{z}}{\sqrt{2}\,z'}\right) - \mathrm{erf}\left(\frac{z_{lean} - \overline{z}}{\sqrt{2}\,z'}\right)\right] \tag{8.16}$$

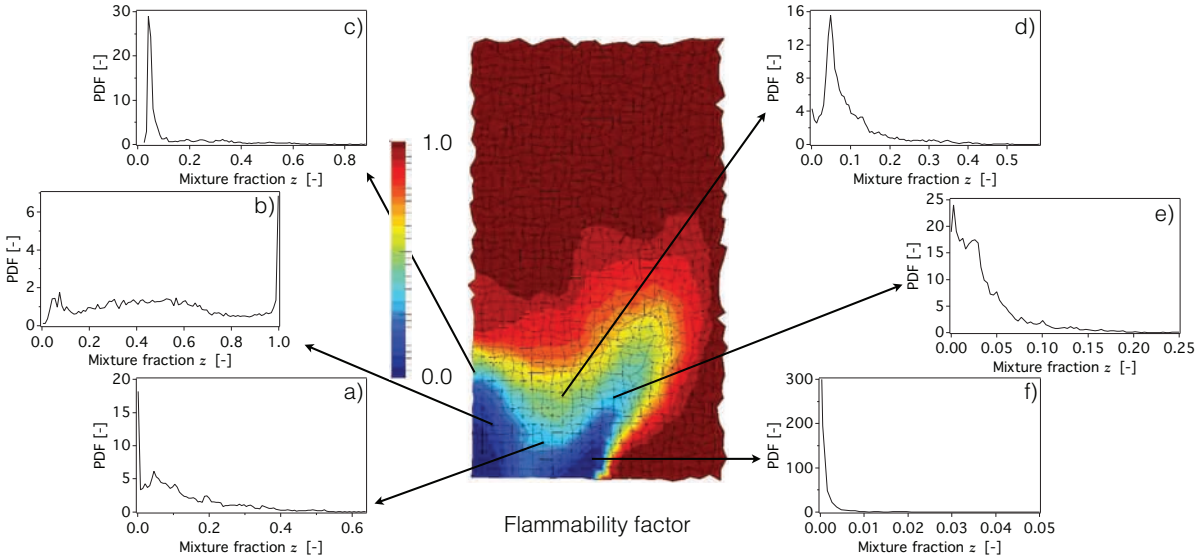

Figure 8.13: Map of flammability factor F_f obtained from LES recorded PDF(z). From a) to f), PDF of z at a few selected locations in the mixing region.

- Log-normal distribution:

$$F_{f,logN} = \frac{1}{2}\left[\mathrm{erf}\left(\frac{\ln(z_{rich}) - \mu}{\sqrt{2}\,\sigma^2}\right) - \mathrm{erf}\left(\frac{\ln(z_{lean}) - \mu}{\sqrt{2}\,\sigma^2}\right)\right] \tag{8.17}$$

  where μ and σ are the log-normal law parameters given by:

$$\mu = \ln(\overline{z}) - \frac{1}{2}\ln\left(1 + \frac{z'}{\overline{z}^2}\right) \quad \text{and} \quad \sigma = \ln\left(1 + \frac{z'}{\overline{z}^2}\right) \tag{8.18}$$

- β-PDF distribution:

$$F_{f,\beta} = I_{z_{rich}}(\alpha,\beta) - I_{z_{lean}}(\alpha,\beta) = \frac{B_{z_{rich}}(\alpha,\beta)}{B(\alpha,\beta)} - \frac{B_{z_{lean}}(\alpha,\beta)}{B(\alpha,\beta)} \tag{8.19}$$

  where $B_z(\alpha,\beta)$ is the incomplete beta function and $I_z(\alpha,\beta)$ the regularized incomplete beta function of parameters α and β given by:

$$\alpha = \overline{z}\left(\frac{\overline{z}(1-\overline{z})}{z'} - 1\right) \quad \text{and} \quad \beta = (1-\overline{z})\left(\frac{\overline{z}(1-\overline{z})}{z'} - 1\right) \tag{8.20}$$

  Note that the β-PDF is found to diverge for very high values of β, so that $F_{f,\beta} = F_{f,logN}$ where $z' < 1.0e^{-2}$.

The reconstructed fields of F_f based on the three presumed PDF shapes, using the moments from the LES, are presented in Fig. 8.14 and compared to the map obtained from the true z-PDF presented in Fig. 8.13. As expected from the good mixing properties of the injector, all reconstructed F_f reproduce quite well the downstream region where mixture fluctuations are very

low. However, significant differences appear at the vicinity of the methane jet: $F_{f,gauss}$ exhibits a too large central region of low flammability as expected from the skewness map presented in Fig. 8.12 and is unable to recover PDF such as Fig. 8.13(e) so that the wake of the lean SWJ is not well captured. Using a log-normal law, the reconstructed PDF is able to reproduce a positive skewness and to better capture the profiles of F_f near the central methane jet and the SWJ but the transition between the pure methane region and the SWJ is not well captured since the log-normal law is not able reproduce distribution such as Fig. 8.13(b). The β-PDF gives satisfactory results for a large portion of the mixing region but is unable to reproduce very narrow distribution with long tail such as Fig. 8.13(c) for which the log-normal law is more adapted.

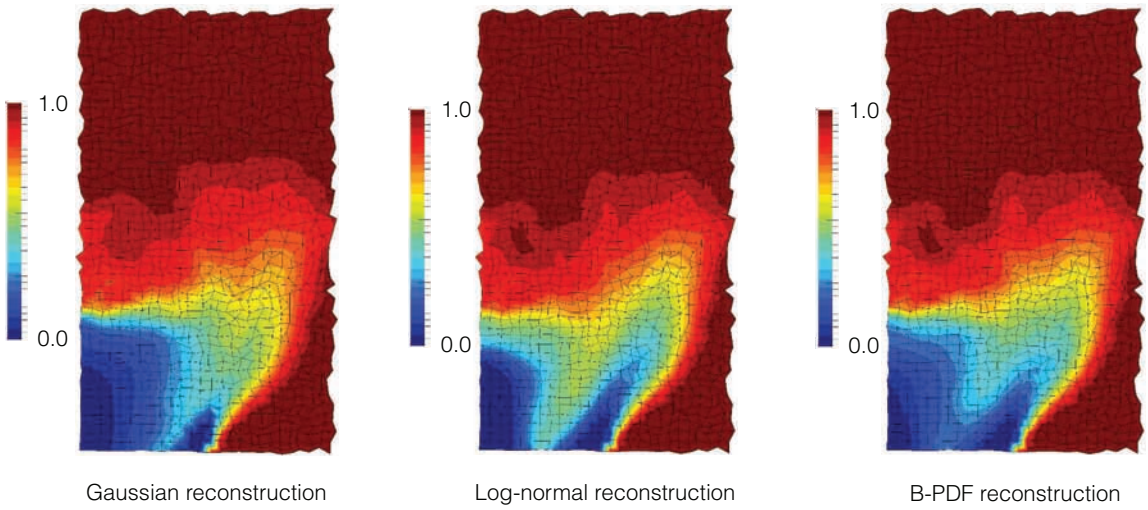

Figure 8.14: Map of flammability factor F_f obtained from the first two statistical moments of z assuming Gaussian (left), Log-Normal (center) or β-PDF (right) shapes.

In a tentative to improve these results, we propose to use a composite distribution based on both log-normal and β-PDF, in order to reproduce the wide variety of distributions observed throughout the combustion chamber. The log-normal distribution is used for the vast majority of the chamber since it is able to match very narrow and slightly skewed distributions, while the β-PDF is employed in regions of high mixture fluctuations corresponding to $\overline{z} \simeq 0.5$ where it is able to reproduce very flat distributions (Fig. 8.13(b)). The final formula for F_f is given by:

$$F_{f,model} = \gamma F_{f,\beta} + (1-\gamma) F_{f,logN} \tag{8.21}$$

where γ is a blending parameter, solely based on the level of mixture fraction fluctuations:

$$\gamma = 0.5 \left(1 + \tanh \left(\frac{z' - 0.15}{0.04} \right) \right) \tag{8.22}$$

The reconstructed field of F_f obtained with Eq. (8.21) is presented in Fig. 8.15 and compared again to the results of Fig. 8.13, reported on the right side of Fig. 8.15. The model is able to reproduce the main features of the flammability factor map but discrepancies remains up to an absolute error of 0.2 near the core of the methane jet.

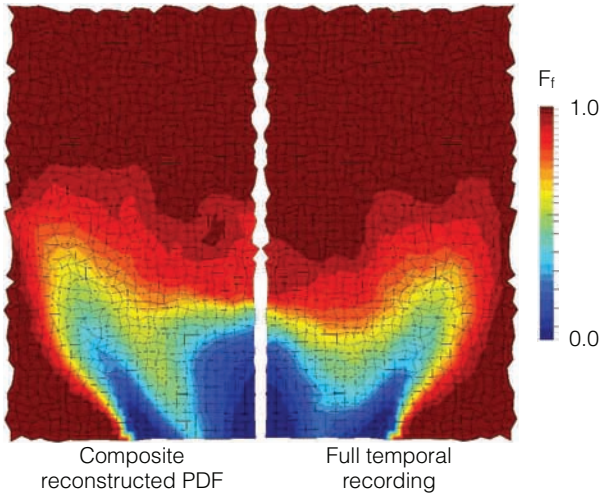

Figure 8.15: Map of flammability factor F_f obtained from Eq. (8.21) (left) and LES recorded PDF(z) (right).

Local mixture fraction

The second mixture characteristic that is needed to include the effect of the mixture on the kernel development is an estimate of the local mixture fraction. However, the direct use of the mean mixture fraction is inadequate since it can temporarily be out of the flammability limits even though a flammable mixture can be found at this location at other times. Therefore, the mean flammable mixture fraction $\overline{z}|_{z_{lean}<z<z_{rich}}$ is preferred, given by:

$$\overline{z}|_{z_{lean}<z<z_{rich}} = \frac{\int_{z_{lean}}^{z_{rich}} zP(z)\,dz}{F_f} \tag{8.23}$$

where $\overline{z}|_{z_{lean}<z<z_{rich}}$ gives the mean mixture fraction when the mixture is flammable, at a given location. Taking $P(z)$ as the composite PDF including the log-normal and the β-PDF introduced in Eq. (8.21), the mean flammable z is given by:

$$\begin{aligned}\overline{z}|_{z_{lean}<z<z_{rich}} = \Bigg(&\gamma \int_{z_{lean}}^{z_{rich}} \frac{1}{B(\alpha,\beta)} z^{\alpha}(1-z)^{\beta-1}\,dz \\ &+(1-\gamma)\int_{z_{lean}}^{z_{rich}} \frac{1}{\sigma\sqrt{2\pi}} \exp^{-\frac{(\ln(z)-\mu)^2}{2\sigma^2}}\,dz\Bigg)/F_{f,model}\end{aligned} \tag{8.24}$$

The results obtained with the LES recorded PDF and the composite PDF model are compared in Fig. 8.16. Although the match is not perfect between the two fields, the PDF model provides a reasonable value of $\overline{z}|_{z_{lean}<z<z_{rich}}$ and follows the same pattern as LES recorded PDF. Note that the convergence of the PDF obtained from the temporal recordings could be improved to lower the variability on such advanced statistics.

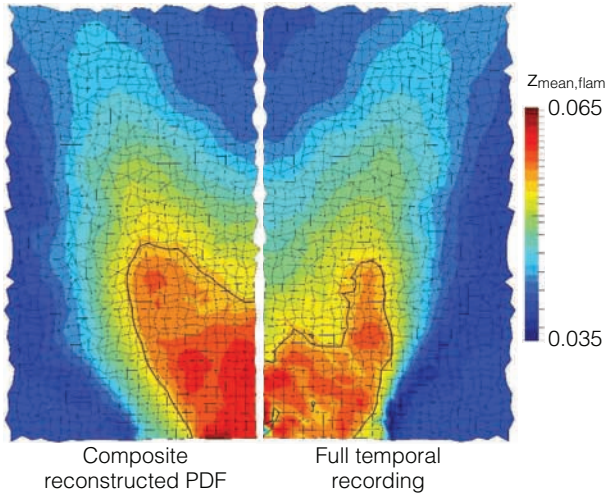

Figure 8.16: Map of the mean flammable mixture fraction obtained from Eq. (8.24) (left) and the LES recorded PDF (right). The black iso-contour indicates the position of the stoichiometric (z_{st}) iso-line.

8.2.3.b Turbulence characteristics

The second mechanism responsible for flame kernel quenching results from the interaction of the flame kernel with the turbulence. In particular, the large scale deformations of the flame kernel have been found to be responsible of significant quenching due to flame/flame interaction and fragmentation of the flame kernel. To take into account this effect in the ignition model, the kernel/turbulence interaction must be characterized with a quenching criterion. Following the previous work of Wilson *et al.* (1999) and Neophytou *et al.* (2012), a criterion based on the Karlovitz number is developed. The estimation of Ka of Abdel-Gayed & Bradley (1985) is used:

$$Ka = 0.157 \left(\nu \frac{u'^3}{l_t} \right)^{1/2} \frac{1}{S_L^{0\,2}} \tag{8.25}$$

where u' is the turbulent velocity magnitude (obtained from the non-reacting time-averaged statistics), ν is the kinematic viscosity, l_t the integral length scale and S_L^0 the laminar flame velocity. S_L^0 is a function of z and can be locally estimated using the mean flammable z defined in Eq. (8.24). It is however more difficult to estimate the integral length scale from the time-averaged statistics of the non-reacting flow. Using the constant turbulent dissipation assumption, $\varepsilon = u'^3/l_t$ (in isotropic homogeneous turbulence), Eq. (8.25) can be recasted:

$$Ka = 0.157 \frac{(\nu\varepsilon)^{1/2}}{S_L^{0\,2}} \tag{8.26}$$

The objective is now to estimate the dissipation rate ε from the non-reacting flow time-averaged data. ε is given by (Pope, 2000) as:

$$\varepsilon = 2\nu_{tot} S_{i,j} S_{i,j} \tag{8.27}$$

where $S_{i,j}$ is the velocity deformation tensor and $\nu_{tot} = \nu + \nu_t$ includes the sub-grid scale viscosity provided by the turbulence LES model. Evaluating ε from the mean velocity field is inadequate but it can be estimated from the velocity fluctuations:

$$s_{i,j} = \frac{1}{2}\left(\frac{\partial u_i'}{\partial x_j} + \frac{\partial u_j'}{\partial x_i}\right) \tag{8.28}$$

Figure 8.17 shows the Karlovitz number field obtained from Eq. (8.25) and time-averaged statistics, compared to an ensemble-averaged values of Ka computed from 250 instantaneous LES solutions for which the evaluation of ε is straightforward. The agreement between the two quantities is fairly good, with the region of high Ka number well reproduced as well as the moderate Ka number values located in the wake of the SWJ.

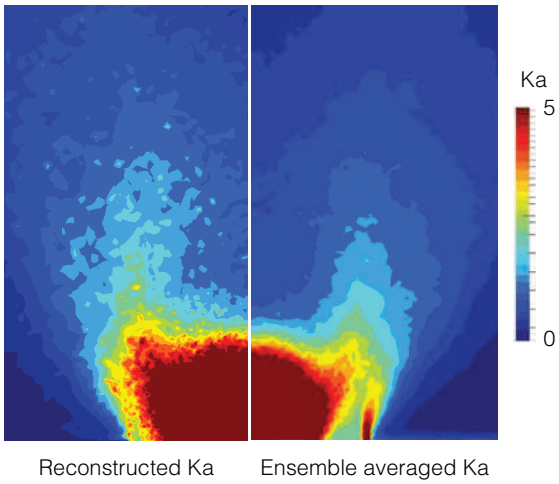

Figure 8.17: Comparison of the Karlovitz number field reconstructed from time-averaged data (left) and ensemble-averaged data (right).

To encompass quenching due to aerodynamic stretch, a critical value Ka_c must be determined, above which the flame is supposed to quench. A value of Ka_c reported in the literature (Abdel-Gayed & Bradley, 1985; Neophytou *et al.*, 2012) for premixed flame is about 1.5. However, for the present case, this value results in a too large region of flame quenching. Cordier (2013) uses $Ka_c = 4.5$ based on the agreement of its ignition model with experimental data. As this value appears more consistent with our Ka field, it is retained. Note on Figure 8.17 that Ka rapidly decreases beyond the central jet region so that the region where $Ka > Ka_c$ is not very sensitive to values of Ka_c above 2.5.

8.2.4 Combination of both statistics

The objective now is to combine the kernel presence PDF with the statistics of the non-reacting flow in order to evaluate the ignition probability. The first step is to construct the conditioned

kernel presence PDF by:

$$P_{pres,cond}(\boldsymbol{x},t) = F_f(\boldsymbol{x}).C_{Ka}(\boldsymbol{x}).P_{pres}(\boldsymbol{x},t) \tag{8.29}$$

where $C_{Ka}(\boldsymbol{x})$ is the critical Ka criterion defined as:

$$C_{Ka} = \begin{cases} 1 & \text{if } Ka(\boldsymbol{x}) < Ka_c \\ 0 & \text{otherwise} \end{cases} \tag{8.30}$$

The ignition probability is then evaluated by a direct integration of $P_{pres,cond}(\boldsymbol{x},t)$ over the computational domain:

$$P_{ign} = \int_{\boldsymbol{x}} P_{pres,cond}(\boldsymbol{x},t)\ d\boldsymbol{x} \tag{8.31}$$

However, two elements must be taken into account: 1) the flame kernel resulting from the energy deposit is in over-adiabaticity conditions, 2) a criterion for ignition success needs to be selected to remove from the computation kernels that can no longer be quenched by local flow effect.

8.2.4.a Initial deposit relaxation time

When considering spark ignition, two phases of the kernel development can be distinguished: at first the kernel growth is sustained by the high temperature (above the adiabatic flame temperature) of the energy deposit while later, as the kernel temperature drops to T_{ad}, the kernel expansion is driven by combustion. During the first phase, the kernel can survive to a lack of flammable mixture or strong turbulence (with reconstruction mechanisms (Vasudeo *et al.*, 2010) for instance). This is taken into account in the present model by evaluating the time required for the temperature to drop from the initial deposit maximum temperature to the adiabatic flame temperature. During this time, the kernel is convected in the computational domain, but local quenching parameters are not applied. The initial kernel state is taken from the ED model (Lacaze, 2009): given the amount of energy ε_i and the deposit size Δ_s, the maximum temperature is given by (assuming no reaction during the deposition duration):

$$T_{k,max} = T_f + \frac{1}{\rho_f C_p} \frac{\varepsilon_i}{(2\pi)^{3/2}\sigma_s^3} \tag{8.32}$$

where $\sigma_s = \Delta_s / 2\sqrt{ln10^4}$ (see Sec. 7.3.2). The initial temperature and density (T_f and ρ_f) are extracted from the LES field. The temperature balance of the kernel is then evaluated in 0D by:

$$\frac{dT}{dt} = \dot{\omega}_T(z) + \frac{D_{th}}{r_k^2}(T_\infty - T) \tag{8.33}$$

where T_∞ is the temperature around the energy deposit and the first term on the RHS results from the consumption of fuel and is evaluated at the deposit location with the mean flammable mixture fraction provided by Eq. (8.24):

$$\dot{\omega}_T(z) = \frac{Y_F(z) S_L^0(z) \mathcal{Q}_r}{C_p \delta_L(z)} \tag{8.34}$$

with $\mathcal{Q}_r$ the heat of combustion. The second term is a 0D approximation of the diffusive fluxes where the diffusivity is given by Akindele *et al.* (1982):

$$D_{th} = D_{lam} + D_{turb} = \frac{\lambda}{\rho C_p} + 0.44 u' l_t \left(1 - \exp\left(-\frac{u' t}{0.44 l_t}\right)\right) \tag{8.35}$$

where the turbulent diffusivity progressively increases from 0 to its fully developed value to take into account the notion of effective turbulent velocity u'_{eff} introduced in Sec. 5.1.2. Finally, the kernel growth is taken into account following a laminar asymptotic growth (Boudier *et al.*, 1992):

$$\frac{dr_k}{dt} = \frac{T_b}{T_f} S_L^0(z) \tag{8.36}$$

The flow characteristics at the spark location are used as inputs for the temperature balance equation: the kernel displacement during this short initial phase is neglected. Equation 8.33 is then resolved numerically to obtain the time required for the kernel temperature to cool down to the adiabatic flame temperature.

8.2.4.b Kernel growth

To identify the end of the kernel phase, the size of the kernel must be evaluated in time. The growth rate of the flame kernel depends on both the local mixture composition and turbulence level through the turbulent flame speed (Abdel-Gayed *et al.*, 1987; Cordier, 2013):

$$S_t = S_L^0 + n \left(\frac{u'}{S_L^0}\right)^c . S_L^0 \tag{8.37}$$

where S_t is the turbulent flame velocity, n and c are the model constants evaluated by Cordier (2013). As the kernel is convected through the computational domain, the local flow characteristics are used to evaluate the kernel radius increase. The local value of the radius at $t + dt$ is the probability-weighted averaged value of all the possible pathways:

$$r_k(\boldsymbol{x}, t) = \frac{\sum_{n=1}^{N_{emis}} r_k(\boldsymbol{x_n}, t - dt).V(n).P_{pres}(\boldsymbol{x_n}, t - dt)}{P_{pres}(\boldsymbol{x}, t)} \tag{8.38}$$

Finally a critical value of the kernel diameter $r_{k,c}$ above which the kernel can no longer be quenched by local inflammable mixture or supercritical Ka value must selected. A rigorous evaluation of $r_{k,c}$ is uneasy and as a first approximation, the value $r_{k,c} = 15$ mm, which is of the order of magnitude of the integral length scales reported in Tab. 7.1, is selected as it provide reasonable results on the premixed case. In further developments, the value of $r_{k,c}$ should be related to the local value of the integral length scale l_t. Kernels having a diameter larger than $r_{k,c}$ are removed from the kernel presence PDF and added to the ignition probability.

8.3 Results

The model is now applied to the KIAI single burner configuration in both premixed and non-premixed operating modes. The aim is to reproduce the ignition probability maps obtained

experimentally (Cordier, 2013) and presented in Fig. 8.18. Large differences are observed between the two operating modes: for the premixed condition, a large region of low ignition probability is located in the IRZ along the central axis while for the non-premixed mode the ignition probability increases rapidly along the central axis but remains low on the wake of the SWJ. Cordier (2013) indicates that the near stoichiometric conditions encountered at the bottom of the IRZ in the non-premixed mode allow the flame kernel to sustain the locally high turbulence intensity, reducing the occurrence of quenching in this region.

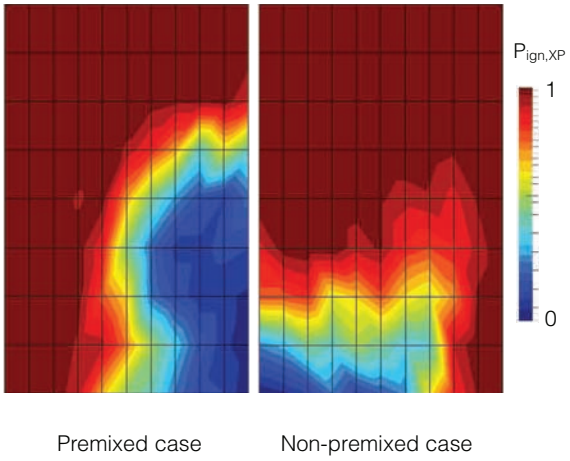

Figure 8.18: Experimental ignition maps: premixed case (left) and non-premixed case (right). Extracted from Cordier (2013).

The ignition model will now be applied to both configurations in order to construct ignition probability maps and see if the model is able to discriminate the effect of the partial premixing.

8.3.1 Premixed case

The premixed case is first investigated as it only involves the aerodynamic quenching mechanism. The spark energy ε_i and size σ_s are similar to the one used in fully resolved LES of ignition sequences performed in Chap. Fig. 7: $\varepsilon_i = 29$ mJ and $\Delta_s = 7.5$ mm. The value of the critical kernel radius is fixed $r_{k,c} = 15$ mm.

The ignition map reproduced by the model is first compared to the experiments in Fig. 8.19, to globally evaluate the performance of the model. The shape of the ignition probability contours predicted by the model are in fairly good agreement with the experimental results: a large region of low ignition probability is found along axis of the injection system up to an axial position of $x/D_{ext} = 1.2$. The shape of this region is found to globally follow the shape of the IRZ, indicating that transport effects from downstream position towards the injector nozzle are responsible from this large region of low ignition probability. Aside from this central region, the ignition probability is 1 in the upper part of the map as well as for large radius.

To show the interest of including the transport in the ignition probability evaluation, an

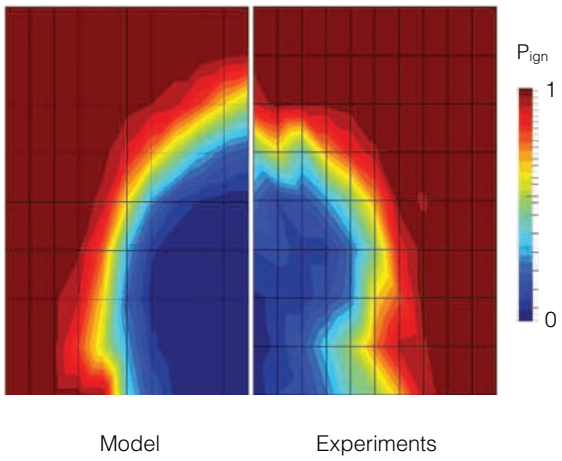

Figure 8.19: Premixed case: ignition maps predicted by the model (left) versus experimental results (right) (Cordier, 2013).

example of sparking along the injector axis at an axial location $z/D_{ext} = 1.0$ is presented in Fig. 8.20 showing several snapshots of the projected $P_{pres,cond}(\boldsymbol{x}, t)$ conditioned only by the criterion $C_{Ka}(\boldsymbol{x})$. The conditioned kernel presence PDF is found to be convected toward the injector nozzle and to be dispersed by the turbulent activity in the IRZ. As it meet the bottom of the IRZ, significant quenching occurs due to the high Ka region located near the central jet.

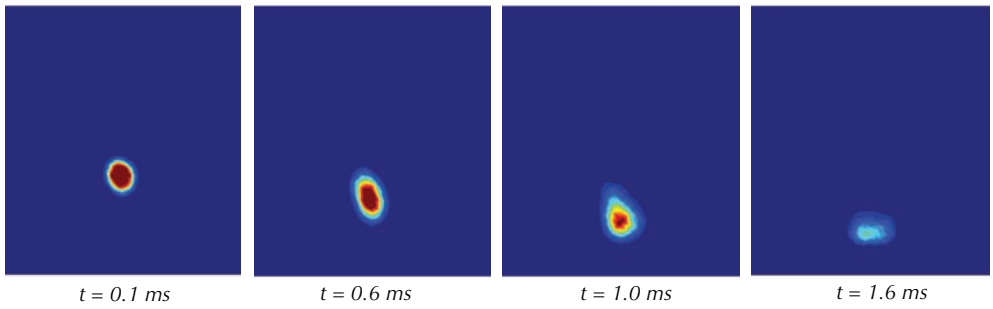

Figure 8.20: Snapshots of the projected $P_{pres,cond}(\boldsymbol{x}, t)$ following sparking at $z/D_{ext} = 1.0$, $x/D_{ext} = 0.0$.

The temporal evolution of P_{ign} is plotted in Fig. 8.21 showing that the kernel is first sparked in a region favorable to the kernel survival, but as the kernel is convected towards the injector nozzle, P_{ign} drops to zero due to aerodynamic quenching. The example presented here clearly demonstrates the relevance of including the transport effect in the evaluation of P_{ign} since a pointwise methodology such as I_CRIT_LES (Eyssartier *et al.*, 2013) can only reproduce the contours of the critical Ka region shown in Fig. 8.17.

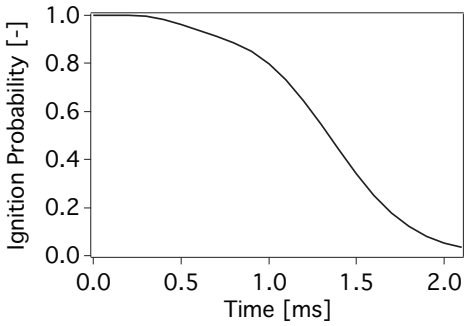

Figure 8.21: Temporal evolution of P_{ign} following sparking at $z/D_{ext} = 1.0$, $x/D_{ext} = 0.0$

8.3.2 Non-premixed case

The ignition model is applied to the non-premixed case using the same spark characteristics as in the premixed case, but the critical kernel radius value is $r_{k,c} = 5$ mm. The ignition map predicted by the model is compared to the experimental results in Fig. 8.22. The model is able to reproduce some of the effect of the partial premixing on the ignition probability contours: the lower ignition probability in the wake of the SWJ is captured as well as the central region of low probability near the methane jet. The extent of the central however, is not well reproduced by the model and is sensitive to the choice of $r_{k,c}$.

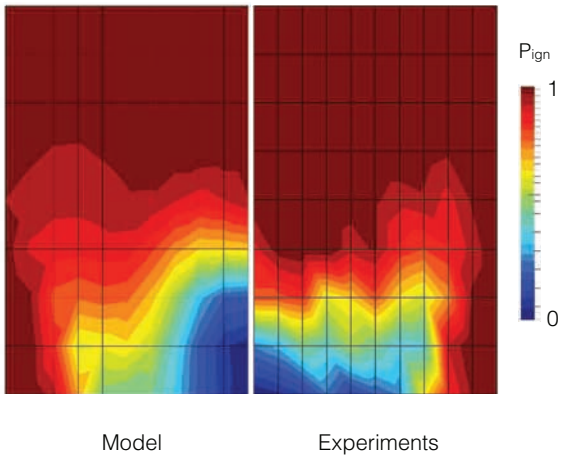

Figure 8.22: Non-premixed case: ignition maps predicted by the model (left) versus experimental results (right) (Cordier, 2013).

To investigate the origin of the discrepancies between the model prediction and the experimental results, the data extracted from the fully resolved LES performed in Chap. Fig. 7 are used. Table 8.1 gives: 1) the ignition probability obtained in experiments, 2) the data extracted from the LES: the ignition probability, the kernel initiation probability and the flammability factor, 3) the ignition probability and the flammability factor (see Eq. (8.21)) obtained from the model.

	Expe	**LES**			**Model**	
	$P_{ign,XP}$	$P_{ign,LES}$	$P_{ker,LES}$	$F_{f,LES}$	$P_{ign,model}$	$F_{f,model}$
PT1	28-70%	40%	0.80	90 %	10%	0.42
PT2	50%	50%	0.46	70 %	45%	0.38
PT3	80%	75%	0.81	85 %	85%	0.81

Table 8.1: Comparison of $P_{ign,XP}$, $P_{ign,LES}$,$P_{ker,LES}$, $F_{f,LES}$, $P_{ign,model}$, and $F_{f,model}$ at the three ignition locations PT1, PT2 and PT3.

The differences between $P_{ign,LES}$ and $P_{ker,LES}$ show that the effect of transport on the overall ignition probability are significant only for PT1 where more than half of the kernel successfully ignited are subsequently quenched during the kernel phase. Note that $P_{ign,XP}$ at PT1 is in region of strong gradient indicating a possible change in the kernel dynamic. The transport effects are however less significant at PT2 and PT3 for which the $P_{ign,LES}$ and $P_{ker,LES}$ are closer. The results of the model $P_{ign,model}$ shows that the model underestimates the ignition probability at PT1 where a pointwise model based on F_f provides more accurate prediction of the ignition probability. This is in contradiction with LES results indicating that transport effects are significant at PT1. Because PT1 is located in a region of strong F_f gradient, it is more difficult to predict the value of F_f from the non-reacting flow statistics using Eq. (8.21): indeed the model prediction $F_{f,model}$ is largely below the value obtained from the LES recorded PDF $F_{f,LES}$.

8.4 Conclusions

A new model including the effect of kernel transport by constructing a statistic of the kernel trajectories is proposed to evaluate the probability of ignition success at the end of the kernel phase. The model derivation relies on an estimation of the kernel presence PDF, which is evaluated by propagating a multivariate Gaussian distribution through the computational domain. From the LES database constructed in Chap. Fig. 7, the physic leading to kernel quenching is included by computing statistics of the non-reacting flow: the flammability factor and the Karlovitz number. Both statistics are then combined taking into account the initial kernel high temperature state and the progressive growth of the kernel. The different ingredient of the model are validated against LES data when possible.

The model is then applied to the KIAI single burner configuration in both premixed and non-premixed mode. The results on the premixed case are encouraging, since the model is able to reproduce at least qualitatively the shape of the ignition probability contours. The interest of including transport effects over a simple pointwise statistics as in the I_CRIT_LES model (Eyssartier *et al.*, 2013) is also highlighted. The results on the non-premixed case are more controversial since the inclusion of transport degrade the results as compared to a pointwise approach. The LES results indicate that transport effects in this case might be limited. The inaccurate prediction of the model at some given location are shown to be related to the estimation of the flammability factor and a computation with F_f extracted from the LES recorded PDF could helps differentiate the error due to the transport from the error introduced by the underestimation of F_f near the central jet.

Part III

Inter-sector flame propagation

Chapter 9

Inter-sector flame propagation: literature review

In annular engine configurations, ignition of the first burner is followed by the light-around phase during which the flame must propagate from one burner to the next one. Very sparse literature is available on the light-around phase of the ignition sequence, at least in the open literature. This fact is easily explained by the cost and complexity of experimental test rigs and the high CPU cost and feasibility of simulations required to study the flame propagation. The early work in this direction is performed with LES by Boileau *et al.* (2008). In this pioneering work, two diametrically opposed torch flames trigger the light around of a full annular helicopter combustor. Although no experimental data were available to validate numerical results, the study gives first insights on the mechanisms driving the flame: the burnt gas expansion pushes the flame in the azimuthal direction, resulting in a absolute flame speed much higher than the turbulent flame velocity. Figure 9.1 shows the flame position at various instants during the light-around process. The flame front is found to first accelerate the fresh gases due to expansion effect. The flame front velocity then reaches a constant value much higher than the turbulent flame speed until the two flame fronts evolving in opposite azimuthal direction start interacting with each other. Boileau *et al.* (2008) investigate the path followed by the flame leading point and show that after an initial phase of axial expansion where the leading point is located in the upper part of the combustion chamber, the flame then propagates in the lower part close to the injection systems. The flame front interacts with the SWJ generated by the injection system and is able to enter the IRZ where it stabilizes. Moreover, comparing a gaseous and a two-phase flow simulations, using an Euler-Euler approach, of the light around in this annular combustion chamber, Boileau (2007) shows that the azimuthal propagation is faster in the single phase simulation, due to of the higher consumption rate of the gaseous flame that induces stronger expansion effects.

Very recently, three research teams at CORIA, Cambridge University and EM2C have built multi-burner experimental test rigs. The test bench installed at CORIA (Cordier, 2013) is designed to study the effect of inter-injector distance on the inter-sector flame propagation. The rig consists of an in-line combustion chamber equipped with a variable number of injection systems. Direct visualization of the flame front during ignition shows different propagation modes depending on the inter-injector distance (Cordier *et al.*, 2013*a*): 1) for low spacing, the flame propagates

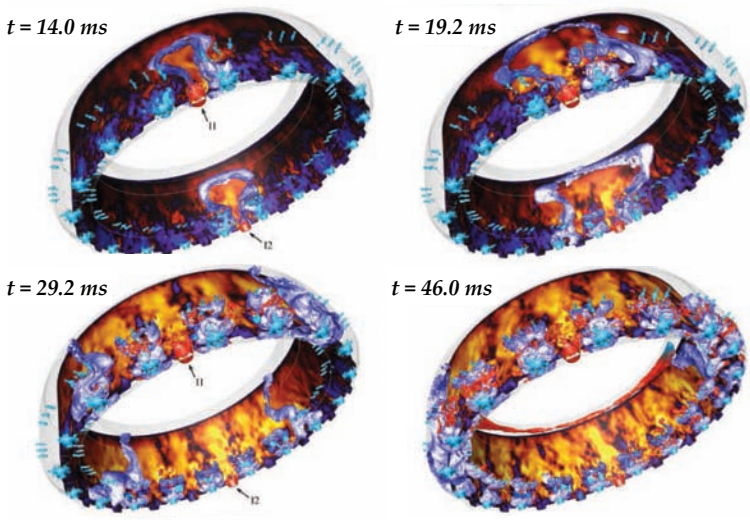

Figure 9.1: Flame light-around in an helicopter gas turbine extracted from Boileau *et al.* (2008). Flame tracked by iso-surface of reaction colored (shiny light blue).

rapidly in a radial direction, 2) for large spacing, the flame first expands axially before being captured by the IRZ of the next injector. The other two rigs are annular configurations which mainly aim to study azimuthal combustion instabilities. Bach *et al.* (2013) study a methane/air burner composed of 18 swirled injection systems at ambient conditions and a global equivalence ratio of 0.7. This study indicates that to propagate from one burner to another, the flame has to be captured by the top of the IRZ, confirming the findings of Boileau *et al.* (2008). They show that the propagation of the lower flame front in Fig. 9.2 is promoted by the swirl motion induced by individual swirlers. The effect of swirl is more pronounced for the lower flame front since the shortest flame path follows the inner radius of the azimuthal chamber in which the flame propagates in the same direction as the swirl motion. The bulk flow velocity is shown to have a detrimental effect on the overall ignition delay as displayed in Fig. 9.2. Note that the overall ignition delay increases with the bulk velocity because the flame kernel growth during the early instants after sparking is slowed by the higher turbulence. LES of the Cambridge experiments are performed in the work of Bauerheim (2014) to study azimuthal instabilities, demonstrating that LES of such complex configuration is reachable with current computational resources.

Bourgouin *et al.* (2013) focus on a propane/air annular burner fitted with 16 swirled injectors designated MICCA, operated in ambient conditions with a global equivalence ratio of 0.76. The flame is found to propagates along the bottom wall of the combustion chamber in the region of intense turbulence induced by the swirler and, confirming the numerical work of Boileau *et al.* (2008), the flame propagation velocity is shown to result of the gas volumetric expansion. These experimental findings are supported by G-equation simulations where the density drop across the flame front is found to accelerate the flame motion. The effect of the swirl motion on the flame front velocity is also observed. The overall ignition time reduces with increasing bulk velocity as shown in Fig. 9.3 which is in contradiction with the result of Bach *et al.* (2013). The opposite response to bulk velocity increase in term of overall ignition delay is shown to be related to the kernel development phase rather than the light-around phase.

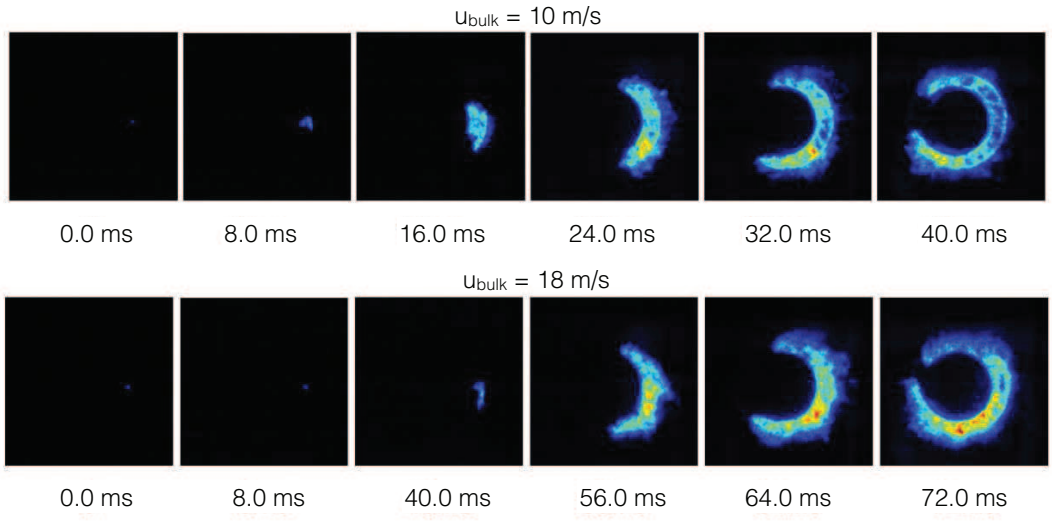

Figure 9.2: Top view direct visualization of the flame light-around in the Cambridge combustion chamber for two bulk velocities (Bach *et al.*, 2013).

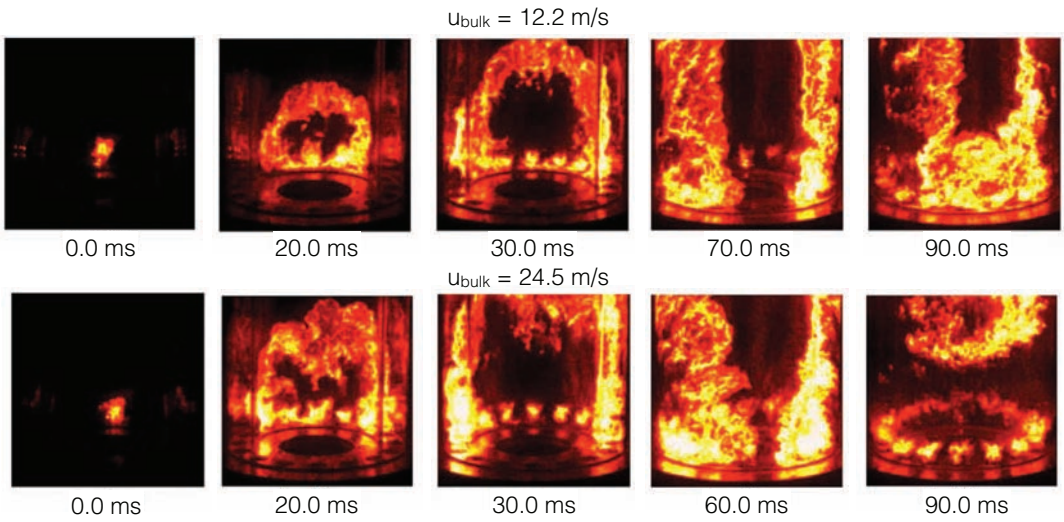

Figure 9.3: Side view direct visualization of the flame light-around in the EM2C MICCA experiments at two bulk velocities (Bourgouin *et al.*, 2013).

LES of ignition sequences in the MICCA configurations is performed with AVBP using a TTC-FTACLES (Fiorina *et al.*, 2010) combustion model in Philip *et al.* (2014*b*). The complete ignition sequence is computed and LES is shown to be in qualitative agreement with the experimental observation in terms of flame front shape and dynamic. Quantitative comparisons with experiments also indicate that LES is able to reproduce the overall ignition delay. Two LES studies of the ignition of the MICCA burner are performed under a PRACE grant with the objective of comparing two combustion model: DTFLES and FTACLES. The results presented in Philip *et al.* (2014*a*) demonstrate that both models reproduce accurately the propagation phase.

To the author's knowledge, these studies are the only ones reported in the open literature although the flame inter-sector flame propagation is a critical phase of the ignition sequence. This very sparse literature highlights the need for detailed experimental and numerical research on this last phase of ignition. This need is also promoted by recent design trends which tend to reduce the number of ignition systems to lower weight and cost: such changes could directly affect the capability of the flame to propagate from one burner to the other. The development and validation of numerical tools, such as LES, able to evaluate the relight capabilities is thus required. To this end, LES of ignition sequences in the configuration of (Cordier, 2013) is performed and the results are reported in Chap. 10. Then the LES results of ignition sequence in the configuration of Bourgouin *et al.* (2013) are reported in Chap. 11.

Chapter 10

Inter-sector flame propagation in KIAI multi-injector burner

Contents

10.1 Experimental configuration 168
10.2 Numerical Set-up 169
10.2.1 Computational domain 169
10.2.2 Numerical solver parameters 170
10.2.3 Operating conditions 171
10.3 Non-reacting flow 171
10.3.1 Flow structures 171
10.3.2 Comparison of LES with experiments 172
10.3.3 Effect of spanwise confinement 173
10.4 Flame propagation modes 175
10.4.1 Initial conditions 175
10.4.2 Spanwise flame propagation 176
10.4.3 Axial flame propagation 178
10.4.4 Hybrid flame propagation 180
10.4.5 Ignition delays 181
10.5 Flame propagation mechanisms 185
10.5.1 Flame front displacement 186
10.5.2 Effect of the flow structures on the flame propagation 186
10.5.3 Thrust effect 189
10.5.4 Flow impact on the flame structure 190
10.6 Conclusion 192

The next step toward a better understanding of the ignition process in full scale configuration is to focus on the last phase of the ignition sequence. The size and complexity of both experimental and numerical set-up required to tackle the light-around process are the major obstacles

to its investigation. A detailed study requires simple, well controlled test rig in which experimental diagnostics are available to bring insights on the ignition process and serve as test cases for validation of numerical approaches at the same time. The objective of the present study is to investigate the effect of the distance between injectors on the ignition light-around process using both experimental measurements and LES. The direct comparison of experiments and simulations in the propagative phase of an ignition sequence brings new insights on the involved mechanisms. First LES of the experiment is performed under cold conditions to validate the approach by quantitative comparisons with measurements, as a prerequisite before studying ignition. LES of ignition sequences are then confronted to experiments in terms of propagation dynamics to verify the consistency of both approaches. Analysis is then conducted in an attempt to provide further understanding of the ignition transients.

The experiment are also performed by M. Cordier and co-worker from CORIA, and more details on the experimental techniques can be found in Cordier (2013). The numerical study is conducted with D. Barré (Barré, 2014) and L.Y.M. Gicquel. Most of the content of this section has been first presented at ASME TurboExpo Conference Cordier *et al.* (2013*c*) and published in a joint experimental and numerical paper published in Combustion & Flames Barré (2014):

Cordier M., Vandel A., Renou B., Cabot G., Boukhalfa M.A., Esclapez L., Barré D., Riber E., Cuenot B., & Gicquel L.Y.M. 2013. Experimental and numerical analysis of an ignition sequence in a multiple-injectors burner. *Proceedings of ASME Turbo Expo 2013* **GT2013-94681**.

Barré D., Esclapez L., Cordier M., Riber E., Cuenot B., Staffelbach G., Renou B., Vandel A., Gicquel L.Y.M. & Cabot G. 2014. Flame propagation in aeronautical swirled multi-burners: Experimental and numerical investigation. *Combustion and Flames* **161** (9), 2387-2405.

10.1 Experimental configuration

The experimental test rig is the direct extension of the configuration presented in Chap. 6 toward study of inter-sector flame propagation and is also part of the KIAI European project. To specifically investigate the inter-sector flame propagation and more particularly the influence of the distance between two consecutive injectors, several injectors similar to the one studied in Chap. 6 are aligned in a combustor. The rig allows to gradually increase the inter-injector spacing L_{sp} from 90 mm to a maximum of 250 mm. However, the maximum size of the test rig does not allows to keep a constant number of injector while increasing L_{sp}, so that the number of injectors drops from 5 for $L_{sp} = 90$ mm to 2 for $L_{sp} = 250$ mm. A picture of the experiments is shown in Fig. 10.1(left) along with a schematic top view of the injectors layout for the spacing studied in LES. The injection system is the one studied in Chap. 6 with a change of the plenum feeding lines due to space requirement. The combustion chamber is of variable spanwise length but of constant 100 mm depth and 270 mm height. Large optical access on the front and side faces allows to perform laser diagnostics, while the back consists of the metallic plate holding the spark plug. The numbering convention regarding injectors from left to right as illustrated in Fig. 10.1(right) is adopted hereafter. The main axial length of the burner is referred as the z-axis which also

coincides with the main flow direction. The origin of the axial direction is located at the injection systems inlets plane. The x and y-axes respectively referred to as spanwise and cross-stream coordinates, correspond to the injector alignment direction and the chamber width.

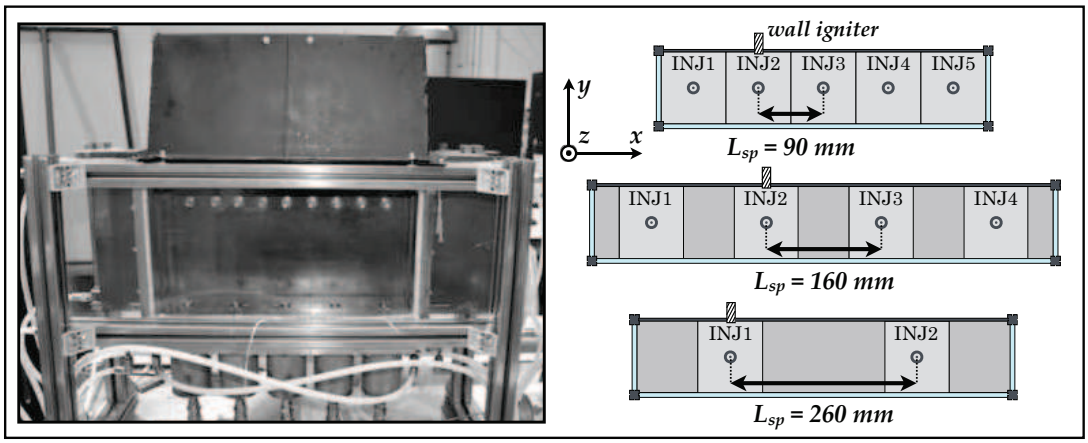

Figure 10.1: Picture of the experimental test bench (left) and schematic top view of the injectors layout for LES cases (right).

To keep as constant as possible the flow aerodynamics induced by the injectors, a 5.0 g/s air mass flow rate per injector is kept constant while the overall mass flow rate through the combustor is reduced as less injectors are employed. Experiments are conducted for 9 values of L_{sp} for which 20 tries are performed in order to obtained statistics on the key indicators of the ignition sequence. The burner is operated at $\phi = 0.66$, in leaner condition than the study performed in Chapter 7 since preliminary experimental tests have shown it brings out the influence of the inter-injector spacing on the ignition process. In the experiments, an ignition probability close to 1 is observed regardless of L_{sp}: sparking almost always results in a successful ignition of all the injectors.

10.2 Numerical Set-up

10.2.1 Computational domain

The computational domain comprises 5, 4 or 2 injection systems (plenum and swirler), the combustion chamber and a convergent exit. The geometrical characteristics of the injection system have been described in Chap. 6, and the mesh size in the plenum and swirler vanes is close to the one used in the single injector study. To study the flame propagation in the combustion chamber, a constant grid size of 0.9 mm is maintained in the lower part of the chamber (up to an axial position of 100 mm). This grid resolution is used for the three L_{sp} configuration investigated and the final mesh size for each configuration is mentioned in Table 10.1. The grid is coarser further downstream to limit the computational cost. The mesh in the SP9 configuration is illustrated in Fig. 10.2 with a slice through the injection system and the combustion chamber.

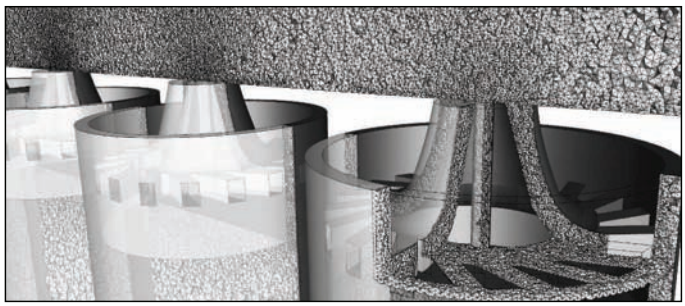

Figure 10.2: Slice of the computational domain showing the mesh refinement in the injection system vicinity for SP9.

	L_{sp} [mm]	Nb. inj. [-]	Nb. tetra. [M]	Nb. vertices [M]	V_{min} [m^3]
SP9	90	5	37.7	6.8	1.8 e^{-12}
SP16	160	4	43.1	7.7	1.8 e^{-12}
SP26	260	2	21.2	3.8	1.8 e^{-12}

Table 10.1: Main characteristics of LES configurations and meshes.

10.2.2 Numerical solver parameters

LES are performed with AVBP and the numerical parameters of the solver are listed in Table 10.2.

	Numerical parameter
Convection scheme	TTGC: $\mathcal{O}(3)$ in space & time (Colin & Rudgyard, 2000)
Diffusion scheme	2Δ operator
SGS model	WALE (Nicoud & Ducros, 1999)
Artif. viscosity	Colin model: $\epsilon^{(2)} = 0.01$, $\epsilon^{(4)} = 0.005$
	Boundary conditions
CH_4 inlets	NSCBC (Poinsot & Lele, 1992) (velocity)
Air inlets	NSCBC (Poinsot & Lele, 1992) (velocity)
Outlet	NSCBC (3D) (Granet *et al.*, 2010) (pressure)
Walls	Adiabatic non-slipping walls

Table 10.2: Numerical parameters of AVBP.

Chemistry source terms are described with the 2S_CH4_BFER two-step mechanism (Franzelli *et al.*, 2012), using PEA adjustment (Franzelli *et al.*, 2010). The DTFLES model is used with efficiency function from Colin *et al.* (2000) to handle the flame front on the LES grid. In the operating conditions simulated, the reduce scheme gives a laminar flame speed $S_L^0 = 0.17\ m.s^{-1}$ and a flame thickness $\delta_L^0 = 0.815\ mm$. The LES grid resolution mentioned in 10.2.1 is about 1.1 δ_L^0, so that thickening factors $\mathcal{F}$ of the order of 6 are expected in regions where the flame consumes mixture at the overall ϕ.

Ignition is triggered by an aeronautical spark plug located at $z = 23\ mm$ and 5 mm from the bottom wall of the chamber. The spark is modeled with the ED model (Lacaze *et al.*, 2009*a*)

using the following parameters values: $\varepsilon_i = 135mJ$ (corresponding to 30% (Teets & Sell, 1988) of the experimental 450 mJ/pulse spark plug), $\Delta_t = 300\mu s$ and $\Delta_s = 15mm$. The flame kernel is generated in a flammable and low turbulence region. In these condition, the probability of extinction during phase 1 is extremely low.

10.2.3 Operating conditions

The burner is operated in ambient conditions, imposed in the LES as a 298 K inlet temperature and a 1 Atm outlet pressure. The operating conditions are listed in Table 10.3.

	T [K]	P [Atm]	$\dot{m}_{air}/inj$ [g/s]	$\dot{m}_{CH4}/inj$ [g/s]	$\dot{m}_{total}$ [g/s]	P_{th} [KW]
SP9	298.0	1.0	5.0	0.192	25.96	48.0
SP16	298.0	1.0	5.0	0.192	20.77	38.4
SP26	298.0	1.0	5.0	0.192	10.38	19.2

Table 10.3: Operating conditions for the 3 configurations.

10.3 Non-reacting flow

Prior to study ignition sequences, experimental and numerical isothermal results are used conjointly to identify the major structures of the flow and point out the changes induced by an increase of the spacing between injectors. The first two statistical moments are obtained by time-averaging. Statistical quantities are collected for 35 ms for the **SP9** and **SP16** cases and 18 ms for the **SP26** configuration in LES, while 1000 PIV of PLIF snapshots are used in experiments.

10.3.1 Flow structures

In all cases, the structure of individual injector is similar to the one described in Chap. 6: the SWJ issued from the swirler induces an adverse axial pressure gradient resulting in an IRZ. At the bottom of the IRZ, a stagnation point is located at the meeting location between the IRZ back flow and the incoming methane jet. This stagnation point is located approximatively 10mm downstream the injection nozzle for all cases. Finally, on the outer part the SWJ, secondary recirculation zone called here Lateral Recirculation Zones (LRZ) are present. Due to the larger size of the combustion chamber, the IRZ is closed further downstream as compared to the single injector case. These flow structures are schematically depicted in Fig. 10.3 along with time-averaged axial velocity contours.

Large scale counter-rotating vortices are observed in LRZ, resulting in low velocity reverse flow.

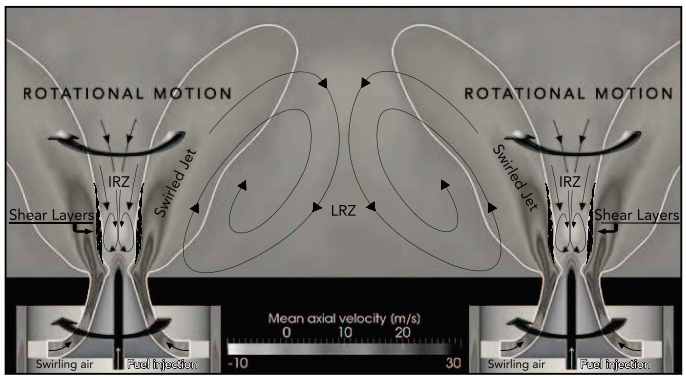

Figure 10.3: Characteristic zones of a swirled flow. Grayscale corresponds to the LES time-averaged z-component velocity in a y-normal cut. The white line highlights the limits of the SWJ and schematic arrows illustrate fluid motion in both IRZ and LRZ.

10.3.2 Comparison of LES with experiments

10.3.2.a Time-averaged velocity profiles

The accuracy of the LES results is evaluated by comparing time-averaged velocity profiles to experimental data at 3 axial positions corresponding to $z/D = 0.25$; 1; 1.5 in the local cylindrical reference frame (r,θ,z) associated to one specific injector: *i.e.* with origin located at the bottom end of the whole chamber on the center-line of the injector of interest. Figure 10.4 displays the comparison of the axial and radial components for the **SP9** case. For this configuration, the simulation captures well the 3 typical zones of the swirling flow. The location of the stagnation point is also well recovered and the SWJ opening as well as recirculation zone sizes are reproduced. Note that the penetration of the methane jet in LES is consistent with single injector results but greater in experiments: the change in feeding lines shape have a direct effect on the jet. The magnitude of the time-averaged axial and radial velocity components is overall satisfying compared to measurements. Similar results are obtained for the **SP16** and **SP26** cases when compared to experimental data (not detailed here).

10.3.2.b Mixing

Mixing is assessed by comparing the equivalence ratio profiles of LES and experiments shown in Fig. 10.5. LES results are in good agreement with measurements for the 3 cases, identifying homogeneous mixtures in the LRZ thanks to the rapid mixing between air and methane after injection. It is also noted that mixing is slightly more efficient for larger spacing, probably due to a narrower SWJ opening. The experimental measurements for the mixture fraction fluctuations of Cordier (2013) show that the equivalence ratio fluctuations further than $z/D = 0.5$ and $r/D = 0.75$ are negligible, and so we can treat the flame evolution from the spark location with premixed flame concepts.

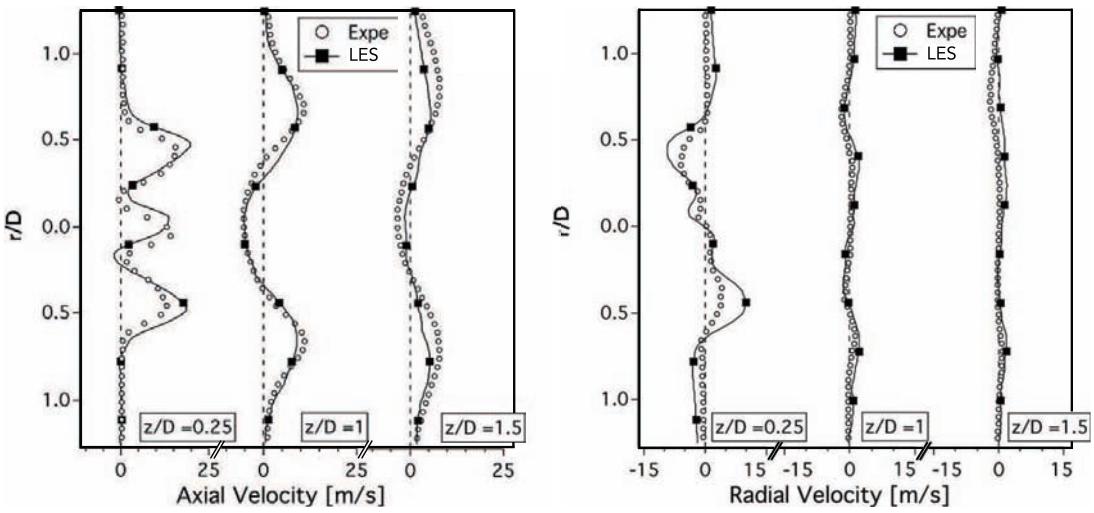

Figure 10.4: Experiments versus LES: time-averaged axial (left) and radial (right) velocities for the **SP9** case.

10.3.3 Effect of spanwise confinement

Figure 10.6 details the shape of the SWJ for the three configurations. The jet opening is clearly larger in the **SP9** case and the angle decreases with increasing injector spacing. The jet penetration is found to be independent of the confinement and no substantial differences are observed on the time-averaged radial velocity profiles between the three cases. These observations are in agreement with experimental findings of Cordier (2013). When injectors are close, their SWJ interacts at a small distance from the bottom of the combustion chamber. As L_{sp} is increased, the SWJ penetrates further in the combustion chamber and their interaction stops.

The change from the interaction to the independence regime also modifies the shape and size of the LRZ. Figure 10.7 shows a central cut plane through the combustion chamber colored by the time-averaged axial velocity along with projected streamlines. A constant LRZ height to width ratio of 2 is found for all cases. In the independence regime larges counter-rotative vortices are located in the LRZ, while in the interaction regime the meeting of the SWJ result in a more turbulent flow.

The shape of the LRZ is also modified in the transverse direction (between the injector and the wall) as illustrated on Fig. 10.8: time-averaged axial velocity field is plotted in a x-normal cut with iso-contour of zero axial velocity in black. The spark position is schematically represented and the height of the LRZ highlighted by the dashed line. A non-trivial behavior is found with the LRZ length first increasing with injector spacing between **SP9** and **SP16** then strongly decreasing when the spacing is further increased to **SP26**. While spark is located in the LRZ for the **SP9** and **SP16** cases, it is above the LRZ closure location for the **SP26** case. Note that the spark is close to the time-averaged LRZ end in the **SP26** case and that flow variability could have a significant impact.

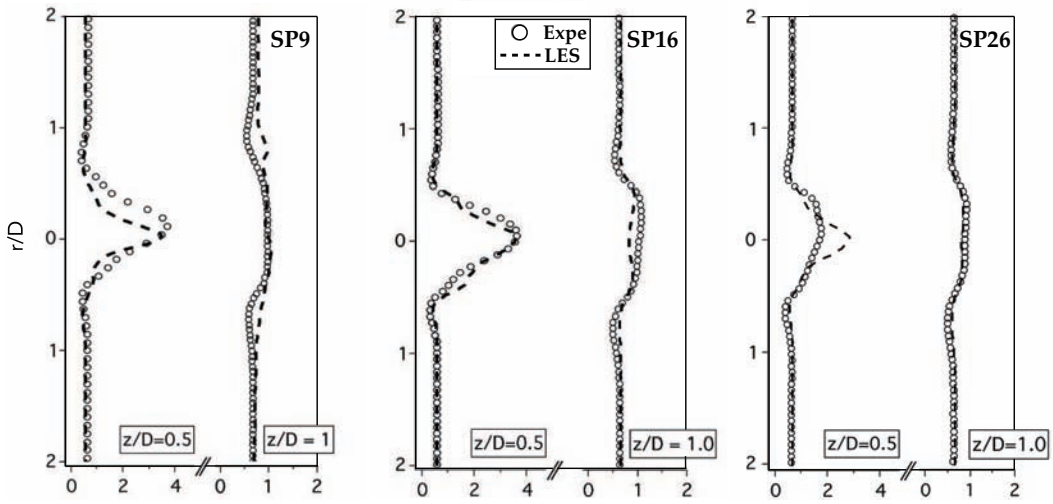

Figure 10.5: Experiments versus LES: time-averaged equivalence ratio for **SP9** (left), **SP16** (center) and **SP26** (right) cases.

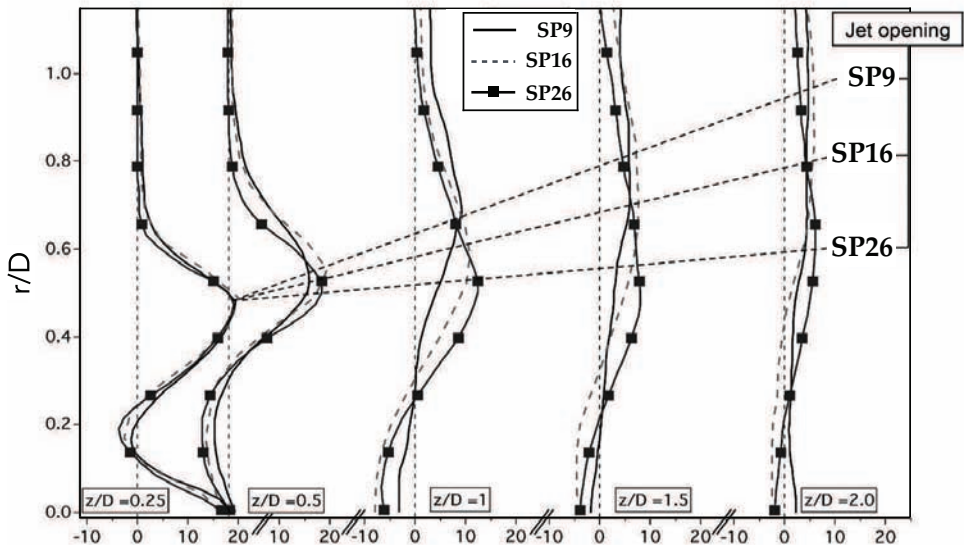

Figure 10.6: LES: time-averaged axial velocity component illustrating the jet opening angle obtained in the three configurations.

Finally, the swirl motion of individual injectors induces a global circumferential motion in the combustion chamber. This motion is proportional to both the volume of the combustion chamber and the rotational momentum. The latter depends on the number of injectors while the former is changed between cases. The maximum strength of the circumferential motion occurs in the **SP9** case, and is the weakest in the **SP26**.

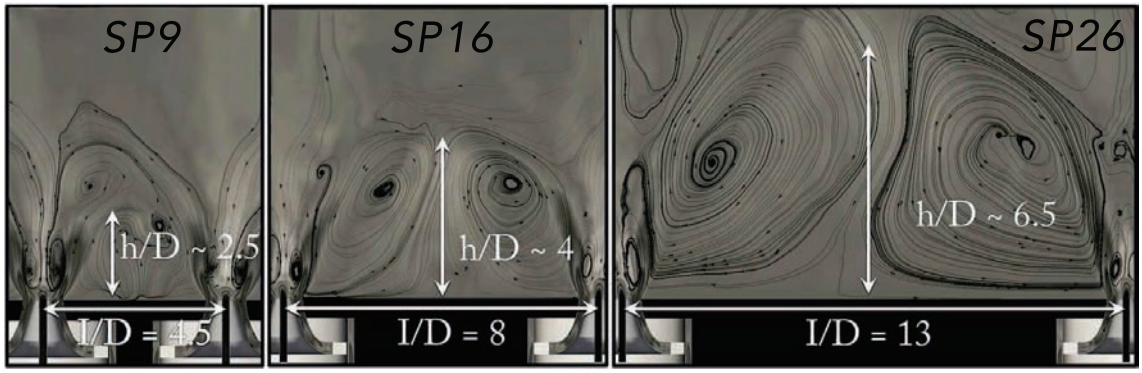

Figure 10.7: LES: time-averaged axial velocity component along with projected streamlines. An estimated of the width and height of LRZ is also provided for each case.

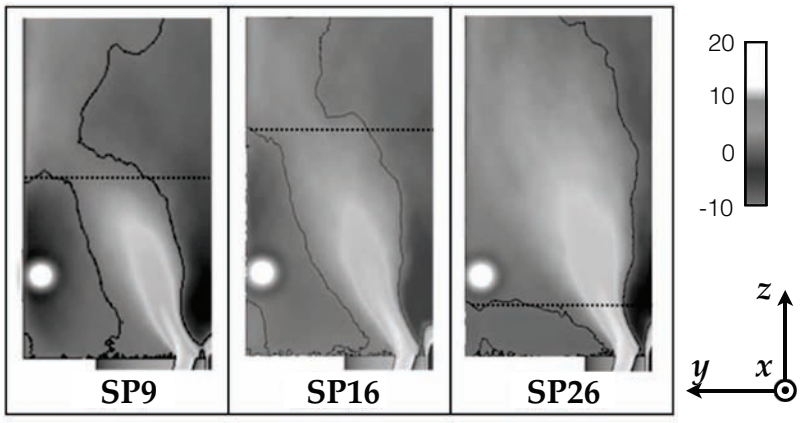

Figure 10.8: LES results: schematic view of the spark plug location ($z/D = 1.15$). Grayscale: time-averaged axial velocity, dashed lines: height of the LRZ, solid lines: iso-contour of zero axial velocity.

10.4 Flame propagation modes

Flow conditions at the ignition time play a major role in the ignition process and are presented first. Flames dynamics are then described and analyzed using instantaneous snapshots extracted at several key instants of the ignition sequences, from both experimental and numerical data, with a complementary analysis based on the flame kernel position for the **SP9** and **SP26** configurations. Finally, ignition sequences are compared in terms of ignition delays of the individual injectors.

10.4.1 Initial conditions

The study conducted in Chap. 7 or the study of Subramanian *et al.* (2010) show that the variability of the initial conditions propagates through the whole ignition sequence. For this config-

uration, experimentalist observed variations of the overall ignition delays. To evaluate the role of the cold flow state, for the intermediate spacing case (**SP16** configuration), two ignition sequences (**SP16(1)** and **SP16(2)**) are performed, starting at two different instants ($t1$ and $t2$) of the stationary cold flow. The first instant is chosen arbitrarily while the second is chosen so that the flow at the spark is significantly different from the flow at $t1$.

The time evolution of the cold flow velocity components at the spark location is detailed in Fig. 10.9. The profiles are shifted in time to place the instant of ignition at t = 0 ms. Ignition in the **SP9** configuration is performed in a zone presenting high positive spanwise velocity while the **SP16** and **SP26** cases present a lower component partly induced by the lower circumferential mean flow. Axial velocities are slightly higher in the **SP16** case than in the **SP9** case, but still have negative values while in the **SP26** case the change in confinement places the energy deposition in a zone of positive axial velocity as seen in Fig. 10.8.

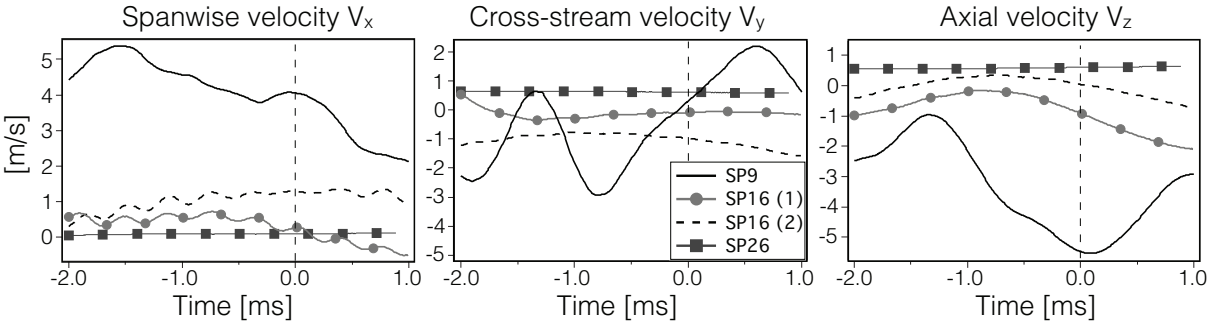

Figure 10.9: LES results: temporal evolution of the instantaneous spanwise, cross-stream and axial velocity components at the spark location for each case.

10.4.2 Spanwise flame propagation

The first ignition mode is identified experimentally for spacings ranging between 90 mm and 150 mm and is illustrated on the **SP9** configuration. Figure 10.10 presents snapshots of the signal recording of the experiments that account for the CH and C2 light emissions. LES visualizations of volume rendering of heat release for the same case are shown in Fig. 10.11. In both figures, the times of visualization are the same and correspond approximately to the successive ignition of each injector. Despite the stochastic nature of ignition, experiments and LES agree well on both the successive injector ignition order and the time delay between them.

Early after sparking, the flame interacts directly with the nearby injector swirling flow (INJ2). Then it is rapidly swept by the flow induced by INJ2 and INJ3 leading to the birth of two distinct branches as shown in Fig. 10.11 (t = 11 ms). As time proceeds, the flame follows essentially a lateral/spanwise motion in the bottom part of the chamber. This spanwise flame propagation process keeps on spreading at t = 23.5 ms (Figs. 10.10 and 10.11) with still a pronounced winding around the injector while the flame reaches INJ2. The following successive ignitions of INJ3 and INJ4 occur at t = 34 ms and t = 37.5 ms in respectively LES, slightly before the corresponding events in the experiments. The strong expansion of burnt gases leads to a large amount of burnt

gases at the exhaust at this time. The last two injectors are reached by the flame lastly approximatively at t = 47.5 ms and 57.5 ms (60 ms for experiment) to finally obtain fully stabilized flames on all injectors.

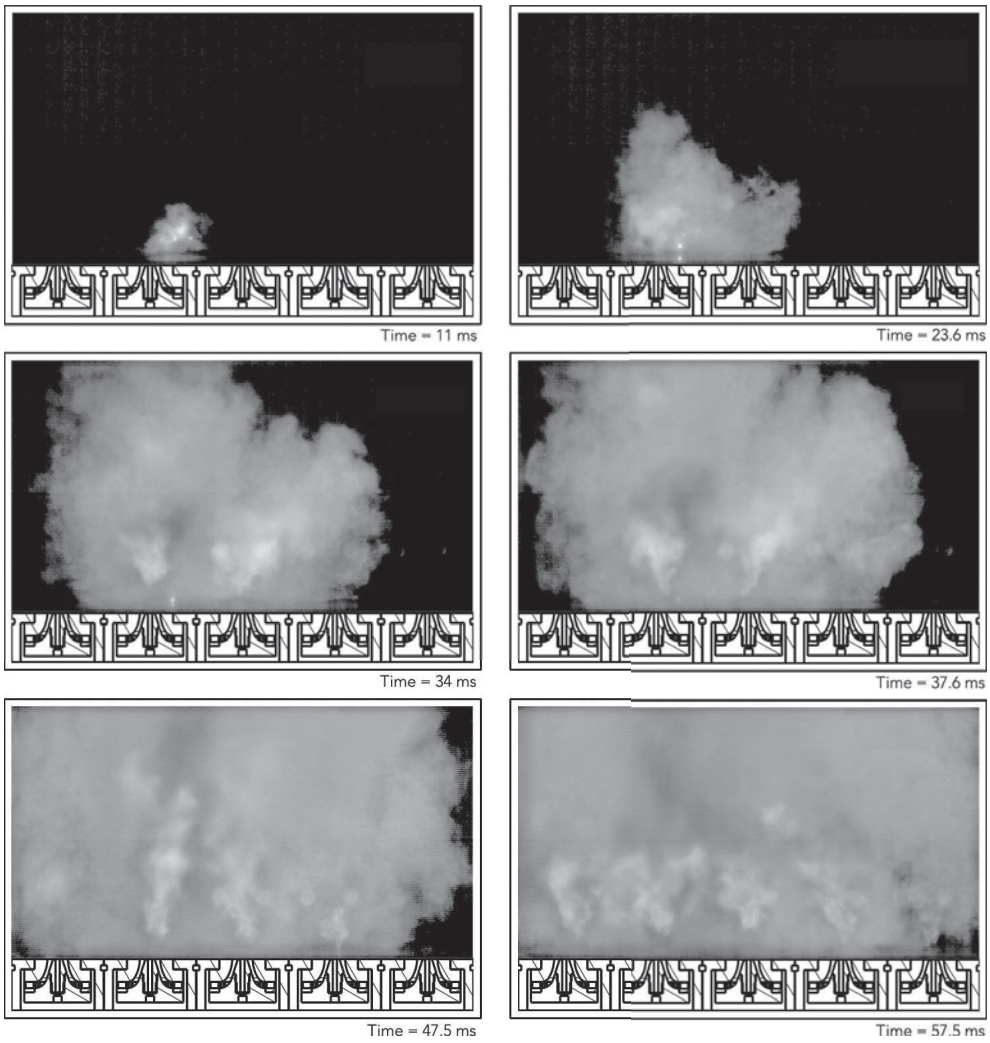

Figure 10.10: Experiments: fast visualization of the flame showing a spanwise propagation for SP9 case.

Figure 10.12 shows a quantitative evaluation of the flame propagation based on flame contour detection and flame front position calculation from instantaneous snapshots, in the axial and spanwise directions. The radius is evaluated as the distance between the initial flame kernel position and the flame spanwise or axial location. A quasi isotropic evolution of the flame front is observed experimentally while numerically, the flame development is non-isotropic with a larger spanwise radius. Note that the results are averaged over 10 experimental ignition sequences while a single LES realization is available which might explain the offset between experimental and numerical findings.

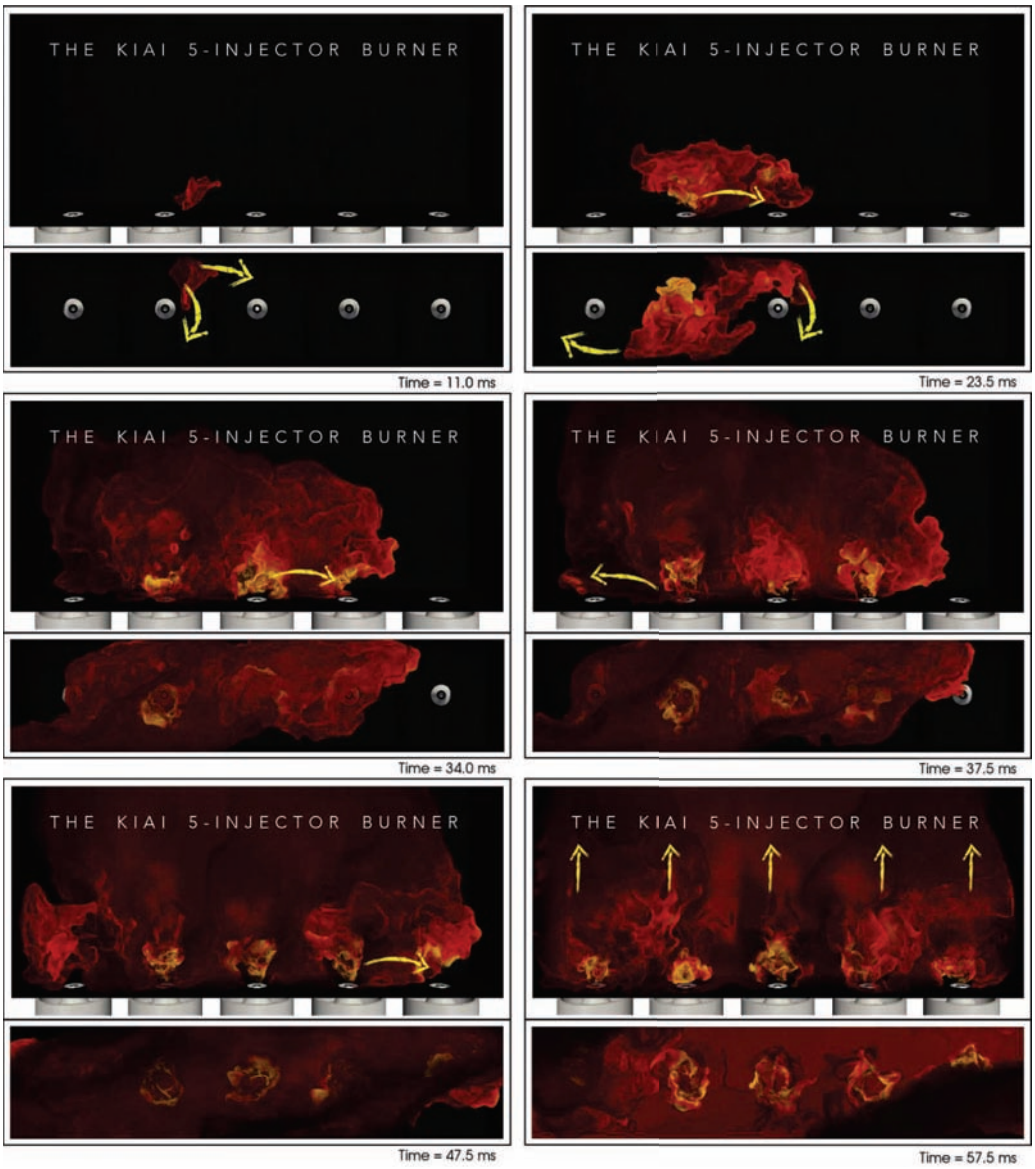

Figure 10.11: LES results: instantaneous snapshots of the SP9 ignition sequence visualized by the volume rendering of heat release (front and top views).

10.4.3 Axial flame propagation

The second ignition mechanism is found experimentally for the largest spacings, between 200 mm and 260 mm. It is mainly dominated by an axial flame propagation. Figures 10.13 and 10.14 present ignition sequences obtained for the largest spacing configuration **SP26** in experiments and LES respectively. Both the ignition times of the first injector and the subsequent delay to ignite the second injector obtained in LES are in good agreement with the experimental results.

After the spark, the flame kernel survives but no increase of flame surface is observed for a few milliseconds (Fig. 10.13, t = 14 ms). During this time, the flame remains sensitive to extinction.

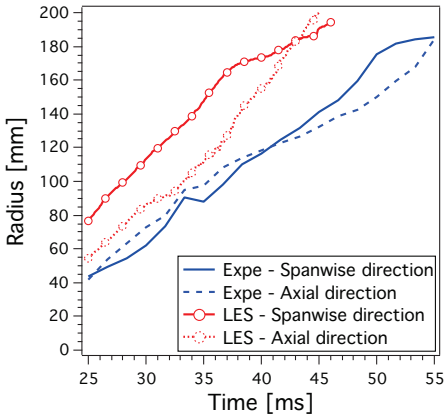

Figure 10.12: Experiments versus LES: estimations of local flame propagation for SP9 case.

Then, the flame develops and is mainly convected in the axial direction (Figs. 10.13 and 10.14, t = 14 ms). As time proceeds, the flame expands in a region confined between the SWJ of INJ1 and the wall. It starts filling the top of the combustion chamber until a fragment is captured by the IRZ to propagate upstream and finally ignite INJ1 at t = 46.2 ms in LES and t = 54.3 ms in experiments (Fig. 10.18). The flame extends far downstream and is eventually captured by the IRZ of INJ2 to ignite it at t = 117 ms and t = 137.3 ms in experiments (Fig. 10.18). Ignition of INJ2 requires the flame to circumvent the SWJ and penetrate the IRZ but due to the high turbulent behavior of the SWJ, the ignition time of INJ2 is subject to high fluctuations. Note that in real combustors, such flame propagation mechanism is not likely to occur when secondary air dilution is present.

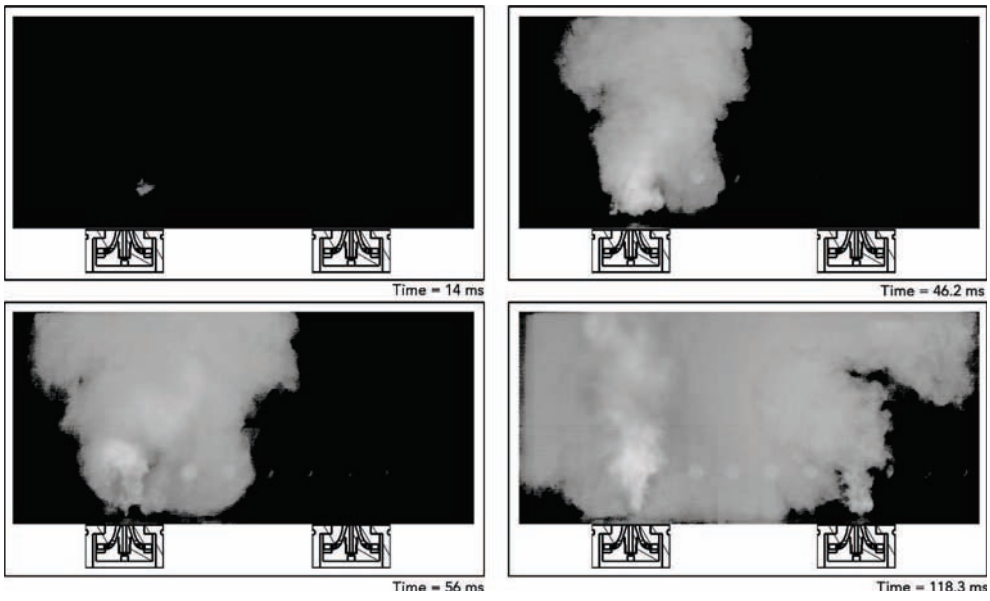

Figure 10.13: Experiments: fast visualization of the flame showing an axial propagation for SP26 case.

The quantitative evaluation of the flame propagation reveals in this case a non-isotropic evolution (Fig. 10.15). For both LES and experiments, the axial flame radius is higher than the



Figure 10.14: LES results: instantaneous snapshots of the SP26 case ignition sequence visualized by the volume rendering of heat release (front and top views).

spanwise one and differences increase with time. These trends completely differ from **SP9** configuration (Fig. 10.12), confirming the different propagation mode.

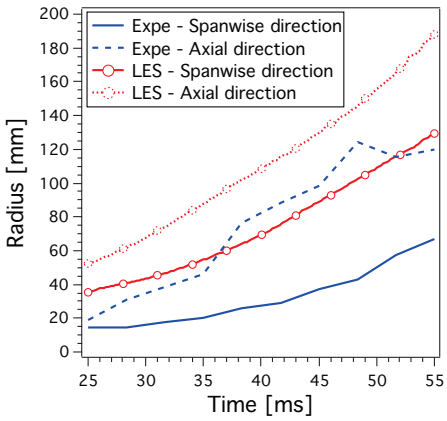

Figure 10.15: Experiments versus LES: estimations of local flame propagation for SP26 case.

10.4.4 Hybrid flame propagation

The third ignition mechanism is observed for intermediate spacings between 160 and 180 mm and is illustrated in **SP16** in Figs. 10.16 and 10.17 for experiments and LES respectively.

After the kernel creation, low flame development or convection is observed in both axial and spanwise directions while the flame is rapidly swept by the SWJ of INJ2 (Figs. 10.16 & 10.17, t = 14 ms). Once INJ2 is ignited, a flame front propagates on each side, where a hybrid propagation mode is observed with competing spanwise and axial motions. Figures 10.16 & 10.17 at t = 48 ms or 57 ms show pathways of the flame front (highlighted with arrows). The flame front is convected by the SWJ and fills the IRZ in the axial direction to a certain extent, while it also propagates in the spanwise direction in the low velocity LRZ under the action of the volumetric burnt gas expansion. Early after sparking the **SP16(1)** exhibits a more axial flame development as compared to **SP16(2)** due to the different initial flow conditions (Fig. 10.17) delaying the spanwise flame propagation. This initial time delay is further increased as time proceeds since in the **SP16(2)** the flame front follows a more spanwise pathway in the lower part of the combustion chamber while in the **SP16(1)** a flat flame front is observed (Fig. 10.17 at t = 57 ms).

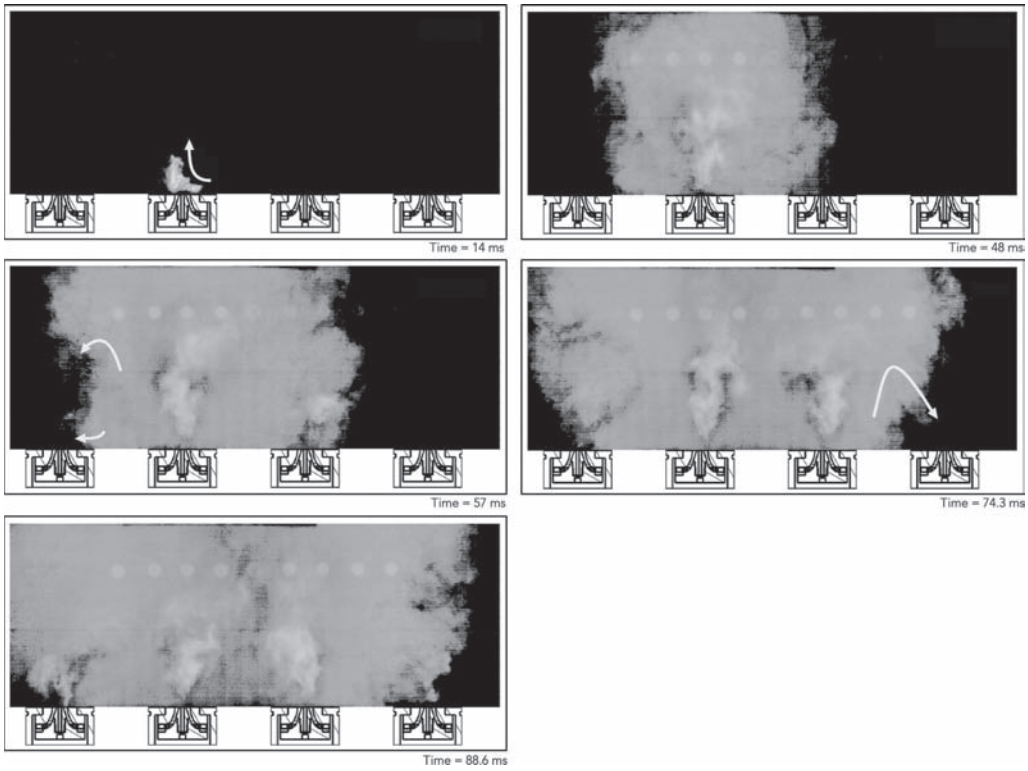

Figure 10.16: Experiments: fast flame visualization showing a hybrid propagating mode for SP16 case.

10.4.5 Ignition delays

10.4.5.a Individual injector ignition

As the flame reaches the injector location, it eventually penetrates and stabilizes in the IRZ. When the flame enters the lower part of the IRZ, the richer mixture induces higher light emission in the experiments. Similar behavior is observed in the LES visualization of heat release and is used to evaluate ignition times in both experiments and simulations. The methodology consists in

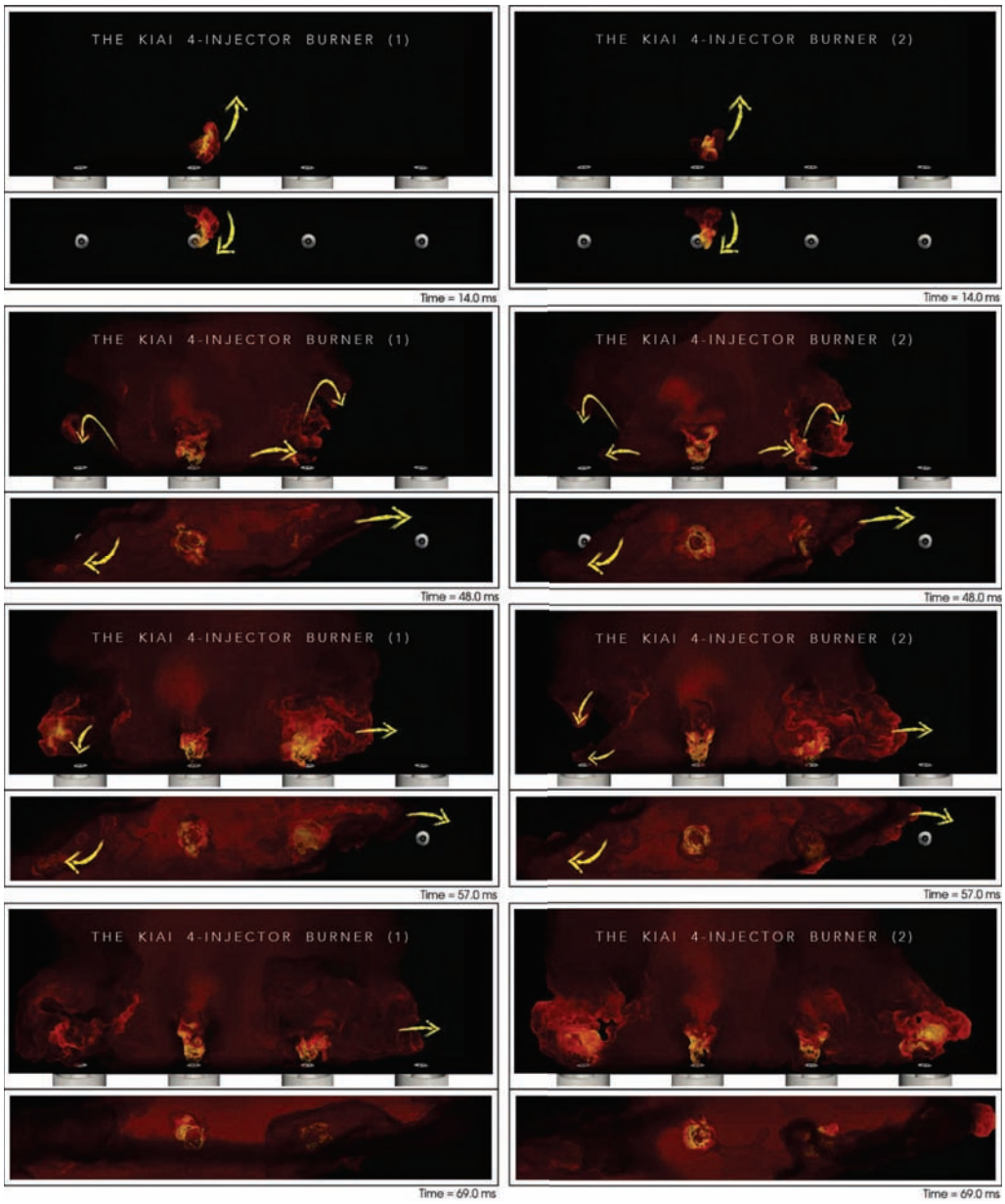

Figure 10.17: LES results: instantaneous snapshots of **SP16(1)** (left) and **SP16(2)** (right) ignition sequences visualized by the volume rendering of heat release (front and top views).

detecting visually the sudden heat release increase on the recordings. Note that in experiments, multiple tests also provide an evaluation of variability. This methodology is obviously associated to some uncertainty and it has been evaluated with a more quantitative approach based on the mean heat release in the IRZ extracted from LES data in the **SP9** case.

Individual injector ignition times are listed in Fig. 10.18 for experiments and LES. The first observation from Fig. 10.18 is the good agreement between LES and experiments concerning the delays between successive injector ignition times. These results show that LES accurately

reproduces the propagative phase of the ignition sequence. The order of injector firing is directly linked to the flame propagation dynamics in the combustion chamber described in Sec. 10.5. A 10 ms offset is estimated between the simulated ignition time of INJ2 and the mean experimental one in the **SP9** case and reported in all cases. The origin of this offset may come from the uncertainty of the kernel created by the ED model, the transition from a laminar flame kernel to a turbulent expanding flame that is not perfectly handled by the combustion model and the uncertainty of the above methodology for the ignition time estimation.

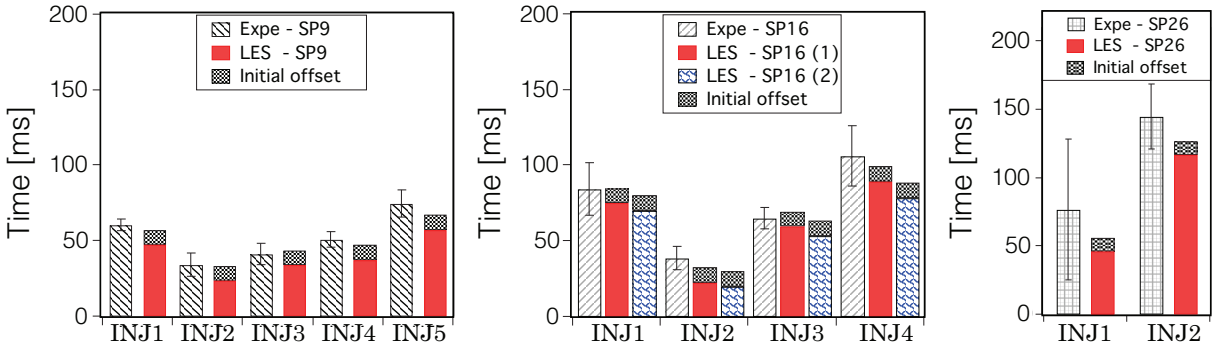

Figure 10.18: Experiments versus LES: injectors successive ignition times [ms].

10.4.5.b Inter-sector propagation delay

Another interesting feature for the design of the burner is the injector to injector flame propagation time. It is evaluated here between the first and second injector ignition and is shown in Fig. 10.19 where experimental data is averaged over 20 ignition tests and numerical results correspond to a single realization. Error bars on the experimental points show the variability of the experimental results. The agreement between LES and experiments is excellent, demonstrating that LES captures the main controlling processes. Two main trends are identified. The injector/injector time evolves linearly with the spacing in the low spacing range where ignition is governed by the spanwise propagation. Error bars show a low variability in the experiments, qualifying spanwise ignition as a safe mode. For a spacing of 160 mm, the injector/injector time increases more markedly as well as the variability of the experimental results. For large spacings, the propagation from one injector to its neighbor becomes more random and conditioned by the capture of a flame portion by the IRZ of the neighboring injector.

10.4.5.c Overall flame growth

The direct comparison between experiments and LES is not an easy task. To construct integral indicators tracking the ignition advancement, the temporal evolution of the integrated light emission is extracted from the high speed camera recording. The camera is equipped with band-pass filter in order to capture only emission of CH and C_2. These species are not present in the LES, but can be closely related to the heat release rate. This point is investigated using laminar premixed flames computed with CANTERA using the GRIMECH 3.0 detailed mechanism.

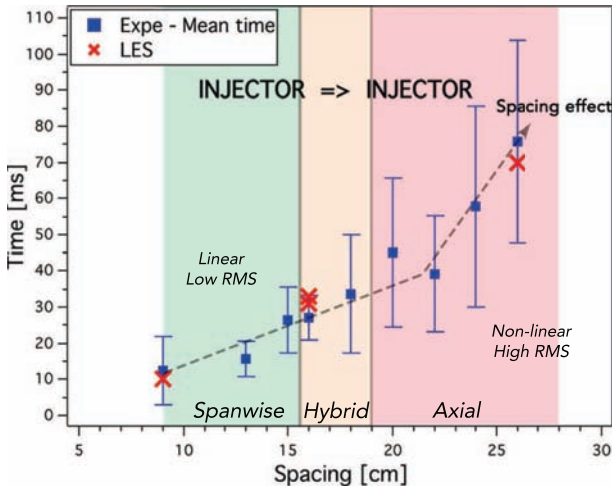

Figure 10.19: Experiments versus LES: spacing effect on the first injector/injector propagation time.

The results are presented in Fig. 10.20 showing a collection of laminar premixed flame at various equivalence ratio. Only the CH is present in the GRIMECH 3.0 mechanism, but for the conditions spanned, the heat release peak and CH mass fraction are found to be very close.

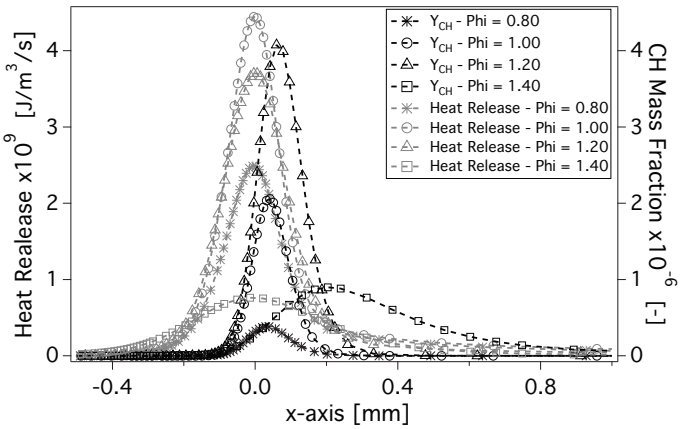

Figure 10.20: Experiments versus LES: spacing effect on the first injector/injector propagation time.

The spatial integration of pixel intensities in both experimental (C_2 and CH emissions) and LES (heat release) snapshots enable to obtain a comparable line of sight integrated representation of the flame evolution. This is represented in Fig. 10.21 as a function of time where both quantities are normalized by their respective maximum values. Results show a fairly good agreement, demonstrating again the capability of LES to capture the main features and mechanisms of the ignition process. It also highlights the much slower growth rate of the **SP26** case compared to the **SP9** and **SP16** cases, and the experimental variability.

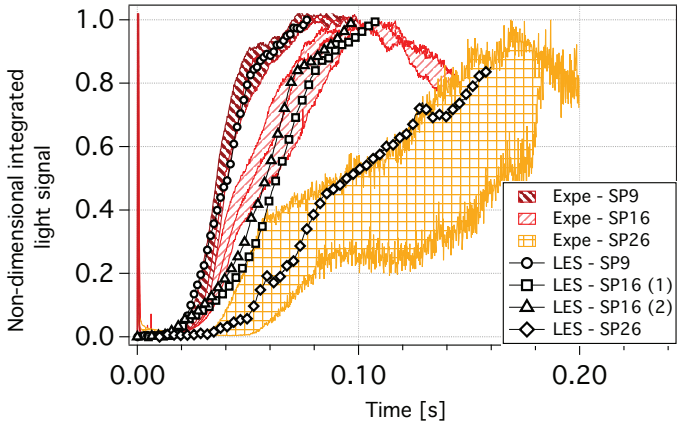

Figure 10.21: Experiments versus LES: temporal evolution of the integrated light signal.

10.4.5.d Temporal evolution of the thermal power

The temporal evolution of the burner thermal power is another interesting quantity to track during the ignition transient. The integral of the heat release in the combustion chamber is computed and normalized by the thermal power of the burner in stable regime assuming the complete combustion of the fuel: 48 kW, 38.4 kW and 19.2 kW for the **SP9**, **SP16** and **SP26** cases respectively. The results are showed in Fig. 10.22 along with the timing of the individual injector ignition. The first observation is that the integrated heat release rate does not follows the same trend than the indicator reported in Fig. 10.21: the integral of the light intensity is closer to the evolution of the burnt gases volume than the heat release one. For **SP9** & **SP16** cases the heat release rate remains low prior to the ignition of the first burner while it is already more than twice that of the stable regime when igniting the first injector in the **SP26** case. The maximum heat release rate is found to be several time the level of the stable regime because of the large flame area attained during the flame propagation. From a design point of view, the overshoot of heat release strongly increase the pressure in the combustor and can also induce an early increase of the mass flow rate through the combustion chamber due to acceleration of the turbine.

10.5 Flame propagation mechanisms

A simple calculation based on the length of the combustion chamber and the overall ignition delay evaluates the mean spanwise flame velocity over the complete **SP9** sequence at about 5 m/s which is much higher than a typical turbulent flame speed: this means that the flow plays a major role in this process. In the following, the extreme **SP9** and **SP26** cases, where the spanwise and axial propagation modes are clearly identified, are further investigated.

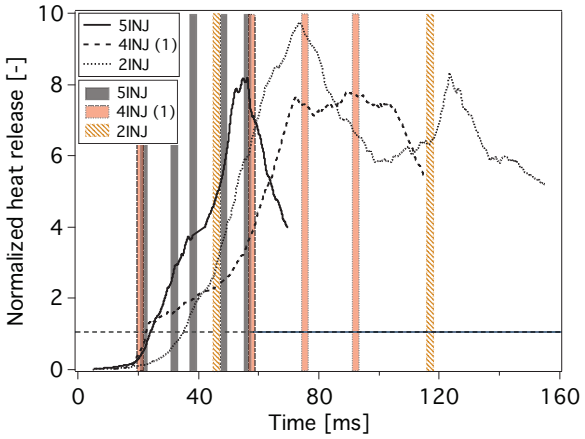

Figure 10.22: LES result: temporal evolution of the integrated heat release for the spacing studied in LES.

10.5.1 Flame front displacement

Past studies have shown that the competition between convection speed and flame displacement speed plays a crucial role in the success of ignition especially during the propagation phase where the flame front must reach the injector nozzle in order to stabilize. In cases of low gas velocity, the flame is able to propagate upstream Ahmed & Mastorakos (2006); Ahmed *et al.* (2007*a*) while in configurations with high gas velocity, the flame tends to be convected downstream Ahmed *et al.* (2007*a*); Read *et al.* (2008); Marchione *et al.* (2009).

The competition of the convective and thermo-diffusive flame propagation processes is investigated using the various definition of the flame speed introduced in Sec. 3.2.1.b. Contributions of S_d^* and $|\boldsymbol{w}|$ to the flame front speed are given for the **SP9** and **SP26** cases in Fig. 10.23, showing the PDF of the flame displacement speed and the flow speed calculated along the flame front ($0.18 < c < 0.22$) at two different times, taken before and after the flame reaches the SWJ (illustrated in Fig. 10.11 at t = 11 ms and t = 23.5 ms for the **SP9** case). First, it is remarkable that the flame displacement speed has a much smaller direct contribution to the total flame speed as compared to the flow speed, whatever the number of injectors or the instant considered.

Regarding the flow velocity, the PDF at early stages shows lower values in the **SP26** than in the **SP9** configuration, as expected due to a weaker circumferential motion in the LRZ. After the flame reaches the SWJ, the flow velocity at the flame location is spread over a wide range [0.0-20.0 m/s] in the **SP9** case while the main part of the flame surface remains in the range [0.0-5.0 m/s] for the **SP26** case since the flame has mainly propagated downstream in low velocity regions. Thus the flame is more convected by the underlying gaseous flow rather than self-propagating.

10.5.2 Effect of the flow structures on the flame propagation

The convective flow speed $\boldsymbol{u}$ being the major contribution to the total flame speed, the flow structures are now studied to determine their role in the appearance of either propagation mode.

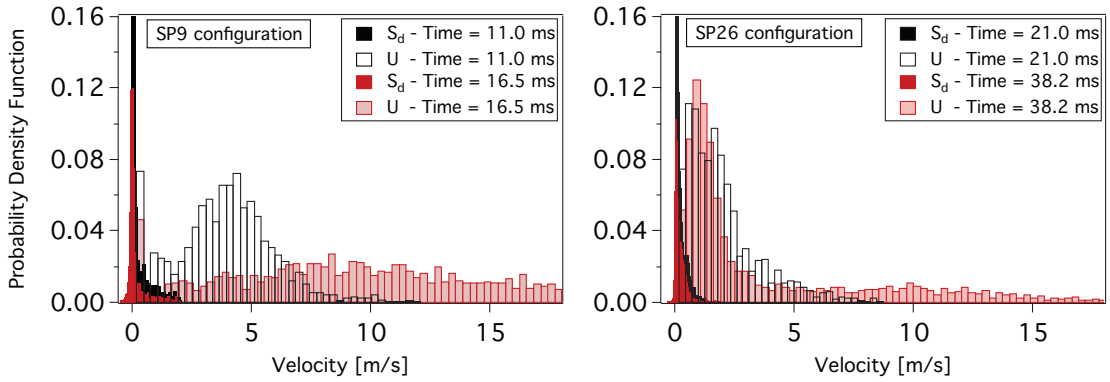

Figure 10.23: LES results: PDF of the flame front displacement S_d^* and the flow velocity magnitude $|\boldsymbol{u}|$ at two different times before and after the flame reaches the SWJ for the **SP9** (left) and **SP26** (right) configurations.

10.5.2.a Flame kernel trajectory

Figure 10.24 illustrates the different behaviors of the flame kernel motion by describing the Flame Centre of Gravity (FCG) position during the first instants after ignition defined by:

$$x_{i,FCG} = \sum_{n=1}^{N} \frac{\rho_n V_n \, x_{i,n}}{\rho_n V_n} \tag{10.1}$$

where $x_{i,FCG}$ is the i-th coordinate, ρ_n and V_n the density and volume at the n-th node and N the number of nodes having a temperature higher than 600K.

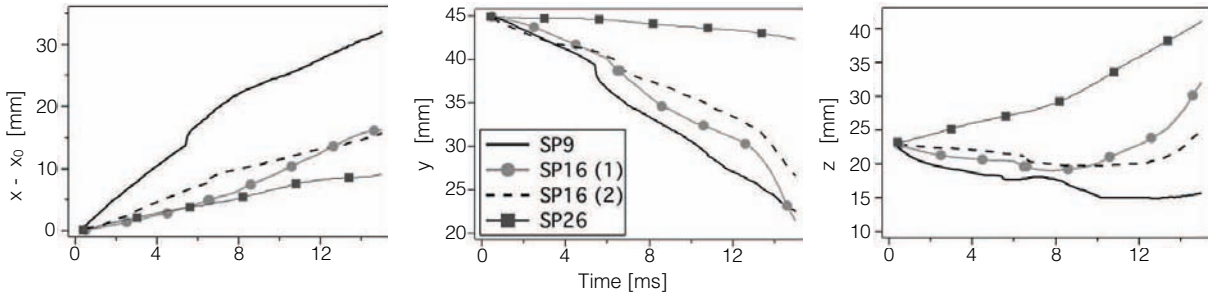

Figure 10.24: LES results: Temporal evolution of the position of the FCG during the first instants for the three configurations. (left) spanwise, (center) cross-stream, (right) axial positions

Note that because the energy deposit x_0-coordinate varies with the three configurations, the relative x-coordinate x-x_0 is used in Fig. 10.24. At the spark location, the flow is dominated by the circumferential motion. The latter is strongest in the **SP9** case, promoting a fast convection of the flame kernel in the spanwise direction (Fig. 10.24(left)), favorable to the spanwise propagation mode. The narrower SWJ in the **SP26** case prevents the flame from being quickly swept by the closest injector, and the consequence is a small cross-stream displacement of the

FCG as compared to the other cases (Fig. 10.24(center)). For this case, changes in LRZ shapes (Fig. 10.6) induce a convection mainly in the axial direction, premise of the axial propagation mode (Fig. 10.24(right)).

10.5.2.b Effects of the swirl motion

As the flame further expands, it eventually meets the strongly rotating flow in the vicinity of the SWJ. To illustrate the interaction of the flame front with the swirl motion, Fig. 10.25 shows a top view of the combustion chamber with the flame front position in the **SP9** case from both experimental and numerical sequence visualizations. Experimental results are obtained by the binarization of images at an adequate light intensity threshold to detect the flame contour. Following the flame kernel convection in the positive spanwise direction, two flame propagation directions can be identified (t = 14.1 ms). A first flame branch moves essentially along the metallic plate towards INJ3, following the mean flow circumferential motion. A second branch develops in the cross-stream direction and is rapidly captured by the SWJ of INJ2. While the first branch keeps its spanwise direction, the second one progressively rolls-up around INJ2 (t = 17.5 ms and t = 18.7 ms) and finally penetrates the IRZ before stabilizing (t = 21.2 ms). This flame pathway is also observed for the **SP16** cases to a lesser extent and is partially responsible for a strong spanwise motion of the flame of **SP9** and **SP16** cases. The same roll-up mechanism around is observed INJ3 as for INJ2 but at later time. Such flame motion is further delayed in the **SP26** ignition sequence since the flame front interact with the SWJ downstream where the rotational velocity is smaller.

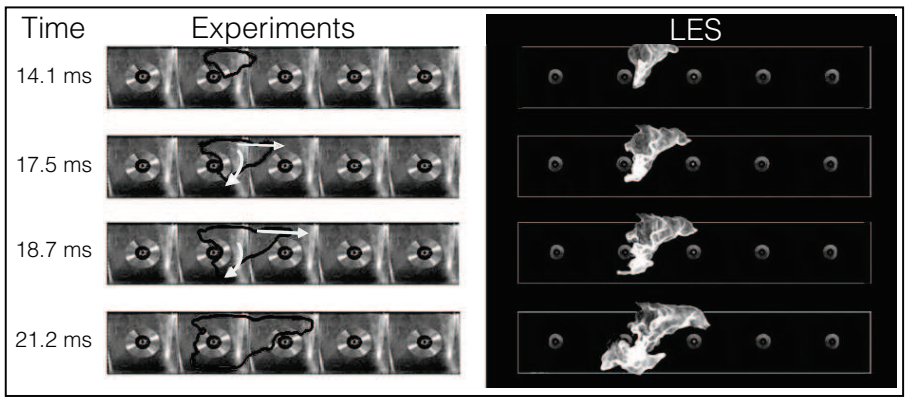

Figure 10.25: Experiments versus LES: early stages of flame propagation for **SP9** case.

This swirl motion is favorable to the spanwise propagation mode and directly affects the ignition order of injectors since the flame must first roll-up around INJ2 before reaching INJ1 while it quickly convects the flame toward INJ3. In a fully annular configuration, this longer pathway results in a time advance of the flame front located in the favorable direction as observed by Bourgouin *et al.* (2013).

10.5.3 Thrust effect

Through heat release, the flame introduces strong velocity divergence and modifies the flow. As the flame surface increases, the global consumption rate progressively increases. It eventually reaches a critical value above which the thermal expansion of the large amount of burnt gases becomes a significant mechanism of flame motion by accelerating the fresh gases in front of the flame. This is illustrated in Fig. 10.26 for the **SP9** and **SP26** cases at instants when the flame front is spreading between two injectors.

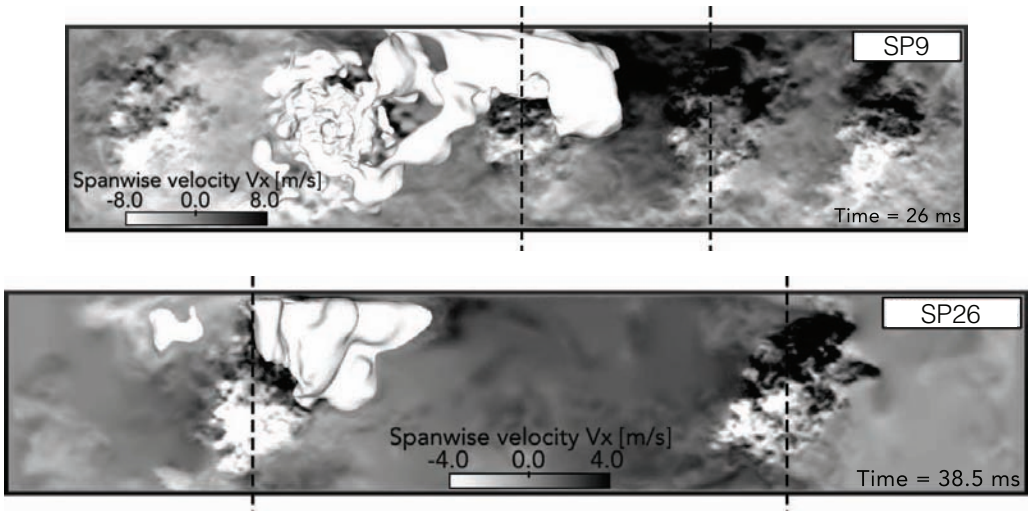

Figure 10.26: LES results: thrust effects of burnt gas expansion for the **SP9**(up) and **SP26**(down) cases, respectively at t = 26 ms and t = 38.2 ms when the flame is between two successive injectors. Two y-cut planes display the spanwise velocity at z/D = 1.5 (**SP9**) and z/D = 2.5 (**SP26**) and the propagating flame (white iso-surface of temperature), bottom view.

Figure 10.26 clearly shows in the **SP9** case the strong interaction between the five high velocity streams due to the five swirlers and the flame, in particular the thrust effect, driven by burnt gas expansion. At the early instants of ignition, the flame location induces an increase of the spanwise velocity, facilitating the flame propagation around the second swirler (Fig. 10.26, t = 26 ms). The SWJ of each injector acts as an obstacle that reduces the cross section resulting in very high spanwise velocity between the SWJ and the lateral wall. The flame is then swiftly convected in these regions and this mechanism greatly contributes to the spanwise propagation mode. When the flame front travels in the LRZ, the flow aerodynamic in the **SP9** case is favorable to a strong expansion in the spanwise direction while in the **SP26** the axial velocity component is stronger. This may explain the low spanwise velocity in the **SP26** configuration (Fig. 10.26, t = 38.2 ms).

To quantify the thrust effect in these two cases, a sample volume has been defined between the center axis of two successive injectors over the whole length of the combustion chamber (dashed lines in Fig. 10.26). The PDF of the spanwise velocity has been extracted from LES in this sample volume at t = 26 ms (**SP9**, Fig. 10.27(left)) and t =38.2 ms (**SP26**, Fig. 10.27(right)), when the flame propagates through the sample volume. For comparison, the same PDF is extracted from an instantaneous isothermal LES solution for both cases in order to reveal the modifications induced

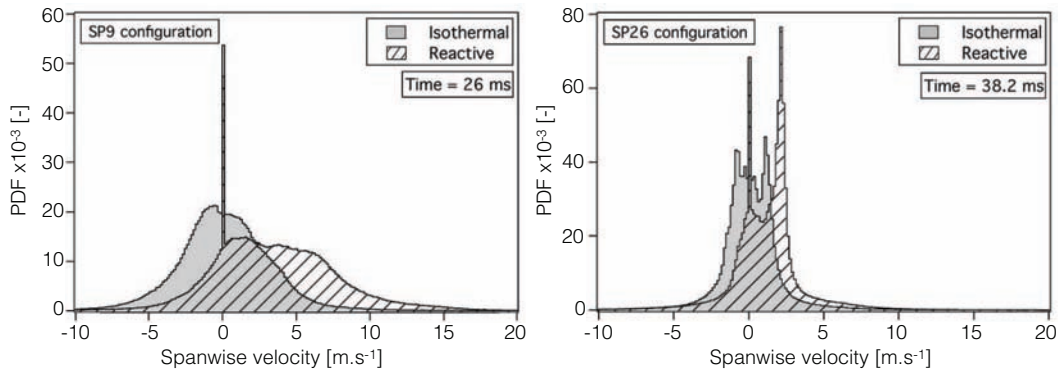

Figure 10.27: LES results: PDF of the spanwise velocity in a restricted zone located between two successive injectors and identified in Fig. 10.26. PDF are obtained from reacting and non-reacting LES for the **SP9** case at t = 26 ms (left) and the **SP26** case at t = 38.2 ms (right).

by the flame. While both isothermal PDF are almost symmetrical and centered at a close to zero velocity in the spanwise direction, the reactive **SP9** PDF clearly shifts toward positive spanwise velocity. On the contrary the reactive **SP26** case PDF is a lot less modified as compared to its isothermal counterpart. It indicates the crucial role of expansion in traveling through initially (in isothermal conditions) low velocity LRZ.

10.5.4 Flow impact on the flame structure

Due to the rapid mixing induced by the swirled injection systems, the turbulent premixed combustion regime is dominant throughout the entire ignition sequences. As mentioned previously, such flame consumption rate is sensitive to equivalence ratio fluctuations, curvature and strain rate. In regions of highly perturbed flow the flame can be locally quenched, delaying its propagation. The equivalence ratio is almost constant over the entire combustion chamber except in the vicinity of a burner, where the mixing time is reduced. In these region, the local heat release is increased because the premixed flame encounters higher equivalence ratios and higher turbulence. Locally the flame may be converted into a diffusion flame. This particular observation is supported by Fig. 10.28(left) where the locally negative Takeno Index (Yamashita *et al.*, 1996) evidences the presence of diffusion flames. Mixture fraction/temperature scatterplot colored by the Takeno index (Fig. 10.28(right)) illustrates the wide range of equivalence ratios encountered, characteristic of partially premixed flames.

To evaluate the effect of the flow on the flame displacement speed, both the shear stress and the curvature are used as indicators. The shear stress may be determined using the Tresca formula (Tresca, 1864) as the difference between the maximum and the minimum of the eigenvalues of the stress tensor. PDFs of this shear stress at two instants are given in Fig. 10.29 (left) and (right), respectively for the **SP9** and **SP26** configurations. The first instant is chosen before the flame encounters the SWJ, while it keeps spreading in a quiet area where the flow shear stress is expected to be low (t_1 = 6.5 ms (**SP9**) and t_1 = 21 ms (**SP26**)). The second instant brings attention to a situation where part of the flame has been swept by the swirl motion and is subject

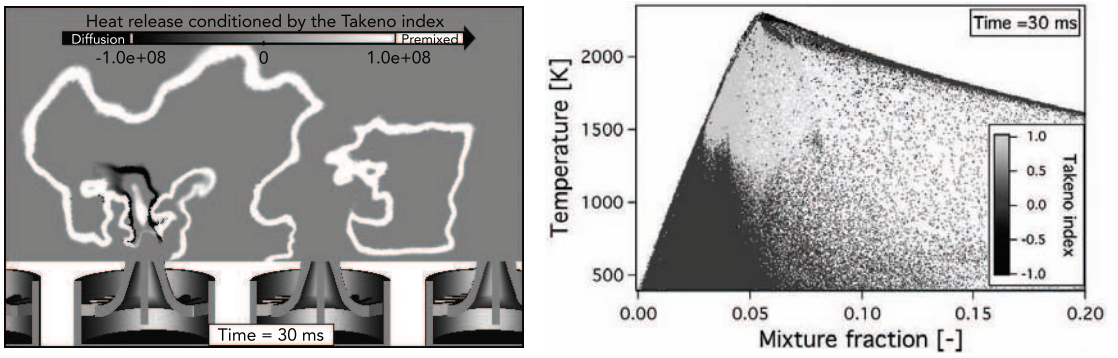

Figure 10.28: LES results: cut of heat release field conditioned by the Takeno index (left) and scatterplot of temperature as a function of the mixture fraction colored by theTakeno index (right), at t = 30 ms for the **SP9** case.

to high turbulence in the SWJ (t_2 = 16.5 ms (**SP9**) and t_2 = 38.2 ms (**SP26**)). Figure 10.29 clearly shows much higher levels of stress applied to the flame in the **SP9** case compared to the **SP26** case, even prior to meeting the SWJ. It highlights the more perturbed velocity field in the **SP9** case. As the flame reaches the SWJ, PDFs show very high shear stress values susceptible to locally quench the flame, especially in the **SP9** case (Fig. 10.29 (left) t_2 = 16.5 ms).

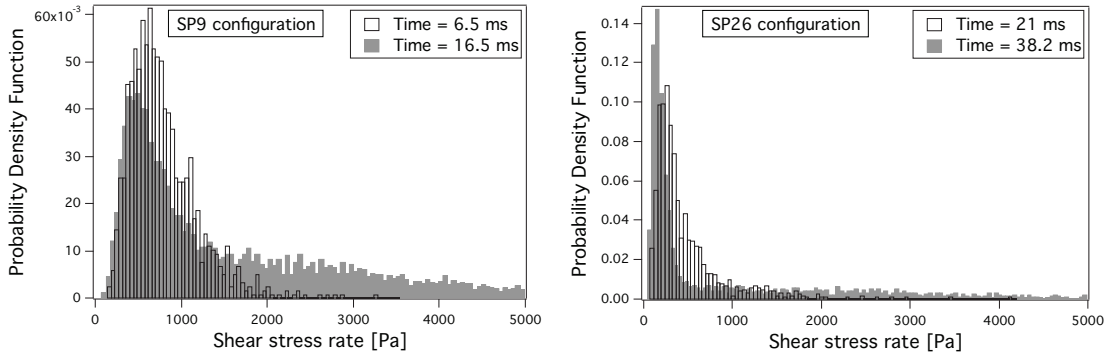

Figure 10.29: LES results: PDF of the shear stress rate in the flame front (in the fresh gas side) at two different stages before and after the flame begins to reach the SWJ for the **SP9** (left) and **SP26** (right) configurations.

Two distinct regimes are identified, in the inter-injector region and close to the SWJ respectively. The former is characterized by low shear stress (< 1000 Pa.s^{-1}), where the flame displacement speed is mainly driven by flame surface wrinkling due to large scale turbulence, while the latter corresponds to high shear stress (> 1000 Pa.s^{-1}) and small scale curvature. These different regimes are characterized in terms of S_d^* and curvature in Fig. 10.30 for **SP9** case at the same time as Fig. 10.30. The color scale corresponds to the level of sub-grid turbulent velocity computed using the $OP2$ operator of Colin *et al.* (2000). As already found by Peters *et al.* (1998), S_d^* globally follows a linear decrease with curvature. Lowest negative curvatures correspond to

concave flames associated to positive S_d^*, while the highest positive curvature leads to thickened convex flames as revealed by the negative S_d^* (Chakraborty *et al.*, 2007). Compared to the low shear region Fig. 10.30 (left), the high shear stress region (Fig. 10.30(right)) shows a wider range of curvature and more spreading of S_d^* due to the higher level of sub-grid velocity. This leads to local flame quenching, resulting in a decrease of the total flame speed. This also explains the difficulty of the flame to penetrate in the SWJ and the increased traveling time to reach INJ1.

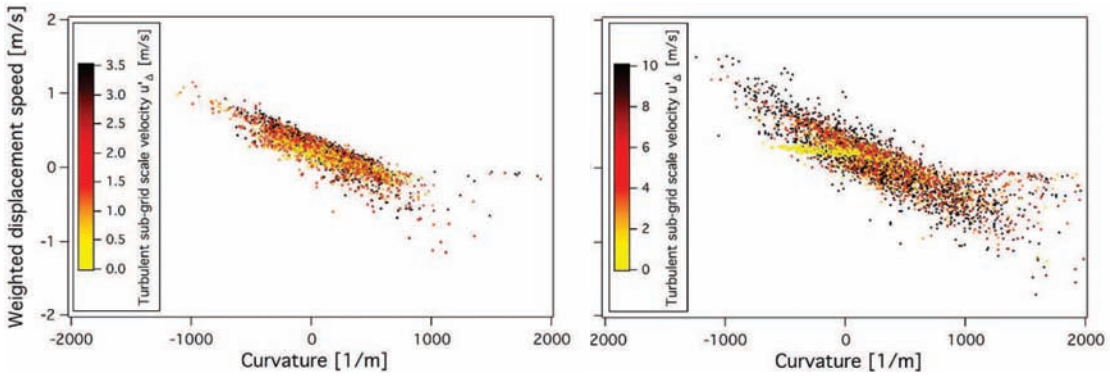

Figure 10.30: LES results: scatterplot of the density-weighted displacement speed for the **SP9** case at time t = 16.5 ms for low shear stress ($< 1000\ Pa.s^{-1}$) (left) and high shear stress ($> 1000\ Pa.s^{-1}$) regions (right), colored by the sub-grid velocity.

10.6 Conclusion

Experiments and numerical simulation of ignition in a multi-injectors burner have been performed to study the effect of the distance between injectors on the ignition process and contribute to a better understanding of the mechanisms driving the light-around flame propagation. Comparisons between experiments and simulations and joint analysis provide valuable new information. First, non-reacting cases have emphasized great differences on the main flow features at ignition time depending on the spacing between injectors. Modifications of the SWJ penetration and opening angle result in changes of the width and height of LRZ. The studied experimental set-up induces a reduction of the overall mass flow rate when the number of injectors decreases. The main consequence is a reduction of the swirl-induced circumferential motion.

Increasing spacing between consecutive injectors directly impact the flame propagation mode and thus the ignition delay and variability. Two major propagation modes were identified both in LES and experiments. Small spacings (below 150 mm) allow a purely spanwise, rapid and safe propagation. A critical distance is identified (160 mm), above which propagation mechanisms begin to change. Above this limit, propagation occurs not only in the spanwise direction, but also in the axial direction. When this distance is further increased, flame propagation becomes mainly axial and full ignition is delayed or fails (seen only in the experiments).

A detailed analysis showed that the different propagation modes where essentially driven by two key mechanisms:

- The flame is affected by the flow aerodynamics which changes with the injector spacing. Low spacing flow aerodynamic promotes a rapid suction by the swirled motion leading to a spanwise flame propagation mode while high spacing flow structure changes are favorable to an axial propagation mode. The spanwise propagation mode is associated with short traveling time of the flame from one injector to the other and a low variability while the axial propagation mode is characterized by longer propagation times and a much higher variability.
- A thrust effect due to the thermal expansion of the burnt gases has been highlighted. It produces a continuous flame progress which modifies the surrounding cold gas flow. It may increase the spanwise velocity and is the major mechanism of flame propagation in regions of weak mean flow such as LRZ.

These propagation modes result in different overall ignition times which increase with injector spacing. Comparisons between experiments and LES have shown the capability of LES to reproduce ignition sequences as well as the added value of LES in this investigation of ignition process thanks to the additional data available.

Chapter 11

Light-round in the MICCA annular combustion chamber

Contents

11.1 Experimental configuration 196
11.2 Numerical set-up 197
11.2.1 Computational domain 197
11.2.2 Numerical parameters 198
11.3 Non-reacting flow 199
11.4 Ignition sequence 203
11.4.1 Light-around dynamics 203
11.4.2 Overall burning rate 203
11.4.3 Flame path 205
11.4.4 Effect of burnt gas expansion 207
11.4.5 Conclusion 211

To investigate ignition in a more realistic configuration, LES of the light-round in the MICCA annular combustion chamber of EM2C (Bourgouin *et al.*, 2013) is performed and analyzed in this Chapter. The annular configuration allows to avoid the side effects of the KIAI straight multi-burner configuration studied in Chapter 10: small number of injection systems, in-line configuration and limited light-around phase. However, it is also more difficult to provide fine experimental data in such a test rig. The characterization of the flow dynamics in the full configuration prior to ignition is not available, and the direct visualization of the flame is biased by the deformation induced by the cylindrical transparent walls. Nonetheless, such configuration is an excellent candidate to investigate the flame development through an azimuthal combustion chamber.

As in the KIAI multi-burner study, the first objective here is to investigate the capability of LES to reproduce qualitatively and quantitatively the light-around process by direct comparison with the experimental results. Furthermore, this numerical study is performed in collaboration

with the EM2C team within the SIMAC PRACE project, offering a unique opportunity to compare two combustion models, DTFLES and F-TACLES (Philip *et al.*, 2014*a*) all other things being equal, in a complex configuration.

The MICCA experimental configuration is first presented and in a second time, the capability of LES to capture the non-reacting flow generated by the swirler is evaluated in a single burner configuration. The LES results are then compared qualitatively with experiments and the ignition sequence is investigated in detail.

11.1 Experimental configuration

The MICCA experimental test rig installed at EM2C laboratory is composed of an annular plenum fed by 8 lines, a combustion chamber made of two cylindrical quartz tubes and 16 swirled injection systems (Fig. 11.1). The injection system consists of 6 circular radial passages of 3 mm diameter connecting the plenum and an inner tube of 10 mm diameter, and 40 mm long ending in the combustion chamber. The transparent combustor walls allow a direct visualization of the flame front and the combustion chamber directly ends to the environment. The experimental geometry is shown in Fig. 11.1 and more details on the technical set-up can be found in Bourgouin *et al.* (2013). Ignition is triggered with a spark plug of 25 mJ deposit energy located on the bottom wall at a 191 mm radius near an injection system (see Fig. 11.1). The flame motion during light-around is captured using a high speed camera at 6000 Hz, without filtering. However, the cylindrical configuration does not allow precise experimental diagnostics to track the velocity field during the flame propagation. The arc length between two consecutive injectors is about 69 mm while the radial width of the combustor 50 mm. Comparing with the dimensions of the KIAI configuration, a rapid flame propagation along the bottom of the combustion chamber is expected.

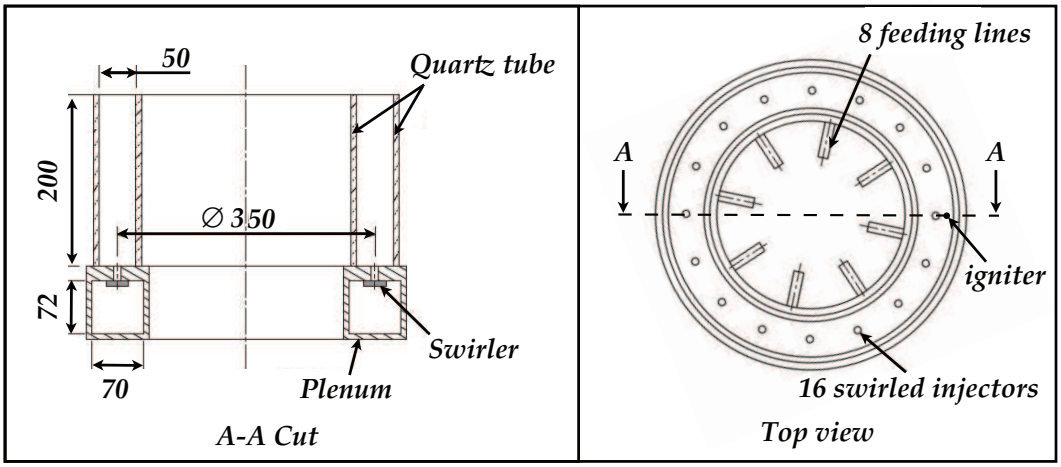

Figure 11.1: Sketch of the MICCA experimental test rig. Dimensions are given in mm (extracted from Bourgouin *et al.* (2013)).

The test rig is operated at atmospheric conditions. The plenum is fed with a perfectly premixed propane-air mixture at an equivalence ratio of 0.76, with a total mass flow rate of 24.53 g/s

and a thermal power of 52 kW. The bulk velocity estimated in the swirler inner tubes is 17.1 m/s, corresponding to a Reynolds number of 11 000. The swirl number of the injection system has been estimated to 0.82 in a confined single injector configuration. Note that, experiments have shown a strong dependency of the overall ignition time to the thermal state of the test facility: ignition is longer when the combustion chamber is cold and shortens when the combustor is pre-heated (Bourgouin, 2014). The LES analysed hereafter are performed in preheated conditions, which differ from the experimental data presented in Bourgouin *et al.* (2013).

11.2 Numerical set-up

11.2.1 Computational domain

The complete geometry of Fig. 11.1 is used to study the ignition sequence with LES. A large volume is placed at the combustion chamber outlet to mimic the experimental configuration and minimize the influence of the outlet boundary condition on the ignition sequence. The whole computational domain as well as details of the swirler are presented in Fig. 11.2. The injector centers are located at the combustion chamber mean radius $R_{mean} = 175mm$.

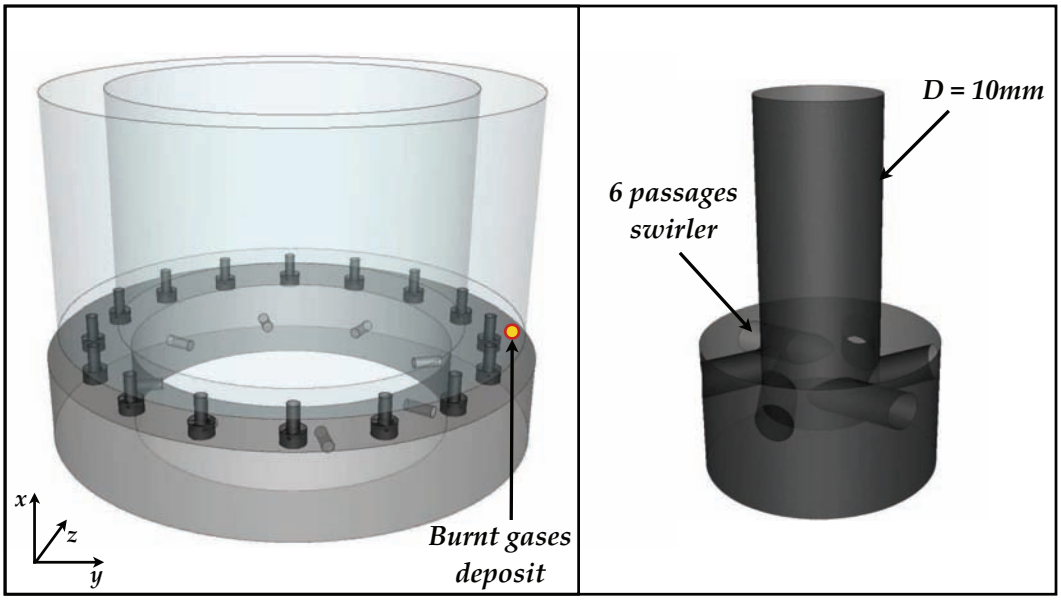

Figure 11.2: Annular computational domain (left), details of the 6 passages swirler (right). The large volume at the combustion chamber outlet is not shown here.

The overall LES grid size is about 310 millions of tetrahedral cells (Fig. 11.3), with a mesh characteristic size of 0.15 mm in the swirler passages and a linear increase from 0.15 mm to 0.5 mm in the inner tube of the injection system. In order to adequately capture the flame propagation in the whole chamber during light-around, the largest characteristic size of the grid is 1 mm at the combustion chamber exit which corresponds to 1.5 δ_L^0, where δ_L^0 is the laminar flame thickness at equivalence ratio $\phi = 0.76$

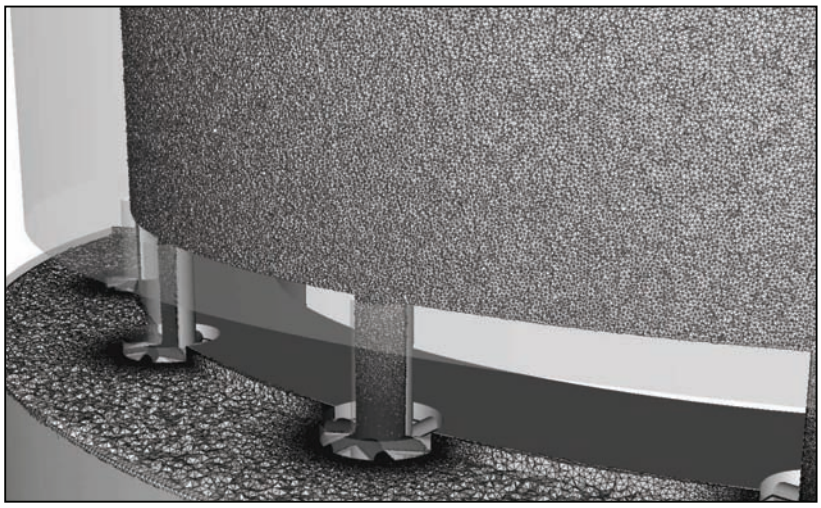

Figure 11.3: Slices of the computational domain showing characteristic mesh size in the swirler passages and in the combustion chamber.

Note that the geometry being periodic in the azimuthal direction, the non-reacting flow prior to ignition has been computed only in one eighth of the whole domain and duplicated eight times to generate the initial conditions for the full annular ignition simulation.

The analysis of the flow pattern has been performed on a single sector configuration since the cylindrical shape of the combustor prevents the use of PIV. The computational domain used to investigate the non-reacting flow is shown in Fig. 11.4. A cylindrical plenum is placed upstream of the injection system and the combustion chamber is a 50 mm diameter cylinder with transparent walls to enable optical access. The grid characteristic size is similar to the one used in the annular configuration.

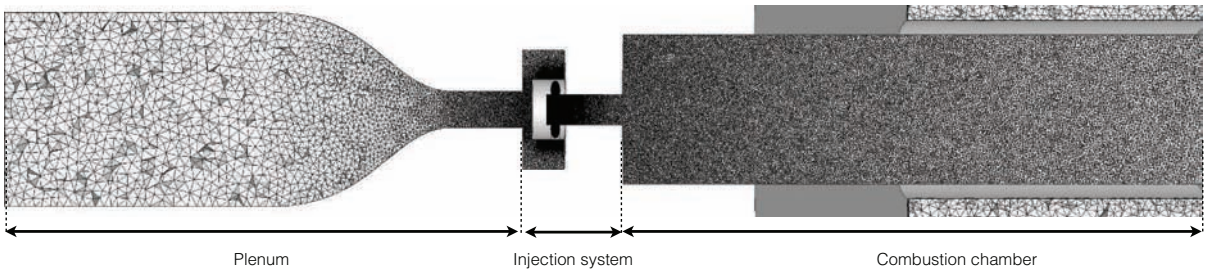

Figure 11.4: Computational domain and characteristic mesh size in a central cut-plane for the single injector non-reacting flow study.

11.2.2 Numerical parameters

The numerical set-up is summarized in Table 11.1. Ambient conditions are imposed numerically targeting a 101325 Pa outlet pressure and a 298 K inlet mixture temperature.

Propane/air chemistry is described with a two-step global mechanism constructed to repro-

	Numerical parameter
Convection scheme	TTGC: $\mathcal{O}(3)$ in space & time (Colin & Rudgyard, 2000)
Diffusion scheme	2Δ operator
SGS model	WALE (Nicoud & Ducros, 1999)
Artif. viscosity	Colin model: $\epsilon^{(2)} = 0.05$, $\epsilon^{(4)} = 0.005$
	Boundary conditions
Mixture inlets	NSCBC (Poinsot & Lele, 1992) (mass flow rate)
Atmosphere inlet	NSCBC (Poinsot & Lele, 1992) (velocity)
Outlet	NSCBC (3D) (Granet *et al.*, 2010) (pressure)
Walls	Adiabatic non-slipping walls

Table 11.1: Numerical parameters for LES of the MICCA configuration.

duce the laminar flame speed at $\phi = 0.76$, $S_{l,0} = 0.239m/s$, in analogy with the mechanism proposed in Franzelli *et al.* (2010). The mechanism is described in Sec. 4.4. The DTFLES model is used with the efficiency function from Charlette *et al.* (2002) to model the flame/turbulence interactions. Considering the grid resolution compared to the laminar flame thickness $\Delta_x/\delta_L^0 = 1.5$, the thickening factor $\mathcal{F}$ ranges from 5 to 8 from the bottom to the top of the combustion chamber. The simulation performed by the EM2C team in the SIMAC project framework used Tabulated Thermo-chemistry (TTC) model (Vicquelin *et al.*, 2011) to describe the chemistry and the flame/turbulence interactions are modeled using the F-TACLES approach (Fiorina *et al.*, 2010).

In order to compare both combustion models, ignition is triggered with a 3 mm-wide burned gases spherical kernel centered at the same position as the experimental spark plug (see Fig. 11.2). Indeed, the ED model used in the KIAI configurations is not compatible with the TTC/F-TACLES approach. Both the perfectly premixed conditions and the low level of turbulence in the energy deposit region guarantee the success of the early stages of ignition.

11.3 Non-reacting flow

The non-reacting flow generated by the swirler is first validated by comparison with experiments in a single injector configuration. These simulations have been performed by the EM2C team and are reported here to provide a complete description of the conditions prior to ignition. The full study evaluates the effect of mesh resolution, numerical scheme and subgrid scale modeling on the accuracy of the LES results. In the following, only the numerical set-up used for the full ignition sequence is compared to experimental results.

The non-reacting flow pattern is very similar to the KIAI configuration studied in Chap. 6 and the main flow structures are presented in Fig. 11.5 with 2D projected streamlines: the IRZ and CRZ are separated by the SWJ and intense shear layers are located at the interface between the SWJ and the two recirculation zones. The IRZ spreads from the bottom of the injector tube to downstream in the combustion chamber.

Figure 11.6 shows the mean and RMS components of the velocity field obtained from temporal averaging during 80 ms. The velocity is found to adopt constant profiles in the injector tube and

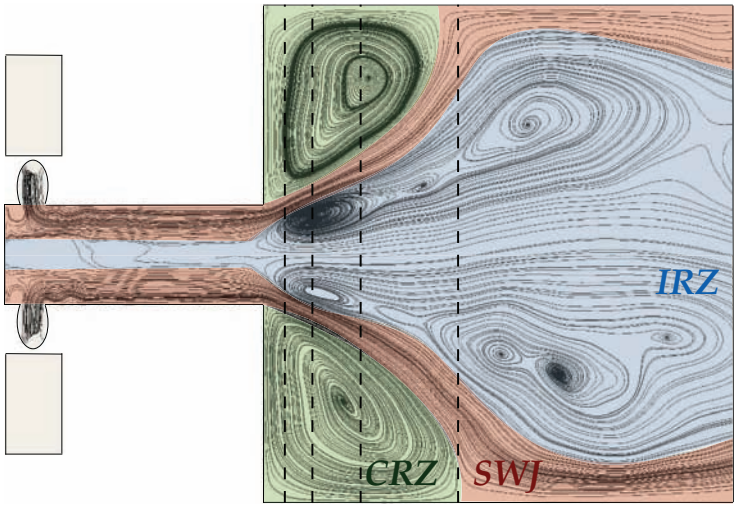

Figure 11.5: Time-averaged streamlines in the central cut plane of the single injector configuration. The main flow regions are identified: Swirled Jet (SWJ), Inner Recirculation Zone (IRZ) and Corner Recirculation Zone (CRZ). Dashed vertical lines correspond to the velocity profile measure locations.

to rapidly expand at the combustion chamber dump plane. The strong rotation induced by the radial swirler is clearly demonstrated by the high magnitude of azimuthal velocity in the injector tube. A region of strong turbulent activity is located at the entrance plane in the combustion chamber: axial velocity fluctuations are strong in the outer shear layer denoting vortex shedding while both radial and azimuthal velocity fluctuations are strong both along the injector axis and in the chamber.

For a quantitative evaluation of the LES results, the mean axial and azimuthal velocity components are extracted at 4 axial positions (see Fig. 11.5) and compared with experiments in Fig. 11.7. Both components are in fairly good agreement with experiments even though the SWJ opening is slightly underestimated in LES.

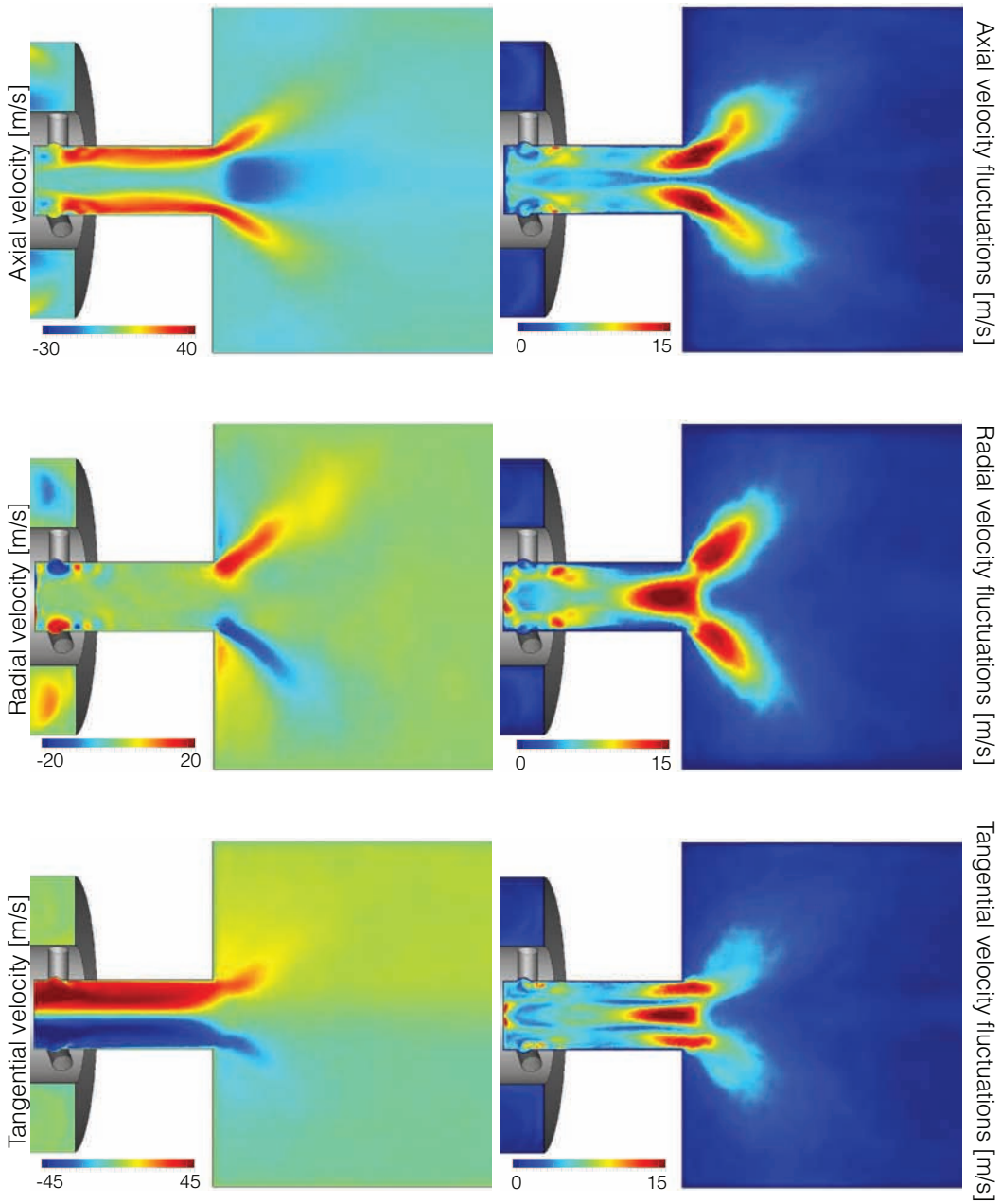

Figure 11.6: Mean and RMS velocity components in the central cut plane through the combustion chamber of the single injector configuration.

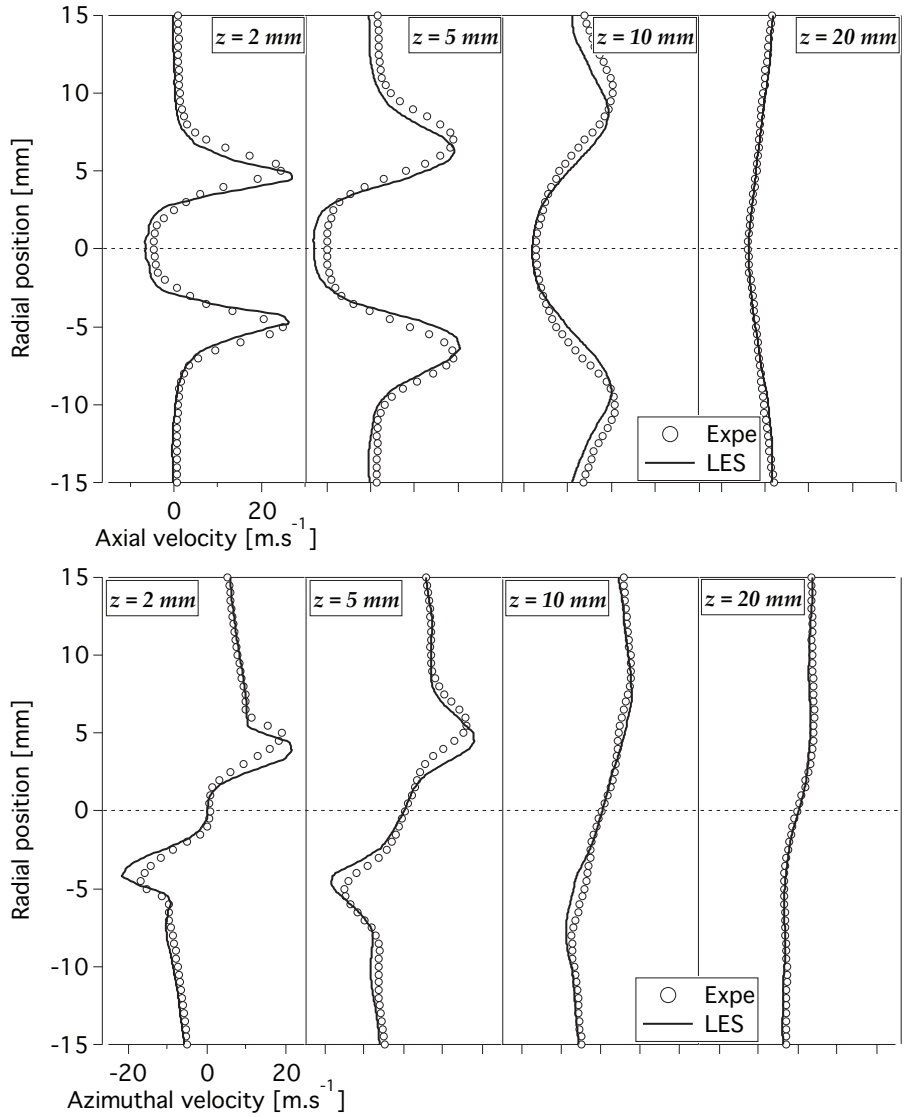

Figure 11.7: LES versus experiments: mean axial and azimuthal velocity components profiles at 4 axial positions $z = 2$ mm, 5 mm, 10 mm, 20 mm in the combustion chamber of the single injector configuration.

11.4 Ignition sequence

The experimental variability of the two first ignition phases is low since, similarly to the KIAI multi-injector burner, the energy deposit is performed in a region of low turbulence intensity. However, the duration of the light-around is found to vary: 6% variability is measured from 9 experimental trials. Furthermore, the early flame kernel phase is not computed in the LES. As a consequence, the comparison between LES and experiments during the burner to burner propagation starts after the kernel creation where time is set to 0. In Sec. 11.4.1, the dynamics of the light around is qualitatively compared with experiments. In Sec. 11.4.2 the LES results are analyzed in detail in order to track the flame pathways and identify the mechanisms responsible for the rapid propagation.

11.4.1 Light-around dynamics

The flame position is compared at different instants between LES and experiments in Fig. 11.8. In LES, the flame position is tracked by an iso-surface of temperature at T = 1781 K corresponding to 90 % of the adiabatic temperature while experimentally, the high speed camera enables direct visualization of the flame emissions. The different steps of the ignition sequence observed in the experiments are numerically recovered:

- (I) Initial kernel expansion: laminar kernel growth characterized by a slow increase in heat release rate, ending when the closest injector is ignited.
- (II) Arch-like flame propagation: the flame front meets the quartz windows and propagates towards the neighboring injectors with a half sphere shape. The arch breaks down as the upper front leaves the combustion chamber.
- (III) Two-front propagation: two flame fronts propagate through the combustor in opposite azimuthal directions and ignite the successive injectors as they pass by.
- (IV) Front merging: after the two fronts have spanned almost half of the combustion chamber they join and merge.
- (V) Steady state: burnt gases produced by the flame stabilized at the injector nozzle push the remaining flame front out of the combustor and a steady state is reached.

LES is able to reproduce with good accuracy the shape and the dynamics of the flame front. The simulations performed at EM2C using the TTC/F-TACLES model provide similar results (Philip *et al.*, 2014*a*).

11.4.2 Overall burning rate

The temporal evolution of the integral of heat release in the combustion chamber ($\int_V \dot{\omega}_T \ dV$) is plotted in Fig. 11.9 and compared to experimental results corresponding to the light emission

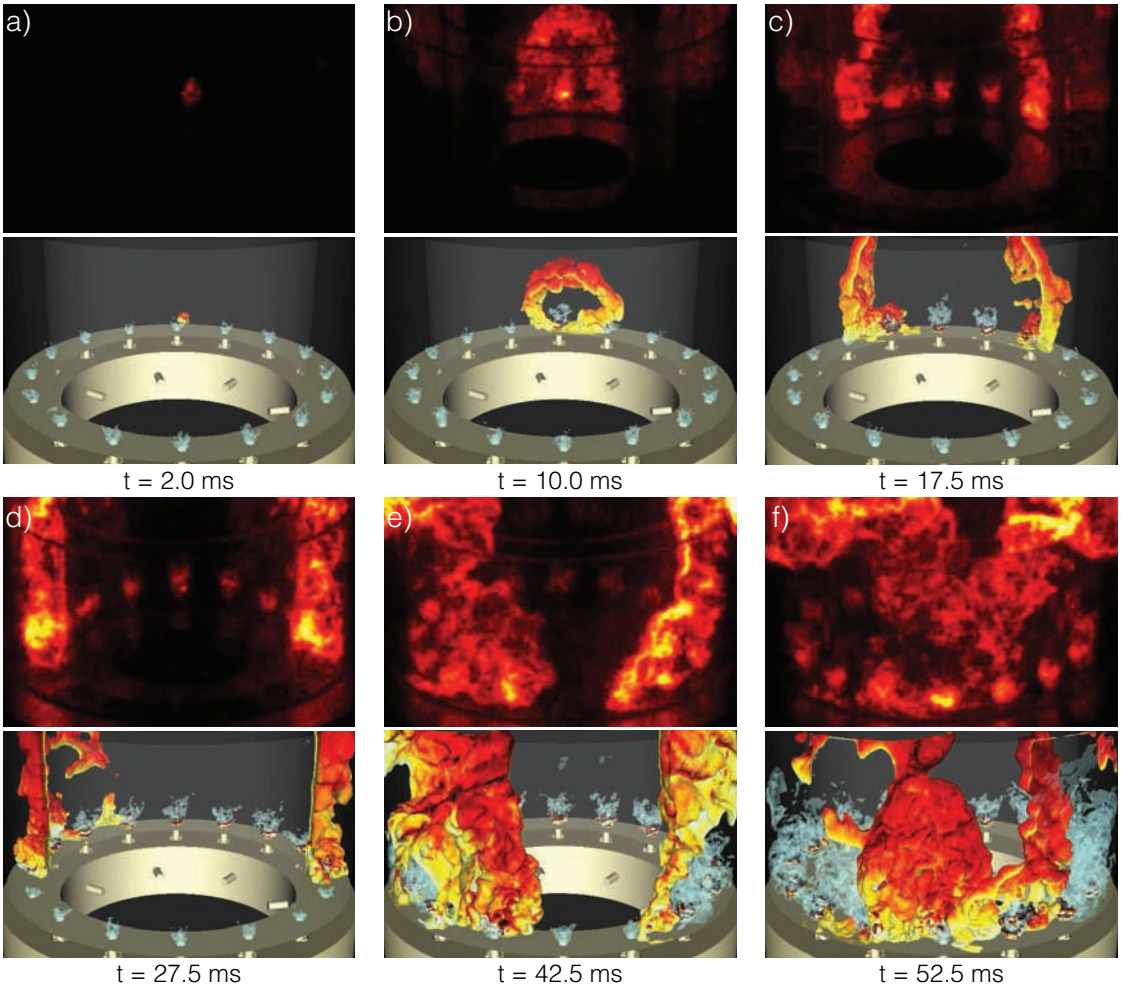

Figure 11.8: Snapshots of the ignition sequence: experimental direct imaging of the flame emission colored for visualization purposes (top rows) versus iso-surfaces of T = 1781 K colored by the axial velocity and U = 25 $m.s^{-1}$ in light blue extracted from the LES (bottom rows).

integral extracted from the high speed camera recordings. The results obtained with the TTC/F-TACLES model (Vicquelin *et al.*, 2011; Fiorina *et al.*, 2010) presented by Philip *et al.* (2014*a*) are also reported. A very good agreement is obtained between models and experiments. All three integrals are normalized by their maximum values. Comparing the results obtained with the DTFLES and the F-TACLES models demonstrates the robustness of the LES approach and its limited sensitivity to the combustion model, at least when investigating the light-around in gaseous flows. The heat release follows a smooth increase during the kernel phase and is followed by a sharp increase during the arch phase. Then during the two-front flame propagation, the heat release continues to increase with a lower slope. The overall heat release is maximum when the flame fronts merge and this maximum is followed by a steep decrease of the heat release as the flame front elements are pushed out of the combustion chamber. Finally, the combustor reaches a stable regime. LES results are found to follow the experiments up to 50 ms where differences appears since the camera captures flame elements outside the combustion chamber (see $t = 52.5$

of Fig. 11.8).

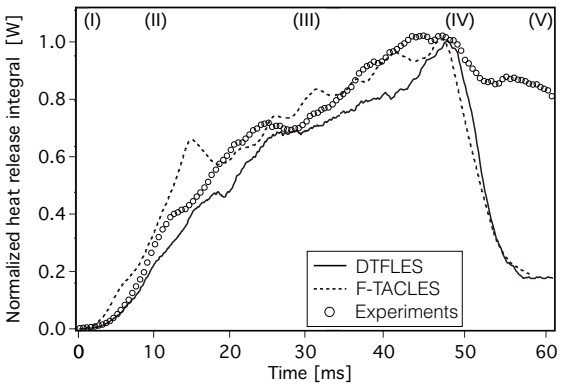

Figure 11.9: Temporal evolution of the integrated heat realease in the combustion chamber. Comparison between experiments, and the two LES using DTLES and TTC/F-TACLES.

To further evaluate the burning rate during the ignition sequence, the mean consumption speed $\overline{S}_c$ is calculated as:

$$\overline{S}_c = \frac{\int_V \dot{\omega}_T \, dV}{\rho_f Y_{F,f} A_{fl} \mathcal{Q}_r} \tag{11.1}$$

where A_{fl} is the total flame surface computed from the FSD (see Eq. (7.9)) and $\mathcal{Q}_r$ is the heat of combustion of propane. The temporal evolution of $\overline{S}_c$ is plotted in Fig. 11.10(left) along with the value of S_L^0. $\overline{S}_c$ is first below S_L^0 mainly due to the effect of stretch induced by the mean positive curvature $\mathcal{K}$ of the flame kernel as shown in Fig. 11.10(right). The curvature is computed as $\mathcal{K} = \boldsymbol{\nabla}.\boldsymbol{n}$ with $\boldsymbol{n}$ the flame surface normal. As the flame front expands, $\overline{S}_c$ increases to a value about 15% higher than S_L^0 and remains at this rate during the whole ignition sequence. Past the arch-like stage, the mean curvature along the flame front reaches a stable low value of about 10 m^{-1}. Note that, the absolute value of $\overline{S}_c$ strongly depends on the evaluation of the flame surface A_{fl}. Defining the flame front surface for a turbulent premixed flame is not an easy task since the flame front has a finite thickness and A_{fl} depends on the c-isolevel chosen. Using Eq. (7.9) in the present analysis could result in an underestimation of the flame surface that can directly increase $\overline{S}_c$ as observed in Fig. 11.10(right).

11.4.3 Flame path

To track the flame front position, a cylindrical reference frame (R,θ,z_{cyl}) is introduced: the axial direction z_{cyl} aligned with the x-axis of the cartesian reference frame corresponding to the symmetry axis of the azimuthal configuration. The angular position θ is zero along the y-axis where ignition is triggered. To better characterize the flame front displacement, two leading points of the flame front are tracked: they are defined as the location on the $T = 1781$ K iso-surface having the maximum absolute value of θ, θ being positive in the upper part of the combustion chamber and negative in the lower part (see Fig. 11.11). The positions of the leading points are plotted in a R-θ map along with the time at which the flame front reaches the different injectors

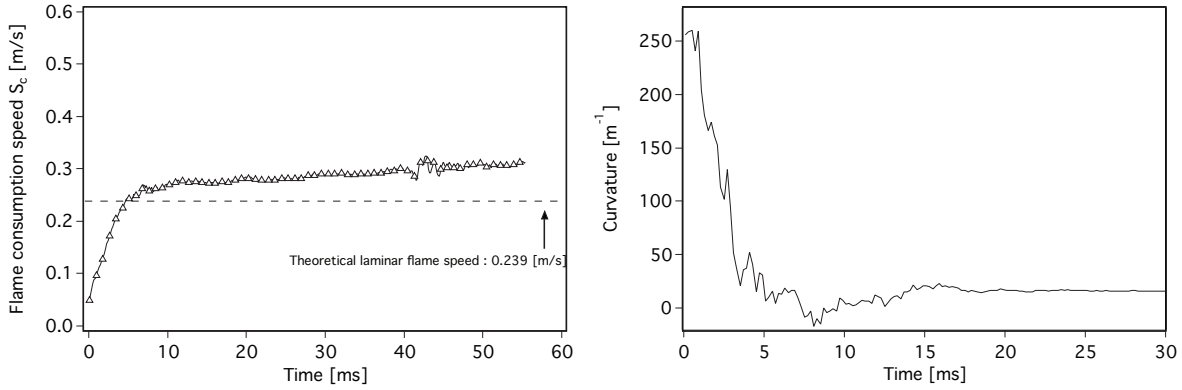

Figure 11.10: Temporal evolution of mean consumption speed $\overline{S}_c$ (left) and mean flame curvature (right).

in Fig. 11.11. Point to point large variations of the leading point position corresponds to a switch between two flame elements. Arrows indicate the motion induced by the injector swirl: in the positive θ direction in the inner part and negative θ direction in the outer part.

Ignition starts at $R_{spark} = 191mm > R_{mean}$. The upper front leading point rapidly shifts to a $R_{lp,up} < R_{mean}$ (where the lp subscript refers to leading point) location as the inner path is shorter than the outer one and the swirl induced motion is favorable to flame displacement. On the contrary for the lower front, the swirl motion has an adverse effect on the flame propagation direction and the leading point radius $R_{lp,low}$ is alternatively lower and higher than R_{mean}. This behavior is coherent with the observations of Bourgouin *et al.* (2013), though a precise flame path has not been observed experimentally.

The times reported in Fig. 11.11 indicate that the upper flame front is delayed as compared to the lower one at first, but finally reaches the opposite injector (located at $\theta = \pi$) sooner than the lower front. Since ignition is triggered at $R_{spark} = 191mm > R_{mean}$, the flame kernel first undergoes a bulk displacement towards negative θ due to the outer negative rotation before being able to propagate in the opposite direction. As observed in the KIAI multi-burner experiment, during the early stage of kernel development, the large scale structures of the non-reacting flow are driving the motion of the flame front. The temporal evolution of the leading point angle is reported in Fig. 11.12, and the initial delay of the upper flame front is shown to be compensated by a higher flame velocity at later times. Due to the advance of the upper front, merging of the two flame fronts is not located at the position opposite to the spark deposit: the merging is switched towards the lower part of the combustion chamber. Once again, this is coherent with the observations of Bourgouin *et al.* (2013).

Finally the axial position of the leading points is reported in Fig. 11.13 as function of the leading point angle while the dashed vertical lines indicate the positions of the swirler inlet. During the kernel and arch phases, the axial position of the leading point gradually increases. As the upper flame front reaches the combustor exit, the two flame fronts flatten and the leading point positions switch towards an upstream locations. During the propagation phase, the leading point of the upper flame front is located approximatively around $z_{cyl,lp,up} = 35mm$ while the lower portion is $z_{cyl,lp,low} = 20mm$. This difference can be related to the position of the maximum azimuthal velocity of each individual injector: the upper flame front propagation is promoted by

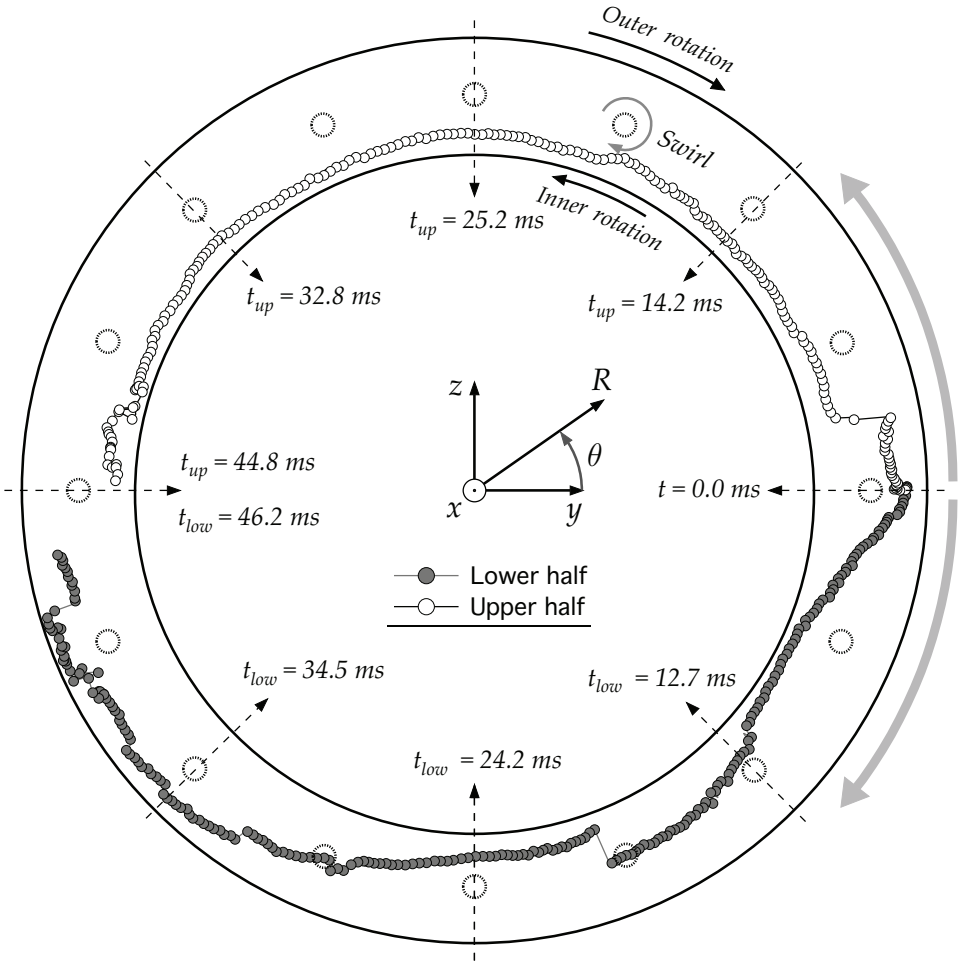

Figure 11.11: Evolution of the upper (white) and lower (grey) leading points in a R-θ map. Time at which the flame reaches injectors located at $\theta = \pi/4$ [$\pi/4$] is indicated.

the swirl motion so that the leading point follows the path exhibiting high velocity. The opposite applies for the lower flame front, where the leading point follows low velocity locations due to the adverse effect of swirl on the propagation. This low velocity region corresponds to the CRZ.

11.4.4 Effect of burnt gas expansion

The magnitude of the mean flame consumption speed reported in Fig. 11.10 is several times lower than the flame propagation speed estimated from the overall ignition delay ($\pi R_{mean}/\tau_{ign} \simeq 11$ m/s) indicating that the flame propagation is not directly responsible from the rapid ignition. Similarly to the study of Boileau *et al.* (2008) or the one for the KIAI burner presented in Chap. 10, the burnt gas expansion is the mechanism driving the propagation. The density drop across the turbulent flame brush results in an acceleration of the fresh gases in front of the flame front. To better understand the flame pathways described in Sec. 11.4.3, it is interesting to evaluate the axial distribution of azimuthal velocity V_θ. The axial distribution of V_θ is evaluated in

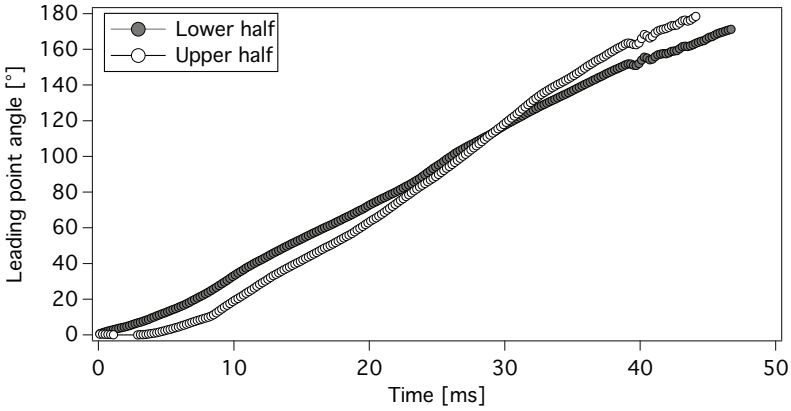

Figure 11.12: Temporal evolution of the position angle of the upper (white) and lower (grey) leading points.

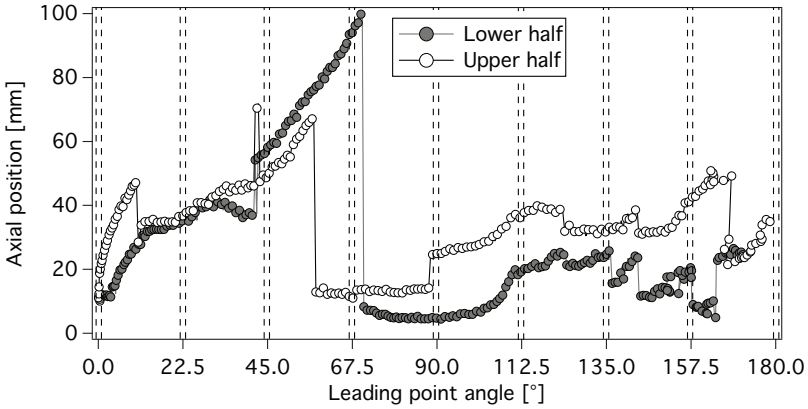

Figure 11.13: Evolution of the upper (white) and lower (grey) leading points axial position as function of the leading point angle. Dashed vertical lines indicate the position of the injectors.

a slice $\theta = -79°$ slice and plotted at 5 instants in Fig. 11.14. The acceleration of the fresh gases is not uniform in the z_{cyl}-direction with maximum values in the lower part of the combustion chamber where the swirl motion adds to the value of V_θ. This explains that the leading point remains in the lower part of the combustion chamber as well as the oblique front observed in LES and experiments during the two-front propagation stage.

To evaluate the spatial distribution of the fresh gas velocity, the azimuthal distribution of the azimuthal velocity V_θ is averaged in a slab of 5 mm through the combustion chamber located at $x = 30$ mm. The results are plotted in Fig. 11.15 for 5 instants during the ignition sequence. The initial distribution is only modulated by the swirl motion induced by the injectors. After 10 ms, V_θ shows a maximum value about 9 m/s near the preheat zone of the flame. The velocity then decreases with increasing distance from the flame. Up to 35 ms, this maximum value of V_θ is observed in the preheat zone but as the opposite flame fronts get closer, the azimuthal maximum value is reduced. The upper and lower flame fronts induce a similar acceleration of the fresh gases but in opposite directions. As they get closer, the fresh gases are unable to accelerate and a backflow is observed ($t = 40$ ms in Fig. 11.15) with a positive azimuthal velocity in the whole

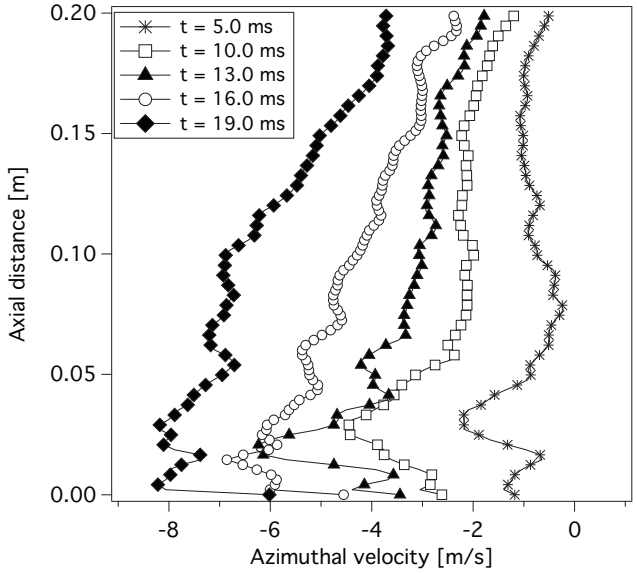

Figure 11.14: Axial distribution of mean V_θ computed in a slice $\theta = -79°$ at 5 instants.

combustion chamber and a reduction of the maximum azimuthal velocity.

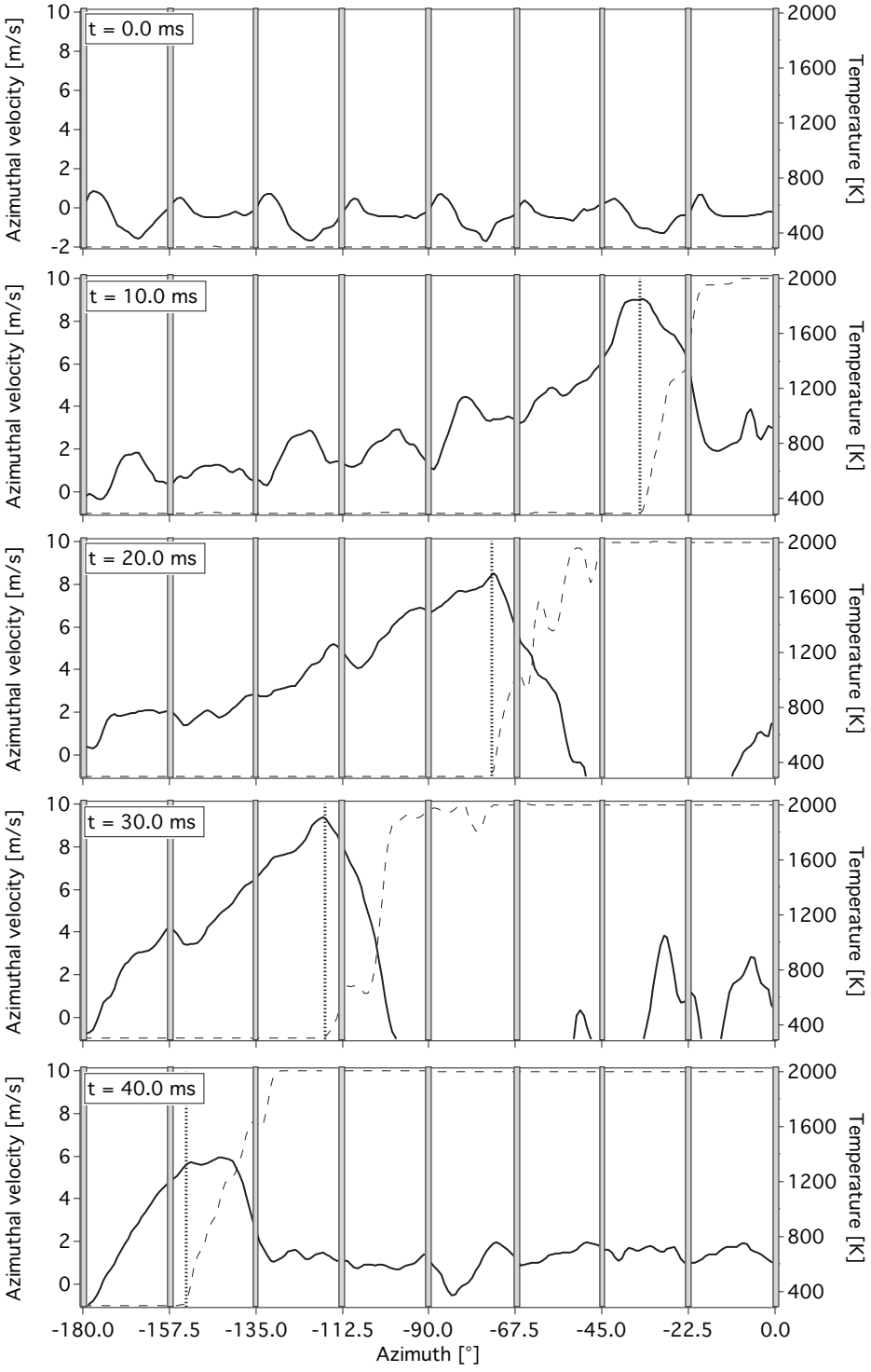

Figure 11.15: Azimuthal distribution of mean azimuthal velocity V_θ (full line) and temperature (dashed line) computed in a 5 mm thick slab at $x = 0.03$. Vertical grey lines indicate the position of the injectors.

11.4.5 Conclusion

The ignition dynamics of an azimuthal configuration has been studied using LES and compared to experiments when available. From the comparison of direct visualization of the flame front, LES is found to reproduce well the flame front shape and motion. A quantitative comparison based on integral values of the light signal on the experiments side and heat release rate on the numerical side confirm that LES is able the reproduce the light-around dynamics. The comparison of the results obtained with another combustion model (TTC-F-TACLES) indicates that the LES results are not highly sensitive to the numerical parameters, at least in this configuration.

The large set of numerical data has then been analyzed to investigate the flame pathway and highlight the effect of the burnt gas expansion on the flame front dynamics. The flame is found to propagate in the lower part of the combustor in accordance with experiments, and its leading point motion is not altered by the flow issued from the swirler. Similarly to a spherically expanding flame, the flame front is found to induce an outward motion of the fresh gases during stage (II). The maximum azimuthal velocity is then found in the flame front and is observed during the whole stage (III) even though burnt gases exit the combustion chamber. At the beginning of stage (IV), the effect of burnt gases expansion is reduced since the two flame front evolve in opposite direction so that the flame front velocity is reduced. The overall ignition delay is driven by the density ratio between fresh and burnt gases, which is coherent with the little sensitivity of the LES results to the combustion model. As compared to the KIAI multi-burner experiment studied in Chap. 10, several observation are formulated:

- the flame propagates in the lower part of the combustion chamber, which is coherent with the spanwise propagation mode described in the KIAI multi-burner configuration.
- the light-around phase duration is longer and numerous injectors are ignited, which allows to investigate the driving mechanisms.
- the annular configuration remove the azimuthal confinement so that the thrust effect due to burnt gas expansion is more pronounced compared to the KIAI multi-burner case. The fresh gases acceleration is observed through the whole combustion chamber.
- the effect the individual injector flow pattern on the ignition dynamic is lower than in the KIAI multi-burner.

This study of the light-around process in an annular configuration is a step towards a better understanding of the ignition process in realistic configurations, and it complement the study on the effect of inter-injector spacing performed in the KIAI multi-burner setup. Nonetheless, both experimental setups are still far from the complexity of realistic gas turbines combustion chambers and several complexity of real combustors are not taken into account: high Reynolds number flow, multi-phase flow or axial confinement of the combustion chamber.

Chapter 12

Conclusions and Perspectives

The work presented in this Ph.D thesis deals with the ignition process of aeronautical gas turbines, from the initial flame kernel generation to the complete light-up of the combustion chamber. Such transient processes are complex and because of the technological complexity of aero-engines, numerical simulations are currently the most promising methods capable of shedding some light on the mechanisms controlling the ignition performances. The present work relies on experimental data to validate LES results, as a starting point of a more detailed study of the driving mechanisms. Two main aspects of the ignition process are studied:

- The kernel initiation and growth in highly swirled partially premixed conditions is studied in Chap. 7. Compared to previous LES study (Lacaze *et al.*, 2009*a*; Jones & Tyliszczack, 2010; Subramanian *et al.*, 2010), the single injector KIAI configuration is more representative of realistic gas turbine applications since it features a swirling flow with higher turbulence levels, recirculation zones and partial premixing effects. Multiple LES of ignition sequences are performed to provide an extensive database of ignition events and construct an ignition probability from brute force LES computations. The study indicates that LES is able to reproduce the experimental ignition probability, proving that LES captures the main mechanisms affecting the ignition process, with the good variability. The LES database is analyzed and confirms the existence of two ignition failure modes observed in simpler configurations (Smith *et al.*, 1986; Ahmed *et al.*, 2007*a*; Mastorakos, 2009): failure of flame kernel initiation and kernel quenching at later times. LES results reveal that the late failure is the result of two main quenching mechanisms: inflammable mixture pockets and kernel dislocations due to large scale deformations and flame/flame interactions. In agreement with experimental studies (Cardin, 2013), the first failure mode is found to be controlled by the amount of fuel readily available in the deposit location surroundings. The second mode is more challenging to predict as it results of the combination of several mechanisms occurring at different times and locations along the kernel trajectory. The results of the LES study are then used to develop a model to predict the ignition probability in Chap. 8. The aim is to include transport of the flame kernel in the prediction of its survival probability. A methodology combining a statistic of the kernel trajectories and of the non-reacting flow characteristics is proposed and applied to the KIAI single burner with success in the premixed case, but with limited performance on the non-premixed case.

- The light-round process is then studied in two experiential test rigs. In the KIAI multi-burner study (Chap. 10), quantitative comparisons with experiments proves that LES is able to recover the effect that the inter-injector distance has on the ignition dynamics. The joint analysis of the experimental and numerical results highlights the existence of two propagation modes: rapid and safe spanwise propagation for low spacings, and longer and uncertain axial propagation for high spacings. The effect of the non-reacting flow pattern and the burnt gas expansion effect on the occurrence of one or the other of the propagation modes is also presented. The ignition sequence in the annular MICCA experiments (Chap. 11) enables to investigate a more realistic configuration, where the light-round phase is more representative of engine configuration. Compared to the KIAI multi-burner configuration, removing the azimuthal confinement allows to evaluate the full extend of the burnt gas expansion effect on the flame front propagation speed. Comparison of the LES results obtained with two combustion models shows that the light-round phase is not highly sensitive to the numerical setup since the flame propagation is driven by the burnt gas expansion, i.e. by the adiabatic flame temperature and the consumption speed, which are well reproduced by most of the combustion models.

In addition to the work presented in this thesis, a study of a realistic combustor relight at high altitude conditions has been performed in the framework of the LEMCOTEC project (see Figs. 12.1 & 12.2). Compared to the several experimental configurations investigated in this work, the increased complexity of the industrial application emphasizes the key features that are still missing to validate the LES tool in realistic configuration:

- the key ingredient missing from all of the experiments presented here is the effect of the two-phase flow on the ignition dynamics. The study of the industrial application clearly highlights the first degree effect of the liquid fuel distribution upon the ignition dynamics, especially at relight conditions.
- although the KIAI experiments is clearly a first step towards realistic flow conditions, the flow in a real combustor is more turbulent and complex, with secondary air flow added to the flame/kernel interactions.

To address these issues, the different laboratories already involved in the work presented here (EM2C, CORIA and CERFACS) are part of the TIMBER project, in a collaborative effort to investigate the effects of the liquid phase on the ignition process. One of the objectives is to construct an experimental database of ignition in two-phase flow in order to validate the LES tool. Both the KIAI single burner (Chap. 7) and multi-burner (Chap. 10) as well as the MICCA annular test bench (Chap. 11) will be equipped of liquid injection(s) to study both **Phase 2** and **Phase 3** of ignition.

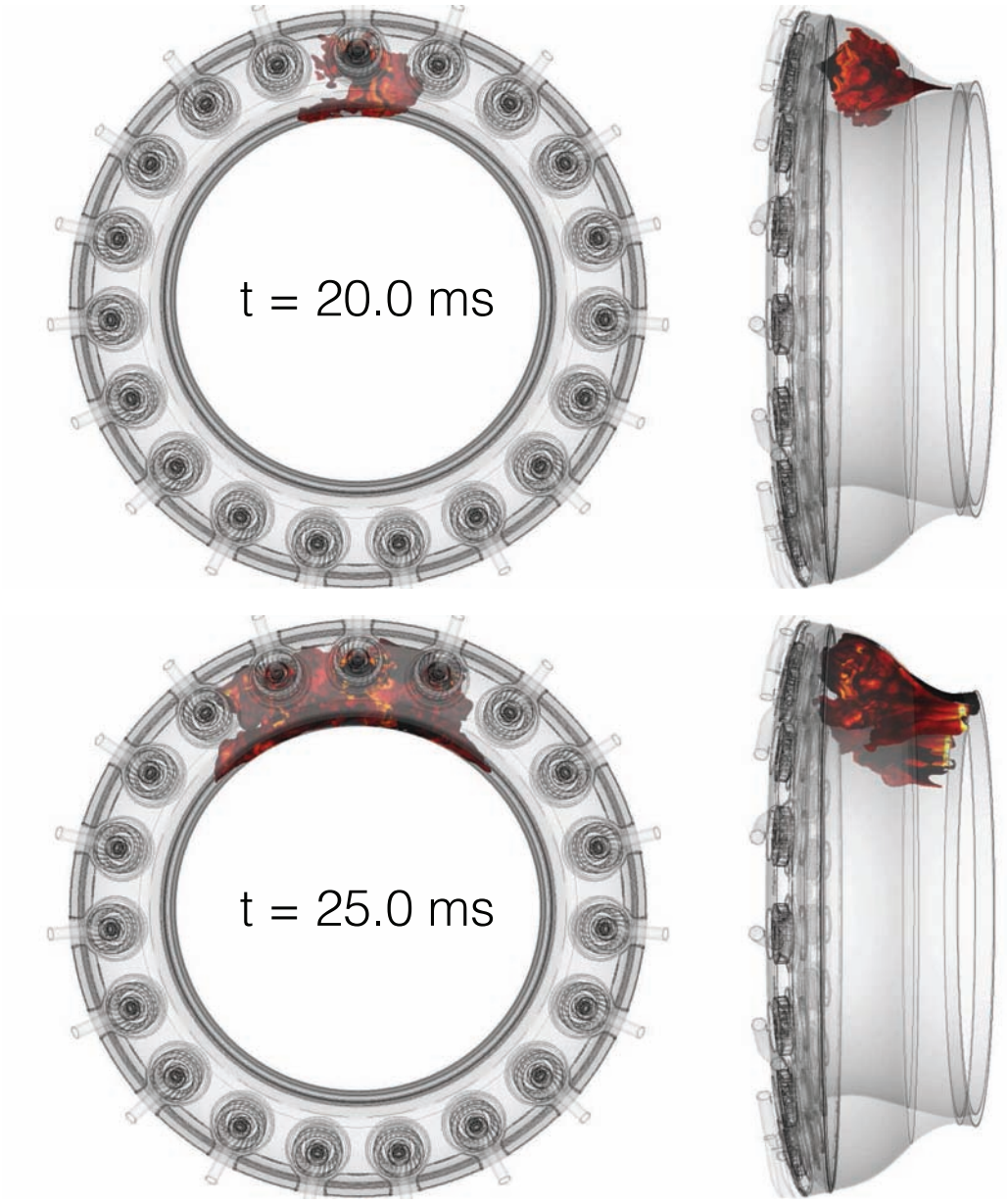

Figure 12.1: Snapshots of the ignition sequence of the annular *low-NO_x* combustor LEMCOTEC.

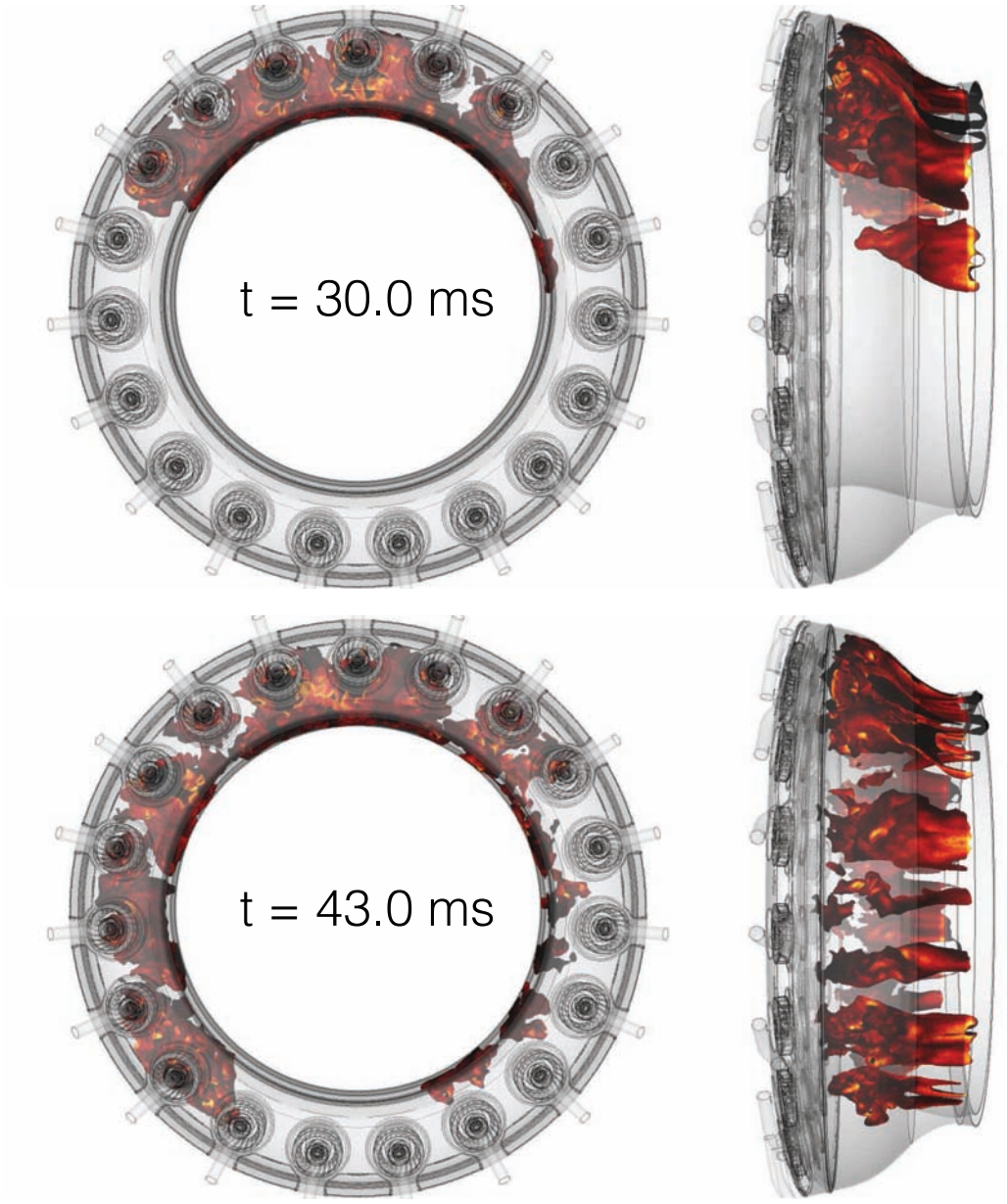

Figure 12.2: Snapshots of the ignition sequence of the annular *low-*NO_x combustor LEMCOTEC.

Bibliography

Abdel-Gayed, R., Al-Khishali, K. & Bradley, D. 1984 Turbulent burning velocities and flame straining in explosions. *Proc. R. Soc. Lond. A* **391**, 393–414. (9, 35, and 66)

Abdel-Gayed, R. & Bradley, D. 1985 Criteria for turbulent propagation limits of premixed flames. *Combustion and Flame* **62**, 61–68. (73, 152, and 153)

Abdel-Gayed, R. & Bradley, D. 1989 Combustion regimes and the straining of turbulent premixed flames. *Combustion and Flame* **76**, 213–218. (134)

Abdel-Gayed, R., Bradley, D. & Lawes, M. 1987 Turbulent burning velocities: a general correlation in terms of straining rates. *Proc. R. Soc. Lond. A* **414**, 389–413. (66, 134, and 155)

Abdel-Gayed, RG, Bradley, D, Lawes, M & Lung, FK-K 1988 Premixed turbulent burning during explosions. *Proceedings of the Combustion Institute* **21** (1), 497–504. (9, 66, and 67)

Advisory Council for Aeronautics Research in Europe 2010 Aeronautics and air transport: Beyond vision 2020 (towards 2050). *Tech. Rep.*. ACARE. (1)

Aggarwal, S. K. 1998 A review of spray ignition phenomena: present status and future research. *Progress in Energy and Combustion Science* **24**, 565–600. (60)

Aggarwal, S. K. & Sirignano, W. A. 1984 Ignition of fuel sprays: deterministic calculations for idealized droplet arrays. *Proceedings of the Combustion Institute* **20**, 1773–1780. (61)

Ahmed, S.F., Balachandran, R., Marchione, T. & Mastorakos, E. 2007*a* Spark ignition of turbulent non premixed bluff-body flames. *Combustion and Flame* **151**, 366–385. (9, 63, 64, 72, 73, 74, 75, 135, 147, 186, and 213)

Ahmed, S.F., Balachandran, R. & Mastorakos, E. 2007*b* Measurments of ignition probability in turbulent non-premixed counterflow flames. *Proc. of the Combustion Institute* **31**, 1507–1513. (9, 135)

Ahmed, S. F. & Mastorakos, E. 2006 Spark ignition of lifted turbulent jet flames. *Combustion and Flame* **146** (1-2), 215–231. (9, 63, 72, 116, 134, 135, and 186)

Akindele, O., Bradley, D., Mak, P. & McMahon, M. 1982 Spark ignition of turbulent gases. *Combustion and Flame* **47**, 129–155. (9, 60, 61, 67, and 155)

Allouis, C., Beretta, F. & Amoresano, A. 2008 Experimental study of lean premixed prevaporized combustion fluctuations in gas turbine burner. *Combustion Science and Technology* **180** (5), 900–909. (2)

Angelberger, C., Veynante, D., Egolfopoulos, F. & Poinsot, T. 1998 Large eddy simulations of combustion instabilities in premixed flames. pp. 61–82. Center for Turbulence Research, NASA Ames/Stanford Univ. (47, 48)

AVBP 2011 *AVBP Handbook - http://cerfacs.fr/∼ avbp/AVBP_V6.X/HANDBOOK*. CERFACS. (44)

Bach, E., Kariuki, J., Dawson, J. R. & Mastorakos, E. 2013 Spark ignition of single bluff-body premixed flames and annular combustors. (10, 164, and 165)

Ballal, D. R. & Lefebvre, A. H. 1975 The influence of flow parameters on minimum ignition energy and quenching distance. *Proc. Combust. Inst.* **15**, 1473–1481. (9, 60)

Ballal, D. R. & Lefebvre, A. H. 1977 Ignition and flame quenching in flowing gaseous mixtures. *Proceedings of the Royal Society of London. Series A* **357**, 163–181. (9, 60, and 61)

Ballal, D. R. & Lefebvre, A. H. 1978 Ignition and flame quenching of quiescent fuel mists. *Proceedings of the Royal Society of London. Series A* **364**, 277–294. (60, 61)

Ballal, D. R. & Lefebvre, A. H. 1979 Ignition and flame quenching of flowing heterogeneous fuel-air mixtures. *Combustion and Flame* **35**, 155–168. (61)

der Bank, R. Von, Donnerhack, S., Rae, A., Cazalens, M., Lundblach, A. & Dietz, M. 2014 Lemcotec: improving the core-engine thermal efficiency. (3)

Barbosa, S., Scouflaire, P. & Ducruix, S. 2009 Time resolved flowfield, flame structure and acoustic characterization of a staged multi-injection burner. *Proc. of the Combustion Institute* . (2)

Barré, D. 2014 Numerical simulation of ignition in aeronautical combustion chambers. PhD thesis, INP Toulouse. (10, 11, 74, 78, 95, 101, 102, and 168)

Barré, D., Kraushaar, M., Staffelbach, G., Moureau, V. & Gicquel, L.Y.M. 2013 Compressible and low Mach number LES of a swirl experimental burner. *Comptes rendus de l'Académie des sciences Mécanique* **341**, 277–287. (89, 91)

Bauerheim, M. 2014 Theoretical and numerical study of symmetry breaking effects on azimuthal thermoacoustic modes in annular combustors. PhD thesis, INP Toulouse. (164)

Baum, M. & Poinsot, T. 1995 Effects of mean flow on premixed flame ignition. *Combustion Science and Technology* **106** (1-3), 19. (60, 65)

Beduneau, J-L. & Kim, B. 2003 Measurements of minimum ignition energy in premixed laminar methane/air flow by using laser induced spark. *Combustion and Flame* **132**, 653–665. (9, 60)

Beer, J. M. & Chigier, N. A. 1983 *Combustion aerodynamics*. Malabar, Florida: Krieger. (3, 82)

Berman, V., Riazantsev, I. & Shevtsova, V. 1981 Asymptotic analysis of the process of igniting a combustible gas mixture by thermal inhomogeneity. *PMM U.R.S.S.* . (58)

Bilger, R.W. 1989 The structure of turbulent nonpremixed flames. *Proceedings of the Combustion Institute* **22** (1), 475–488. (29, 30)

Bilger, R. W., Antonia, R. & Sreenivasan, K. 1976 Determination of intermittency from the probability density function of a passive scalar. *Physics of Fluids* **19** (10), 1471–1474. (132)

Billant, P., Chomaz, J-M. & Huerre, P. 1998 Experimental study of vortex breakdown in swirling jets. *Journal of Fluid Mechanics* **376**, 183–219. (82, 83)

Birch, A. D., Brown, D.R., Dodson, M. G. & Thomas, J. R. 1977 The turbulent concentration field of a methnae jet. *Journal of Fluid Mechanics* **88** (3), 431–449. (132, 147, and 148)

Birch, A. D., Brown, D. R. & Dodson, M. 1981 Ignition probabilities in turbulent mixing flows. *Proc. Combust. Inst.* **18**, 1775–1779. (62, 63, 72, 116, 132, and 147)

Boileau, M. 2007 Simulation aux grandes échelles de l'allumage diphasique des foyers aéronautiques. Phd thesis, INP Toulouse. (11, 75, and 163)

Boileau, M., Staffelbach, G., Cuenot, B., Poinsot, T. & Bérat, C. 2008 LES of an ignition sequence in a gas turbine engine. *Combustion and Flame* **154** (1-2), 2–22. (10, 11, 163, 164, and 207)

Borghi, R. 1985 On the structure and morphology of turbulent premixed flames. In *Rec. Adv. in Aerospace Sci.* (ed. C. Bruno & C. Caseci), pp. 117–138. (68)

Boudier, P., Henriot, S., Poinsot, T. & Baritaud, T. 1992 A model for turbulent flame ignition and propagation in spark ignition engines. *Proceedings of the Combustion Institute* **24**, 503–510. (9, 65, and 155)

Bourgouin, J-F. 2014 Experimental study of azimuthal instabilities in an annular combustion chamber. PhD thesis, Ecole Centrale Paris. (197)

Bourgouin, J-F., Durox, D., Schuller, T., Beaunier, J. & Candel, S. 2013 Ignition dynamics of an annular combustor equipped with multiple swirling injectors. *Combustion and Flame* **160** (8), 1398–1413. (10, 12, 164, 165, 166, 188, 195, 196, 197, and 206)

Boussinesq, J. 1877 Théorie de l'écoulement tourbillant. *Mém. Présentés par Divers Savants. Acad. Sci. Inst. Fr.* **23**, 46–50. (44)

Bradley, D., Gaskell, P. & Gu, X. 1996 Burning velocities, markstein lengths and flame quenching for spherical methane-air flames: a computational study. *Combustion and Flame* **104**, 176–198. (9)

Bradley, D., Lawes, M. & Mansour, M. 2011 Correlation of turbulent burning velocities of ethanol-air measured in a fan-stirred bomb up to 1.2 MPa. *Combustion and Flame* **158**, 123–138. (66)

Bradley, D., Sheppard, C., Suardjaja, I. & Woolley, R. 2004 Fundamentals of high-energy spark ignition with lasers. *Combustion and Flame* **138**, 55–77. (6, 9, 66, and 67)

Bray, K.N.C. & Cant, R.S. 1991 Some applications of kolmogorov's turbulence research in the field of combustion. *Proceedings of the Royal Society of London. Series A: Mathematical and Physical Sciences* **434** (1890), 217–240. (34)

Bray, K. N. C. & Moss, J. B. 1977 A closure model for the turbulent premixed flame with sequential chemistry. *Combustion and Flame* **30**, 125–131. (45)

Buckmaster, J.D. 2002 Edge-flames. *Progress in Energy and Combustion Science* **28** (5), 435–475. (70)

Bush, W. & Fendell, F. 1970 Asymptotic analysis of laminar flame propagation for general lewis numbers. *Combustion Science and Technology* **1** (6), 421–428. (27)

Butler, T. D. & O'Rourke, P. J. 1977 A numerical method for two-dimensional unsteady reacting flows. *Proceedings of the Combustion Institute* **16** (1), 1503 – 1515. (46)

CAEP 2010 CAEP/8 NOx stringency cost-benefit analysis demonstration using AMPT-IMPACTS. *Tech. Rep.*. International Civial Aviation Organization. (2)

Candel, S. & Poinsot, T. J. 1990 Flame stretch and the balance equation for the flame area. *Combustion Science and Technology* **70**, 1–15. (27)

Cardin, C. 2013 Etude expérimentale des phénoménes physico-chimiques de l'allumage dans des écoulements laminaires et turbulents. PhD thesis, INSA Rouen. (9, 62, 63, 67, 125, 129, and 213)

Cardin, C., Renou, B., Cabot, G. & Boukhalfa, A.M. 2013 Experimental analysis of laser-induced spark ignition of lean turbulent premixed flames: New insight into ignition transition. *Combustion and Flame* **160** (8), 1414–1427. (62)

Chakraborty, N. & Cant, R.S. 2004 Unsteady effects of strain rate and curvature on turbulent premixed flames in an inflow-outflow configuration. *Combustion and Flame* **137**, 129–147. (115)

Chakraborty, N. & Mastorakos, E. 2006 Numerical investigation of edge flame propagation characteristics in turbulent mixing layers. *Physics of Fluids* **18**. (9)

Chakraborty, N. & Mastorakos, E. 2008 Direct Numerical Simulations of localised forced ignition in turbulent mixing layers: the effects of mixture fraction and its gradient. *Flow, Turbulence and Combustion* **80**, 155–186. (30, 68)

Chakraborty, N., Mastorakos, E. & Cant, R. S. 2007 Effects of turbulence on spark ignition in inhomogeneous mixtures: a direct numerical simulation study. *Combustion Science and Technology* **179**, 293–317. (65, 68, 69, and 192)

Champion, M., Deshaies, B., Joulin, G. & Kinoshita, K. 1986 Spherical flame initiation: Theory versus experiments for lean propane-air mixtures. *Combustion and Flame* **65** (3), 319–337. (9, 59)

Charlette, F., Veynante, D. & Meneveau, C. 2002 A power-law wrinkling model for LES of premixed turbulent combustion: Part I - non-dynamic formulation and initial tests. *Combustion and Flame* **131**, 159–180. (48, 101, 199, and 246)

Chen, J. H., Choudhary, A., De Supinski, B., DeVries, M., Hawkes, E.R., Klasky, S., Liao, W.K., Ma, K.L., Mellor-Crummey, J., Podhorszki, N. *et al.* 2009 Terascale Direct Numerical Simulations of turbulent combustion using S3D. *Computational Science & Discovery* **2** (1), 015001. (40)

Chen, J. H. & Im, H. G. 1998 Correlation of flame speed with stretch in turbulent premixed methane/air flames. *Proceedings of the Combustion Institute* **27** (1), 819–826. (71, 119, 122, and 239)

Cheng, L., Dianat, M., Spencer, A. & McGuirk, J. J. 2012 Validation of LES predictions of scalar mixing in high-swirl fuel injector flows. *Flow, Turbulence and Combustion* **88** (1-2), 143–168. (93)

Clavin, P. 1985 Dynamic behavior of premixed flame fronts in laminar and turbulent flows. *Progress in Energy and Combustion Science* **11**, 1–59. (27)

Colin, O., Ducros, F., Veynante, D. & Poinsot, T. 2000 A thickened flame model for Large Eddy Simulations of turbulent premixed combustion. *Physics of Fluids* **12** (7), 1843–1863. (45, 47, 170, and 191)

Colin, O. & Rudgyard, M. 2000 Development of high-order Taylor-Galerkin schemes for LES. *Journal of Computational Physics* **162**, 338–371. (53, 81, 99, 101, 170, 199, 241, 244, and 247)

Cook, A. W. & Riley, J. J. 1994 A subgrid model for equilibrium chemistry in turbulent flows. *Physics of Fluids* **6** (8), 2868 – 2870. (46)

Cook, A. W. & Riley, J. J. 1998 Subgrid scale modeling for turbulent reacting flows. *Combustion and Flame* **112**, 593 – 606. (46)

Cordier, M. 2013 Allumage et propagation de flamme dans les écoulements fortement swirlés : études expérimentales et numériques. PhD thesis, INSA Rouen. (10, 12, 73, 77, 79, 92, 93, 95, 96, 97, 103, 104, 109, 116, 125, 129, 138, 153, 155, 156, 157, 158, 163, 166, 168, 172, and 173)

Cordier, M., Vandel, A., Cabot, G., Renou, B. & Boukhalfa, A. 2013*a* Laser-induced spark ignition of premixed confined swirled flames. *Combustion Science and Technology* **185** (3), 379–407. (73, 74, 83, and 163)

Cordier, M., Vandel, A., Renou, B., Cabot, G., Boukhalfa, M. & Cazalens, M. 2013*b* Spark ignition of confined swirled flames: experimental and numerical investigation. *ASME* . (73, 136)

Cordier, M., Vandel, A., Renou, B., Cabot, G., Boukhalfa, M.A., Esclapez, L., Barré, D., Riber, E., Cuenot, B. & Gicquel, L.Y.M. 2013*c* Experimental and numerical analysis of an ignition sequence in a multiple-injectors burner. American Society of Mechanical Engineers. (168)

Cuenot, B. & Poinsot, T. 1994 Effects of curvature and unsteadiness in diffusion flames. implications for turbulent diffusion combustion. *Proceedings of the Combustion Institute* **25** (1), 1383–1390. (36, 37)

Dahms, R., Drake, M., Fansler, T., Kuo, T.-W. & Peters, N. 2011 Undestanding ignition processes in spray-guided gasoline engines using high-speed imaging and the extended spark-ignition model sparkcimm. part a: Spark channel processes and the turbulent flame front propagation. *Combustion and Flame* **158**, 2229–2244. (9)

Dale, J., Checkel, M. & Smy, P. 1997 Application of high energy ignition systems to engines. *Progress in Energy and Combustion Science* **23**, 379–398. (9)

Deshaies, B. & Joulin, G. 1984 On the initiation of a spherical flame kernel. *Combustion Science and Technology* **37** (3-4), 99–116. (9, 58, and 59)

Doerr, T. 2012 Introduction to aero-engine gas turbine combustion. In *Lecture Series 2012-04* (ed. Von Karman Institute for Fluid Dynamics). Von Karman Institute for Fluid Dynamics. (4)

Dold, J. W. 1989 Flame propagation in a nonuniform mixture: analysis of a slowly varying triple flame. *Combustion and Flame* **76**, 71–88. (30)

Domingo, P. & Vervisch, L. 1996 Triple flames and partially premixed combustion in autoignition of non-premixed turbulent mixtures. *Proceedings of the Combustion Institute* **26** (1), 233–240. (30)

Donea, J. & Huerta, A. 2003 *Finite element methods for flow problems*. John Wiley & Sons. (53)

Dopazo, C. 1994 Recent developments in PDF methods. In *Turbulent Reacting Flows* (ed. P. A. Libby & F. A. Williams), pp. 375 – 474. London: Academic. (45)

Driscoll, J. F. 2008 Turbulent premixed combustion: Flamelet structure and its effect on turbulent burning velocities. *Progress in Energy and Combustion Science* **34**, 91–134. (34, 35)

Duclos, J-M. & Colin, O. 2001 Arc and kernel tracking ignition model for 3D Spark-ignition engine calculations. *COMODIA 2001* **5**, 343–350. (65, 134)

Echekki, T. & Chen, J. H. 1996 Unsteady strain rate and curvature effects in turbulent premixed methane-air flames. *Combustion and Flame* **106**, 184–202. (71)

Echekki, T. & Chen, J. H. 1998 Structure and propagation of methanol–air triple flames. *Combustion and Flame* **114** (1), 231–245. (31)

Echekki, T. & Chen, J. H. 1999 Analysis of the contribution of curvature to premixed flame propagation. *Combustion and Flame* **118**, 308–311. (26, 239)

Echekki, T. & Kolera-Gokula, H. 2007 A regime diagram for premixed flame kernel-vortex interactions. *Physics of Fluids* **19**. (68)

Eckhoff, R. K., Ngo, M. & Olsen, W. 2010 On the minimum ignition energy (MIE) for propane/air. *Journal of Hazardous Materials* **175**, 293–297. (9)

Eichenberger, D. & Roberts, W. 1999 Effect of unsteady stretch on spark-ignited flame kernel survival. *Combustion and Flame* **118**, 469–478. (9, 68)

Esclapez, L., Riber, E. & Cuenot, B. 2015 Ignition probability of a partially premixed burner using les. *Proceedings of the Combustion Institute* **65** (3), 3133–3141. (96)

Eyssartier, A. 2012 LES of two-phase reacting flows: stationary and transient operating conditions. PhD thesis, INP Toulouse. (11)

Eyssartier, A., Cuenot, B., Gicquel, L. & Poinsot, T. 2013 Using LES to predict ignition sequences and ignition probability of turbulent two-phase flames. *Combustion and Flame* **160**, 1191–1207. (10, 74, 133, 137, 147, 157, and 159)

Fiorina, B., Gicquel, O., Vervisch, L., Carpentier, S. & Darabiha, N. 2005 Approximating the chemical structure of partially premixed and diffusion counterflow flames using FPI flamelet tabulation. *Combustion and Flame* **140**, 147–160. (112)

Fiorina, B., Gicquel, O. & Veynante, D. 2009 Turbulent flame simuations taking advantage of tabulated chemistry self-similar properties. *Proceedings of the Combustion Institute* **32**, 1687–1694. (49)

Fiorina, B., Vicquelin, R., Auzillon, P., Darabiha, N., Gicquel, O. & Veynante, D. 2010 A filtered tabulated chemistry model for LES of premixed combustion. *Combustion and Flame* **157** (3), 465–475. (45, 166, 199, and 204)

Frank-Kamenetskii, D. 1942 Diffusion and heat exchange in chemical kinetics. *Acta Physicochimica U.R.S.S.* **16**. (58)

Franzelli, B. 2011 Impact of the chemical description on direct numerical simulations and large eddy simulations of turbulent combustion in industrial aero-engines. PhD thesis, INP Toulouse. (50, 51, 52, and 101)

Franzelli, B., Riber, E., Gicquel, L. Y. M. & Poinsot, T. J. 2012 Large Eddy Simulation of combustion instabilities in a lean partially premixed swirled flame. *Combustion and Flame* **159** (2), 621–637. (50, 170)

Franzelli, B., Riber, E., Sanjosé, M. & Poinsot, T. 2010 A two-step chemical scheme for Large Eddy Simulation of kerosene-air flames. *Combustion and Flame* **157** (7), 1364–1373. (170, 199)

Frenillot, J-P. 2011 Etude phénoménologique des processus d'allumage et de stabilisation dans les chambers de combustion turbulente swirlées. PhD thesis, INSA Rouen. (77)

Fru, G., Thévenin, D. & Janiga, G. 2011 Impact of turbulence intensity and equivalence ratio on the burning rate of premixed methane–air flames. *Energies* **4** (6), 878–893. (9, 70, and 71)

Galmiche, B., Halter, F. & Foucher, F. 2012 Effects of high pressure, high temperature and dilution on laminar burning velocities and markstein lengths of iso-octane/air mixtures. *Combustion and Flame* **159** (11), 3286–3299. (9, 66)

Garcia-Rosa, N, Linassier, G, Lecourt, R, Villedieu, P & Lavergne, G 2009 A two-phase model for ignition in a model turbojet combustor. (65)

Garcia-Rosa, N., Linassier, G., Lecourt, R., Villedieu, P. & Lavergne, G. 2011 Experimental and numerical study of high-altitude ignition of a turbojet combustor. *Heat Transfer Engineering* **32**, 949 – 956. (9, 74, 75, 78, and 133)

García-Villalba, M, Fröhlich, J & Rodi, W 2006 Identification and analysis of coherent structures in the near field of a turbulent unconfined annular swirling jet using large eddy simulation. *Physics of Fluids* **18** (5), 055103. (92)

Gashi, S., Hult, J., Jenkins, K.W., Chakraborty, N., Cant, S. & Kaminski, C. 2005 Curvature and wrinkling of premixed flame kernels - comparisons of OH PLIF and DNS data. *Proceedings of the Combustion Institute* **30**, 809–817. (9, 70)

Gebel, G., Mosbach, T., Meier, W. & Aigner, M. 2012 Experimental investigations of the ignition and flame stabilization of a full cone kerosene spray in a lab-scale model combustor. (9)

Giauque, A., Selle, L., Gicquel, L. Y. M., Poinsot, T., Buechner, H., Kaufmann, P. & Krebs, W. 2005 System identification of a large-scale swirled partially premixed copmbustor using LES and measurments. *Journal of Turbulence* **6** (21), 1–20. (11)

Gibson, C. 1968 Fine structure of scalar fields mixed by turbulence. I: Zero-gradient points and minimal gradient surfaces. *Physics of Fluids* **11**. (26)

Gicquel, O., Darabiha, N. & Thevenin, D. 2000 Laminar premixed hydrogen/air counterflow flame simualtions using flame prolongation of ildm with differential diffusion. *Proceedings of the Combustion Institute* **28**, 1901–1908. (49)

Glassman, I. & Yetter, R. 2008 *Combustion*, 4th edn. Academic Press. (60)

Goodwin, David G., Moffat, Harry K. & Speth, Raymond L. 2014 Cantera: An object-oriented software toolkit for chemical kinetics, thermodynamics, and transport processes. http://www.cantera.org, version 2.1.2. (101)

Gorbachev, V. 1981 A contribution to semenov's general theory of thermal ignition regarding thermal analysis. *Journal of Thermal Analysis* **22** (2), 287–289. (58)

Gran, I., Echekki, T. & Chen, J. H. 1996 Negative flame speed in an unsteady 2-D premixed flame: a computational study. *Proceedings of the Combustion Institute* **26**, 323–329. (26, 71, 122, and 239)

Granet, V., Vermorel, O., Leonard, T., Gicquel, L., & Poinsot, T. 2010 Comparison of nonreflecting outlet boundary conditions for compressible solvers on unstructured grids. *AIAA Journal* **48** (10), 2348–2364. (99, 170, 199, 241, 244, and 247)

Hartley, L. & Dold, J. W. 1991 Flame propagation in a nonuniform mixture: analysis of a triple flame. *Combustion Science and Technology* **80**, 23. (68)

Hawkes, E. R. & Cant, S. R. 2000 A flame surface density approach to large eddy simulation of premixed turbulent combustion. *Proceedings of the Combustion Institute* **28**, 51–58. (45)

He, L. 2000 Critical conditions for spherical flame initiation in mixtures with high Lewis numbers. *Combustion Theory and Modelling* **4** (2), 159–172. (59)

Hélie, J. & Trouvé, A. 1998 Turbulent flame propagation in partially premixed combustion. *Proceedings of the Combustion Institute* **27**, 891–898. (239)

Hirschfelder, J. O., Curtiss, C. F. & Bird, R. B. 1969 *Molecular theory of gases and liquids*. New York: John Wiley & Sons. (17)

Huang, C., Shy, S., Liu, C. & Yan, Y. 2007 A transition on minimum ignition energy for lean turbulent methane combustion in flamelet and distributed regimes. *Proceedings of the Combustion Institute* **31**, 1401–1409. (62)

Hughes, C. & Gazzaniga, J. 1989 Low-speed wind tunel performance of high-speed counter-rotation propellers at angle-of-attack. (1)

Ivanic, T., Foucault, E. & Pecheux, J. 2003 Dynamics of swirling jet flows. *Experiments in Fluids* **35** (4), 317–324. (83)

Janus, B., Dreizler, A. & Janicka, J. 2005 Flow and scalar field measurements in an optically accessible model gas turbine combustor. (78)

Jenkins, K.W. & Cant, R. S. 2002 Curvature effects on flame kernels in a turbulent environment. *Proceedings of the Combustion Institute* **29**, 2023–2029. (71)

Jenkins, K.W., Klein, M., Chakraborty, N. & Cant, R.S. 2006 Effects of strain rate and curvature on the propagation of spherical kernel in the thin-reaction-zones regime. *Combustion and Flame* **145**, 415–434. (9, 70, and 115)

Jones, W.P., Lyra, S. & Navarro-Martinez, S. 2011 Large eddy simulation of a swirl stabilized spray flame. , vol. 33, pp. 2153–2160. (10)

Jones, W.P. & Prasad, V.N. 2011 LES-pdf simulation of a spark ignited turbulent methane jet. *Proceedings of the Combustion Institute* **33**, 1355–1363. (65, 72, 75, and 95)

Jones, W. P. & Tyliszczack, A. 2010 Large eddy simulation of spark ignition in a gas turbine combustor. *Flow, Turbulence and Combustion* **85**, 711–734. (10, 75, and 213)

Joulin, G. 1985 Point-source initiation of lean spherical flames of light reactants: An asymptotic theory. *Combustion Science and Technology* **43** (1), 99–113. (9, 59)

Kaminski, C., Hult, J., Alden, M., Lindenmaier, S., Dreizler, A., Maas, U. & Baum, M. 2000 Spark ignition of turbulent methane-air mixtures revealed by time-resolved planar laser-induced fluorescence and direct numerical simulations. *Proceedings of the Combustion Institute* **28**, 399–405. (68)

Karpov, V. P., Semenov, E. & Sokolik, A.S. 1959 Turbulent combution in closed volume. *Dokladi Akademii Nauk SSSR* . (66)

Kent, J. & Bilger, R. W. 1977 The prediciton of turbulent diffusion flame fields and nitric oxide formation. *Proceedings of the Combustion Institute* **16**, 1643–1656. (132)

Kerl, J., Lawn, C. & Beyrau, F. 2013 Three-dimensional flame displacement speed and flame front curvature measurements using quad-plane piv. *Combustion and Flame* **160** (12), 2757–2769. (70)

Kerstein, A. R. 1988 A linear eddy model of turbulent scalar transport and mixing. *Combustion Science and Technology* **60**, 391. (46)

Kioni, P., Rogg, B., Bray, K. N. C. & Linan, A. 1993 Flame spread in laminar mixing layers: the triple flame. *Combustion and Flame* **95** (3), 276–290. (30)

Klein, M., Chakraborty, N. & Cant, R. S. 2008 Effects of turbulence on self-sustained combustion in premixed flame kernels: a direct numerical simulation study. *Flow, Turbulence and Combustion* **81**, 583–607. (61, 74)

Klein, M., Chakraborty, N., Jenkins, K.W. & Cant, R. S. 2006 Effects of initial radius on the propagation of premixed flame kernels in a turbulent environment. *Physics of Fluids* **18**. (71)

Ko, Y., Anderson, R. & Arpaci, V. 1991 Spark ignition of propane-air mixtures near the minimum ignition energy: Part 1. an experimental study. *Combustion and Flame* **83**, 75–87. (9)

Ko, YS & Chung, SH 1999 Propagation of unsteady tribrachial flames in laminar non-premixed jets. *Combustion and Flame* **118** (1), 151–163. (70)

Kolera-Gokula, H. & Echekki, T. 2006 Direct numerical simulation of premixed flame kernel-vortex interactions in hydrogen-air mixtures. *Combustion and Flame* **146**, 155–167. (68, 71)

Kolmogorov, A. N. 1941 The local structure of turbulence in incompressible viscous fluid for very large reynolds numbers. *Comptes rendus de l'Académie des sciences, USSR* **30**, 301. (32, 39, and 44)

Kono, M., Hatori, K. & Iinuma, K. 1984 Investigation on ignition ability of composite sparks in flowing mixtures. *Proc. Combust. Inst.* **20**, 133–140. (9, 60, 61, and 62)

Kraushaar, M. 2011 Application of the compressible and low-mach number approaches to large-eddy simulation of turbulent flows in aero-engines. PhD thesis, INP Toulouse. (81, 89)

Kravchik, T., Sher, E. & Heywood, J. B. 1995 From spark ignition to flame initiation. *Combustion Science and Technology* **108**, 1–30. (64)

Kuo, K. K. 2005 *Principles of combustion*, 2nd edn. Hoboken, New Jersey: John Wiley & Sons, Inc. (15, 19, and 21)

Lacaze, G. 2009 Simualtion aux grandes echelles de l'allumage de moteurs fusées cryotechniques. PhD thesis, INP Toulouse. (11, 154)

Lacaze, G., Cuenot, B., Poinsot, T. J. & Oschwald, M. 2009*a* Large eddy simulation of laser ignition and compressible reacting flow in a rocket-like configuration. *Combustion and Flame* **156** (6), 1166–1180. (65, 170, and 213)

Lacaze, G., Richardson, E. & Poinsot, T. 2009*b* Large eddy simulation of spark ignition in a turbulent methane jet. *Combustion and Flame* **156**, 1993–2009. (10, 72, 95, 100, 102, and 246)

Lam, SH & Goussis, DA 1994 The CSP method for simplifying kinetics. *International Journal of Chemical Kinetics* **26** (4), 461–486. (49)

Lamarque, Nicolas 2007 Schémas numériques et conditions limites pour la simulation aux grandes échelles de la combustion diphasique dans les foyer d'hélicoptères. PhD thesis, INP Toulouse. (53)

Lax, P. D. & Wendroff, B. 1960 Systems of conservation laws. *Communications on Pure and Applied Mathematics* **13**, 217–237. (53)

Lee, D.S., Pitari, G., Grewe, V. & Gierens, K. 2010 Transport impacts on atmosphere and climate: Aviation. *Atmospheric Environment* **44**, 4678–4734. (1)

Lefebvre, A. H. 1989 *Atomization and Sprays*. Taylor & Francis. (5)

Lefebvre, A. H. 1998 *Gas Turbine Combustion*, 2nd edn. Taylor and Francis. (2, 3, 6, 7, 8, 11, 12, and 65)

Légier, J.-Ph. 2001 Simulations numériques des instabilités de combustion dans les foyer aéronautique. PhD thesis, INP Toulouse. (50)

Légier, J.-Ph., Poinsot, T. & Veynante, D. 2000 Dynamically thickened flame LES model for premixed and non-premixed turbulent combustion. pp. 157–168. Center for Turbulence Research, NASA Ames/Stanford Univ. (45, 48)

Letty, C., Mastorakos, E., Masri, A., Juddoo, M. & O'Loughlin, W. 2012 Structure of igniting ethanol and n-heptane spray flames with and without swirl. *Experimental thermal and fluid science* **43**, 47–54. (74)

Lewis, B. & von Elbe, G. 1987 *Combustion, Flames and Explosions of Gases*, 3rd edn. Academic Press. (9, 59, and 60)

Liang, H. & Maxworthy, T. 2005 An experimental investigation of swirling jets. *Journal of Fluid Mechanics* **525**, 115–159. (83, 91)

Libby, P. A. & Williams, F. A. 1994 Turbulent combustion: fundamental aspects and a review. In *Turbulent Reacting Flows*, pp. 2–61. Academic Press London. (29)

Linan, A. 1974 The asymptotic structure of counterflow diffusion flames for large activation energies. *Acta Astronautica* **1** (7), 1007–1039. (29)

Linassier, G. 2012 Etude expérimentale et numérique de l'allumage des turboréacteurs en conditions de haute altitude. PhD thesis, ISAE. (78, 133)

Linassier, G., Bruyat, A., Villedieu, P., Bertier, N., Laurent, C., Rouzaud, O., Lecourt, R., Verdier, H. & Lavergne, G. 2013 Application of numerical simulations to predict aircraft combustor ignition. *Comptes Rendus Mécanique* **341** (1), 201–210. (65)

Lu, T. & Law, C. K. 2006 On the applicability of directed relation graphs to the reduction of reaction mechanisms. *Combustion and Flame* **146** (3), 472–483. (49)

Lucca-Negro, O. & O'Doherty, T. 2001 Vortex breakdown: a review. *Progess in Energy and combustion Science* **27**, 431–481. (82)

Maas, U. & Pope, S. B. 1992 Simplifying chemical kinetics: intrinsic low-dimensional manifolds in composition space. *Combustion and Flame* **88** (3), 239–264. (49)

Maly, R. & Vogel, M. 1978 Initiation and propagation of flame fronts in lean CH4-air mixtures by the three modes of the ignition spark. *Proceedings of the Combustion Institute* **17** (1), 821–831. (6, 59, and 64)

Mansour, M., Peters, N. & Schrader, L.-U. 2008 Experimental study of turbulent flame kernel propagation. *Experimental Thermal and Fluid Science* **32**, 1396–1404. (9)

Marchione, T., Ahmed, S.F. & Mastorakos, E. 2009 Ignition of turbulent swirling n-heptane spray flames using single and multiple sparks. *Combustion and Flame* **156**, 166–180. (9, 74, 135, and 186)

Mastorakos, E. 2009 Ignition of turbulent non-premixed flames. *Progress in Energy and Combustion Science* **35** (1), 57–97. (8, 65, 67, 76, 116, and 213)

Meneveau, C. & Poinsot, T. 1991 Stretching and quenching of flamelets in premixed turbulent combustion. *Combustion and Flame* **86**, 311–332. (28)

Merzhanov, A. & Averson, A. 1971 The present state of the thermal ignition theory: an invited review. *Combustion and Flame* **16**, 89–124. (58)

Mittinti, D. & Dabora, E. 1984 Plasma jet ignition studies. *Proceedings of the Combustion Institute* **20** (1), 169–177. (7)

Mizobuchi, Y., Tachibana, S., Shinio, J., Ogawa, S. & Takeno, T. 2002 A numerical analysis of the structure of a turbulent hydrogen jet lefted flame. *Proceedings of the Combustion Institute* **29**, 2009–2015. (112)

Morton, K. W. & Paisley, M. F. 1989 A finite volume scheme with shock fitting for the steady euler equations. *Journal of Computational Physics* **80**, 168–203. (53)

Moureau, V., Domingo, P. & Vervisch, L. 2011*a* Design of a massively parallel CFD code for complex geometries. *Comptes rendus de l'Académie des sciencesMécanique* **339**, 141–148. (80)

Moureau, V., Domingo, P. & Vervisch, L. 2011*b* From Large-Eddy Simulation to Direct Numerical Simulation of a lean premixed swirl flame: Filtered laminar flame-pdf modeling. *Combustion and Flame* **158**, 1340–1357. (40)

Moureau, V., Fiorina, B. & Pitsch, H. 2009 A level set formulation for premixed combustion LES considering the turbulent flame structure. *Combustion and Flame* **156** (4), 801–812. (45)

Moureau, V., Lartigue, G., Sommerer, Y., Angelberger, C., Colin, O. & Poinsot, T. 2005 Numerical methods for unsteady compressible multi-component reacting flows on fixed and moving grids. *Journal of Computational Physics* **202** (2), 710–736. (53, 54)

Neophytou, A., Mastorakos, E. & Cant, R. S. 2010 Dns of spark ignition and edge flame propagation in turbulent droplet-laden mixing layers. *Combustion and Flame* **157**, 1071–1086. (9, 30)

Neophytou, A., Richardson, E. & Mastorakos, E. 2012 Spark ignition of turbulent recirculating non premixed gas and spray flames: A model for predicting ignition probability. *Combustion and Flame* **159**, 1503–1522. (10, 135, 138, 147, 152, and 153)

Nicholas, J. 2005 *The Jet Engine*, 6th edn. Rolls-Royce plc. (4, 89)

Nicolaides, R. 1987 Deflation of conjugate gradients with applications to boundary value problems. *SIAM J. Numer. Anal.* **24** (2), 355–365. (81)

Nicoud, F., Baya Toda, H., Cabrit, O., Bose, S. & Lee, J. 2011 Using singular values to build a subgrid-scale model for Large Eddy Simulations. *Physics of Fluids* **23** (8), 085106. (44)

Nicoud, F. & Ducros, F. 1999 Subgrid-scale stress modelling based on the square of the velocity gradient tensor. *Flow, Turbulence and Combustion* **62** (3), 183–200. (44, 81, 99, 170, 199, and 247)

Olsen, H., Gayhart, E. & Edmonson, R. 1953 Propagation of incipient spark-ignited flames in hydrogen-air and propane-air mixtures. *Proceedings of the Combustion Institute* **4** (1), 144–148. (59)

Ouarti, N., Lavergne, G. & Bissieres, D. 2003 Modeling of the spray ignition for turbojet engine in-flight re-light. (9, 65)

Palies, P. 2010 Dynamique et instabilités de combustion de flammes swirlées. Phd thesis, Ecole Centrale Paris. (83)

Pascaud, S. 2006 Vers la simulation aux grandes echelles des écoulements turbulents diphasique réactifs: application aux foyers aéronautiques. PhD thesis, INP Toulouse. (11)

Peters, N. 1986 Laminar flamelet concepts in turbulent combustion. *Proceedings of the Combustion Institute* **21** (1), 1231–1250. (27, 68)

Peters, N 1999 The turbulent burning velocity for large-scale and small-scale turbulence. *Journal of Fluid Mechanics* **384**, 107–132. (70, 115)

Peters, N. 2000 *Turbulent combustion*. Cambridge University Press. (21, 25, 26, 34, and 67)

Peters, N., Terhoeven, P., Chen, J. H. & Echekki, T. 1998 Statistics of flame displacement speeds from computations of 2D unsteady methane-air flames. *Proceedings of the Combustion Institute* **27**, 833–839. (26, 191)

Peterson, B., Baum, E., Böhm, B. & Dreizler, A. 2015 Early flame propagation in a spark-ignition engine measured with quasi 4D-diagnostics. *Proceedings of the Combustion Institute* **35** (3), 3829–3837. (70, 71)

Philip, M., Boileau, M., Vicquelin, R., Riber, E., Schmitt, T., Cuenot, B., Durox, D. & Candel, S. 2014*a* Large eddy simulations of the ignition sequence of an annular multiple-injector combustor. (166, 196, 203, and 204)

Philip, M., Boileau, M., Vicquelin, R., Schmitt, T., Durox, D., Bourgouin, J-F. & Candel, S. 2014*b* Simulation of the ignition process in an annular multiple-injector combustor and comparison with experiments. *Journal of Engineering for Gas Turbines and Power* **137** (3). (166)

Phuoc, T.X. & White, F.P. 1999 Laser induced spark ignition of ch4/air mixtures. *Combustion and Flame* **119**, 203–216. (7)

Phuoc, T.X. & White, F.P. 2002 An optical and spectroscopic study of laser-induced sparks to determine available ignition energy. *Proceedings of the Combustion Institute* **29**, 1621 – 1628. (7)

Pischinger, S. & Heywood, J. B. 1990 A model for flame kernel development in a spark-ignition engine. *Proceedings of the Combustion Institute* **23**, 1033–1040. (9)

Pitsch, H. 2006 Large Eddy Simulation of Turbulent Combustion. *Annual Review of Fluid Mechanics* **38**, 453–482. (45)

Poinsot, T. 1991 Flame ignition in a premixed turbulent flow. Annual research briefs. Center for Turbulent Research. (9)

Poinsot, T. & Lele, S. K. 1992 Boundary conditions for direct simulations of compressible viscous flows. *Journal of Computational Physics* **101**, 104–129. (81, 99, 170, 199, 241, and 247)

Poinsot, T. & Veynante, D. 2011 *Theoretical and Numerical Combustion*. Third Edition. (21, 24, 25, 28, 35, 41, 45, 46, and 66)

Poinsot, T., Veynante, D., Trouvé, A. & Ruetsch, G. 1996 Turbulent flame propagation in partially premixed flames. p. 111. Citeseer, Center for Turbulence Research, NASA Ames/Stanford Univ. (68)

Poinsot, T. J., Veynante, D. & Candel, S. 1991 Quenching processes and premixed turbulent combustion diagrams. *Journal of Fluid Mechanics* **228**, 561–606. (35, 36, 54, 65, 66, 68, 70, 100, 105, 117, 119, and 121)

Pope, S. B. 1985 Pdf methods for turbulent reactive flows. *Progress in Energy and Combustion Science* . (46)

Pope, S. B. 2000 *Turbulent Flows*. Cambridge University Press. (32, 98, 139, and 152)

Rao, K. & Lefebvre, A. H. 1976 Minimum ignition energies in flowing kerosine-air mixtures. *Combustion and Flame* **27**, 1–20. (9)

Rashkovsky, S. 1999 Spark ignition of ill-mixed gases. pp. 1403–1411. (60)

Read, R., Rogerson, J. & Hochgreb, S. 2008 Relight imaging at low temperature, low pressure conditions. (9, 75, and 186)

Read, R., Rogerson, J. & Hochgreb, S. 2010 Flame imaging of gas-turbine relight. *AIAA Journal* **48** (9), 1916–1927. (2, 75)

Reddy, H. & Abraham, J. 2011 A numerical study of vortex intereactions with flames developing from ignition kernels in lean methane-air mixtures. *Combustion and Flame* **158**, 401–415. (69)

Reddy, H. & Abraham, J. 2013 Influence of turbulence-kernel intereactions on flame development in lean methane/air mixtures under natural gas-fueled engine conditions. *Fuel* **103**, 1090–1105. (9, 69, 71, and 105)

Renou, Bruno 2001 An experimental study of freely propagating premixed flames at various lewis numbers. *Combustion Science and Technology* **162** (1), 347–370. (9, 66)

Renou, B., Boukhalfa, A., Puechberty, D. & Trinité, M. 2000 Local scalar flame properties of freely propagating premixed turbulent flames at various lewis numbers. *Combustion and Flame* **123**, 507–521. (66)

Renou, B., Samson, E. & Boukhalfa, A. 2004 An experimental study of freely propagating turbulent propane-air flames in stratified inhomogeneous mixtures. *Combustion Science and Technology* **176**, 1867–1890. (9, 67)

Richard, S., Colin, O., Vermorel, O., Benkenida, A., Angelberger, C. & Veynante, D. 2007 Towards Large Eddy Simulation of combustion in spark ignition engines. *Proceedings of the Combustion Institute* **31**, 3059–3066. (65)

Richardson, E. 2007 Ignition modelling for turbulent non-premixed flows. PhD thesis, University of Cambridge. (10)

Richardson, E. S., Chakraborty, N. & Mastorakos, E. 2007 Analysis of direct numerical simulations of ignition fronts in turbulent non-premixed flames in the context of Conditional Moment Closure. *Proceedings of the Combustion Institute* **32**, 1683–1690. (60, 63, 134, and 135)

Richardson, E. S. & Mastorakos, E. 2007 Numerical investigation of forced ignition in laminar counterflow non-premixed methane-air flames. *Combustion Science and Technology* **179**, 21–37. (72)

Richardson, J. 1922 *Weather prediction by numerical process*. Cambridge Univ Press. (32)

Roberts, W., Driscoll, J., Drake, M. & Goss, L. 1993 Images of the quenching of a flame by a vortex—to quantify regimes of turbulent combustion. *Combustion and Flame* **94** (1), 58–69. (35)

Roux, S., Lartigue, G., Poinsot, T., Meier, U. & Bérat, C. 2005 Studies of mean and unsteady flow in a swirled combustor using experiments, acoustic analysis, and Large Eddy Simulations. *Combustion and Flame* **141**, 40–54. (91, 92)

Rudgyard, M. 1993 Cell vertex methods for steady inviscid flow. In *Lectures Series 1993-04* (ed. Von Karman Institute for Fluid Dynamics), , vol. 1993-04. Von Karman Institute for Fluid Dynamics. (53)

Ruetsch, G.R., Vervisch, L. & Liñán, A. 1995 Effects of heat release on triple flames. *Physics of Fluids* **7** (6), 1447–1454. (31)

Ruith, M., Chen, P., Meiburg, E. & Maxworthy, T. 2003 Three-dimensional vortex breakdown in swirling jets and wakes: direct numerical simulation. *Journal of Fluid Mechanics* **486**, 331–378. (91)

Sagaut, P. 2002 *Large eddy simulation for incompressible flows*. Springer. (44)

Sankaran, R., Hawkes, E. R., Chen, J. H., Lu, T. & Law, C. K. 2007 Structure of a spatially developing turbulent lean methane-air Bunsen flame. *Proceedings of the Combustion Institute* **31**, 1291–1298. (50)

Schefer, R., Evans, G., anf A. Ruggles, J. Zhang & Grief, R. 2011 Ignitability limits for combustion of unintended hydrogen releases: experimental and theoretical results. *International journal of hydrogen energy* **36** (2426-2435). (132)

Schönfeld, T. & Rudgyard, M. 1999 Steady and unsteady flows simulations using the hybrid flow solver AVBP. *AIAA Journal* **37** (11), 1378–1385. (11, 53)

Selle, L., Lartigue, G., Poinsot, T., Koch, R., Schildmacher, K.-U., Krebs, W., Prade, B., Kaufmann, P. & Veynante, D. 2004 Compressible large-eddy simulation of turbulent combustion in complex geometry on unstructured meshes. *Combustion and Flame* **137** (4), 489–505. (11)

Semenov, N. 1928 Theories of combustion processes. *Z. Phys. Chem.* **48**, 571–582. (58)

Sheather, S. & Jones, M. 1991 A reliable data-based bandwidth selection method for Kernel Density Estimation. *Journal of the Royal Statistical Society* . (238)

Sher, E., Ben-Ya'ish, J. & Kravchik, T. 1992 On the birth of spark channels. *Combustion and Flame* **89**, 186–194. (64)

Shy, S., Liu, C. & Shih, W. 2010 Ignitino transition in turbulent premixed combustion. *Combustion and Flame* **157**, 341–350. (9, 62)

Silverman, B. W. 1986 *Density Estimation for Statistics and Data Analysis*. London: Chapman and Hall. (117, 238)

Sirignano, W. A. 1999 *Fluid dynamics and transport of droplets and sprays*. Cambridge Univ Press. (61)

Sloane, Thompson 1985 The effect of selective energy deposition on the homogeneous ignition of methane and its implication for flame initiation and combustion enhancement. *Combustion Science and Technology* **42**, 131–144. (65)

Smagorinsky, J. 1963 General circulation experiments with the primitive equations: 1. the basic experiment. *Monthly Weather Review* **91**, 99–164. (44)

Smith, M., Birch, A. D., Brown, D. R. & Fairweather, M. 1986 Studies of ignition and flame propagation in turbulent jets of natural gas, propane and a gas with high hydrogen content. *Proceedings of the Combustion Institute* **21**, 1403–1408. (62, 72, 132, and 213)

Soworka, T., Gerendas, M., Eggels, R.L.G.M. & Mastorakos, E. 2014 Numerical investigation of ignition performance of a lean burn combustor at sub-atmospheric conditions. pp. V04AT04A046–V04AT04A046. American Society of Mechanical Engineers. (136)

Struijs, R. 1994 A multi-dimensional upwind discretization method fot the euler equations on unstructured grids. Phd thesis, Technical University of Delft. (54)

Subramanian, V, Domingo, P & Vervisch, L 2010 Large Eddy Simulation of forced ignition of an annular bluff-body burner. *Combustion and Flame* **157**, 579–601. (10, 73, 74, 95, 105, 125, 175, and 213)

Syred, N. 2006 A review of oscillation mechanisms and the role of the precessing vortex core (PVC) in swirl combustion systems. *Progress in Energy and Combustion Science* **32** (2), 93–161. (92)

Syred, N. & Beér, J. M. 1974 Combustion in swirling flows: a review. *Combustion and Flame* **23**, 143–201. (3)

Syred, N., Chigier, N. A. & Beer, J. M. 1971 Flame stabilization in the recirculation zones of jets with swirl. *Proceedings of the Combustion Institute* **13** (1), 617–624. (3)

Teets, R. & Sell, J. 1988 Calorimetry of ignition sparks. *SAE transactions* **97**, 371–383. (6, 100, and 171)

Thevenin, D., Gicquel, O., Hilbert, R. & Veynante, D. 2002 Two- versus three-dimensional direct simulations of turbulent methane flame kernels using realistic chemistry. *Proceedings of the Combustion Institute* **29**, 2031–2039. (70)

Thiele, M., Selle, S., Riedel, U., Warnatz, J. & Maas, U. 2000 Numerical simulation of spark ignition including ionization. *Proceedings of the Combustion Institute* **28**, 1177–1185. (64)

Thiele, M., Warnatz, J., Dreizler, A., ad R. SchieBl, S. Lindenmaier, Maas, U., Grant, A. & Ewart, P. 2002 Spark ignited hydrogen/air mitures: two dimensional detailed modeling and laser based diagnostics. *Combustion and Flame* **128**, 74–87. (64)

Tomlin, A. S., Pilling, M. J., Turányi, T., Merkin, J. H. & Brindley, J. 1992 Mechanism reduction for the oscillatory oxidation of hydrogen: sensitivity and quasi-steady-state analyses. *Combustion and Flame* **91** (2), 107–130. (49)

Tresca, H. 1864 Memoire sur l'écoulement des solides à de forte pressions. *Acad. Sci. Paris* **2** (1), 59. (190)

Triantafyllidis, A., Mastorakos, E. & Eggels, R.L.G.M. 2009 Large Eddy Simulation of forced ignition of a non premixed bluff-body methane flame with conditional moment closure. *Combustion and Flame* **156**, 2328–2345. (10, 74, and 95)

Trunk, PJ, Boxx, I, Heeger, C, Meier, W, Böhm, B & Dreizler, A 2013 Premixed flame propagation in turbulent flow by means of stereoscopic PIV and dual-plane OH-PLIF at sustained kHz repetition rates. *Proceedings of the Combustion Institute* **34** (2), 3565–3572. (70)

Vasquez-Espi, C. & Linan, A. 2002 Thermal-diffusive ignition and flame initiation by a local energy source. *Combustion Theory and Modelling* **6**, 297–315. (9, 58, and 59)

Vasudeo, N., Echekki, T., Day, M. & Bell, J. 2010 The regime diagram for premixed flame kernel-vortex interactions-revisited. *Physics of Fluids* **22**. (68, 69, 70, and 154)

Veynante, D., Fiorina, B., Domingo, P. & Vervisch, L. 2008 Using self-similar properties of turbulent premixed flames to downsize chemical tables in high-performance numerical simulations. *Combustion Theory and Modelling* **12** (6), 1055–1088. (49)

Veynante, D. & Vervisch, L. 2002 Turbulent combustion modeling. *Progress in Energy and Combustion Science* **28**, 193 – 266. (45)

Veynante, D., Vervisch, L., Poinsot, T., Linan, A. & Ruetsch, G. 1994 Triple flame structure and diffusion flame stabilization. Annual research briefs. Center for Turbulent Research. (30)

Vicquelin, R., Fiorine, B., Payet, S., Darabiha, N. & Gicquel, O. 2011 Coupling tabulated chemistry with compressible CFD solvers. *Proceedings of the Combustion Institute* **33**, 1481–1488. (199, 204)

Wang, G., Boileau, M. & Veynante, D. 2011 Implementation of a dynamic thickened flame model for Large Eddy Simulations of turbulent premixed combustion. *Combustion and Flame* **158** (11), 2199 – 2213. (48)

Weckering, J., Sadiki, A., Janicka, J., Mastorakos, E. & Eggels, R.L.G.M. 2011 A forced ignition probability analysis method using LES and Lagrangian particle monitoring. *Proceedings of the Combustion Institute* **33**, 2919–2925. (135)

Weigand, P., Meier, W., Duan, X.R., Stricker, W. & Aigner, M. 2006 Investigations of swirl flames in a gas turbine model combustor: I. flow field, structures, temperature, and species distributions. *Combustion and Flame* **144** (1-2), 205–224. (78)

Weiss, M., Zarzalis, N. & Suntz, R. 2008 Experimental study of markstein number effects on laminar flamelet velocity in turbulent premixed flames. *Combustion and Flame* **154**, 671–691. (66)

Williams, F. A. 1985 *Combustion Theory*. Menlo Park, CA: Benjamin Cummings. (27, 30, 47, and 60)

Wilson, C.W., Sheppard, C.G.W. & Low, H.C. 1999 A novel technique for predicting the ignition performance of an aero gas turbine combustion chamber. (10, 134, and 152)

Wolf, P., Staffelbach, G., Gicquel, L.Y.M., Muller, J-D. & Poinsot, T. 2012 Acoustic and Large Eddy Simulation studies of azimuthal modes in annular combustion chambers. *Combustion and Flame* **159**, 3398–3413. (11)

Xiong, Y. & Roberts, L. 2002 Obsevations on the interaction between a premixed flame kernel and a vortex of different equivalence ratio. *Proceedings of the Combustion Institute* **29**, 1687–1693. (68)

Xiong, Y., Roberts, L., Drake, M. & Fansler, T. 2001 Investigation of premixed flame kernel-vortex interactions via high-speed imaging. *Combustion and Flame* **126**, 1827–1844. (68)

Yamashita, H, Shimada, M & Takeno, T 1996 A numerical study on flame stability at the transition point of jet diffusion flames. *Proceedings of the Combustion Institute* **26** (1), 27–34. (112, 190)

Zeldovich, Ya.B., Barenblatt, G.I., Librovitch, B.V. & Mikaviladze 1980 *Mathematical Theory of Combustion and Explosion*. Moscow: Nauka. (9, 59)

Zeldovitch, Y. & Frank-Kamenetskii, D. A. 1938 A theory of thermal propagation of flame. *Acta Phisicochimica USSR* **9** (2). (22, 23)

Ziegler, G. F. W., Wagner, E. P. & Maly, R. R. 1985 Ignition of lean methane-air mixtures by high pressure glow and arc discharges. *Proc. Combust. Inst.* **20**, 1817–1824. (9, 60, and 62)

Appendix A

Kernel Density Estimation

A classical method to estimate the Probability Density Function (PDF) of a dataset consists in constructing an histogram: the range spanned by the variable is divided by N and the PDF is estimated simply by counting the number of events in each resulting bin. Such method is very simple to implement, but is very sensitive to the number of bins, especially when the number of sampled is limited. When constructing joint-PDF, this drawback become more problematic.

A solution to overcome this issue is to use a technique called Kernel Density Estimation (KDE) which provide accurate estimations of the PDF regardless the number of samples. Let's consider the dataset of the variable ϕ with a true PDF called f_ϕ. The estimation of this PDF is called f_h and is obtained by combining multiple local probability shapes, known as kernels, as shown in Fig. A.1:

$$f_h(\phi) = \frac{1}{N}\sum_{n=1}^{N} K_h(\phi - \phi_n) \quad \text{with -} \quad K_h(\phi - \phi_i) = \frac{1}{h}K\left(\frac{\phi - \phi_n}{h}\right) \tag{A.1}$$

where K_h is called the kernel function and h is bandwidth or smoothing factor. The kernel function essentially spreads the probability associated with each sample to its neighborhood.

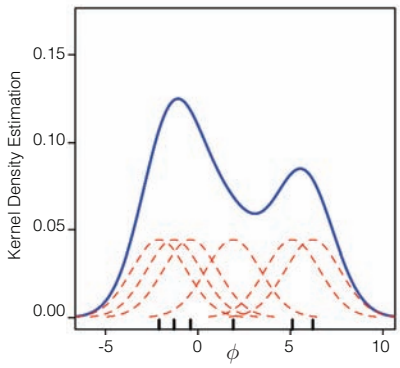

Figure A.1: KDE methodology illustration. Black tick: sample values, red dashed line: kernel associated with each sample, blue line: PDF estimation.

Several kernel function are presented in the literature, but the most widely used is the normal distribution since it provides simple theoretical results. The kernel is smoothed by a factor h which has to be chosen by the user. Nevertheless, this parameter can be evaluated analytically from an optimization of the error between f_α and f_h, leading to an optimal value:

$$h_{opt} = \left(\frac{\mathcal{R}(K)}{\mu_2(K)^2 \mathcal{R}(f''_\phi) N} \right)^{1/5} \tag{A.2}$$

where $\mathcal{R}(g) = \int g(x)^2 dx$ and $\mu(g) = \int x^2 g(x)$.

Obviously, the optimal smoothing factor cannot be rigorously obtained since the true PDF f_ϕ is not known so does its second derivative. An iterative procedure can be constructed by assuming that $f''_\phi \simeq f''_h$. During this work, two methods have been used to estimate the bandwidth h:

- The rule of thumb estimation proposed by Silverman (1986) is a fully analytical formula assuming that the true PDF follows a Gaussian distribution. This method give good result for single mode distribution, but can induce significant error when dealing with multimodal distributions. The bandwidth is given by:

$$h_{opt} = \left(\frac{4.med(\|\phi - med(\phi)\|)}{3.0.6745.N} \right)^{1/5} \tag{A.3}$$

  where med designates the median operator.

- A plug-in method proposed by Sheather & Jones (1991) which requires to solve a minimization problem. This method generally lead to smaller h and is better suited to evaluate multimodal distribution.

In both cases, the bandwidth h is defined using only the sample data ϕ and not the grid resolution on which the PDF will be estimated (corresponding to the number of bins for a classic histogram). Therefore, increasing the resolution of the PDF does not change the estimation of the PDF since h is unchanged (only data can modify its value).

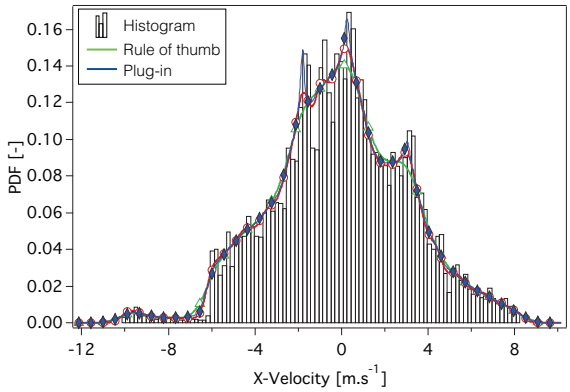

Figure A.2: Exemple of KDE estimations compared to a classical histogram.

Appendix B

Flame displacement speed in TFLES

The notion of flame displacement speed introduced in Sec. 3.2.1.b has been used to analyze DNS data (Gran *et al.*, 1996; Chen & Im, 1998; Echekki & Chen, 1999) and is at the basis of level-set combustion models for LES. Post-processing LES data using S_d has not been done so far, in particular using the DTFLES model. The aim here is to derive the flame displacement speed from AVBP equations and evaluate the capability of the analysis to investigate flame propagation and quenching. To do so, two simple test case are conducted to verify that the computation of S_d is consistent with theoretical results and applied to a 3D turbulent ignition case to evaluate S_d change through the flame front.

B.1 Theoretical framework

To evaluate the flame kernel displacement and in particular the motion of the flame front, LES data are analyzed using the notion introduced in Sec. 3.2.1.b. To do so, the progress variable c must be define. As pointed out by Hélie & Trouvé (1998), the definition of the progress variable must be adapted to partially premixed combustion. Three definitions have been tested in this work based on the reduced temperature:

$$c = \frac{\widetilde{T} - T^0}{T_{ad} - T^0} \tag{B.1}$$

where the three definitions differ depending on the adiabatic flame temperature evaluation:

- A) T_{ad} is kept constant with its value obtained from stoichiometric conditions
- B) adiabatic flame temperature is derived from a single step infinitely fast reaction rate assumption at the local value of z following the equilibrium Burke-Schumann limit:

$$T_{ad}(z) = \begin{cases} T^0 + \frac{z}{z_{st}}(T_{ad}(z_{st}) - T^0) & \text{if } z < z_{st} \\ T_{ad}(z_{st}) + \frac{1-z}{z_{st}}(T_{ad}(z_{st}) - T^0) & \text{if } z_{st} < z < 1 \end{cases} \tag{B.2}$$

- C) T_{ad} is tabulated from the 2S_CH4_BFER scheme and can significantly differ from the previous definition.

A comparison of these definitions is showed in Fig. B.1. The first definition is the only one that guarantee c bounded between 0 and 1: because of mixing within and after the flame front, the local value of T_{ad} obtained from z can differs from the actual burned mixture. As the mixture fraction differs from its stoichiometric value, the offset between the various definitions increases.

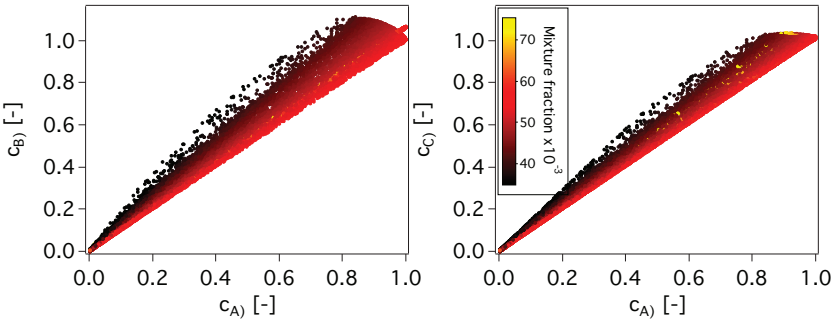

Figure B.1: Comparison of the various definition of the progress variable c: B) versus A) (left), C) versus A) (right).

Since it is the only definition ensuring that c is bounded between 0 and 1, definition A) has been used in this thesis.

Using Eq. (B.1) and Eq. (3.14), S_d is defined as:

$$S_d = \frac{1}{|\boldsymbol{\nabla}\widetilde{\boldsymbol{T}}|}\frac{D\widetilde{T}}{Dt} \tag{B.3}$$

Starting from the energy equation of AVBP written in temperature, and neglecting the pressure and viscous heating term, S_d can be expressed as follows (using the notations of Sec. 4.2.2):

$$S_d = \frac{1}{\overline{\rho}\overline{C_p}|\boldsymbol{\nabla}\widetilde{\boldsymbol{T}}|}\left[\frac{\mathcal{E}}{\mathcal{F}}\dot{\omega}'_T + \boldsymbol{\nabla}\cdot(\mathcal{E}\mathcal{F}\lambda\boldsymbol{\nabla}\widetilde{\boldsymbol{T}}) - \boldsymbol{\nabla}\widetilde{\boldsymbol{T}}\left(\sum_{k=1}^{N} C_{p,k}\overline{J}_{i,k}\right)\right] \tag{B.4}$$

where $\mathcal{E}$ and $\mathcal{F}$ are the DTFLES efficiency function and thickening factor respectively. This definition is very close to the general definition given in Eq. (3.15) but with an additional term for the transport of heat due to species diffusion. Following the splitting performed in Sec. 3.2.1.b, the components of S_d are:

$$S_r = \frac{\mathcal{E}}{\mathcal{F}}\frac{\dot{\omega}'_T}{\overline{\rho}\overline{C_p}|\boldsymbol{\nabla}\widetilde{\boldsymbol{T}}|} \tag{B.5}$$

$$S_{diff,t} = -\mathcal{E}\mathcal{F}D_{th}\boldsymbol{\nabla}\cdot\boldsymbol{n} \tag{B.6}$$

$$S_{diff,n} = \frac{\boldsymbol{n} \cdot \boldsymbol{\nabla}(\overline{\rho}\mathcal{E}\mathcal{F}D_{th}\boldsymbol{n} \cdot \boldsymbol{\nabla}\widetilde{\boldsymbol{T}})}{\overline{\rho}\overline{C_p}|\boldsymbol{\nabla}\widetilde{\boldsymbol{T}}|} \tag{B.7}$$

where the flame normal $\boldsymbol{n}$ is evaluated from the normalized gradient of c. Another interesting value is the mean flame curvature estimated from the divergent of $\boldsymbol{n}$:

$$\mathcal{K} = \frac{1}{2}\boldsymbol{\nabla} \cdot \boldsymbol{n} \tag{B.8}$$

B.2 1D laminar test case

The first, and most simple test case is the 1D laminar steady flame. To evaluate the effect of the thickening, two 1D grids are used: a first grid with a resolution sufficient to fully resolve the flame front (using the 2S_CH4_BFER mechanism) without thickening and a second grid 4 times coarser for which the flame front must be thickened by 4. A post-processing library has been developed to perform the computations presented above.

B.2.1 Set-up

A 1D methane flame at atmospheric conditions (300 K, 1 Atm) and $\phi = 0.8$ is computed on a 20 mm long domain (about 32 $\delta_L^0 = 0.62$ mm). The characteristics of the two grids are listed in Tab. B.1 and the numerical parameter of AVBP in Tab. B.2. Note that AVBP does not handle 1D domain so a pseudo-1D computation of performed with only 1 cell in the vertical direction and symmetry conditions on the upper and lower boundaries.

	Nb. elements	Nb. vertices	Δ_x
Fine	400	801	$5\,e^{-5}$
Coarse	100	201	$2\,e^{-4}$

Table B.1: Characteristics of the pseudo-1D meshes

	Numerical parameter
Convection scheme	TTGC: $\mathcal{O}(3)$ in space & time (Colin & Rudgyard, 2000)
Diffusion scheme	2Δ operator
SGS model	None
Artif. viscosity	Colin model: $\epsilon^{(2)} = 0.00$, $\epsilon^{(4)} = 0.005$
	Boundary conditions
Right: Inlet	NSCBC (Poinsot & Lele, 1992) (velocity)
Left: Outlet	NSCBC (3D) (Granet *et al.*, 2010) (pressure)
Up/Down:	Symmetry

Table B.2: Numerical parameters of AVBP.

B.2.2 Results

The results obtained on the *Fine* grid are presented in Fig. B.2. The left graph shows the classical structure of the laminar flame while the left graph shows the evaluation of the displacement speed terms as function of the progress variable.

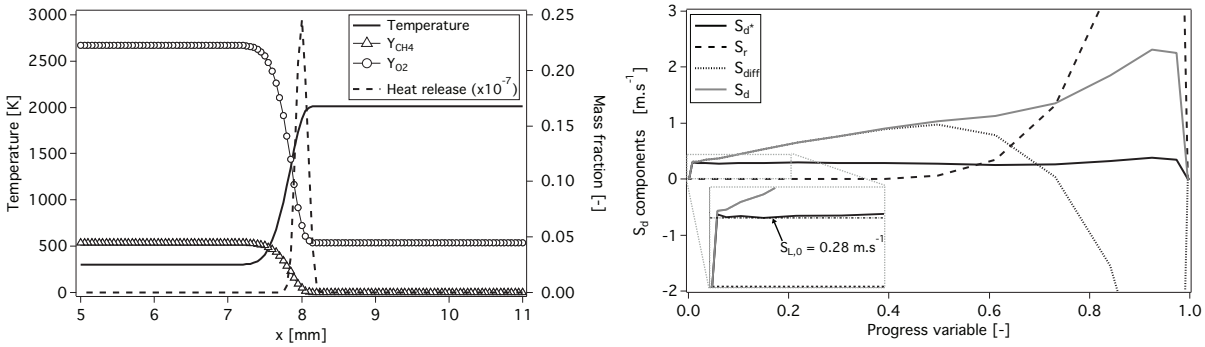

Figure B.2: *Fine* grid: laminar methane/air flame (left), evolution of displacement speed components as function of c (right).

The flame structure demonstrate that the resolution of the *Fine* grid is sufficient to reproduce the heat release peak with more than 5 points. The main two components of S_d are found to evolve in opposite direction:

- the reaction therm S_r is null in the preheat zone and start increase above $c = 0.5$. It reaches very high value near the position of maximum heat release ($S_{r,max} \simeq 6m.s^{-1}$).
- the diffusion term (here the tangential part is null) dominates in the preheat zone and became negative past the inflection point of the temperature slope. It compensates the high positive value of S_r at the reactive part of the flame.

The evolution of the two terms clearly distinguish the convective-diffusive processes of the flame displacement in the preheat zone and the reactive-diffusive in the reactive and post-flame region. S_d is found to progressively increase across the flame front, mainly due to the burnt gases expansion as demonstrated by the curve of S_d^*. The density-weighted displacement speed is found nearly constant through the flame front and its value matches the consumption speed estimation obtained from the methane balance S_c. To evaluate if the thickening coefficient appearing in Eq. (B.4) have an effect on the result, Fig. B.3 shows the same results obtained on the *Coarse* grid, where a constant thickening of 4 has been applied.

The flame structure is clearly thicker than the non-thickened counterpart, but the various contributions of S_d are found similar to the DNS case. From the expression of the displacement speed components presented in the previous Section, the $|\boldsymbol{\nabla}\widetilde{\boldsymbol{T}}|$, $\dot{\omega}_T'$ and the laminar viscosity are plotted in Fig. B.4: the reduction of the heat release rate, temperature gradient are compensated by the increase in viscosity so that the flame displacement speed is maintain through the flame front.

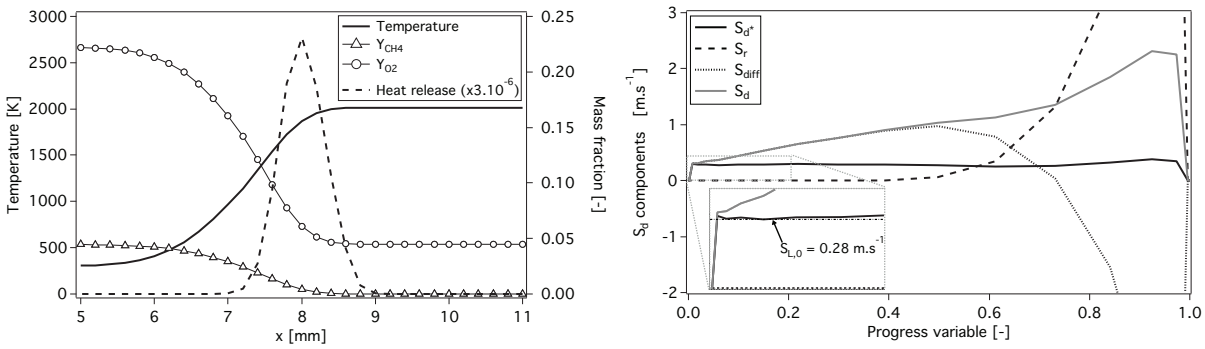

Figure B.3: *Coarse* grid: laminar methane/air flame (left). Evolution of displacement speed components as function of c (right).

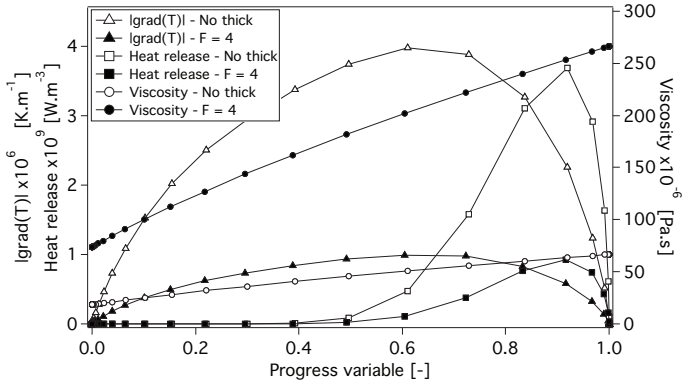

Figure B.4: Comparison of the flame structure in c space on the *Fine* and *Coarse* grids.

B.3 2D cylindrical case

The second test case is a cylindrically expanding flame front in a 2D configuration. Once again two grid resolutions are used: a fine grid where the resolution sufficient to fully resolve the flame front (using the 2S_CH4_BFER mechanism) without thickening and a second grid 4 times coarser for which the flame front must be thickened by 4. Note that the aim here is not to evaluate the stretch response of the 2S_CH4_BFER mechanism, but to evaluate the change in the flame structure as described using S_d due to thickening of the flame front.

B.3.1 Set-up

The 40 mm square 2D computational domain is initially filled with methane at atmospheric conditions (300 K, 1 Atm) and $\phi = 0.8$. The characteristics of the two grids are listed in Tab. B.3 and the numerical parameter of AVBP in Tab. B.4. Combustion is initiated with a burnt gases

volume at the center of the domain with an hyperbolic tangent profile:

$$\psi = \psi_0 + (\psi_1 - \psi_0)\frac{1}{2}\left(1 - \tanh\left(\frac{r - 0.8r_0}{0.0758r_0}\right)\right) \tag{B.9}$$

where the 0 and 1 subscript denote the fresh and burn state of any variable ψ respectively and $r_0 = 5\ mm$ is the initial hot spot size.

	Nb. elements	Nb. vertices	Δ_x
Fine	640000	641601	$2.5\,e^{-9}$
Coarse	40000	40401	$4\,e^{-8}$

Table B.3: Characteristics of the 2D meshes

	Numerical parameter
Convection scheme	TTGC: $\mathcal{O}(3)$ in space & time (Colin & Rudgyard, 2000)
Diffusion scheme	2Δ operator
SGS model	None
Artif. viscosity	Colin model: $\epsilon^{(2)} = 0.00$, $\epsilon^{(4)} = 0.005$
	Boundary conditions
All boundaries	NSCBC (3D) (Granet *et al.*, 2010) (pressure)

Table B.4: Numerical parameters of AVBP.

B.3.2 Results

As a first step, Fig. B.5 shows the temporal evolution of the mean curvature, tangential strain rate and stretch over the whole flame front. Because the initial hyperbolic tangent profile is thiner that the thickened flame thickness, the flame front structure of the coarse case is modified at first. The growth of the flame kernel on the coarse mesh is then delayed and the tangential strain rate experienced at first differs, but the same behavior is observed at later time ($t > 2$ ms). As the kernel expands, the curvature decreases as $1/r_{ker}$ and the strain rate is lower at first since the divergence of the velocity field is altered by the delayed kernel growth.

To investigate the evolution of the flame characteristics across the flame brush, conditional c averaged values of the FSD, curvature, S_d^* and $S_{diff,t}$ are plotted at three instants in Figs. B.6 & B.7. The values of the FSD are coherent with the thickening applied on the flame front and no transient effect are observed (all three instants are superimposed). Curvature decreases with time and at $t = 2.0$ ms, the value obtained on the coarse mesh is significantly higher than the one obtained on the fine grid since the kernel development is delayed in the coarse case. The thicker flame in the coarse case leads to a larger variation of curvature across the flame front, with higher value on the burnt gases side.

In the fine case, S_d^* varies between 0.24 and 0.31 m.s^{-1} across the flame front, but the 3 instants (corresponding to 3 levels of stretch) are superimposed, indicating that S_d^* variations across the flame front are only marginally affected by the stretch (at least in the range of stretch investigated here). On the contrary, in the coarse case S_d^* variations across the flame front change

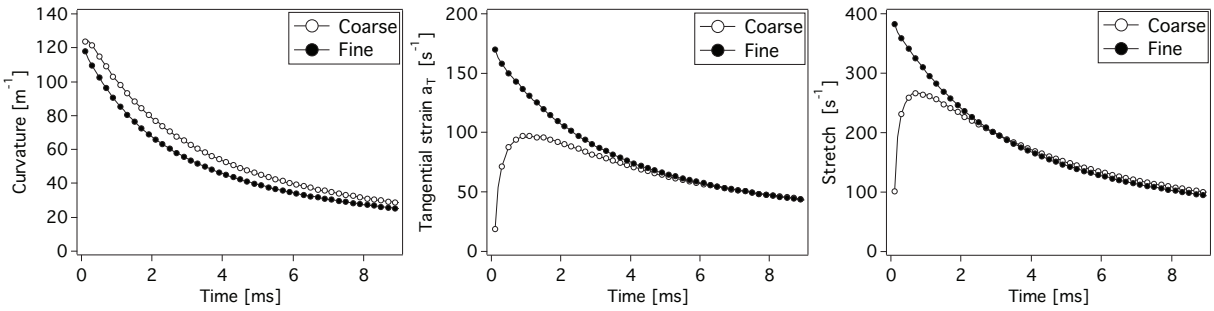

Figure B.5: Temporal evolutions of the mean curvature, tangential strain and stretch over the whole flame front for both coarse and fine cases.

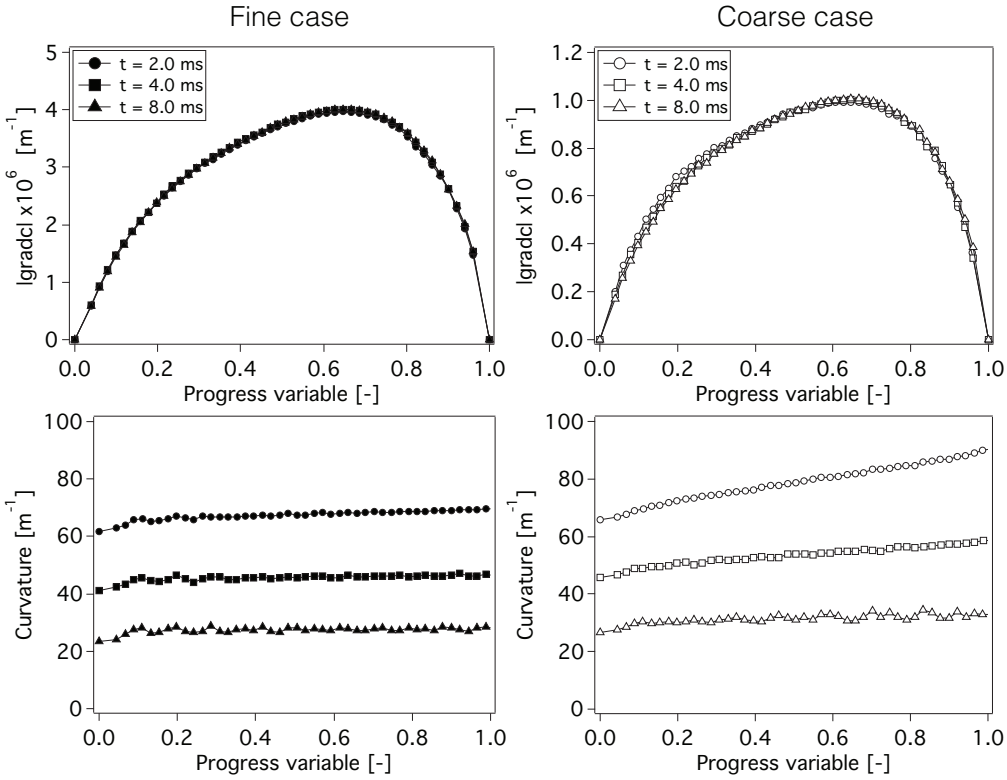

Figure B.6

with stretch: variations of S_d^* between 0.19 and 0.33 m.s^{-1} are observed for high stretch (small time) but the variations are similar to the fine case for low stretch (longer time). The differences between the fine and coarse cases are related to the effect of curvature through the tangential diffusion as shown with the conditional mean evolution of $S_{diff,t}$. From Eq. (B.6) one can see that the flame response to curvature is directly proportional to the thickening factor.

The main effect of thickening on the flame displacement speed is to increase the flame response

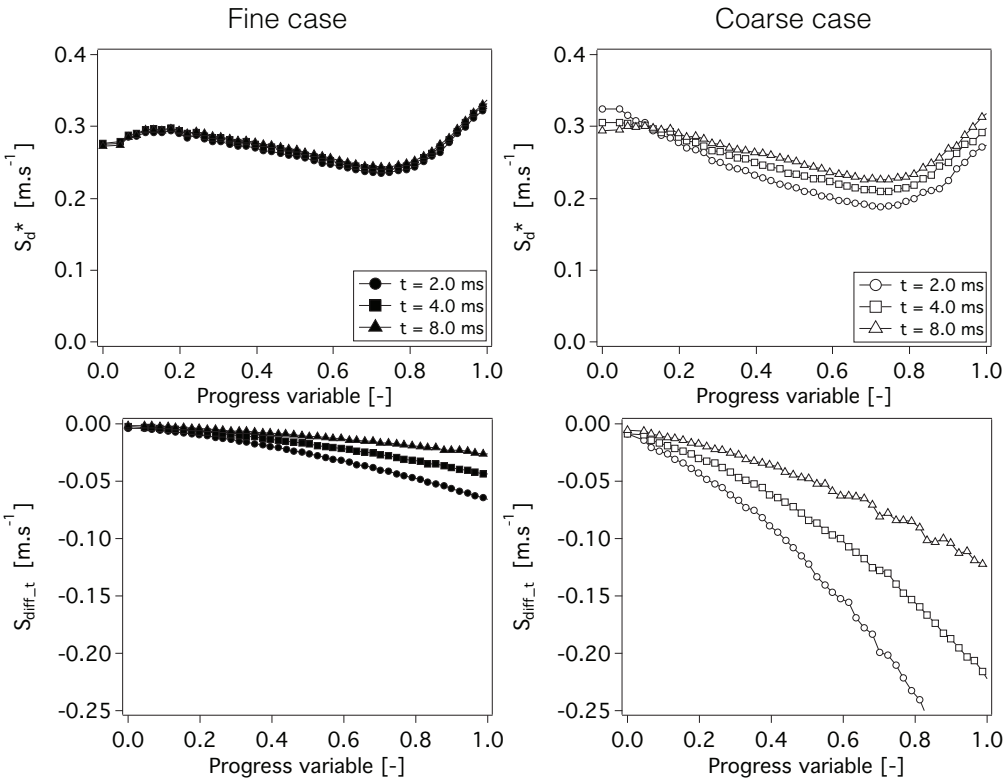

Figure B.7

to curvature, resulting in lower values of S_d^*. This simple case also highlights the detrimental effect of the flame front thickening on the ignition process: for curved flame front, thickening increases both the normal diffusion, which is desirable to recover the laminar flame speed, and the tangential diffusion, which modifies the energy balance of the kernel.

B.4 3D turbulent ignition case

Finally, the turbulent flame propagation following ignition in the KIAI experiment is studied using the flame displacement speed and its components. To minimize to effect of the partial premixing, the case studied is an ignition at PT3.

B.4.1 Set-up

The numerical set-up is the one used in Chap. 7 and the numerical parameters of the computation are listed in Tab. B.5. The DTFLES model is employed with the efficiency function of Charlette *et al.* (2002) and the model parameters are tabulated from a collection of laminar unstrained 1D flame as described in Sec. 7.3.3. Ignition is triggered by the ED model of Lacaze *et al.* (2009*b*)

using $\epsilon_i \simeq 29\ mJ$, $\Delta_t = 100\ \mu s$ and $\Delta_s = 7.5\ mm$.

	Numerical parameter
Convection scheme	TTGC: $\mathcal{O}(3)$ in space & time (Colin & Rudgyard, 2000)
Diffusion scheme	2Δ operator
SGS model	WALE (Nicoud & Ducros, 1999)
Artif. viscosity	Colin model: $\epsilon^{(2)} = 0.01$, $\epsilon^{(4)} = 0.005$
	Boundary conditions
CH_4 inlet	NSCBC (Poinsot & Lele, 1992) (velocity, 10% turbulence)
Air inlet	NSCBC (Poinsot & Lele, 1992) (velocity)
Outlet	NSCBC (3D) (Granet *et al.*, 2010) (pressure)
Walls	Adiabatic non-slipping walls

Table B.5: Numerical parameters of AVBP.

B.4.2 Results

In order to focus on the flame self-propagation, the flame kernel is not studied from the start since the energy deposit induces temperature much higher than the adiabatic flame temperature and enhances the early kernel growth. As the first step, the flame structure is plotted in Fig. B.8 with conditional averaged evolution of FSD, heat release rate and fuel and oxidizer mass fractions. The flame structure is similar to that of the laminar flame reported in Fig. B.4 with a broadening of the reactive layer.

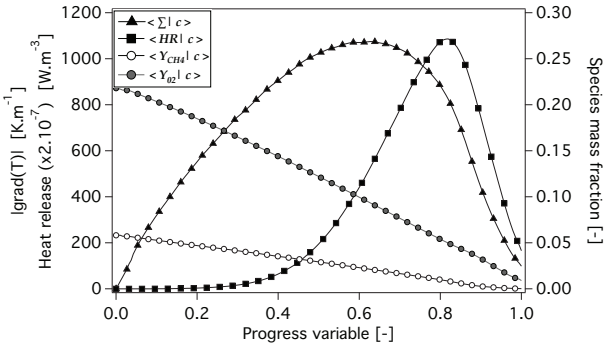

Figure B.8: Turbulent flame brush structure as conditional mean of the FSD, heat release rate and species mass fraction as function of c.

The components of S_d plotted in Fig. B.9(left) have a similar evolution across the flame front as the two previous laminar cases. The flame displacement is completely controlled by the diffusion process in the preheat zone and the reaction term becomes dominant above $c = 0.6$. The magnitude of the component however is much higher than the laminar flames reported in Fig. B.3. Fig. B.9(right) focus on the evolution of the density-weigthed displacement speed which is found to increase of a significant amount through the flame front but to be fairly constant in the $0.1 < c < 0.6$ range. The value of S_d^* is higher than the laminar flame speed and corresponds

to the turbulent flame speed $\mathcal{E}.S_L^0$ modulated by the effect of curvature and strain. Note that the conditional mean gives a smooth evolution of the S_d components, but local values exhibit large dispersion due to locally strong curvature or strain rate.

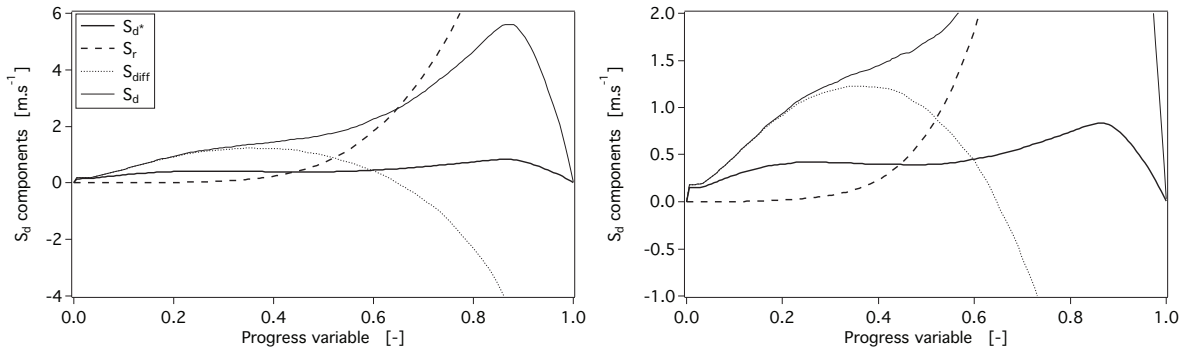

Figure B.9: Evolution of the conditional mean displacement speed components as function of c (left). Focus on the evolution of S_d^* (right).

B.5 Conclusion

An expression for the flame displacement speed S_d is obtained from AVBP energy transport equation, including the thickening factor $\mathcal{F}$ and efficiency function $\mathcal{E}$. The effect of the flame front thickening on the evolution of S_d across the flame front is negligible in a 1D laminar unstretched flame, but to be strong for a 2D stretched flame, especially regarding the flame response to curvature. At a given level of curvature, S_d is lower for the thickened flame as a consequence of a higher tangential diffusion. Variation of S_d across a turbulent flame brush is then evaluated and is coherent with the results obtained on the 1D laminar flame.

Abstract

For safety reasons, in-flight relight of the engine must be guaranteed over a wide range of operating conditions but the increasing stringency of pollutant emission constraints requires the development of new aero-engine combustor whose design might be detrimental to the ignition capability. To improve the knowledge of the ignition process in aeronautical gas turbines and better combine conflicting technological solutions, current research relies on both complex experimental investigations and high fidelity numerical simulations. In this work, numerical study of the ignition process in gas turbines from the energy deposit to the light-around is performed with several objectives: increase the level of confidence of Large Eddy Simulations tool for the analysis of the ignition process, investigate the mechanisms controlling ignition in conditions representative of realistic aeronautical gas turbine flows and improve the low-order methodologies for the prediction of ignition performance. In a first part, LES of the single burner installed at CORIA (France) is carried out and allows to highlight the LES accuracy and to build a database on which the main mechanisms controlling the ignition success are identified. Based on these results, a methodology is developed to predict the ignition performance at a low computational cost using the non-reacting flow statistics only. In a second part, the light-around process is studied on two experimental set-ups and the very good agreement of the LES results with experiments is the starting point from an analysis of the mechanisms driving the flame propagation process.

Keywords: Ignition, Gas turbines, Light-around, Large Eddy Simulations, Turbulent combustion

Résumé

Pour des raisons de sécurité, les moteurs aéronautiques doivent pouvoir redémarrer en vol sur toute leur plage d'opération. Mais les contraintes sur les émissions polluantes nécessitent le dévelopement de nouvelles chambres de combustion dont la conception peut détériorer les capacités d'allumage du moteur. Afin d'améliorer la compréhension du processus d'allumage et d'aider à l'optimization de la conception, les recherches actuelles combinent les des études expérimentales de plus and plus complexes et les simulation numériques hautes fidélités. Dans ce travail, l'étude numérique du processus d'allumage des chambres de combustion aéronautiques, de l'tincelle la propagation azimutale de la flamme, est conduite avec plusieurs objectifs: améliorer la robustesse et la confiance de l'outil LES pour l'étude de l'allumage, étudier les mécanismes qui affectent l'allumage dans des conditions représentatives des conditions réelles et enfin améliorer les méthodes bas-ordre pour la prédiction des performances d'allumage. Dans une premiére partie, la SGE d'un monobruleur installé au CORIA permet de mettre en évidence les bons résultats de la LES et de construire une base de données pour l'analyses des mécanismes d'extinction. Ces données sont aussi utilisées pour developper une méthodologie permettant de prédire les performances d'allumage à bas coût en utilisant les résultats d'une SGE non-réactive. Dans une seconde partie, la propagation inter-secteur est investiguée par l'étude de deux cas expérimentaux et la SGE est capable de reproduire les modes de propagation mais aussi les temps d'allumage avec précision. Sur la base de ces bons résultats, une analyse plus fine de la simulation permet d'identifier les mécanismes qui contrôlent la propagation de la flamme.

Mots-clés: Allumage, Turbine à gas, Propagation inter-secteur, Simulation aux Grandes Echelles, Combustion turbulente